JOURNAL OF THE

Electrochemical Society

l. 112, No. 2 February 1965 in Two Parts — Part I

Part II, 1964 Index — See Inside Back Cover

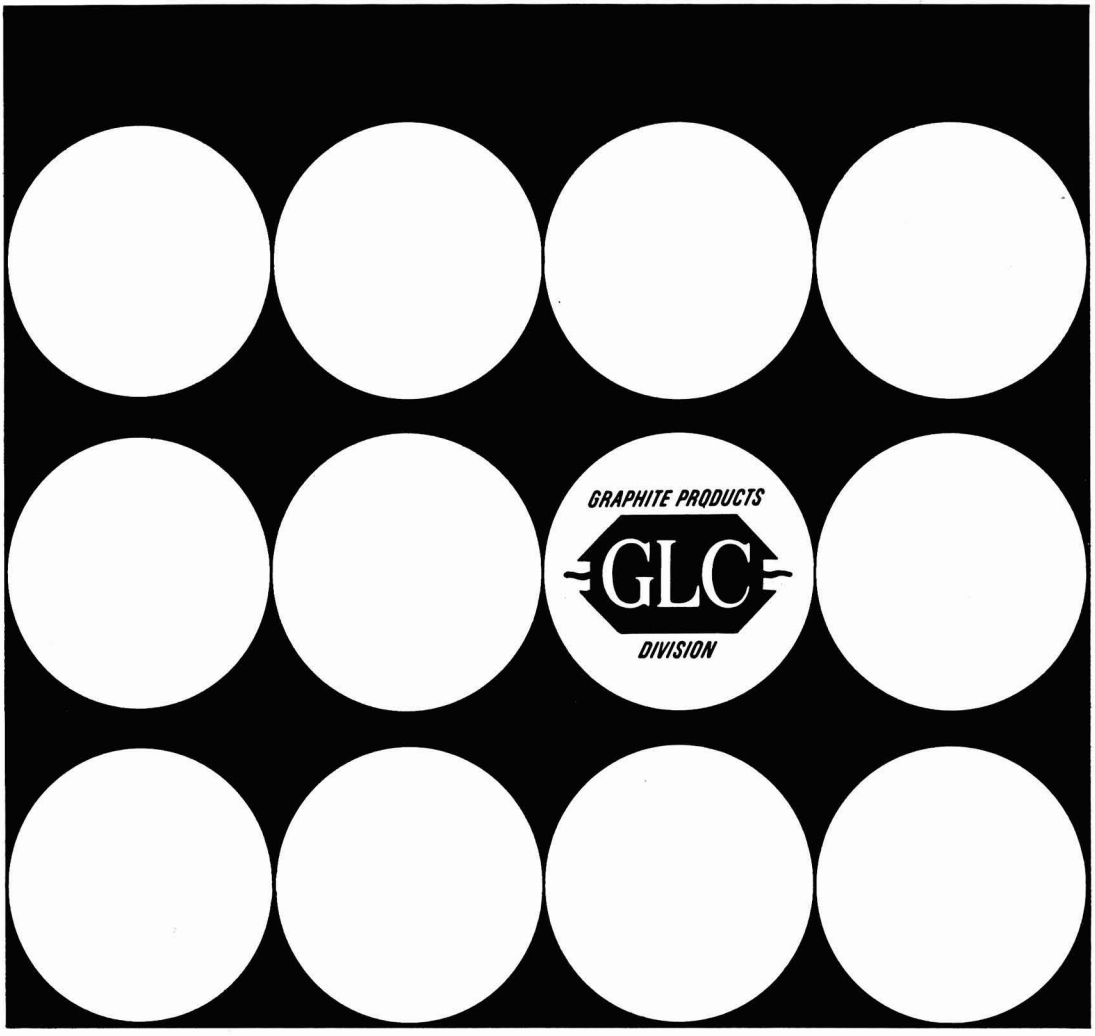

GLC ANODES:

pacesetters of dependability in serving chlor-alkali producers.

PRODUCTS YOU CAN TRUST
GRAPHITE PRODUCTS GLC DIVISION

GREAT LAKES CARBON CORPORATION
18 East 48th Street • New York, N.Y. 10017
OFFICES AND AGENTS IN PRINCIPAL CITIES AROUND THE WORLD

Great Lakes Carbon Corporation is one of the world's largest manufacturers of graphite for electrochemical and electrothermic processes—and for aerospace, nuclear, metallurgical and other industrial uses.

WHAT MAKES A STACKPOLE ANODE BETTER?

Rigid processing control. At Stackpole, close supervision of mixing, baking, graphitizing and impregnating produces a product of the highest quality and uniformity.

For instance, Stackpole's oil treating process impregnates the anode for keeps. Bleeding during operation is cut to a minimum. This means fewer diaphragm changes for you . . . longer cell life, lower maintenance costs.

Stackpole GraphAnodes® can be designed with any feature you need, such as holes, slots or bevels. Careful planing of all anode surfaces insures perfect cell alignment for maximum efficiency and life.

Let us tell you more about the difference in GraphAnodes, write: Stackpole Carbon Company, Carbon Division, St. Marys, Pa. Phone: 814-834-1521 TWX: 814-826-4808.

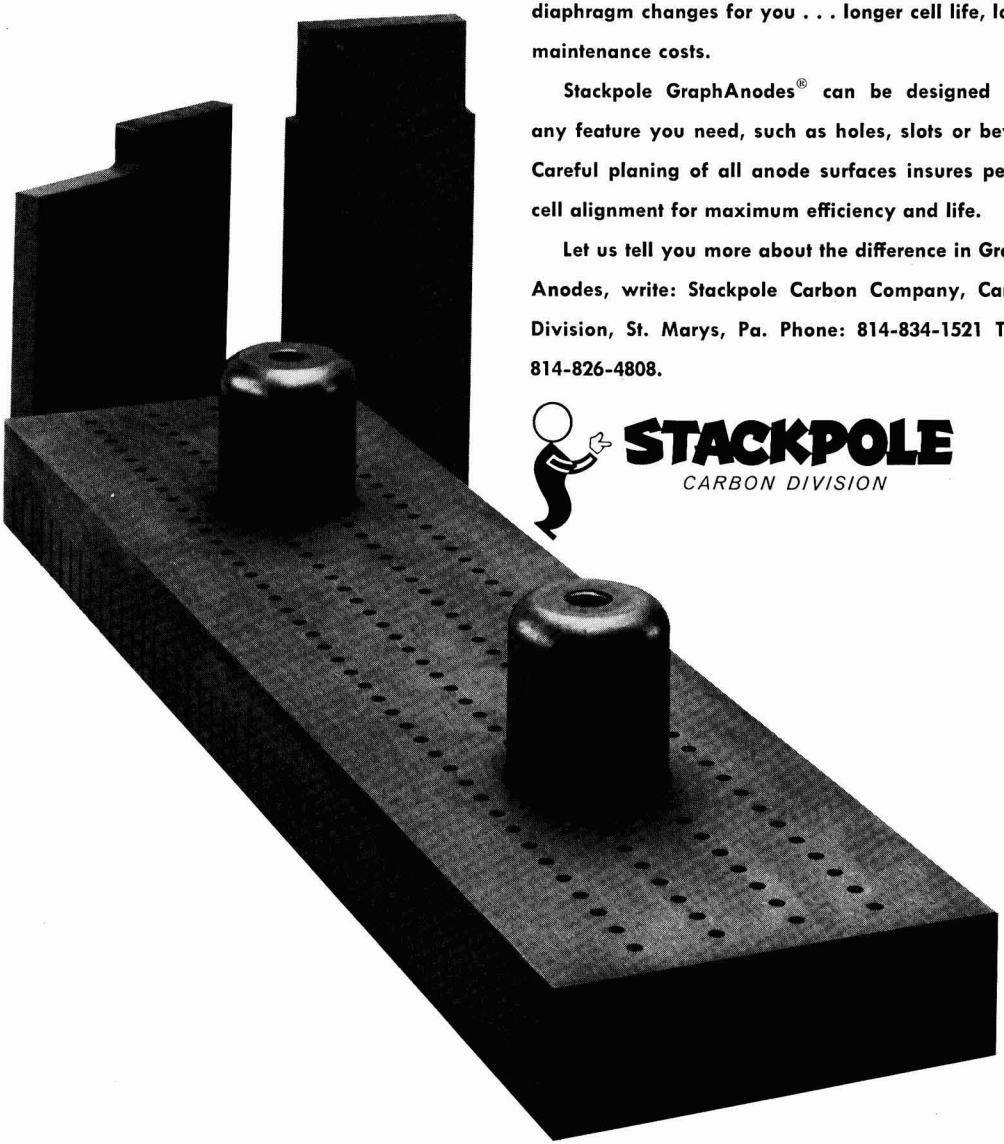

STACKPOLE
CARBON DIVISION

JOURNAL OF THE

C. L. Faust, Chairman, Publication Committee
R. A. Kolbe, Manager of Publications

FEBRUARY 1965

EDITORIAL

TECHNICAL PAPERS

ELECTROCHEMICAL SOCIETY

VOL. 112 • NO. 2

Manuscripts submitted to the Journal should be sent, in triplicate, to the Editorial Office at 30 East 42 St., New York, N. Y., 10017. They should conform to the revised Instructions to Authors published on pp. 35C-36C of this issue. Manuscripts so submitted become the property of The Electrochemical Society and may not be published elsewhere, in whole or in part, unless permission is requested of and granted by the Editor.

The Electrochemical Society does not maintain a supply of reprints of papers appearing in its Journal. A photoprint copy of any particular paper, however, may be obtained by corresponding direct with the Engineering Societies Library, 345 E. 47 St., New York, N. Y., 10017.

Inquiries re positive microfilm copies of volumes should be addressed to University Microfilms, Inc., 313 N. First St., Ann Arbor, Mich.

Walter J. Johnson, Inc., 111 Fifth Ave., New York, N. Y., 10003, have reprint rights to out-of-print volumes of the Journal, and also have available for sale back volumes and single issues, with the exception of the current calendar year. Anyone interested in securing back copies should correspond direct with them.

Published monthly by The Electrochemical Society, Inc., at 215 Canal St., Manchester, N. H.; **Executive Offices, Editorial Office** and **Circulation Dept.**, and **Advertising Office** at 30 East 42 St., New York, N. Y., 10017, combining the JOURNAL and TRANSACTIONS OF THE ELECTROCHEMICAL SOCIETY. Statements and opinions given in articles and papers in the JOURNAL OF THE ELECTROCHEMICAL SOCIETY are those of the contributors, and The Electrochemical Society assumes no responsibility for them.

Claims for missing numbers will not be allowed if received more than 60 days from date of mailing plus time normally required for postal delivery of JOURNAL and claim. No claims allowed because of failure to notify the Circulation Dept., The Electrochemical Society, 30 East 42 St., New York, N. Y., 10017, of a change of address, or because copy is "missing from files." Subscription to members as part of membership service; subscription to nonmembers $24.00 plus $1.50 for postage outside U.S. and Canada. Single copies $1.70 to members, $2.25 to nonmembers.

Entered as second-class matter at the Post Office at Manchester N. H., under the act of August 24, 1912. Postage paid at Manchester, N. H.

Editorial

College Chemistry

A reviewer of Linus Pauling's latest edition reminds us that Francis Bacon once said "books must follow science, and not science books." When Dr. Pauling's first edition was published some of us felt that the book indeed was following science, but which science? The reviewer says that in the new edition the extensive descriptive material has been brought up to date and the whole sequence of topics has been made smoother and more logical. He thinks Dr. Pauling has made a good case for his thesis that "an understanding of statistical mechanics is more easily obtained by the beginning student than an understanding of chemical thermodynamics." He questions "the relevance of the chapter on Fundamental Particles in the absence of the possibility of Professor Gell-Mann as a guest lecturer." He regrets the omission of the previous chapter on Solubility Product and Precipitation, topics which do not even appear in the index. He says "All will envy the treatment of Russell-Saunders Coupling, though some will question its appropriateness. But why quibble, the book is a marvel."—We heartily agree with the reviewer. Dr. Pauling's books are erudite, useful, and successful.

A reviewer of another new text ("Chemistry: A Physical Approach," by William F. Sheehan) is less optimistic, although he does say that if chemistry texts are to depart so drastically from tradition this may be one of the best. His view is that "Everyone teaching freshman chemistry should read this book, but not every class will be able to use it." Purely descriptive chemistry has been kept to a minimum since the author's goal has been to "offer the student the means of learning his own chemical facts at the time he needs them." The author admits "There is a modest but real reliance on high school chemistry and physics."

The reviewer explains that all the usual topics of physical chemistry are discussed, but without direct use of the calculus. Schrödinger's name is only mentioned and the wave equation is not given. Neither Schrödinger nor Heisenberg are listed in the index; one does find Boltzmann distribution, quantum statistics, Bose-Einstein statistics, uncertainty principle, exclusion principle, Aufbau principle, Debye-Hückel theory, Gibbs free energy, Bravais lattices, Hakala relation, Kossel plot, Lennard-Jones potential, Madelung constants, Néel point, Paschen-Bach effect, Rayleigh's law, Schottky defect, and Vegard's law. The reviewer feels that most students would need a considerable amount of additional explanatory material, and that few professors can lecture at the level of the text without extensive outside reading. He implies that the professor can learn a lot; as for the student "It will remain for the laboratory class and for later courses in organic and inorganic chemistry to provide most of the facts which relate to the experimental and especially to the descriptive side of chemistry." —Our comment: why try to teach science backwards? Or is it true that if one learns all the energy levels in the hydrated copper ion, one need not know the color of the salts?

Recently it was my pleasure to answer a young lady who wrote as follows: "American Gas & Chemicals. . . . Dear Sirs: In my Science Class I, we are doing a chapter on chemicals and later will be doing something on gas. Do you have any information on these subjects that will help us? Anything about these subjects would help. Thank you."

With a valiant effort on the part of the lower schools to arouse and maintain interest, and a little outside help with the factual information, some of the students may be able to plow through the college textbooks of the future.

—CVK

A New High-Performance Fuel Cell Employing Conducting-Porous-Teflon Electrodes and Liquid Electrolytes

L. W. Niedrach and H. R. Alford

Research Laboratory, General Electric Company, Schenectady, New York

ABSTRACT

A low-temperature, aqueous electrolyte fuel cell employing new, "conducting-porous-Teflon electrodes" is described. The new electrodes show excellent performance characteristics with a variety of fuels (including hydrocarbons) and with both oxygen and air as the oxidant. Preparation methods are discussed, and performance data obtained with ambient temperature, hydrogen-oxygen and hydrogen-air cells are presented to illustrate their properties.

In earlier publications the use of "Conducting-Porous-Teflon Electrodes" in regenerative, matrix-type cells has been described (1, 2). While these cells are of some interest, particularly for applications in gravity-free space, they have not been given serious consideration for operation on a continuous feed basis. Under the latter conditions the matrix is responsible for some operational disadvantages; *e.g.*, at high current densities concentration polarization can occur at the electrodes, maintenance of the proper water balance in the electrolyte introduces design problems, and the internal resistances of the cells are higher than desired. In order to overcome these difficulties, work was directed at modifying and improving the original electrode structure so that the matrix could be eliminated. This has resulted in a new, high-performance fuel cell which operates with an aqueous electrolyte.

In seeking this objective two important restrictions concerning operation were deliberately imposed as being desirable: (i) The fuel (oxidant) gas-electrolyte interface was to be established within the electrode structure by "controlled wetting," and (ii) the electrodes were to be capable of operation at ambient atmospheric pressure. In addition emphasis was placed on retaining a relatively thin structure.

The new electrodes which are 5-10 mils thick, consist of a Teflon-catalyst mix that is pressed and sintered onto a suitable supporting screen which also serves as an excellent electronic conductor to carry current to the terminals of the cell. A porous Teflon film on the gas side of the electrode provides for proper control of wetting so that both the electrolyte and reacting gas have satisfactory access to the catalyst incorporated into the electrode. While alternative means of preparing electrodes were considered, *e.g.*, use of high Teflon-to-catalyst ratios and laminar structures with two different Teflon-to-catalyst ratios, the results obtained with the film covered electrodes were by far the most encouraging. These electrodes were found to be exceedingly reliable and readily manufactured in the laboratory. It was therefore elected to concentrate on electrodes of this type. The present paper is devoted to a discussion of their preparation and properties as exemplified by their performance in ambient temperature, hydrogen-oxygen and hydrogen-air cells. Platinum black was used almost exclusively as the electrocatalyst in the work to be reviewed and 6*N* KOH and 5*N* H_2SO_4 were the principal electrolytes.

The electrodes are exceedingly versatile, and some performance data obtained with other fuels and electrolytes have already been published. Thus, excellent performances have been reported for a variety of hydrocarbons, with a sulfuric acid electrolyte up to 89°C (3) and with a phosphoric acid electrolyte up to 200°C (3-5). In addition they have also been used effectively with methanol and a cesium carbonate electrolyte at temperatures up to 185°C (6).

Structure of the New Electrodes

Examples of the new electrodes are shown in Fig. 1. These were prepared by bonding platinum black-Teflon mixtures to the central areas of nickel screens. One quarter-inch-wide rings of 5-mil-thick Teflon sheet (du Pont's FEP Fluorocarbon Film) were used as seals around the peripheries. In mounting the electrodes in cell housings these seals are buried under the gaskets that are used. In another version the outer ring has been eliminated and the catalyst-Teflon mix has been spread uniformly over the entire circular area of the screen. Such electrodes perform equally well electrically and retain the electrolyte more reliably.

The important differences in the two surfaces of the electrodes are shown clearly in Fig. 1. The surface of the electrode on the left is coated with the porous Teflon film and is obviously exceedingly hydrophobic. In operation this side faces one of the gases. The untreated, electrolyte side of the electrode on the right has been wetted by drops of water placed upon it.

The photomicrograph in Fig. 2 brings out additional details of the electrode structure. It shows the surface film clearly at the top. As shown by the wire at the left, the screen is entirely imbedded in the catalyst-Teflon mix. It is pertinent to note that the starting catalyst consists of agglomerates of particles about 0.01μ in size. The ultimate size of the Teflon particles is about 0.2-0.5μ.

Experimental

Preparation of electrodes.—Most of the electrodes used in this work were prepared by a standard procedure. A Teflon suspension (du Pont's Teflon-30, which contained 59.6% solids by weight) was the

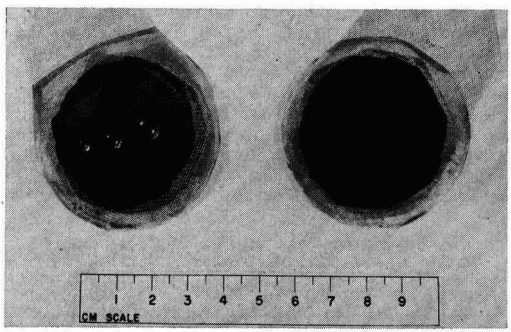

Fig. 1. Typical electrodes showing wetting characteristics

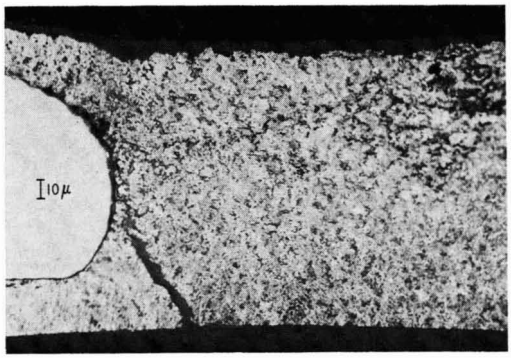

Fig. 2. Photomicrograph of a sectioned electrode showing the surface film on one side. Electrode No. 375. Body: 34 mg Pt black, 3.1 mg Teflon/cm^2; film: 2.4 mg Teflon/cm^2; nickel screen, 40 mesh; 4.5 mil wire. Magnification approximately 330X.

source of the binding material. Platinum black from Engelhard Industries, Inc., was used as the catalyst in most cases, but a few other catalysts were also used. Screen materials that were employed are listed in Table I. The nickel and silver were satisfactory in alkaline cells while the platinum screens could be used with the acidic cells as well.

While electrodes can be made with finer mesh screens of smaller wire size, it has been found that their resistances are high enough to be unattractive. In most of the work, therefore, 40- to 45-mesh screen made of 5- to 8-mil wire was used. In order to minimize the thickness of the electrodes, such screens were regularly rolled to a thickness corresponding to that of the individual wires. It was found necessary to leave wide tabs on the screens in order to reduce ohmic losses during operation of cells at high current densities.

Before making the electrodes themselves, a supply of Teflon films was prepared for use as surface coatings. This was done by spraying a Teflon-30 suspension diluted with seven volumes of water onto an aluminum foil using an air brush (Paasche, Type V). Films corresponding to 0.79, 1.6, 2.4, and 3.9 mg Teflon per cm^2 were used. In preparing these films a 5- by 5-in.^{2} area was marked on the aluminum foil, and an appropriate amount of the diluted Teflon suspension was used to coat this area to the desired thickness. Before spraying, a pattern of four circles having the diameter of the ultimately desired electrodes was scribed within the square to facilitate later steps in the preparation.

A fine spray was used so that several retracings of the pattern could be made in order to obtain a uniform thickness. During application, the aluminum foil was mounted on the bed of a hot plate which was maintained at 120°-150°C to facilitate evaporation of the water from the spray. The rate of application was such that wet areas did not develop and run on the foil.

Following the spraying, the foil was placed on the bed of the press (6-in. bed Carver press with individually heated platens) at 350°C and the jaws were closed to a gap of about ⅛ in. for about a minute. During this treatment the nonionic wetting agent in the Teflon suspension was rejected, and sintering of the Teflon particles occurred to form the desired film (7).

Spreads of platinum black (or other catalyst) with the Teflon-30 suspension were then prepared on circular areas on two aluminum foils, one of which had previously been coated with Teflon as described above. In preparing a typical spread to cover the entire circular area of the screen (17.7 cm^2), a 0.03 cc aliquot of the Teflon-30 suspension was first placed on the foil along with a suitable volume of dilution water, about 0.6 cc. After mixing, 0.3g of platinum black (previously sifted through a 325-mesh screen) was added and a thin, cream-like slurry was made by mixing with a small spatula. This was then dispersed as uniformly as possible over the area and slowly dried on a hot plate. It was necessary to raise the temperature very slowly during the initial phases to obtain a satisfactory deposit. Ultimately, however, the bed of the hot plate was raised to 250°-350°C to dispel the wetting agent as white fumes from the Teflon suspension.

The screen having a tab was then centered over one of the spreads, and a strip of Teflon sheet was placed across the tab as a seal. The second spread was then placed on top of the screen with the catalyst mix again facing the screen. This assembly, with the two aluminum foils facing outward, was sandwiched between two ferrotype plates and placed on the bed of the press. Sintering was performed at 350°C for 2 min at the desired pressure, usually 1800-3000 lb/in^2 of electrode surface.

Following the heat treatment, the aluminum foil was dissolved from the electrode with warm 20% NaOH. A water rinse and an air drying then resulted in a finished electrode. In most of the work, electrodes, either with or without the peripheral Teflon rings, were prepared as outlined above. The occasional variations that were introduced will be described as they arise.

Test cell.—The completed electrodes were housed as shown in the exploded view of a cell in Fig. 3. The two electrodes were separated by a ⅛-in. thick spacer which formed a 1½-in. diameter pocket for the free electrolyte. Appropriate gaskets and face plates formed chambers for the fuel and oxidant gases. All plastic parts were of Lucite, and gaskets were of silicone rubber or poly(ethylene-butene) copolymer. Gasketing was such that the effective working areas of the electrodes were 1½-in. diameter circles. Platinum and Teflon tubing were used for the connections that encountered electrolyte. Gases were flowed through polyethylene tubing. For operation on air one of the faceplates contained a 1½-in. diameter hole. This gave free access of air to the electrode.

Electrolytic hydrogen and purified oxygen were employed during operation. At low current densities static gases could be used, but at high current densities (>250 ma/cm^2) it was generally found desirable to maintain slow flows of the gases through a cell. This was particularly true of the oxygen which contained enough nitrogen and argon as impurities to accumulate rapidly in the cell chambers and cause "smothering."

Table I. Reinforcing screens used in electrode fabrication

Metal	Mesh, wires/in.	Wire size, diameter, mils
Platinum	80	3
	45	7.8
Nickel	40	4.5
Silver	40	7.5

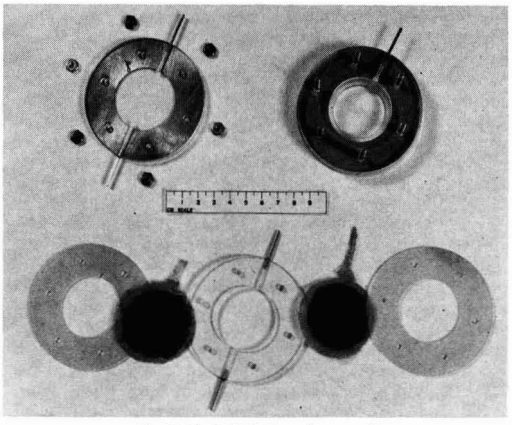

Fig. 3. Exploded view of test cell

In order to prevent the water produced in the cell reaction from diluting the electrolyte excessively, the electrolyte was circulated between the cell and a relatively large reservoir. In initial experiments, forced circulation was achieved by means of gravity flow from a reservoir above the cell level. Electrolyte which drained from the cell was then returned to the reservoir with the aid of a Teflon bellows pump.

It was soon found that the circulation provided by means of a thermal loop was adequate to maintain the cell performance. This simpler arrangement was therefore used for most of the work. A polyethylene bottle connected to the cell with Teflon tubing served as the reservoir.

A reference electrode was prepared by mounting one of the new-type electrodes in a separate housing and exposing one side to hydrogen. Electrolyte in the other chamber of the reference cell then made contact with the working system, *via* a bridge of Teflon tubing filled with the common electrolyte. Individual electrode performances in the cell under test were then obtained *vs.* the reference from measurements with a Kordesch-Marko bridge (8). Use of the bridge also permitted the measurement of IR-free voltages.

Although most of the measurements were made with the aid of the Kordesch-Marko bridge, over-all polarization curves were frequently obtained during direct discharge of cells through resistive loads. These invariably agreed well with the over-all curves obtained with the pulsating current derived from the bridge.

Results and Discussion

Before examining the effects of a number of individual parameters, it is of interest to consider the general performance characteristics of the new cells with alkaline and acidic electrolytes. For this purpose polarization curves for cells employing 6*M* KOH and 5*N* H_2SO_4 electrolytes are shown in Fig. 4 and 5, respectively. It is significant to note that current densities as high as 1000 ma/cm² have been delivered by the alkaline cells operating on hydrogen and oxygen. At such high current densities, of course, considerable internal heating occurs, and operation is therefore not isothermal. For example, electrolyte and electrode temperatures of about 70°C have been measured on both acidic and alkaline, hydrogen-oxygen cells at current densities of about 500 ma/cm². While the voltage (and hence efficiency) is low at these high current densities, the polarization curve gives assurance that the new electrodes will be able to handle surge currents well above the 100-200 ma/cm² that might be considered as the normal operating range. The performance of hydrogen-oxygen cells with acidic electrolytes is similar to that observed with the alkaline electrolyte.

Even when air is used as the oxidant, relatively high current densities can be obtained with the new cell before evidence of mass transfer polarization appears in the form of a sharp decline in the voltage with increasing load. Somewhat lower voltages are observed when air is substituted for oxygen, *e.g.*, at 200 ma/cm² 0.70v *vs.* 0.76v for the alkaline cell and 0.60v *vs.* 0.69v for the acidic cell. While partially resulting from the concentration effect involved in the Nernst equation, the lower voltages obtained with air probably also reflect the fact that better cooling is accomplished during air operation. As a result, internal resistances are higher and electrode reactions are more sluggish than when oxygen is used and higher temperatures are reached in the cell.

The new electrodes also do an excellent job of retaining the aqueous electrolytes. A small amount of seepage has, however, been observed with all the electrodes tested to date. In practice then, it may be necessary to provide some means of recycling the seepage.

Effect of the thickness of the surface film.—The first series of experiments was devoted to an examination of the effect of the thickness of the Teflon surface film on cell performance. All electrodes used in this series were prepared with rolled 40-mesh nickel screens having wire diameters of 4.5 mils. Two identical electrodes with peripheral Teflon rings were used in each of the test cells. Surface films of 0.79, 1.6, 2.4, and 3.9 mg Teflon/cm² were tested. All of the experiments were performed with alkaline electrolytes, 6*M* KOH. Most of the polarization data shown in Fig. 6 and 7 were obtained with the Kordesch-Marko bridge and show the potentials of the fuel and oxidant electrodes against the hydrogen reference. Also shown are the over-all performance curves (IR drop included) for the cells

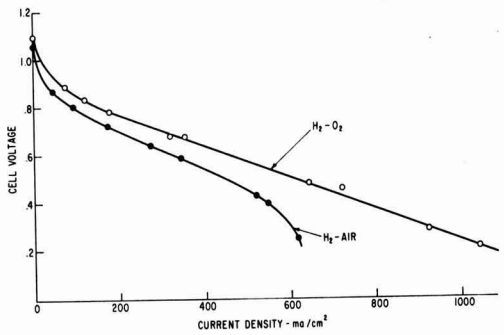

Fig. 4. Performance with alkaline electrolyte. Cell LFC-267. Electrolyte, 6M KOH; electrodes: body (35 mg Pt, 3.2 mg Teflon)/cm²; film, 1.6 mg Teflon/cm².

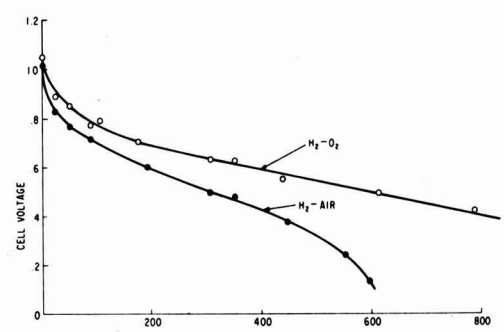

Fig. 5. Performance with acidic electrolyte. Cell SPL-1. Electrolyte, 5N H_2SO_4; electrodes: body (35 mg Pt, 3.2 mg Teflon)/cm²; film, 1.6 mg Teflon/cm².

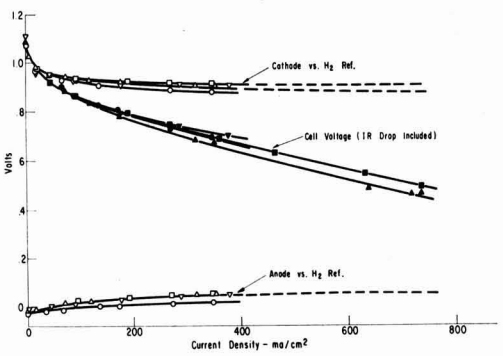

Fig. 6. Effect of film thickness on performance with H_2 and O_2. Electrolyte, 6M KOH; electrodes, body (35 mg Pt, 3.2 mg Teflon)/cm²; film: ○, ●, 0.79 mg Teflon/cm² LFC-270; △, ▲, 1.6 mg Teflon/cm² LFC-267 (9); ▽, ▼, 2.4 mg Teflon/cm² LFC-271; □, ■, 3.9 mg Teflon/cm² LFC-275.

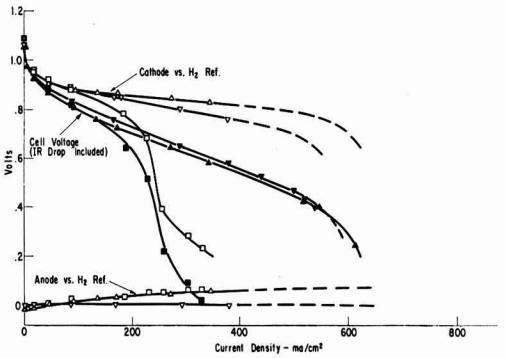

Fig. 7. Effect of film thickness on performance with H_2 and air. Electrolyte, 6M KOH; electrodes, body (35 mg Pt, 3.2 mg Teflon)/cm²; film: △, ▲, 1.6 mg Teflon/cm² LFC-267 (9); ▽, ▼, 2.4 mg Teflon/cm² LFC-271; □, ■, 3.9 mg Teflon/cm² LFC-275.

operating on oxygen and on air. At the time that these tests were made the bridge could handle a maximum current of about 4.5 amp. The data obtained at higher current densities were therefore obtained by direct discharge of the cells through resistive loads. The agreement between both types of data attest to the satisfactory functioning of the system.

It is seen that the effect of the film thickness on the performance of oxygen and hydrogen electrodes is not very pronounced. With air as the oxidant, however, it is evident from the data in Fig. 7 that the thinner films result in better performances. This is reasonable in view of the lower permeability that would be anticipated for the heavier films, and hence the greater tendency toward blockage with nitrogen.

Since an important purpose served by the film is the prevention of electrode drowning, as well as gross leakage of the electrolyte through larger pores, a word is in order about these aspects of performance. Electrode drowning manifests itself by severe polarization over a narrow range of current density. It is therefore evident from the data for the hydrogen and oxygen electrodes in Fig. 6 and 7 that drowning is not a problem.

Some electrolyte leakage occurred with all of the electrodes used in this series of tests, but it was found to be concentrated in the boundary region between the active area and the peripheral Teflon rings. It was therefore impossible to obtain meaningful quantitative data. Qualitatively, however, it was observed that the active electrode areas were freer from seepage droplets, the thicker the film.

It would therefore appear that practical electrodes, particularly air electrodes, will require an optimization between rate of seepage and gas accessibility. From the above, as well as repeated experiments with similar electrodes, it is our opinion that at the present state of development, film thicknesses between 0.79 and 2.4 mg Teflon/cm² are the most attractive with regard to over-all performance.

Effect of Other Electrode Parameters and Processing Variables

With the platinum black catalyst several other electrode parameters and processing variables were examined briefly. These included: (*a*) effect of screen wire size, mesh, and material; (*b*) effect of pressure used in final sintering; (*c*) effect of ratio of catalyst to Teflon; (*d*) effect of amount of platinum and Teflon; and (*e*) effect of using a commercially available Teflon film for the surface layer.

Screen characteristics.—Changes in the supporting screens manifested themselves by affecting the cell resistance and the associated IR drop. Even in the small laboratory cells, electrodes constructed with 80-mesh, 3-mil platinum wire screens showed excessively high ohmic drops, particularly when electrodes with narrow tabs were used. At the other extreme were electrodes employing low-resistance silver screens with 7.5-mil wires and wide tabs. The 40- to 45-mesh platinum and nickel screens that were used in most of the work were intermediate in performance.

Sintering pressure.—Variation in the pressure used in preparing electrodes was not examined in detail nor over a wide range. Those prepared at the lowest pressure tested, 180 lb/in.² were lacking in strength, although their electrical performance was excellent. With these electrodes, however, the gaskets from the cell were capable of inducing appreciable flow of the catalyst-Teflon mix and failures occurred around the edges. In general, pressures of the order of 1800 to 3000 lb/in.² were considered most satisfactory for the preparation of electrodes.

Ratio of catalyst to binder.—Electrodes of satisfactory strength and performance can be obtained within the range of platinum-to-Teflon weight ratios from 1:0.05 to 1:0.5. Most of the work was done with the ratio 1:0.09 (*i.e.*, 1g platinum black to 0.10 cc Teflon-30 solution).

Amount of platinum and Teflon.—Experiments were run with alkaline cells using electrodes containing from 17 to 45 mg platinum/cm² (a constant weight ratio of platinum-to-Teflon binder of 1:0.09 was used and the film thickness was maintained at 2.4 mg Teflon/cm²). Pronounced effects were not observed although the thinnest electrodes leaked excessively. Electrodes containing in the range 30-40 mg platinum/cm² appeared to be quite satisfactory and were adopted for most of the remaining work.

Commercial films as surface coatings.—While the major portion of the effort employed sprayed films of Teflon, a few electrodes were made with commercially available Teflon films that had a nominal thickness of ⅛ mil (obtained from Dielectrix, Inc.). These electrodes were prepared in the standard fashion except that the film was added in an extra pressing operation at the end of the regular procedures. At 200 ma/cm² hydrogen-oxygen cell potentials of greater than 0.70v can be realized with such electrodes. Current densities of 500 to 600 ma/cm² can be supported on hydrogen and oxygen but at greatly reduced potentials.

In this connection it is of interest to note that the permeation rates shown in Table II were obtained for the film with the mass spectrometer.[1] Because all spectrometer peaks were established rapidly on placing the gases on the high-pressure side of the film, it was concluded that pores were present. Assuming linear relationships, the tabulated data correspond to permeation rates of 0.073 and 0.063 cc (STP)/min/cm² of the ⅛-mil film for hydrogen and oxygen, respectively, at a pressure differential of 1 atm. The observed currents

[1] The authors are indebted to Dr. F. J. Norton for these measurements.

Table II. Permeation rates for Dielectrix, Inc., ⅛-mil Teflon film

permeation rate, p, in $\frac{\text{cm}^3\text{(STP)}}{\text{sec}} \cdot \frac{\text{mm thickness}}{\text{cm}^2\text{ area} \cdot \text{cm Hg pres.}}$

Temp, °C	H_2	He	O_2	N_2	Ar	SF_6
28	5.1×10^{-8}	2.7×10^{-8}	4.4×10^{-8}	6.8×10^{-8}	2.45×10^{-8}	—
53	2.4×10^{-7}	1.6×10^{-7}	1.45×10^{-7}	1.3×10^{-7}	1.2×10^{-7}	2.55×10^{-8}

of about 500 ma/cm² call for gas consumption rates of about 3.4 and 1.75 cc/min for the hydrogen and oxygen. This would indicate that the film ruptured sufficiently during processing to permit the passage of the additional gas to the catalyst.

While the electrical properties of these electrodes were comparable with the others, seepage of electrolyte through the pores was also comparable.

Effect of Operating Conditions on Cell Performance

Several important operating parameters were varied during the course of the work. In particular, the effects of the liquid and gas pressure heads were considered, as was the effect of the electrolyte concentration. In addition, tests were made to determine the need for an external circulation loop and reservoir.

Effect of electrolyte head.—Polarization data were obtained for several alkaline cells as the electrolyte heads were varied over the range 3-24 in. above the tops of the electrodes. During these tests the circulating loop to the reservoir was not closed. Instead, a "standpipe" arrangement was used with a thin tube filled with electrolyte serving to provide the hydrostatic pressure. Hydrogen and oxygen gas pressures of about 2-3 in. of water were used. The range of pressures covered should easily include the highest excess electrolyte pressures which will be encountered in practical size cells having electrodes up to 20 in. on a side.

Increasing the liquid head results in little change in the electrical performance of the cell or in that of the individual electrodes. A slightly poorer over-all polarization curve obtained with the largest liquid head does, however, appear to be real and may reflect some penetration of the electrolyte into the pores of the electrodes. Reduction of the pressure reversed this effect.

In the small laboratory cells the pressure gradient varies by only 1½ in. from the top of the electrode to the bottom. In a practical device, with its larger electrodes, the gradient will vary considerably more. These experiments indicate, however, that the electrical performance at the different levels will not differ significantly.

Effect of gas pressure.—In looking at the effect of gas pressure on cell performance, a range from 1 to 22 in. of water was covered. The cells were arranged with the electrolyte in a closed loop with a head of 2 or 6 in. above the tops of the electrodes. In these tests a ⅜ in. thick spacer was used between the electrodes to minimize the danger of bridging the gap should gases bubble into the electrolyte. The cells therefore had a somewhat higher internal resistance than normal. As a result the over-all polarization curves obtained with these cells were slightly inferior to others in this paper. It was found that the cells could be operated with gas pressures exceeding the hydraulic head of the electrolyte by as much as 20 in. of water without bubbling into the electrolyte occurring. No pronounced effects that can be attributed directly to changes in the gas pressures were encountered. Indeed, the data were exceptionally reproducible even at the higher current densities.

At the higher current densities the temperatures in the cells were also high. For example, with a cell containing 6*M* KOH as electrolyte at a current density of 580 ma/cm², an electrolyte temperature of 83°C was measured. Under these conditions the anode and cathode temperatures were 82° and 88°C, respectively, and the reservoir measured 38°C. Similar temperatures were obtained with acidic electrolytes. At such temperatures the partial pressure of water is fairly high, particularly at the water-producing electrode where the electrolyte is diluted. For this reason, as well as the fact that cell performance at high current densities is sensitive to gas flow rate, it appears highly likely that steam blanketing of the electrodes may occur.

Effect of the electrolyte concentration.—As noted in the previous section, some cells operating on hydrogen and oxygen and employing 6*M* KOH or 5*N* H_2SO_4 as the electrolytes have shown evidence of some steam blanketing at the electrodes. In an effort to reduce this effect, a number of cells were run with more concentrated electrolytes over which the vapor pressure of water was considerably less.

When 12*M* KOH was used there was, indeed, a slight improvement in performance at high current densities. Unfortunately, however, because of its higher resistivity, this electrolyte tended to heat more than 6*M KOH* at corresponding current densities. In addition, its higher viscosity resulted in less circulation through the external loop and this also contributed to a higher temperature in the cell, *e.g.*, 96° *vs.* 83°C at a current density of 580 ma/cm². This attempt to reduce the vapor pressure of the water was therefore largely self-defeating. In general, however, 12*M* KOH appeared to be an attractive electrolyte. In particular, its higher viscosity resulted in lower seepage rates through the electrodes than were seen with 6*M* KOH.

Attempts to examine the effect of increasing the electrolyte concentration with the acid were unsatisfactory. Sulfuric acid is less effective than potassium hydroxide in reducing the vapor pressure of water, and a 23*N* solution is required to accomplish the reduction equivalent to 12*M* KOH. This concentration of acid proved unsatisfactory. When it heated to a temperature of 60°-70°C, direct reaction with the hydrogen occurred, and hydrogen sulfide formed and poisoned the fuel electrode. A similar behavior was observed with 17*N* H_2SO_4, but in this case when the temperature reached 80°-90°C.

Effect of electrolyte circulation.—Because an external circulation loop such as that used in much of the present work may prove cumbersome in the designing of practical cells, it was of interest to determine whether this is required for satisfactory operation. For this purpose an air-breathing, acid cell was placed in operation without any external circulation. Instead, a small funnel was attached to the top inlet tube on the electrolyte chamber, and water (to compensate for evaporation losses) was added directly to the cell chamber.

That adequate mixing of the electrolyte can be achieved in this way was clearly attested to by steady operation at 0.68 ± 0.02v when the current was held constant at 88 ma/cm². The steady potential was maintained for 25-hr periods both during operation of the cell in this fashion and during operation with a thermal loop when the makeup water was added to the reservoir. Even with larger cells, thermal mixing within the electrolyte chamber should be more than adequate to prevent stratification of the electrolyte when the water is introduced at the top. If stratification were to occur and a water layer formed at the top, the resistance across that layer would be much greater than in the lower acidic region. The current would therefore be concentrated at the bottom of the cell and more power would be dissipated there than at the top. The heat so generated would therefore be distributed in a way to promote convective mixing and thereby destroy concentration gradients within the electrolyte.

If desired, however, makeup water could be introduced at the bottom of the cell chamber. In this case density differences between the makeup water and the electrolyte already in the cell would contribute to the mixing.

Alternative Electrocatalysts

A few exploratory experiments were performed with alternative electrocatalysts. These included silver and activated carbons. Electrodes of both types performed reasonably well with oxygen. This is shown by the data in Fig. 8. The silver electrode used in cell LFC-264 contained approximately 70 mg Silflake-131 (Handy and Harmon) and 7 mg Teflon binder/cm². It was coated with a surface film containing 2.4 mg Teflon/cm². The platinized carbon electrode of cell LFC-282 contained 17 mg amorphous carbon containing 10%

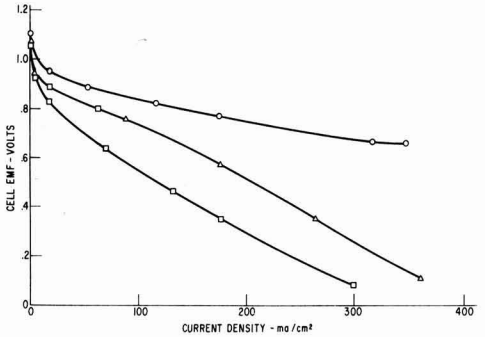

Fig. 8. Performance of cells with various oxygen electrode catalysts. Electrolyte, 6M KOH; anodes, Pt black; cathodes: ○, Pt black LFC-269; △, 10% Pt on amorphous carbon LFC-282; □, Silflake LFC-264; IR drop included.

platinum and 3 mg Teflon binder/cm². It too was coated with a surface film containing 2.4 mg Teflon/cm². The anodes in both of these cells were made with platinum black.

These data are included merely to indicate the promise of some of these less expensive materials as practical electrocatalysts. Actually, the carbon-base material has shown even better performance with both oxygen and hydrogen in the earlier matrix type cells (9). This implies strongly that the carbon electrode of the present example does not represent the optimum in wetting control.

Alternative Electrolytes

In most applications it is desirable to be able to operate a fuel cell on air. With an acidic electrolyte this is no problem since carbon dioxide from the air is not absorbed. However, such electrolytes are more corrosive than caustic electrolytes, and the latter therefore have some advantages in practical cells. These electrolytes, however, are converted to carbonates by the carbon dioxide in the air.

While the resistances of carbonate electrolytes are higher than those of caustics or acids, the difference is not enough to preclude their consideration for use in fuel cells (6,10,11). It was therefore of interest to examine the performances of a number of them covering the range of compositions that might be encountered as equilibrium electrolytes in air-breathing cells. Room temperature polarization curves for a family of electrolytes from KOH to K_2CO_3 are shown in Fig. 9. The ohmic drop has been eliminated from all of these

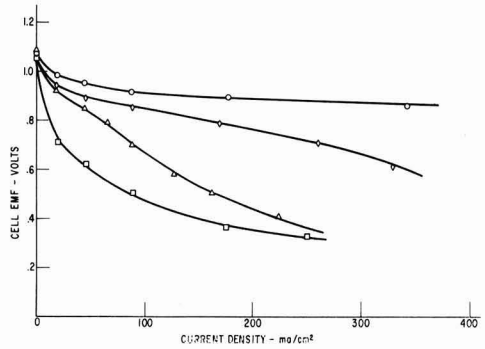

Fig. 9. Effect of carbonate on H_2-O_2 cell performance. Cell LFC-273. Electrodes: body, 35 mg Pt, 3.2 mg Teflon/cm²; film, 2.4 mg Teflon/cm². ○, 6M KOH; ◇, 3M KOH, 1.5M K_2CO_3; △, 1.5M KOH, 2.25M K_2CO_3; □, 3M K_2CO_3; IR drop eliminated.

Table IV. Phosphate solutions tested as fuel cell electrolytes

Solution No.	Electrolyte and concentration	pH
1	5*M* H_3PO_4	<0.0
2	2.5*M* H_3PO_4-2.5*M* NaH_2PO_4	0.8
3	5*M* NaH_2PO_4	3.4
4	2.5*M* NaH_2PO_4-2.5*M* K_2HPO_4	7
5	1.25*M* NaH_2PO_4-1.25*M* K_2HPO_4	7
6	5*M* K_2HPO_4	9

curves, but in no case was the total cell resistance greater than 0.08 ohm.

It is evident that the carbonate has a pronounced effect on performance, largely in the form of adverse effects on electrode polarization. From work with carbonate and bicarbonate electrolytes in the older, low-temperature, matrix-type cells, it was found that the hydrogen electrode is the one that is strongly affected; this appears to be the result of direct reaction between hydrogen and carbonate to form CO or a related species on the electrode surface which then inhibits the electrooxidation of hydrogen (9).

Because of the volatility of CO_2 the composition of the equilibrium electrolyte in an operating cell will be affected by such parameters as temperature, current density, concentration and volume of electrolyte, and other variables. From the data presently available, it is therefore impossible to predict the magnitude of inhibition that will be experienced with such an electrolyte under practical conditions. It is possible, however, that an appreciable penalty will be paid.

In view of the adverse effect of carbonate on cell performance, some attention was given to the possibility of using phosphate solutions as CO_2 rejecting electrolytes. Some of the solutions tested had moderate buffer capacity in the intermediate *p*H region where corrosion problems would be less severe than with strong acids. The electrolytes in Table IV were examined.

It is to be noted that the sodium and potassium salts were chosen for solutions 3 and 6, respectively, on the basis of solubility considerations. The mixture used for solution 4 was also chosen in an effort to avoid precipitation. This was not entirely successful, and some precipitate formed slowly. The less concentrated solution 5 was therefore prepared for additional tests at essentially the same *p*H.

At ambient temperature all of these phosphate electrolytes were inferior to sulfuric acid. In part this was a result of their higher resistances, but there were also pronounced effects on electrode behavior. The oxygen electrode was affected more strongly than the hydrogen electrode, and the effect became more pronounced as the *p*H increased. It is possible that these effects were caused by adsorbed phosphate ions (especially $HPO^{-}{}_{4}-$), but a straight *p*H effect cannot be precluded. In either case, phosphate solutions, with the exception of those containing phosphoric acid, do not appear attractive as electrolytes.

Performance during Continuous Operation

Seven cells were placed on continuous operation at current densities of 88, 176, or 263 ma/cm² for periods of from 5 days to over 5 months. The first cell was operated with forced circulation of the electrolyte. All of the remaining units were operated with thermal loops.

The hydrogen supply was sufficiently pure to permit operation on static heads of gas with an occasional short purge (a few seconds) to sweep out impurities that slowly accumulated in the fuel electrode's gas chamber. Because the impurity level of the oxygen was higher, it was necessary to continuously vent a slow stream of oxygen from the cells; a rate of less than 1 cc/min was maintained.

Graduated traps in the vent lines permitted the collection of liquid that accumulated in the gas chambers. This included seepage as well as water which distilled from the electrodes to the faceplates of the cells. All

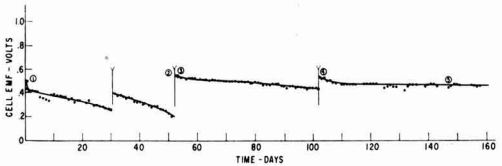

Fig. 10. Performance of acidic H_2-air cell with platinum black electrodes on continuous load. Cell LFC 260. Electrodes, platinum black; electrolyte, 5*N* H_2SO_4; load, 2 amp (176 ma/cm²). Circled numbers refer to polarization curves; Y refers to replacement of electrolyte.

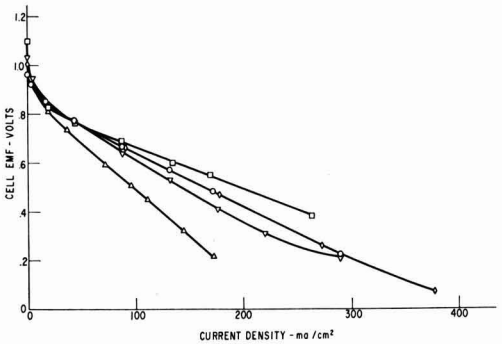

Fig. 11. Polarization curves obtained during tests on continuous load. Cell LFC-260, air cell. Electrodes, platinum black; electrolyte, 5*N* H_2SO_4; ○, initial operation; △, after 52 days' operation; □, after 52 days' operation and cleaning of electrodes; ▽, after 102 days' operation; ◇, after 147 days' operation; IR drop included.

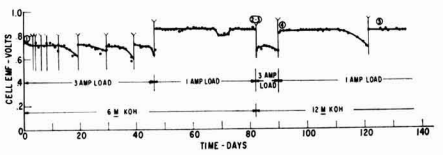

Fig. 12. Performance of alkaline H_2-O_2 cell with platinum black electrodes on continuous load. Cell LFC 269. Electrodes, platinum black; electrolyte, 6 and 12*M* KOH; load, 1 amp (88 ma/cm²) and 3 amp (263 ma/cm²). Circled numbers refer to polarization curves; Y refers to replacement of electrolyte.

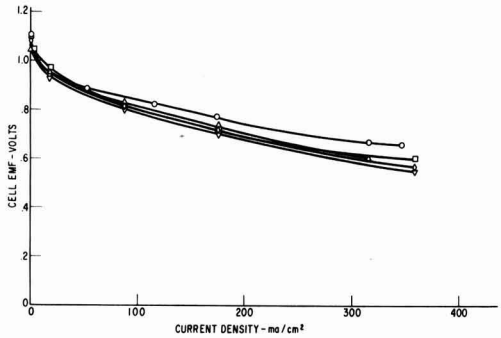

Fig. 13. Polarization curves obtained during tests on continuous load. Cell LFC 269. Electrodes, platinum black; electrolyte, 6 and 12*M* KOH; ○, 6*M* KOH initial operation; △, 6*M* KOH after 82 days' operation; □, 12*M* KOH after 82 days' operation on 6*M* KOH; ▽, 12*M* KOH after 90 days' operation; ◇, 12*M* KOH after 126 days' operation; IR drop included.

was recycled back to the reservoirs. To minimize seepage, electrolyte heads were held to about 1 in. above the tops of the electrodes.

During air operation with a fully exposed electrode, more water was evaporated than was produced in the cell reaction. In such cases makeup water was added periodically to the reservoir.

During operation on oxygen the water formed in the cell reaction gradually diluted the electrolyte so that periodic replacement was required. The need for replacement was generally indicated by a decline in cell performance; the response of the cell to fresh electrolyte was immediate. During early tests about 80 cc of electrolyte were used in charging a system. Later this was increased to about 250 cc in order to extend the periods between replacements.

Some representative performance data are summarized in Fig. 10 through 13. Shown are cell voltages on load as well as polarization curves obtained after various periods of operation. No cell failures occurred during these tests apart from leaks which developed in cell housings.

Cell LFC-260 was one of the first cells to be assembled. Its electrodes are reinforced with 80-mesh, 3-mil wire, platinum screens having narrow tabs. As a result its internal resistance was high, 0.12 ohm, and a drop of about 0.15v occurred in the tabs themselves at the operating current of 2 amp (176 ma/cm²). Nevertheless, this acid cell gave excellent performance on hydrogen and air for over 160 days as attested to by the data in Fig. 10 and 11.

A word is in order about the performance of this cell during the first 52 days. During this period silicone rubber gaskets were used on the cell. Gradual attack from the acid produced silica which accumulated in the pores of the electrodes. On the 52nd day the cell was disassembled and the electrodes were leached with warm sodium hydroxide. After reassembly with poly(ethylene-butene) copolymer gaskets, the cell performed excellently for over 110 additional days.

Cell LFC-269 contained the same electrodes as provided the data in Fig. 4. They were reinforced with 40-mesh, 4.5-mil wire, rolled nickel screens having wide tabs. This alkaline cell had a considerably lower resistance than LFC-260, *i.e.*, 0.06 ohm. It was operated on hydrogen and oxygen for over 140 days at the current densities indicated in Fig. 12. During the first 19 days a small reservoir charged with 80 ml of electrolyte was used. This was subsequently changed to a larger reservoir with charges of about 250 ml of fresh electrolyte, although the amount was reduced again upon switching to 12*M* KOH. In general, the performance of this cell was excellent, and as shown by the polarization data in Fig. 13 there was no decline in its ability to handle overloads.

Summary and Conclusions

The structure of conducting-porous-Teflon electrodes has been improved with regard to strength, conductivity, and wetting characteristics. In their new form these very thin electrodes (5-10 mils thick) may be employed with aqueous electrolytes without the need for the matrix-type support previously used. The result is a fuel cell having excellent performance characteristics. These include an ability to operate on air at practical current densities of 100-200 ma/cm². In other work the new electrodes have also been shown to have excellent performance characteristics with hydrocarbon fuels and with methanol.

The new cells may be operated with the electrolyte circulated through an external loop by thermal pumping, or the electrolyte may be used without such circulation.

A number of cells have been operated continuously for periods of months with encouraging results. One of our first hydrogen-oxygen cells was operated with an acid electrolyte and air as oxidant at a current density

of 176 ma/cm² for over 5 months. A similar alkaline cell was operated on hydrogen and oxygen at current densities of 263 and 88 ma/cm² for a similar period.

Acknowledgments

The authors are indebted to H. A. Liebhafsky, E. J. Cairns, and W. T. Grubb for helpful discussions during the course of this investigation. They also appreciate the assistance of F. J. Norton who measured the permeability of one of the Teflon films, and that of E. F. Koch and R. R. Russell who obtained the photomicrographs of electrodes.

Manuscript received July 1, 1964. This paper was presented at the Washington Meeting, Oct. 11-15, 1964.

Any discussion of this paper will appear in a Discussion Section to be published in the December 1965 JOURNAL.

REFERENCES

1. J. S. Bone, S. Gilman, L. W. Niedrach, and M. D. Read, Proceedings 15th Annual Power Sources Conference, Atlantic City, N. J., p. 47 (1961).
2. L. W. Niedrach, Belgian Pat. No. 617,375 (1962).
3. W. T. Grubb and L. W. Niedrach, Proceedings 17th Annual Power Sources Conference, Atlantic City, N. J., p. 69 (1963).
4. W. T. Grubb and L. W. Niedrach, *This Journal*, **110**, 1086 (1963).
5. W. T. Grubb and C. J. Michalske, *This Journal*, **111**, 1015 (1964).
6. E. J. Cairns and D. C. Bartosik, *This Journal*, **111**, 1205 (1964).
7. Information Bulletin No. -X-50d, E. I. du Pont de Nemours & Co.
8. K. Kordesch and A. Marko, *This Journal*, **107**, 480 (1960).
9. L. W. Niedrach, Unpublished results.
10. E. J. Cairns and D. I. Macdonald, *Electrochem. Technol.*, **2**, 65 (1964).
11. E. Justi, "High Drain Hydrogen-Diffusion Electrode Operating at Ambient Temperature and Low Pressure," 1959. Trans. by T. E. Burton, Res. Inf. Service, Div. Pergamon International Corp., 40 East 23rd St., New York 10, N. Y.

The Active Iron Electrode

I. Iron Dissolution and Hydrogen Evolution Reactions in Acidic Sulfate Solutions[1]

Eugene J. Kelly

The Chemistry Division, Oak Ridge National Laboratory, Oak Ridge, Tennessee

ABSTRACT

The *p*H and potential dependencies of the steady-state iron dissolution and hydrogen evolution reactions were determined for zone-refined iron in H_2-saturated acidic sulfate solutions. The mechanistic significance of the data is examined in detail. The results of this investigation serve to resolve the conflict concerning the mechanism of iron dissolution in noninhibiting media and to provide an experimental and mechanistic base for the interpretation of the electrochemical behavior of the active iron electrode in inhibiting media.

A comparative study has been made of the electrochemical behavior of the active iron electrode in typical inhibiting and noninhibiting media. The purpose of the investigation was to determine the changes produced in the kinetics and mechanistics of a noninhibited system as a result of specific adsorption of an inhibitor. Such information is not only essential to the understanding of corrosion inhibition, but is also relevant to the interpretation of kinetic data for other electrode processes involving adsorption.

The many recent investigations of the active iron electrode in noninhibiting media such as deoxygenated acidic sulfate, perchlorate, and chloride solutions have led to a variety of conflicting results. According to Bonhoeffer (1, 2) and Heusler (1-3), the mechanism of the iron dissolution reaction in sulfate and perchlorate solutions is given by Eq. [1]-[3],

$$Fe + OH^- \rightleftharpoons (FeOH)_{ads} + e^- \quad [1]$$

$$Fe + OH^- + (FeOH)_{ads} \rightarrow (FeOH)_{ads} + (FeOH)^+ + 2e^- \quad [2]$$

$$(FeOH)^+ + H^+ = Fe^{++} + H_2O \quad [3]$$

in which the surface species, $(FeOH)_{ads}$, serves simply as a catalyst for reaction [2]. This system of reactions may be described by Eq. [4] and [5]

$$i_a/\mathbf{F} = \bar{k}_1 a_{(OH^-)}(1-\theta) - \bar{k}_{-1}\beta\theta + 2\bar{k}_2 a_{(OH^-)}\beta\theta \quad [4]$$

$$\beta d\theta/dt = \bar{k}_1 a_{(OH^-)}(1-\theta) - \bar{k}_{-1}\beta\theta \quad [5]$$

where i_a is the net anodic current density corresponding to the iron dissolution reaction, and $\bar{k}_j$ are electrochemical rate constants which, assuming transfer coefficients of ½, are equal to $k_j \exp(\pm\lambda_j \mathbf{F}E/2RT)$, where λ_j is the number of electrons transferred per occurrence of the j^{th} reaction, and the plus and minus signs refer to anodic and cathodic processes, respectively. The definitions of β and θ follow from $(FeOH)_{ads} = \beta\theta$, where $(FeOH)_{ads}$ is the concentration of the catalyst expressed in moles/cm², θ is the fraction of the surface occupied by the catalyst, and β is a proportionality constant. The other symbols have their customary meanings. If $2\bar{k}_2 a_{(OH^-)}\beta\theta >> \bar{k}_1 a_{(OH^-)}(1-\theta) - \bar{k}_{-1}\beta\theta$, *i.e.*, if the contribution of reaction [1] to the net anodic current density is negligible compared to that of reaction [2], then Eq. [4] reduces to Eq. [6]

$$i_a/\mathbf{F} = 2\bar{k}_a a_{(OH^-)}\beta\theta \quad [6]$$

With $d\theta/dt$ equal to zero and $(1-\theta) \approx 1$, Eq. [5] and [6] lead to the steady-state solution

$$\frac{i_{a,\infty}}{\mathbf{F}} = 2k_2\left(\frac{k_1}{k_{-1}}\right) a^2_{(OH^-)} \exp(2\mathbf{F}E/RT) \quad [7]$$

i.e., the steady-state system should be characterized by an anodic Tafel slope of 30 mv/decade, 2.303 $RT/2\mathbf{F}$, and a second order dependency on the hydroxyl ion activity. Using fast polarization techniques, these authors were also able to observe a transient anodic Tafel line having a slope of 60 mv/decade, 2.303 $RT/\mathbf{F}$. This result was accounted for assuming that during the short time interval required to fix the transient anodic Tafel

[1] Research sponsored by U.S. Atomic Energy Commission under contract with the Union Carbide Corporation.

line, θ remains constant at θ_o. Then Eq. [6] becomes Eq. [8]

$$i_{a,o}/\mathbf{F} = 2k_2 a_{(OH^-)}\beta\theta_o \exp(\mathbf{F}E/RT) \quad [8]$$

which shows the first order dependency of reaction [2] on the hydroxyl ion activity, as well as the observed effect of potential on this reaction.

According to Bockris *et al.* (4-6), in sulfate solution the steady-state anodic dissolution reaction is characterized by an anodic Tafel slope of 40 mv/decade, (2/3) (2.303 $RT/\mathbf{F}$), and a first order dependency on the hydroxyl ion activity. To account for their results, they suggested the mechanism

$$Fe + H_2O \rightleftharpoons (FeOH)_{ads} + H^+ + e^- \quad [9]$$

$$(FeOH)_{ads} \rightarrow (FeOH)^+ + e^- \text{ (rate-determining)} \quad [10]$$

$$(FeOH)^+ + H^+ = Fe^{++} + H_2O \quad [11]$$

in which the surface species, $(FeOH)_{ads}$, acts as a reaction intermediate rather than a catalyst. This reaction mechanism is described by Eq. [12] and [13]

$$i_a/\mathbf{F} = \bar{k}_1(1-\theta) - \bar{k}_{-1}a_{(H^+)}\beta\theta + \bar{k}_2\beta\theta \quad [12]$$

$$\beta d\theta/dt = \bar{k}_1(1-\theta) - \bar{k}_{-1}a_{(H^+)}\beta\theta - \bar{k}_2\beta\theta \quad [13]$$

where $a_{(H^+)}$ is the proton activity, and the other symbols retain their previous definitions. For the steady-state case, $d\theta/dt$ is equal to zero. Then, if $\bar{k}_{-1}a_{(H^+)}\beta\theta >> \bar{k}_2\beta\theta$ and $(1-\theta) \approx 1$, Eq. [12] reduces to Eq. [14]

$$\frac{i_{a,\infty}}{\mathbf{F}} = 2\frac{k_1k_2}{k_{-1}a_{(H^+)}}\exp(3\mathbf{F}E/2RT) \quad [14]$$

which is consistent with the observed 40 mv/decade Tafel slope and the first order dependency on the hydroxyl ion activity. These authors also reported a transient anodic Tafel line having a slope of approximately 2.303 $RT/\mathbf{F}$. This was interpreted by assuming that in the process of anodic charging, reaction [9] rapidly attains a state of pseudo-equilibrium, during the attainment of which, the diffusion of protons from the double layer to the bulk of the solution is negligible. Consequently, Eq. [14] gives the current density corresponding to the pseudo-equilibrium state, but with $a_{(H^+)}$ now referring to the pseudo-equilibrium activity of protons, $a_{(H^+),o}$, in the double layer. If the change in potential is sufficiently large to justify the approximation, $a_{(H^+),o} = \beta\theta_o$, then Eq. [14] may be written as Eq. [15]

$$i_{a,0} = i_{a,1}\left(\frac{a_{(H^+)}}{\beta\theta}\right)_1^{1/2}\exp\left[\frac{\mathbf{F}}{RT}(E-E_1)\right] \quad [15]$$

where the subscript one refers to the initial steady state from which the transient measurements originate.

In partial confirmation of the Heusler mechanism, Heusler and Cartledge (7) reported steady-state and transient anodic Tafel slopes of 30 mv/decade and 60 mv/decade, respectively, in 0.5f H_2SO_4, and used the mechanism of reactions [1]-[3] as a basis for the interpretation of the inhibition of iron dissolution by iodide ion and carbon monoxide. Lorenz, Yamaoka, and Fischer (8) reported a steady-state anodic Tafel slope of 30 mv/decade in HCl and (HCl + KCl) solutions, subject to the condition that $pH > 1.5$ and $pH > 2$ for the two types of solutions, respectively. These authors criticized the mechanism of Bockris and co-workers, who had earlier criticized the Heusler mechanism. In sulfate and chloride solutions, Hoar (9) and Hurlen (9, 10) found a 30 mv/decade steady-state anodic Tafel line, but a first rather than second order dependency of the anodic reaction on the hydroxyl ion activity. Steady-state anodic Tafel slopes of 30-40 and 50-60 mv/decade in sulfate solution have been reported by Makrides (11), 30 mv/decade in perchlorate solution by Kaesche (12), approximately 100 mv/decade in sulfate solution by Okamoto *et al.* (13), 54 mv/decade in chloride solution by Makrides *et al.* (15), and 68 mv/decade in chloride solution by Stern and Roth (14). Neither order determinations nor detailed mechanisms were included in this latter group of studies.

There is general agreement that the cathodic Tafel line corresponding to the hydrogen evolution reaction in these media has a slope of —120 mv/decade, $-2(2.303\ RT/\mathbf{F})$. That the reaction is first order in proton activity would also appear to be reasonably well-established (4, 10). The steady-state current density, $i_{c,\infty}$, is therefore given by Eq. [16]

$$|i_{c,\infty}|/\mathbf{F} = k_c a_{(H^+)}\exp(-\mathbf{F}E/2RT) \quad [16]$$

The mechanistic significance of this equation will be considered in the discussion section.

Relations between the corrosion potential and pH and the corrosion current density and pH may be determined by equating the expressions for the steady-state anodic and cathodic current densities, for example, Eq. [7] and [16] or Eq. [14] and [16]. Bockris and co-workers reported values of —60 mv/pH or $-2.303\ RT/\mathbf{F}$ and —½ for $(dE_{corr}/dp\text{H})$ and $(d \log i_{corr}/dp\text{H})$, respectively, values which are consistent with Eq. [14] and [16]. Hurlen gave corresponding values of —48 mv/pH or $-(4/5)(2.303\ RT/\mathbf{F})$ and —3/5, values which are consistent with Eq. [16] and his expression for the steady-state anodic current density

$$i_{a,\infty}/\mathbf{F} = k_a a_{(OH^-)}\exp(2\mathbf{F}E/RT) \quad [17]$$

On the other hand, Bonhoeffer and Heusler found the corrosion rate to be independent of pH, in agreement with Stern (16), and reported a value of —45 mv/pH for $(dE_{corr}/dp\text{H})$. An inspection of Eq. [7] and [16] shows these observations to be internally inconsistent with the mechanism proposed by these authors, a fact noted by Bockris *et al.* (4). A few of the many other values reported for $(dE_{corr}/dp\text{H})$ are —60 mv/pH by D'Ans and Breckheimer (17), —56 mv/pH by Stern (16) who emphasized the fact that the result was less than $-2.303\ RT/\mathbf{F}$, —52 mv/pH by Kaesche (12), and —47 mv/pH by Makrides *et al.* (15) who also reported a logarithmic relation between the corrosion rate and pH.

The preceding review clearly suggests that, prior to attempting to resolve the more complicated inhibited systems, the electrochemical behavior of active iron in noninhibiting media should be re-examined. This paper reports on the results obtained in acidic sulfate solution.

Experimental

In order to circumvent contamination problems associated with the use of rubber, lubricants, etc., the entire cell assembly was made of Pyrex glass and Teflon. The apparatus was so designed that essential operations, such as rapid addition of pre-electrolyzed solutions and the removal of used solutions, could be accomplished without opening the apparatus to the atmosphere. The test electrode compartment, a flat-bottomed cylinder, was fashioned from the male component of a 55/50 TS ground glass joint. The ground surface was carefully removed by fire-polishing, and the rest of the cylinder was provided with a glass jacket by means of which, in conjunction with a circulating water bath, a constant solution temperature of 25.00° ± 0.03°C was maintained. The cap was machined from Teflon, and had a total of nine ports, four standard-taper ports for electrode holders and the remainder for variable position hydrogen inlet and outlet tubes, solution inlet tubes, and a Haber-Luggin capillary probe. These tubes were connected *via* flexible Teflon "spaghetti" tubing (1/16 or 1/8 in. ID) to a hydrogen manifold, reservoirs containing pre-electrolyzed, hydrogen-saturated solutions, and an external reference electrode compartment, respectively. The

reference electrode compartment, holding a saturated calomel electrode, was also jacketed and maintained at 25.00° ± 0.03°C. A tube passed from the bottom of the test electrode compartment, through the wall of the jacket, to a Teflon "T-bore" stopcock. The second arm of the stopcock led to an external counterelectrode compartment, while the third arm served to drain both compartments. A Teflon coated bar-magnet provided stirring in the test electrode compartment.

Iron electrodes studied in this investigation were machined from a small ingot of high-purity, zone-refined electrolytic iron.[2] The analysis of the ingot (Bar 27, Specimen D, Lot 7) in parts per million was as follows: C(10), N(2), H(0.1), S(5), Al(15), Cr(5), Co(1), Cu(2), Mn(0.5), Ni(12), Si(10), and (Sb, As, Ca, Cd, Pb, Mo, Sn, Ti, W, Va, Zn, Zr) not detected.[3] The electrodes were cylindrical, ½ in. long, and either ⅛ (small) or ¼ (large) in. in diameter. The electrodes were mounted on conventional Teflon electrode holders (19).

Sulfuric acid and sodium sulfate solutions were prepared from reagent grade materials and triply distilled water. All solutions were pre-electrolyzed, using an iron cathode, and saturated with hydrogen. Electrolytic hydrogen was purified at 450°C over copper and palladium, and presaturated with water vapor at 25°C.

In a typical experiment, the cell and auxiliary apparatus were cleaned in hot acid solution (equal parts of concentrated H_2SO_4, concentrated HNO_3, and distilled water), rinsed in distilled water, assembled, and leached with test solution. Test electrodes were initially etched in the same acid solution, rinsed in distilled water, and transferred to the cell. Test electrodes remained in test solution from one to several days prior to recording any data, during which period the test solution was replaced frequently by fresh solution from a reservoir. A well-behaved system exhibited no polarization hysteresis phenomena, and this fact was used as the basic criterion by which the suitability of the system for investigation was determined.

Potentials were measured with a high impedance (10^{11} ohms) L&N Model 7664 *p*H and EMF meter, and recorded with a 10 mv Brown recorder. In this investigation, concerned only with the steady-state behavior of iron, a galvanostat was employed in the determination of polarization curves. Steady-states were established within the response time of the recorder, *i.e.*, approximately 3 sec full-scale. For current densities in excess of roughly 1 ma/cm², it was necessary to employ an internal iron counterelectrode in place of the external counterelectrode. A stream of hydrogen through the test solution was maintained at all times, enabling the solution *p*H to be measured with a platinum-hydrogen electrode. The platinum was immersed in the solution only momentarily and then retracted to a position above the solution in order to prevent contamination. Ferrous ion concentration was held to a negligible level by frequent change of the test solution.

Results

A Tafel diagram of typical data obtained in 0.5M H_2SO_4 is shown in Fig. 1, in which the absolute value of the net current density, $|i_n|$, is represented by the solid line passing through the encircled experimental points. The partial cathodic current density, $|i_c|$, corresponding to the hydrogen evolution reaction, exhibits Tafel behavior with the cathodic Tafel line (dashed) having a slope of $-2(2.303\ RT/\mathbf{F})$. Concentration polarization accounts for the deviation from Tafel behavior at high cathodic current densities. The partial anodic current density, i_a, corresponding to the iron dissolution reaction, shows a Tafel region over which the slope is 40 mv/decade, *i.e.*, $(2/3)(2.303\ RT/\mathbf{F})$. No concentration polarization is observed on the anodic side, but at current densities above those shown in Fig. 1, deviation from Tafel behavior as a result of IR-drop becomes significant. The extrapolated anodic and cathodic Tafel lines (dashed) intersect at the observed open-circuit potential, E_{corr}, and fix the magnitude of the corrosion current density, i_{corr}. The partial and net current densities satisfy the relation, $i_n = i_a + i_c$.

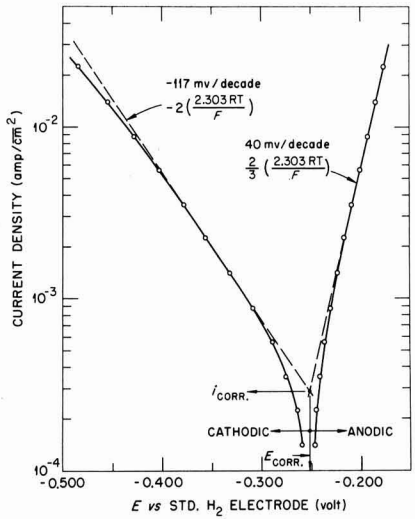

Fig. 1. Polarization of iron in H_2-saturated 0.50M H_2SO_4; T = 30°C.

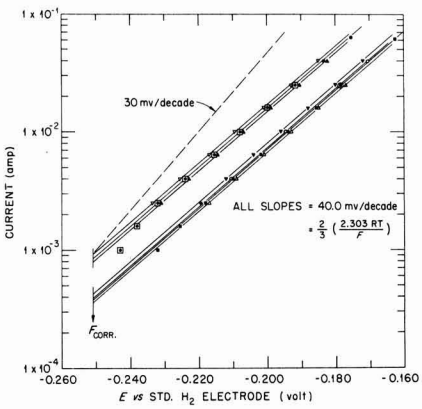

Fig. 2. Anodic polarization of iron in H_2-saturated 0.50M H_2SO_4 (T = 30°C). Data shown for 4 large and 4 small electrodes, each in freshly prepared solution; initial apparent area ratio = 2.86 cm²/1.35 cm² = 2.12.

The purpose of the experiment summarized in Fig. 2 was to resolve the conflict concerning the magnitude of the steady-state anodic Tafel slope. To this end, the anodic polarization characteristics of numerous iron electrodes, each in freshly prepared 0.5M H_2SO_4, were determined. The results clearly show that the steady-state anodic Tafel slope is 40 mv/decade, *i.e.*, $(2/3)(2.303\ RT/\mathbf{F})$, and not 30 mv/decade, as frequently reported, or some other value of less diagnostic significance. For comparative purposes, a line having a slope of 30 mv/decade has been included in Fig. 2. The results also show that a rather high degree of accuracy may be expected when comparing polarization data for different electrodes on the basis of apparent surface areas. At a given potential, the ratio of the average current for the four large electrodes to

[2] Prepared, analyzed, and distributed by Battelle Memorial Institute on behalf of the American Iron and Steel Institute.

[3] See Table I of ref. (18) for limits of detection.

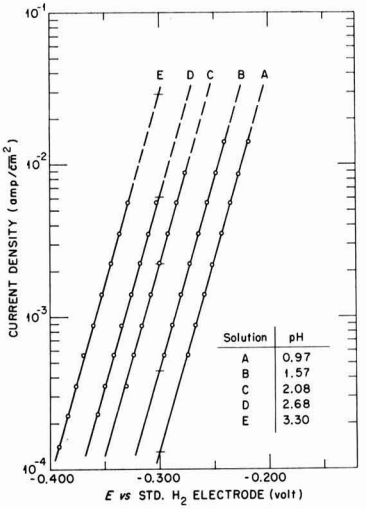

Fig. 3. Anodic polarization of iron in H_2-saturated 0.50M (H_2SO_4 + Na_2SO_4) at various pH values; T = 30°C.

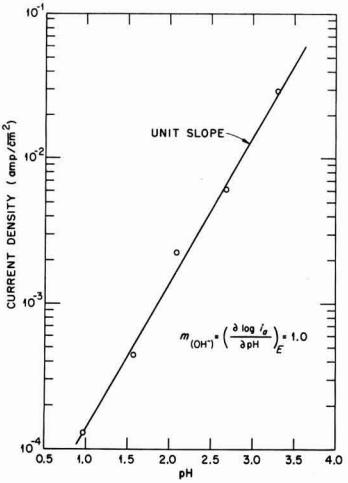

Fig. 4. Anodic current density of iron electrode as function of pH at constant potential (E = —0.300v vs. std. H_2 electrode) in H_2-saturated 0.50M (H_2SO_4 + Na_2SO_4); T = 30°C.

that for the four small electrodes is 2.19, while the apparent area ratio of the large and small electrodes is 2.12. Contamination of the electrode surface by solution impurities, as evidenced by the presence of slow polarization hysteresis phenomena, was occasionally encountered in studies at higher pH values, *i.e.*, in solutions prepared from Na_2SO_4. In such cases, the electrode was found to be less polarizable than normal, and no true Tafel behavior was observed. Normal behavior was restored by replacing the solution and re-etching the test electrode.

On the basis of the results just described, the partial anodic and cathodic current densities may be expressed by Eq. [18] and [19], respectively

$$i_a = k_a a_{(OH^-)}^m \exp(3\mathbf{F}E/2RT) \quad [18]$$

$$|i_c| = k_c a_{(H^+)}^n \exp(-\mathbf{F}E/2RT) \quad [19]$$

in which the reaction orders, m and n, remain to be determined. A direct evaluation of the order of the anodic reaction with respect to the hydroxyl ion activity was made. A single test electrode was placed in solution having a pH of 3.30, and the anodic Tafel line was determined. The pH was then lowered by running H_2-saturated, pre-electrolyzed dilute sulfuric acid directly from a storage reservoir into the cell *via* Teflon tubing and stopcocks connecting the two compartments. In this fashion, the system was maintained in a completely closed state. At each pH, the anodic Tafel line was determined. The results of this experiment are summarized in Fig. 3 which shows the displacement of the anodic Tafel line accompanying changes in solution pH. According to Eq. [18], the reaction order is given by Eq. [20]

$$m = (\partial \log i_a/\partial \mathrm{pH})_E \quad [20]$$

Using the current densities observed at E = —0.300v (marked in Fig. 3 by a horizontal bar), the order plot shown in Fig. 4 was constructed. As the figure shows, a straight line drawn with a unit slope fits the data very closely. Consequently, the anodic reaction is first order in hydroxyl ion activity, and not second order.

According to Eq. [21], which follows directly from Eq. [18]

$$(\partial E/\partial \mathrm{pH})_{i_a} = -(2m/3)(2.303\ RT/\mathbf{F}) \quad [21]$$

the electrode potential at a constant anodic current density should be a linear function of pH and, if m = 1, the proportionality constant should be equal to —40 mv/pH. Using this approach, the results of anodic order determinations performed on several different electrodes are conveniently summarized in Fig. 5. The straight line drawn with a slope of —40 mv/pH fits the data, further confirming the fact that m = 1.

A satisfactory direct evaluation of n, the order of the hydrogen evolution reaction with respect to proton activity, is precluded by concentration polarization. However, at open-circuit, $i_a = |i_c| = i_{corr}$, and $E = E_{corr}$. Consequently, it follows from Eq. [18] and [19] that

$$(dE_{corr}/d\mathrm{pH}) = -(m + n)(2.303\ RT/2\mathbf{F}) \quad [22]$$

i.e., a plot of E_{corr} *vs.* pH should yield a straight line having a slope of $-(m + n)(2.303\ RT/2\mathbf{F})$. Since it has already been established that m = 1, this approach allows an indirect evaluation of n to be made. The results of experiments performed on several different electrodes are shown in Fig. 6. In some instances the data were obtained in a matter of minutes by following the procedure used to determine m, *i.e.*, by starting at the highest pH and then reducing the pH in steps by running H_2SO_4 into the cell from a reservoir. In other cases, the electrodes remained several days at each pH, during which time they were subjected to various polarization experiments. The results confirm the linear

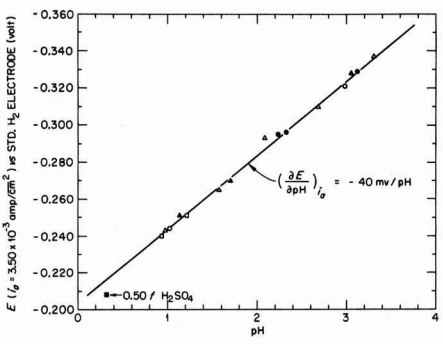

Fig. 5. Variation of the potential corresponding to a partial anodic current density of 3.50 x 10^{-3} amp/cm² with pH for several iron electrodes in H_2-saturated 0.50M (H_2SO_4 + Na_2SO_4); T = 30°C.

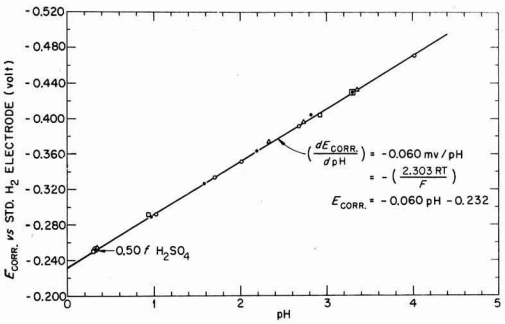

Fig. 6. Variation of the corrosion potential of iron with pH in H_2-saturated 0.50M (H_2SO_4 + Na_2SO_4); T = 30°C. Different electrodes are represented by different symbols (○ and • by fast technique).

relation between E_{corr} and pH and, according to Eq. [22], the observed slope of precisely —60 mv/pH, —2.303 $RT/\mathbf{F}$, means that the hydrogen evolution reaction is first order in proton activity.

Discussion

The experimental results of this investigation are summarized in the following set of self-consistent equations

$$i_{a,\infty} = k_a a_{(OH^-)} \exp(3\mathbf{F}E/2RT) \quad [23]$$

$$|i_{c,\infty}| = k_c a_{(H^+)} \exp(-\mathbf{F}E/2RT) \quad [24]$$

$$E_{corr} = -0.232 - (2.303\,RT/\mathbf{F})\,pH \quad [25]$$

$$\log i_{corr} = -3.15 - (1/2)\,pH \quad [26]$$

in which current densities are expressed in units of amp/cm², and the electrode potential, in volts, is referred to the standard hydrogen electrode. The value of the constant appearing in Eq. [26], —3.15, is based on data obtained in Na_2SO_4 solutions, Fig. 3-5. For 0.5M H_2SO_4, Fig. 1, 2, the constant has a slightly more negative value of —3.38. Equations [25] and [26] show that (dE_{corr}/pH) and ($d \log i_{corr}/pH$) are equal to —60 mv/pH and —½, respectively, and these values may be compared with those cited in the introduction. As a matter of convenience, the hydrogen evolution and iron dissolution reactions are discussed separately.

Hydrogen evolution reaction.—The general reaction scheme for the hydrogen evolution reaction is given by Eq. [27]-[29]

$$H^+ + e^- \rightleftharpoons H_{ads} \quad [27]$$

$$H_{ads} + H^+ + e^- \rightarrow H_2 \quad [28]$$

$$2H_{ads} \rightarrow H_2 \quad [29]$$

in which for the prevailing experimental conditions, dissociation of H_2 can be neglected. If reaction [27] is coupled with reaction [28], the appropriate kinetic equations are Eq. [30] and [31]

$$-i_c/\mathbf{F} = \bar{k}_1 a_{(H^+)}(1-\theta_H) - \bar{k}_{-1}\beta_H\theta_H + \bar{k}_2 a_{(H^+)}\beta_H\theta_H \quad [30]$$

$$\beta_H d\theta_H/dt = \bar{k}_1 a_{(H^+)}(1-\theta_H) - \bar{k}_{-1}\beta_H\theta_H - \bar{k}_2 a_{(H^+)}\beta_H\theta_H \quad [31]$$

in which $\bar{k}_j$ are electrochemical rate constants. The definitions of β_H and θ_H derive from the relation, $[H_{ads}] = \beta_H\theta_H$, where $[H_{ads}]$ is the concentration of adsorbed hydrogen atoms expressed in mole/cm², θ_H is the fraction of the surface occupied by the hydrogen atoms, and β_H is a proportionality constant. In order to achieve agreement with Eq. [24], it is necessary that $(\bar{k}_1 a_{(H^+)} + \bar{k}_2 a_{(H^+)}\beta_H) >> \bar{k}_{-1}\beta_H$, in which case, with $d\theta_H/dt = 0$, Eq. [30] and [31] lead to the steady-state solution represented by Eq. [32] and [33]

$$\theta_{H,\infty} = k_1/(k_1 + k_2\beta_H) \quad [32]$$

$$-i_{c,\infty}/\mathbf{F} = 2\bar{k}_2 a_{(H^+)}\beta_H\theta_{H,\infty} = 2k_2 a_{(H^+)}\beta_H \left(\frac{k_1}{k_1 + k_2\beta_H}\right) \exp(-\mathbf{F}E/2RT) \quad [33]$$

If reaction [27] is coupled with reaction [29], the kinetics are described by Eq. [34] and [35]

$$-i_c/\mathbf{F} = \bar{k}_1 a_{(H^+)}(1-\theta_H) - \bar{k}_{-1}\beta_H\theta_H \quad [34]$$

$$\beta_H d\theta_H/dt = \bar{k}_1 a_{(H^+)}(1-\theta_H) - \bar{k}_{-1}\beta_H\theta_H - 2k_3\beta_H^2\theta_H^2 \quad [35]$$

In this case, agreement with Eq. [24] requires that $2k_3\beta_H^2\theta_H^2 >> \bar{k}_{-1}\beta_H\theta_H$ and $(1-\theta_H) \approx 1$. With these restrictions, the steady-state solution derived from Eq. [34] and [35] is given by Eq. [36] and [37]

$$\theta_{H,\infty} = (k_1 a_{(H^+)}/2k_3\beta_H^2)^{1/2} \exp(-\mathbf{F}E/4RT) \quad [36]$$

$$-i_{c,\infty}/\mathbf{F} = 2k_3\beta_H^2\theta_{H,\infty}^2 = k_1 a_{(H^+)} \exp(-\mathbf{F}E/2RT) \quad [37]$$

The preceding analysis shows that the observed results are consistent with three well-known mechanisms (20),

(*A*) slow discharge-fast electrochemical desorption; Eq. [32], [33], $k_2\beta_H >> k_1$, $(1-\theta_H) \approx 1$

(*B*) fast discharge-slow electrochemical desorption; Eq. [32], [33], $k_1 >> k_2\beta_H$, $\theta_H \approx 1$

(*C*) slow discharge-fast catalytic desorption; Eq. [36], [37], $(1-\theta_H) \approx 1$.

The inability to distinguish among these mechanisms merely on the basis of the dependence of the current density on pH and potential, the inaccessibility of a stoichiometric number for actively corroding iron, and the conflicting opinions generated by various theoretical attempts to establish the rate-determining step (21,22), have resulted in a dilemma which has only recently been resolved with any degree of certainty.

Under certain conditions (23), the steady-state flux of hydrogen atoms diffusing through an iron membrane electrode which divides a cell into two otherwise isolated compartments is given by Eq. [38]

$$f_\infty = \frac{Dk_i\theta_{H,\infty}/k_o l}{1 + (2D/k_o l)} \quad [38]$$

where D is the diffusion coefficient of hydrogen in iron, l is the thickness of the membrane, and k_i and k_o are rate constants associated with the transfer of adsorbed hydrogen atoms from the surface to the interior of the membrane and *vice versa*, respectively. The flux results in a net transfer of hydrogen atoms from the "polarization" side of the membrane, where the surface coverage by adsorbed hydrogen atoms is $\theta_{H,\infty}$, to the "diffusion" side of the membrane. According to Eq. [32], which applies to mechanisms (*A*) and (*B*), $\theta_{H,\infty}$ and, consequently, f_∞ are independent of the potential of the polarization side of the membrane. For mechanism (*C*), Eq. [36] applies and, therefore, $\partial \ln f_\infty/\partial E$ is equal to $-\mathbf{F}/4RT$. This latter result was observed by Devanathan (24), who employed an Armco iron membrane in acidic sulfate solution. At very large cathodic overvoltages, electrochemical desorption predominated, *i.e.*, mechanism (*C*) was replaced by mechanism (*A*). Again, according to Eq. [33], [37], and [38], the steady-state flux should be proportional to $|i_{c,\infty}|$ for mechanisms (*A*) and (*B*), and to $(|i_{c,\infty}|)^{1/2}$ for mechanism (*C*). The latter observation has been reported many times for Armco and comparable irons (23).

In experiments of the type just described, the kinetics of the hydrogen evolution reaction occurring on the polarization side of the membrane are examined. An alternative approach is to study the effects produced by diffusing atomic hydrogen on the kinetics of

the hydrogen evolution reaction occurring on the diffusion side of the membrane (25). Differentiation of Eq. 34 leads to Eq. [39]

$$\left(\frac{dE}{d\theta_H}\right)_{i_c} = \frac{(-2RT/F)(\bar{k}_1 a_{(H^+)} + \bar{k}_{-1}\beta_H)}{\bar{k}_1 a_{(H^+)}(1-\theta_H) + \bar{k}_{-1}\beta_H\theta_H} \quad [39]$$

from which it is apparent that $(dE/d\theta_H)_{i_c}$ is negative, *i.e.*, for mechanism (*C*) an increase in θ_H resulting from diffusion of hydrogen from the polarization side of the membrane to the diffusion side causes the potential of the latter surface, under cathodic polarization at a constant current density, to become less noble. Similarly, differentiation of Eq. [30] gives Eq. [40]

$$\left(\frac{dE}{d\theta_H}\right)_{i_c} = \frac{(-2RT/F)(\bar{k}_1 a_{(H^+)} + \bar{k}_{-1}\beta_H - \bar{k}_2 a_{(H^+)}\beta_H)}{\bar{k}_1 a_{(H^+)}(1-\theta_H) + \bar{k}_{-1}\beta_H\theta_H + \bar{k}_2 a_{(H^+)}\beta_H\theta_H} \quad [40]$$

and if $\bar{k}_1 a_{(H^+)} > \bar{k}_2 a_{(H^+)}\beta_H$, as in mechanism (*B*), then $(dE/d\theta_H)_{i_c}$ is again negative. On the other hand, if $\bar{k}_2 a_{(H^+)}\beta_H > \bar{k}_1 a_{(H^+)}$, then $(dE/d\theta_H)_{i_c}$ is positive except for the unlikely case where $\bar{k}_2 a_{(H^+)}\beta_H - \bar{k}_1 a_{(H^+)} < \bar{k}_{-1}\beta_H$, a condition which when coupled with the restriction leading to Eq. [32], [33], $\bar{k}_1 a_{(H^+)} + \bar{k}_2 a_{(H^+)}\beta_H >> \bar{k}_{-1}\beta_H$, would require $k_1 \approx k_2\beta_H$. With $\bar{k}_2 a_{(H^+)}\beta_H >> \bar{k}_1 a_{(H^+)}$, as in mechanism (*A*), $(dE/d\theta_H)_{i_c}$ is positive. Kovba and Bagotskaya (26) found that for zone-refined iron in 0.5M H_2SO_4, $(dE/d\theta_H)_{i_c}$ is positive, *i.e.*, mechanism (*A*) prevails. For Armco iron in the same medium, the results were less definitive, but were interpreted as being indicative of mechanism (*C*), in agreement with Devanathan's findings.

Bockris and Koch (27) examined the relative rates of hydrogen and deuterium evolution on spectroscopically pure iron and found the results to be consistent only with a slow discharge mechanism. The absence of any significant pseudocapacity associated with changes in θ_H, together with the fact that $(1-\theta_H) \approx 1$, also establishes slow discharge as the rate-determining reaction, both on zone-refined (6) and Armco (24) iron.

Contrary to previous reports favoring slow electrochemical desorption as the rate-determining step, [28], [29], all of the results just described confirm slow proton discharge, $H^+ + e^- \rightarrow H_{ads}$, as the rate-determining reaction for hydrogen evolution on iron. For zone-refined iron, the preceding discussion indicates that the experimental results of the present investigation, Eq. [24], may be attributed to mechanism (*A*), slow discharge-fast electrochemical desorption.

Iron dissolution reaction.—As is shown by Eq. [23], the steady-state anodic Tafel slope, $(\partial E/\partial \log i_{a,\infty})_{pH}$, is equal to 40 mv/decade, *i.e.*, (2/3) (2.303 *RT*/**F**), and the reaction is first order in hydroxyl ion activity. These results are in agreement only with those of Bockris *et al.* (4-6), as may be seen by comparing Eq. [23] and [14]. Equation [23] may be interpreted in terms of the following mechanism

$$Fe + H_2O \rightleftharpoons Fe(H_2O)_{ads} \quad [41]$$

$$Fe(H_2O)_{ads} \rightleftharpoons Fe(OH^-)_{ads} + H^+ \quad [42]$$

$$Fe(OH^-)_{ads} \rightleftharpoons (FeOH)_{ads} + e^- \quad [43]$$

$$(FeOH)_{ads} \rightarrow (FeOH)^+ + e^- \text{ (rate-determining)} \quad [44]$$

$$(FeOH)^+ + H^+ = Fe^{++} + H_2O \quad [45]$$

which takes formal account of the simultaneous coverage of the electrode surface by adsorbed water molecules, hydroxyl ions, and the surface intermediate, $(FeOH)_{ads}$. A kinetic description of this mechanism is given by Eq. [46]-[49]

$$i_a/\mathbf{F} = \bar{k}_3\beta\theta_2 - \bar{k}_{-3}\beta\theta_3 + \bar{k}_4\beta\theta_3 \quad [46]$$

$$\beta d\theta_1/dt = \bar{k}_1(1-\theta_T) - \bar{k}_{-1}\beta\theta_1 - \bar{k}_2\beta\theta_1 + \bar{k}_{-2}a_{(H^+)}\beta\theta_2 \quad [47]$$

$$\beta d\theta_2/dt = \bar{k}_2\beta\theta_1 - \bar{k}_{-2}a_{(H^+)}\beta\theta_2 - \bar{k}_3\beta\theta_2 + \bar{k}_{-3}\beta\theta_3 \quad [48]$$

$$\beta d\theta_3/dt = \bar{k}_3\beta\theta_2 - \bar{k}_{-3}\beta\theta_3 - \bar{k}_4\beta\theta_3 \quad [49]$$

in which $\bar{k}_j$ are electrochemical rate constants, and θ_1, θ_2, and θ_3 represent the fractions of the electrode surface occupied by $Fe(H_2O)_{ads}$, $Fe(OH^-)_{ads}$, and $(FeOH)_{ads}$, respectively, *i.e.*,

$$Fe(H_2O)_{ads} = \beta\theta_1, \quad Fe(OH^-)_{ads} = \beta\theta_2, \quad (FeOH)_{ads} = \beta\theta_3$$

where the surface concentrations are expressed in mole/cm^2, and β is a proportionality constant. The total fraction of the surface occupied, θ_T, is equal to $(\theta_1 + \theta_2 + \theta_3)$. Equations [46]-[49] reduce to the steady-state solution

$$i_{a,\infty}/\mathbf{F} = 2k_4\beta \frac{k_3k_2}{k_{-3}k_{-2}a_{(H^+)}} \left(\frac{k_1}{k_1 + k_{-1}\beta}\right) \exp(3\mathbf{F}E/2RT) \quad [50]$$

which agrees with the observed results, Eq. [23]. The conditions leading to Eq. [50] are $\bar{k}_{-3} >> \bar{k}_4$ and $1 >> (\theta_2 + \theta_3)$. With $\theta_T \approx 1$, the latter condition means that $\theta_1 \approx 1$, *i.e.*, $k_1/(k_1 + k_{-1}\beta) \approx 1$. An alternative approach is to assume that for an instantaneous value of θ_3, the remainder of the occupied surface is divided between θ_1 and θ_2 in accordance with reaction [42] in equilibrium, *i.e.*, $\theta_1/\theta_2 = \bar{k}_{-2}a_{(H^+)}/\bar{k}_2$. Then, with $\theta_1/\theta_2 >> 1$ and $\theta_T \approx 1$, Eq. [46] and [49] reduce to Eq. [51] and [52].

$$i_a/\mathbf{F} = \bar{k}_3\beta(\bar{k}_2/\bar{k}_{-2}a_{(H^+)})(1-\theta_3) - \bar{k}_{-3}\beta\theta_3 + \bar{k}_4\beta\theta_3 \quad [51]$$

$$\beta d\theta_3/dt = \bar{k}_3\beta(\bar{k}_2/\bar{k}_{-2}a_{(H^+)})(1-\theta_3) - \bar{k}_{-3}\beta\theta_3 - \bar{k}_4\beta\theta_3 \quad [52]$$

If $\bar{k}_{-3} >> \bar{k}_4$ and $(1-\theta_3) \approx 1$, then in the steady-state, $d\theta_3/dt = 0$, the current density is again given by Eq. [50].

A comparison of Eq. [51], [52], and [50] with Eq. [12], [13], and [14], respectively, reveals that the mechanism presented here, Eq. [41]-[45], is basically equivalent to that proposed by Bockris *et al.* (4-6), Eq. [9]-[11], in which the adsorption of water and hydroxyl ions was ignored. The necessity for taking into account the adsorption of these species becomes evident when specific adsorption of an anion inhibitor is considered, as in the second paper of this series. In advocating a modified form of the Heusler mechanism, Lorenz, Yamaoka, and Fischer (8) criticized the Bockris mechanism on several counts. Their objections may be dealt with more effectively if, first, the original and modified forms of the Heusler mechanism are examined. The modified version is shown by Eq. [53]-[56]

$$Fe + OH^- \rightleftharpoons (FeOH)_{ads} + e^- \quad \text{fast} \quad [53]$$

$$(FeOH)_{ads} + Fe \rightleftharpoons Fe(OHFe)_{ads} \equiv K \quad \text{slow} \quad [54]$$

$$Fe(OHFe)_{ads} + OH^- \rightleftharpoons FeOH^+ + (FeOH)_{ads} + 2e^- \quad \text{r.d.s.} \quad [55]$$

$$FeOH^+ + x\cdot H_2O \rightleftharpoons Fe^{++}\cdot aq + OH^- \quad \text{fast} \quad [56]$$

In both the original and modified versions, the steady-state and transient anodic current densities are given by Eq. [7] and [8], respectively, although in the modified version, $k_2\beta\theta_o$ is replaced by k_3K_o in Eq. [8] and k_2 is replaced by k_3k_2/k_{-2} in Eq. [7]. Equating $i_{a,\infty}$ and $|i_{c,\infty}|$, the latter being given by Eq. [19], one finds that (dE_{corr}/dpH) and $(d \log i_{corr}/dpH)$ are equal to $-(2/5)(n+2)(2.303\ RT/\mathbf{F})$ and $-(4n-2)/5$, respectively. The order of the hydrogen evolution reaction with respect to proton activity was not determined by Heusler, but with the reported value of zero for $(d \log i_{corr}/dpH)$, n would necessarily be equal to ½,

and (dE_{corr}/dpH) would then be $-2.303\ RT/F$, *i.e.*, -60 mv/pH. Not only does $n = \frac{1}{2}$ have no theoretical basis, but it is now established that $n = 1$. With $n = 1$, (dE_{corr}/dpH) and $d \log i_{corr}/dpH)$ would be equal to $-(6/5)\ (2.303\ RT/F)$, *i.e.*, -70 mv/pH, and $-2/5$, respectively. The reported values of -45 mv/pH and 0 constitute an internal inconsistency in both versions of the mechanism. According to Eq. [7] and [8], the steady-state and transient current densities are second and first order in hydroxyl ion activity, respectively. In view of the discrepancies just cited, it is of interest to examine the method employed in determining these reaction orders. Equations [7] and [8] are of the form

$$i_a = k_a a_{(OH^-)}{}^m \exp\ (\alpha FE/RT)$$

from which it follows that m is given by Eq. [57]

$$m = \left(\frac{\partial \log i_a}{\partial pH}\right)_E = -\left(\frac{\partial E}{\partial pH}\right)_{i_a} \Big/ \left(\frac{\partial E}{\partial \log i_a}\right)_{pH} \qquad [57]$$

However, $(\partial E/\partial pH)_{i_a}$ was identified with (dE_{corr}/dpH), which is possible only if $(d \log i_{corr}/dpH)$ is zero. With (dE_{corr}/dpH) equal to -45 mv/pH and $(\partial E/\partial \log i_a)$ equal to 60 mv/decade and 30 mv/decade for the transient and steady-state, respectively, the corresponding reaction orders were 3/4 and 3/2. Conceding that (dE_{corr}/dpH) should probably be -60 mv/pH, the orders were promoted from 3/4 and 3/2 to 1 and 2. One can only conclude that either $n = \frac{1}{2}$, an experimentally and theoretically unacceptable value, or Eq. [7] and [8] are incorrect. A further discrepancy in the original Heusler mechanism is revealed by a consideration of anodic transients under potentiostatic conditions. Heusler found that at constant potential log $(i_{a,\infty} - i_{a,t})$ was a linear function of time. Data were presented for two values of the electrode potential, and a 40 mv increase in the potential was accompanied by a decrease in the time constant, $-dt/dln\ (i_{a,\infty} - i_{a,t})$, from 0.28 sec to 0.25 sec. At constant potential, Eq. [5] may be solved for θ as a function of time, and if the result is substituted into Eq. [4], the anodic current density is given by Eq. [58]

$$(i_{a,\infty} - i_{a,t}) = (i_{a,\infty} - i_{a,o}) \exp\ (-\bar{k}_{-1}t) \qquad [58]$$

which shows that the time constant is actually $1/\bar{k}_{-1}$ and, consequently, potential-dependent. In contrast to the observed effect, an increase of 40 mv in the potential should have caused the time constant to increase by a factor of 4.64. In the modified version of the mechanism, this discrepancy, the existence of which was not noted, has been inadvertently overcome since in this formulation the time constant would be equal to $1/k_{-2}$ and, therefore, potential independent. An additional difficulty in either version arises from the fact that the hydroxyl ion concentration is far too low in acid solution to support the current densities observed. This problem is not circumvented by the suggestion (3) that the hydroxyl ion concentration at the electrode surface can be much greater than in the interior of the solution if hydroxyl ions are more strongly adsorbed than water dipoles for, from a kinetic viewpoint, it would still be necessary to replace Eq. [1] and [53] by Eq. [41]-[43], and OH^- by $Fe(OH^-)_{ads}$ in Eq. [2] and [55]. However, this would raise a question concerning the potential dependency of reactions [2] and [55], since the pre-electrode plane could no longer be identified with the outer Helmholtz plane. Finally, the use of two electron transfer reactions such as reactions [2] and [55] has been appropriately criticized by Bockris *et al.* (4). In reply to the criticism, it has been suggested (8) that two electron transfer reactions may be regarded as the sum of two parallel one electron transfer reactions, but this would result in the reaction having a potential dependency characteristic of a one electron transfer reaction, *i.e.*, $FE/2RT$ and not FE/RT.

In contrast to the serious defects present in the original and modified forms of the Heusler mechanism, the criticisms leveled by Lorenz, Yamaoka, and Fischer (8) against the Bockris mechanism and, by equability, the mechanism of Eq. [41]-[45], may be shown to be without substance. The following criticisms were leveled against the Bockris mechanism:

1. The steady-state relation derived from the transient current density-potential relation calls for a Tafel slope of 40 mv/decade instead of the reproducible experimental value of 30 mv/decade.
2. The steady-state relation also calls for an electrochemical reaction order with respect to hydroxyl ion activity of 1 instead of 2.
3. The transient current density-potential relation offers no precise statement concerning the electrochemical reaction order.
4. The initial polarization value in the potential-time curve does not disappear when an iron rotating-disk electrode ($\omega = 4800$ rpm) is used.

The first two points require no comment beyond pointing out that the steady-state results, Eq. [23], derive only from direct steady-state measurements and not from transient measurements. Interpretations of transient data which lead to a conflict with Eq. [23] must necessarily be incorrect. The present investigation, being limited to steady-state measurements, offers no direct experimental confirmation of the interpretation suggested by Bockris *et al.* (5, 6) for the transient anodic Tafel line. However, the feasibility of their interpretation, an interpretation which is not in conflict with steady-state results, is not lessened by the third and fourth criticisms listed above. The third point can only be regarded as a matter of semantics for, as was shown in the introduction, the relation between the anodic current density and proton activity is precisely defined, *i.e.*, the anodic current density is inversely proportional to the existing proton activity in the double layer, both in the transient and steady states. With regard to the fourth point, the interpretation of the transient Tafel line observed during anodic charging is based on the assumption that during the time required for reaction [9] to attain a pseudo-equilibrium state, $\bar{k}_{-1}\beta\theta_H a_{(H^+,D.L.)} >> f_{diff}$ (here f_{diff} represents the net diffusion flux of protons from the double layer, where the proton activity is $a_{(H^+,D.L.)}$, to the bulk of the solution). Rotation of the electrode does not necessarily invalidate this inequality and, consequently, although it would affect the rate of decay of the transient, it may have no effect whatsoever on the transient Tafel line, *i.e.*, the observation that the initial polarization value does not disappear (or diminish) can not be regarded as evidence against the interpretation proposed by Bockris *et al.* (5, 6) for the transient Tafel line.

The diversity in the results obtained by other investigators may be attributed to contamination of the electrode surface, as evidenced by the presence of slow polarization hysteresis phenomena. In such contaminated systems, illusory steady-state Tafel behavior is observed if the time lapse in the determination of log *i vs. E* curves is small compared to the time required to significantly alter the state of the electrode surface (30).

Summary

The electrochemical behavior of the active iron electrode in the absence of an inhibitor has been determined, and the results may serve as an experimental and mechanistic base for the interpretation of the electrochemical behavior of iron in inhibited systems. In addition, the results of this investigation suggest that the electrochemical behavior of cobalt in noninhibiting media be carefully re-examined since, in acidic sulfate solution, the system has been interpreted (31-32) in terms of the Heusler mechanism for iron, although there is earlier evidence (33) which indicates that the mechanism presented here may be more appropriate.

Acknowledgment

The author is especially indebted to Dr. G. H. Cartledge for his continued encouragement and resolute support. He also wishes to acknowledge the kind support of Dr. P. H. Emmett.

Manuscript received July 20, 1964.

Any discussion of this paper will appear in a Discussion Section to be published in the December 1965 JOURNAL.

REFERENCES

1. K. F. Bonhoeffer and K. E. Heusler, *Z. physik. Chem., N.F.*, **8**, 390 (1956).
2. K. F. Bonhoeffer and K. E. Heusler, *Z. Elektrochem.*, **61**, 122 (1957).
3. K. E. Heusler, *ibid.*, **62**, 582 (1958).
4. J. O'M. Bockris, D. Drazic, and A. R. Despic, *Electrochim. Acta*, **4**, 325 (1961).
5. J. O'M. Bockris and H. Kita, *This Journal*, **108**, 676 (1961).
6. J. O'M. Bockris and D. Drazic, *Electrochim. Acta*, **7**, 293 (1962).
7. K. E. Heusler and G. H. Cartledge, *This Journal*, **108**, 732 (1961).
8. W. Lorenz, H. Yamaoka, and H. Fischer, *Ber. Bunsenges. Physik. Chem.*, **67**, 932 (1963).
9. T. P. Hoar and T. Hurlen, Proc. 8th Meeting CITCE, Madrid, 1956, p. 445, Butterworths, London (1958).
10. T. Hurlen, *Acta Chem. Scand.*, **14**, 1533, 1555, 1564 (1960).
11. A. C. Makrides, *This Journal*, **107**, 869 (1960).
12. H. Kaesche, *Z. Elektrochem.*, **63**, 492 (1959).
13. G. Okamoto, M. Nagayama, and N. Sato, Proc. 8th Meeting CITCE, Madrid, 1956, p. 72, Butterworths, London (1958).
14. M. Stern and R. M. Roth, *This Journal*, **104**, 390 (1957).
15. A. C. Makrides, N. W. Komodromos, and N. Hackerman, *ibid.*, **102**, 363 (1955).
16. M. Stern, *ibid.*, **102**, 609 (1955).
17. J. D'Ans and W. Breckheimer, *Z. Elektrochem.*, **56**, 585 (1952).
18. R. E. Heffelfinger, D. L. Chase, G. W. Regnstorff, and W. Henry, *Anal. Chem.*, **30**, 112 (1958).
19. R. E. Meyer, *This Journal*, **106**, 930 (1959).
20. J. O'M. Bockris and H. Mauser, *Can. J. Chem.*, **37**, 475 (1959).
21. B. E. Conway and J. O'M. Bockris, *J. Chem. Phys.*, **26**, 532 (1957).
22. L. I. Krishtalik, *Zh. Fiz. Khim.*, **34**, 117 (1960).
23. L. I. Freiman and V. A. Titov, *ibid.*, **34**, 23 (1960).
24. M. A. V. Devanathan and Z. Stachurski, *This Journal*, **111**, 619 (1964).
25. A. N. Frumkin, *Zh. Fiz. Khim.*, **31**, 1875 (1957).
26. L. D. Kovba and I. A. Bagotskaya, *ibid.*, **38**, 217 (1964).
27. J. O'M. Bockris and D. F. A. Koch, *J. Phys. Chem.*, **65**, 1941 (1961).
28. N. Pentland, J. O'M. Bockris, and E. Sheldon, *This Journal*, **104**, 182 (1957).
29. J. O'M. Bockris, Proc. 4th Conf. Electrochem., Moscow, 1956, pp. 56, 101, Academy of Science, Moscow (1959).
30. E. J. Kelly, Chem. Div. Ann. Prog. Rept. June 20, 1963, ORNL-3488, p. 93.
31 K. E. Heusler, *Z. Elektrochem.*, **66**, 177 (1962).
32. Z. A. Iofa and Bao-Min Bei, *Zh. Fiz. Khim.*, **36**, 2558 (1962).
33. V. I. Kravtsov and O. G. Lokshtanova, *ibid.*, **36**, 2362 (1962).

On the Initiation and Growth of Stress Corrosion Cracks in Tarnished Brass

A. J. McEvily, Jr., and A. P. Bond

Scientific Laboratory, Ford Motor Company, Dearborn, Michigan

ABSTRACT

Stress corrosion cracking of α-brass was studied in nearly neutral ammoniacal copper sulfate. Under the test conditions, this solution produced a thin, adherent oxide film on the brass. Microstructural studies of the fracture surfaces suggest that alternate formation and rupture of this film leads to initiation and propagation of stress corrosion cracks. Crack propagation rates were measured in sheet specimens with a central notch and found to be proportional to $\sigma_K{}^2 l$, where σ_K is the applied stress and l is the semicrack length.

Among the various mechanisms proposed for stress corrosion cracking are those based on film rupture (1), on structure sensitive sites together with dislocation interactions, on stacking faults, on short range order (2-7), on strain assisted anodic dissolution (8, 9), on stress-sorption (10), and on solid solution effects (11). Such a variety of proposals is an indication that no general mechanism exists, but that one or another is applicable under certain circumstances. However, the lack of a comprehensive study of the role of stress on the initiation and growth of stress corrosion cracks contributes to the uncertainty in deciding which of the many proposed mechanisms is applicable to a case at hand. In the present investigation the role of stress in crack initiation and growth was determined for the stress corrosion of α-brass in an ammoniacal solution. Since it has been suggested (12, 13) that the tarnish which forms on α-brass plays an important role in stress corrosion cracking, it appeared desirable to examine the characteristics of this tarnish in some detail.

Experimental

Materials.—α-brass (70 w/o Cu-30 w/o Zn) (w/o is weight per cent) in both the annealed as well as a cold-worked condition, was chosen for this study because information is available on its susceptibility to stress corrosion cracking under various environmental conditions (13, 14). Annealed specimens, obtained from sheet material, were 0.031 in. thick, and were heat-treated for 2 hr at 500°C in an argon atmosphere. The cold-worked specimens (75% reduction) were 0.015 in. thick. The tensile properties of the materials used were as follows:

	Proportional limit, psi	Yield strength, psi	Tensile strength, psi
Cold Rolled	60,000	95,000	98,000
Annealed	15,000	18,000	52,000

Specimens.—An electropolished tensile strip, ½ in. wide, was used primarily to study the characteristics of the tarnish. A second type of specimen, shown in Fig. 1, was used to study crack growth. A centrally located stress-raising slit localized the region of crack initiation and was made by drilling a hole and then slitting further in the width direction to the desired slit length. Slitting was accomplished by the reciprocating action of a thread impregnated with diamond paste, and provided a reproducible stress-raiser essentially free of

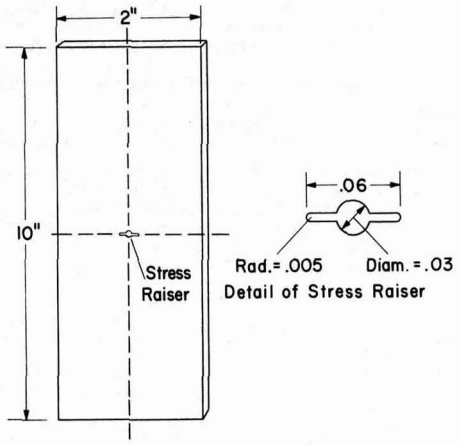

Fig. 1. Specimen used in the determination of rate of crack propagation.

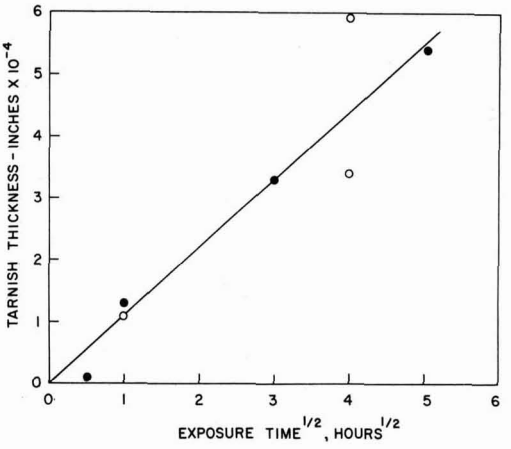

Fig. 2. Tarnishing of brass in 0.05M $CuSO_4$ + 0.48M $(NH_4)_2SO_4$ of pH = 7.25; ○, annealed; ●, cold rolled.

the residual stresses which are characteristic of machined slits or notches. The surfaces of these specimens were lightly polished using metallographic techniques to facilitate the observation of crack growth.

Solution.—The solution shown by Mattson (13) to lead to rapid stress corrosion cracking of α-brass was used. It was 0.05M in $CuSO_4$ and 0.48M in $(NH_4)_2SO_4$ with the pH adjusted to 7.25 ± 0.05 with NH_4OH. As Mattson noted (13), the reproducibility is somewhat improved by aging the solution about 24 hr. A small amount of precipitate is formed during this period, but little if any further precipitation was observed subsequently, even during long-time stress corrosion runs.

Tests.—Specimens were tested in a dead-weight, lever-type creep machine, load being transmitted to the specimen through a universal joint to eliminate bending stresses. A plexiglass container, sealed to the specimen below the notch by means of a rubber gasket, was filled with solution after loading. To minimize changes in solution composition, fresh solution was continuously introduced into the cell at a rate of about 80 ml/hr. Initial experiments revealed that attack was rapid at the solution-air interface. To avoid this effect, specimens were coated with Glyptal in the vicinity of the interface.

Crack growth was observed with a low-power microscope (30X) equipped with a micrometer eyepiece. A light source was used to illuminate the specimen surface, and cracks were easily visible through the solution. The lengths of the cracks developed from each end of the slit on both faces were recorded as a function of time. A timer equipped with a cut-off switch automatically recorded the total time to rupture. The applied load was fixed during most of the tests, but in a few instances was altered during a test in order to study the influence of prior load history on the rate of growth of the cracks.

Results

The tarnish.—Forty and Humble (12) concluded that tarnish consists of Cu_2O platelets in a dezincified matrix, with the volume of tarnish about the same as that of the brass replaced. Pickering and Swann (4) have also observed Cu_2O particles in the surface of α-brass exposed to an ammoniacal atmosphere. The tarnish is not the only corrosion product since our tarnished specimens exhibited a weight loss rather than a weight gain. Thus an appreciable fraction of the corrosion products is soluble.

The rate of formation of tarnish, measured by taper-sectioning unstressed specimens which had been immersed in the tarnishing solution for various periods of time, is shown in Fig. 2. Some difficulty was experienced in preparing these taper sections as a consequence of the weak and friable nature of the tarnish. The thickness of the tarnish, x, can be approximated by the equation

$$x = c\sqrt{t} \qquad [1]$$

where c is a constant equal to 1.1 x 10^{-4} in./$hr^{1/2}$, and t is the immersion time in hours. This relation indicates that the rate of tarnish formation is governed by a diffusion process. Figure 2 shows that the average rate of tarnish formation was about the same for annealed and cold-worked specimens, and this is consistent with Pickering and Swann's observation that static dislocations are not sites of preferential chemical attack. *It has been reported that in annealed brass the rate* of tarnish formation at grain boundaries is greater than within the grains (12).

A micrograph of a taper section through the tarnish layer is shown in Fig. 3. Electron micrographs of replicas stripped from the tarnished surfaces showed that the surface roughened with increasing exposure time.

In order to determine the effect of stress applied during tarnishing, tensile strips of cold-worked brass were loaded to various levels below the proportional limit, and the change in length was noted as a function of time. In the absence of the solution, no extension occurred. Results for tarnished specimens are shown in Fig. 4. Although the specimens were tested within the supposed elastic range, in each case the rate of extension of the specimens increased with time until rupture occurred. Examination of the specimens revealed distribution of cracks in the tarnish, so that the observed extension is a result of the growth of these cracks prior to

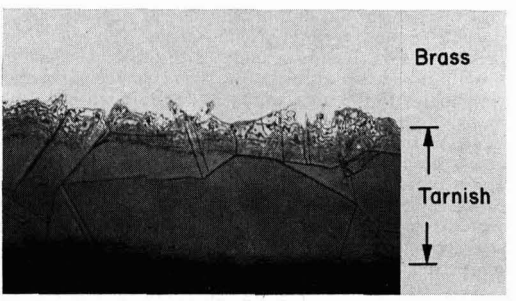

Fig. 3. Taper section (taper ratio 12.3:1) through tarnish formed on annealed brass by a 16 hr exposure to the tarnishing solution. Magnification approximately 300X.

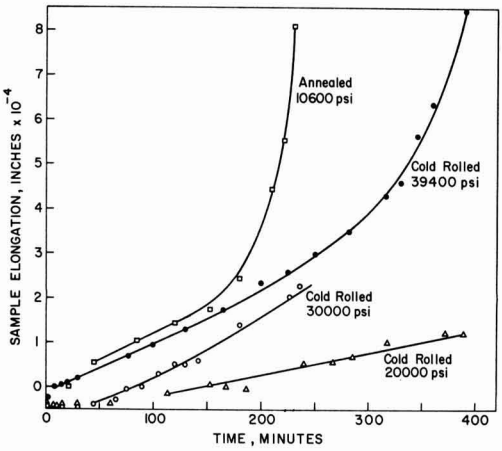

Fig. 4. Elongation of tensile specimens of brass exposed to the tarnishing solution at the indicated stress levels.

final rupture. This result was somewhat unexpected since the work of Forty and Humble, with annealed specimens, appears to indicate that plastic deformation involving slipbands in the brass substrate would be required to initiate cracking of the tarnish. To check on this further, an annealed specimen with a proportional limit of 15,000 psi was tested at 10,000 psi, and behavior similar to that for the cold-worked brass was observed, as shown in Fig. 4. Failure of annealed α-brass below the yield strength in an ammoniacal environment has been previously noted (3, 15). It appears therefore that, although the exact mode of failure is uncertain and may indeed involve dislocation motion on a microscale within the tarnish or at the tarnish-metal interface, massive plastic deformation associated with slip bands is not necessary. Massive plastic deformation can, of course, rupture a surface film, but this would be true for any surface film, such as aluminum oxide, whether or not the material is susceptible to stress-corrosion cracking.

As observed by Forty and Humble (12), the cracking appeared to be confined to the tarnish layer, with cracks being blunted and arrested at the interface between the brittle tarnish and the ductile substrate as shown in Fig. 5 for a cold-worked specimen.[1] It has been suggested (16) that pore formation due to dezincification of the brass might serve to advance the crack in a brittle manner beyond the tarnish layer. In order to obtain some indication of the effect of porosity on ductility, a brass specimen was dezincified by annealing for 30 hr in a vacuum at 850°C, which resulted in a void volume of 17%. Nevertheless, the material was quite ductile, thereby indicating that only the tarnish is brittle in the present case.

Short range order has also been considered to influence the process of stress corrosion cracking by providing a preferred path for corrosive attack due to the destruction of short range order by dislocation motion (4). To check on this point for brass, the time to rupture for tensile specimens of disordered material was compared with that for material possessing a degree of short range order. Disordered material was obtained by water quenching from an annealing temperature of 450°C (the bulk of the tests described in this paper involved disordered material); short range ordered material was obtained by heating quenched material to 190°C and maintaining that temperature for 24 hr (17). The times to failure at three stress levels of the disordered and short-range-ordered α-brass specimens in the tarnishing solution were as follows:

Condition	Applied stress, psi	Time to failure, hr
Short-range-ordered	16,000	4.2, 11.32
Disordered	16,000	2.5, 6.76
Short-range-ordered	18,600	2.77, 4.01
Disordered	18,600	3.0, 4.55
Short-range-ordered	22,700	2.0, 3.08
Disordered	22,700	1.75, 2.65

These results show no obvious correlation between degree of short range order and time to failure. The above results indicate that stress corrosion cracking occurs because of the weak nature of the protective tarnish film and that the strength of the tarnish does not depend on the condition of the underlying brass.

Crack growth.—The experimental approach employed in determining the rate of growth of cracks was similar to that used for fatigue cracks (18). In the latter case, a centrally located slit serves as a stress raiser at which cracks are initiated. The growth of the cracks is observed with a low power microscope and related to the number of load cycles applied; from these data the rate of growth is determined. It has been shown that the rate can be expressed as a single valued function of the parameter $\sigma_g\sqrt{l}$, where σ_g is the maximum applied gross-section stress in the loading cycle, and l is the semilength of the fatigue crack (19). This correlation is not unexpected, since $\sigma_g\sqrt{l}$ is related to the stress intensity at the tip of a growing crack (20) if the crack length is less than half the sheet width.

In the present study the rate is, of course, expressed as a function of time rather than of the number of load cycles.

General Observations

For annealed specimens, the level of stress required to initiate cracks in a short time also caused extensive plastic deformation in the vicinity of the central slit. As a consequence, many cracks appeared in time (Fig. 6). The main crack advanced by a linking up of the smaller cracks, a circumstance which made the determination of a crack front uncertain; therefore, quantitative information with annealed specimens could not be obtained. The cracks in these specimens were usually intergranular. As the cracks deepened, they became much more blunt (Fig. 7).

Crack growth along the surface of cold-worked brass

[1] These cracks are "transgranular," but it is noted that they do not penetrate the α-brass grains themselves.

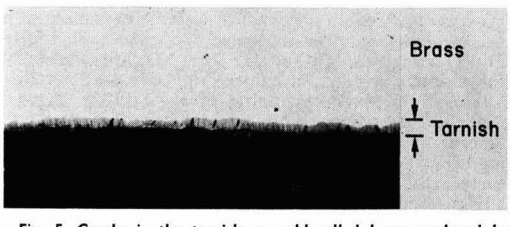

Fig. 5. Cracks in the tarnish on cold rolled brass produced by stressing the base metal in tension after the tarnish had formed. Note that cracks do not penetrate the untarnished metal. Magnification approximately 800X.

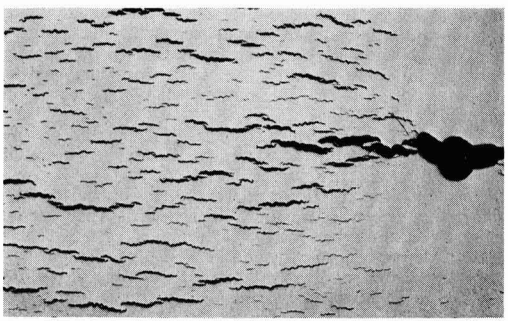

Fig. 6. Multiplicity of cracks on the surface of a notched annealed specimen exposed to the $CuSO_4$—$(NH_4)_2SO_4$ solution for 21 hr at a stress of 13,000 psi. Magnification approximately 7X.

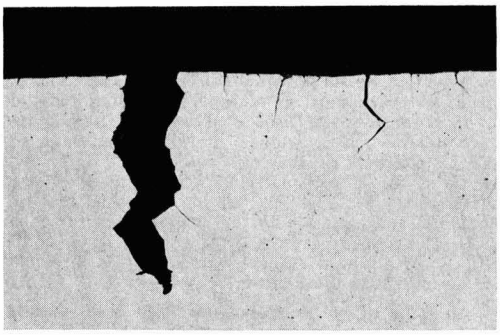

Fig. 7. Cross section of stress corrosion cracks in annealed brass. Magnification approximately 170X.

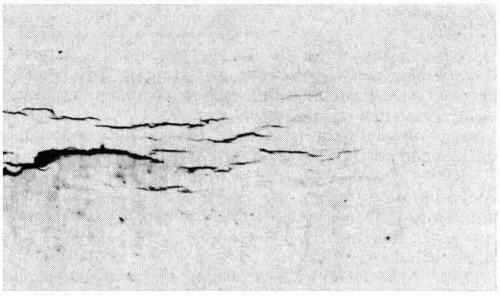

Fig. 8. Surface appearance of the tip of a stress corrosion crack growing in a notched, cold rolled brass specimen exposed 5 hr at 57,000 psi. Magnification approximately 170X.

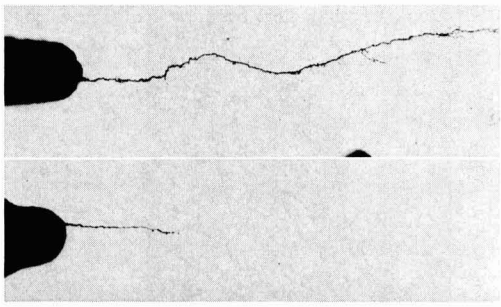

Fig. 9. Crack lengths in a notched, cold rolled brass specimen after 53 hr exposure to the cracking solution at a stress of 17,000 psi; (top), near surface; (bottom) near center of the specimen. Magnification approximately 30X.

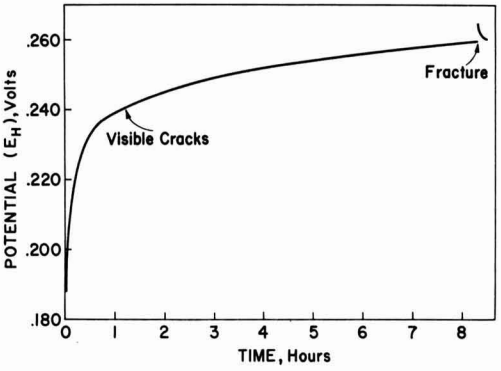

Fig. 10. Potential of a cold rolled, notched stress corrosion specimen as a function of time exposed in 0.05M $CuSO_4$ + 0.48M $(NH_4)_2SO_4$, pH = 7.25 at 50,000 psi.

was much easier to follow. A well-defined main crack advanced along the surface by linking up with microcracks formed in the small plastic zone at the tip of the crack. Microcracks were not visible through the low power microscope, and therefore only the advance of the main crack was recorded. An example of this microcracking is shown in Fig. 8.

In both the annealed and cold-worked specimens the plane of initial crack growth was perpendicular to the specimen surfaces. As the cracks increased in length, the average plane gradually shifted toward 45° to the specimen surfaces, the distance to the transition region being an inverse function of the applied stress. It is noted that the greater proportion of total crack life was spent in the first of these two modes. A shift in crack plane orientation is also observed in fatigue crack growth and can be explained (21) in terms of the size of the plastic zone at the tip of the crack. When the zone size is small with respect to the thickness of the sheet, plane strain conditions prevail at the tip and the fracture plane is normal to the surface. As the crack increases in length, the size of the plastic zone increases also, and when it approaches the sheet thickness a condition of plane stress exists in the plastic zone at the crack tip with the result that the fracture plane shifts to a 45° inclination with respect to the surface.

The shape of the crack front itself depended on the applied stress level. At low stresses, the cracks were well advanced along the surface with respect to the interior. As the stress level increased, the disparity between the two was considerably reduced. An extreme example of the crack leading at the surface was found in the case of a crack formed at 17,000 psi. This crack apparently stopped growing after developing along the surface to a length of 0.094 in. As shown in Fig. 9, its length in the interior was only 0.023 in.

As viewed through the microscope, the growth of cracks in both annealed and cold-worked specimens appeared to be continuous in time; that is, no pauses and subsequent bursts of crack growth were noted. Electrode potential measurements, which have been reported to be sensitive to bursts of crack growth in other systems (22), did not show bursts of growth in the present instance. After an initial fairly rapid drift in the noble direction, the rate of potential change slowed considerably (Fig. 10). Except at fracture, no pronounced discontinuities were observed, and no detectable change in potential occurred at the onset of visible cracking, even though the Luggin capillary employed in these measurements was placed near the crack tip. These results suggest that any active metal surface exposed by the cracking process was too small a fraction of the total surface to have an appreciable effect on the electrode potential. Similar results were obtained for both annealed and cold-worked specimens. In all cases, the potential is in the region corresponding to Cu_2O as the reaction product according to Mattson's calculated potential-pH diagram for this system.

Replicas of the fracture surfaces examined in an electron microscope indicated that discontinuities in growth occurred on a very fine scale. An example of a fracture surface of an annealed specimen is shown in Fig. 11a. Figures 11b and 11c show the appearance of the fracture surfaces of cold-worked brass at two different stress levels. Scanning of the replicas showed that the fracture markings remained parallel over distances much larger than the grain diameter. These markings are similar to those observed on the fracture surfaces of fatigue specimens as a consequence of the advance and blunting of the fatigue crack during each loading cycle.

Rate of Crack Growth

The log of the rate of crack growth for cold-worked brass is a single valued function of the crack stress tip

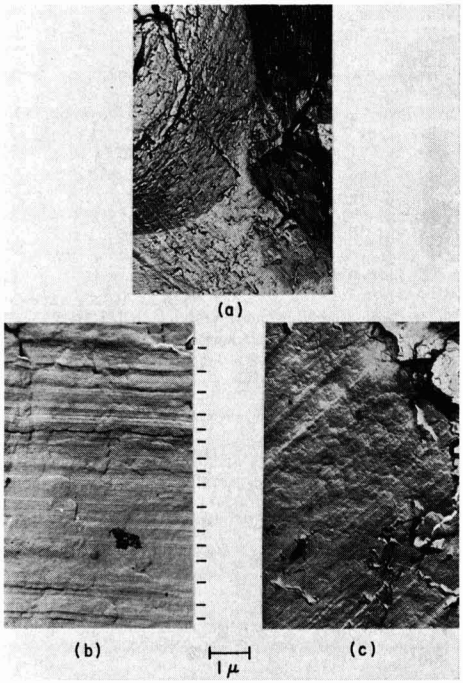

Fig. 11. Electron micrographs of replicas of stress corrosion fracture surfaces. (a) annealed brass at 14,600 psi; (b) cold rolled brass at 30,900 psi (main rupture markings indicated in margin); (c) cold rolled brass at 67,000 psi. Magnification approximately 7000X.

intensity parameter, $\sigma_g\sqrt{l}$, over a wide range of values (Fig. 12). The data can be approximated by a line whose equation is

$$\log dl/dt = \log A + 2 \log \sigma_g\sqrt{l} \qquad [2]$$

or

$$dl/dt = A\sigma_g{}^2 l \qquad [3]$$

where A is a material constant.

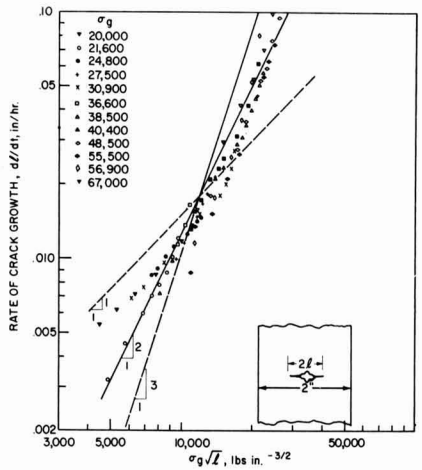

Fig. 12. Rate of stress corrosion crack propagation in cold rolled brass exposed to 0.05M $CuSO_4$ + 0.48M $(NH_4)_2SO_4$, pH = 7.25.

This equation holds for values of $\sigma_g\sqrt{l} > 4000$ lb-in.$^{-3/2}$. Below this value cracks propagate at a much slower rate than given by Eq. [3].

Equation [3] may be integrated to give

$$\ln l_R/l_o = A\sigma_g{}^2 t_R \qquad [4]$$

where t_R is the time to rupture, if crack initiation occurs instantaneously, l_o is the initial crack length, and l_R is the crack length at rupture. Since most of the time is spent in growing the crack at lengths much below l_R, variations in l_R, a number which would actually decrease with increasing applied stress, can be neglected with only small error. If this is done, then

$$t_R \propto \frac{1}{\sigma_g{}^2} \qquad [5]$$

A logarithmic plot of the data *vs.* time to rupture is given in Fig. 13; the observed slope of −2 shows that the time to rupture does indeed depend inversely on the square of the applied stress level. If the numerical value of A determined from the rate plot (Fig. 12) is used, then the quantitative prediction is with 20% of the measured value, indicating that the assumptions used above are reasonable.

Specimens which were prestressed in compression to introduce a state of residual tensile stress at the notch tip and an increase in notch sharpness, cracked at stress levels below the minimum for specimens not prestressed. Specimens prestressed in tension, required much longer times for development of cracking than in the absence of the preload.

When the amplitude of tensile loading was varied during the test the results also reflected the influence of prior load history. Denoting the time spent at the nth stress level as t_n and t_{Rn} as the time to rupture at the nth level, then changing from high loads to low increased the total life as given by

$$n = \sum_{1,2}^{n} \frac{t_n}{t_{Rn}} \qquad [6]$$

whereas going from a low load to a high had little effect on the rate of growth at the higher load level. It appears then that the above summation will yield a

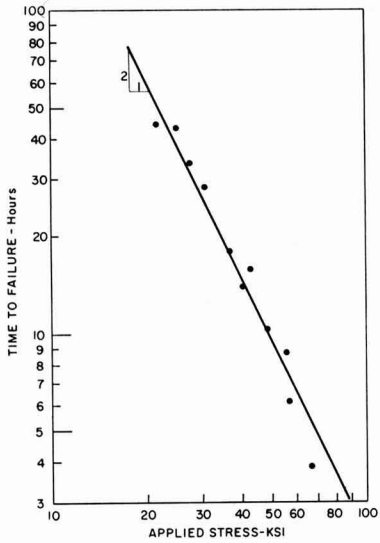

Fig. 13. Time to rupture as a function of applied stress for notched, cold rolled brass specimens exposed to the cracking solution.

value equal to or greater than unity for tensile loading. Therefore a simple prediction based on the time spent at each load level would lead to a conservative prediction of total lifetime. However, if a compressive load were applied, it would accelerate cracking in the next stage of tensile loading due to its effect on residual stresses and shape of the crack tip. In this event the above summation would be reduced. These effects of prior load history on the growth of stress corrosion cracks are similar to those observed in the case of fatigue crack growth.

Discussion

Of the various suggested mechanisms for stress corrosion cracking, our results are in best accord with the film rupture mechanism proposed by Logan (1). Exposure of brass to ammoniacal cupric sulfate solution rapidly produces a protective film, consisting mainly of cuprous oxide, which reduces the over-all corrosion rate to a fairly low level. Cracking of this film exposes a small area of bare metal which is anodic to the film. Rapid anodic attack on the exposed brass leads to reformation of the protective film. After the protective tarnish is again established its rate of thickening is expected to be controlled by diffusion processes within the film.

Stress corrosion cracking was found experimentally to consist of three steps: (*a*) crack initiation, followed by (*b*) crack advance along the surface into regions already tarnished, and simultaneously, (*c*) crack penetration from the surface into the interior of the specimen.

Crack initiation.—Cracks appeared in the notched specimens within the plastic zone at the tip of the stress raiser as the tarnish layer formed. It seems unlikely that the formation of an extremely thin film could have caused a motion of the static array of dislocations initially present in the substrate and thereby rupture the film. It seems more likely that rupture involved a decrease in resistance to fracture of the film with increasing thickness. That such a strength-thickness relationship exists is inferred from the work on thin films of silver and gold which has demonstrated that the fracture stress decreases sharply with increasing thickness up to about 1000Å (23, 24). In addition, epitaxial stresses in the tarnish, which would be expected to increase with thickness, may also lower the fracture resistance. Such an interpretation is consistent with the behavior of unnotched specimens which extended and failed, even in the nominally elastic range, at rates which increased with the stress level.

Crack growth along the surface.—This mode of crack advance in the plastic zone ahead of the main crack (Fig. 8) is associated with the advance of the crack into a region which has already been tarnished. Plastic deformation of the underlying brass results in the opening up of microcracks already present in the tarnish and the further cracking of the tarnish. The mechanism is probably similar to that described by Forty and Humble: planar glide, induced by a low stacking fault energy, introduces a severe stress concentration when blocked by the surface layer.

Crack growth in interior.—The cracking of the subsurface section of the specimens controls the over-all rate at which cracks propagate. Because of the accelerated cracking in the unconstrained plastic zones at the surface, the crack front takes on a curved shape which is more pronounced at low stress levels. Since cracks penetrate only to the tarnish-metal interface, the important step in crack propagation is the repeated formation and rupture of the tarnish layer along the crack front; therefore, the process of crack growth has much in common with crack initiation. This view is supported by the regular nature of the markings found on the fracture surface (Fig. 11). Such markings are not expected if a simple dissolution process or some random blocking of the crack tip occurred. These markings are thought to be due to the plastic deformation which occurs each time the tarnished film ruptures and the crack advances to the interface where it is arrested by plastic blunting, as shown in Fig. 14. The figure also indicates how secondary markings due to slip bands may be present on the fracture surface and between main markings.

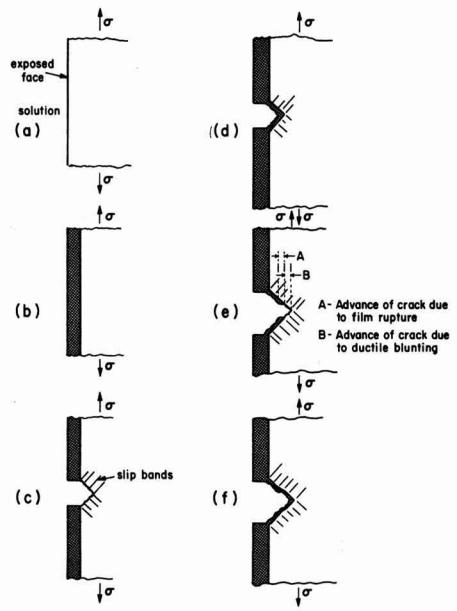

Fig. 14. Schematic representation of initiation and growth of stress corrosion cracks by the process of tarnish rupture.

The rate of formation of cracked area by such a mechanism is given by

$$r = B\frac{\Delta l}{\Delta t_R} = B\frac{\Delta l_T + \Delta l_B}{\Delta t_R} \qquad [7]$$

where B is a numerical factor that relates the shape of the crack front to the dimensions and shape of the specimen. This factor is considered in the present example to be independent of stress, but in fact does depend somewhat on the applied stress, particularly at low stress levels. Δl is the increment of crack growth due to tarnish rupture and plastic blunting (A + B, Fig. 14) and is the sum of the incremental advance due to tarnish rupture, Δl_T, plus that due to plastic blunting, Δl_B; and Δt_R is the time for the formation of the film measured from the end of one increment of crack advance until the tarnish ruptures again.

If we neglect the contribution of plastic blunting to the advance of the crack and assume the rate of thickening of the film at the tip is a diffusion controlled process, we can write

$$\Delta l = \Delta l_T = c\sqrt{\Delta t_R} \qquad [8]$$

With respect to this assumption, it is of course likely that when the film is very thin the rate of reaction is controlled by the activation polarization characteristics of the brass. It has been shown that copper can dissolve at very high anodic rates (25), and it is reasonable to expect that brass does also. In this case, the film soon thickens to the point that diffusion processes within the film become rate controlling so that during most of the period of film growth, the rate-determining step is diffusion within the film. However, another possibility to be considered is that diffusion within the crack of reactants to the tip or products to the bulk solution is rate controlling. Hines has shown that this concentration polarization is unlikely to be of im-

portance in the cracking of austenite stainless steels (9). In the present case the principal anodic reaction is $2Cu+H_2O \rightarrow Cu_2O+2H^+$. Thus the only reactant supplied by diffusion is water which is present in great excess and the only product removed by diffusion is the hydrogen ion which has the highest diffusivity of all ions. Also the buffer capacity of the electrolyte should minimize effects of changes in hydrogen ion concentration. This system is therefore less likely to be subject to considerable concentration polarization within the crack than would the stainless steel system considered by Hines so that concentration polarization does not seem to be rate controlling in the present case. It therefore appears reasonable that diffusion within the tarnish controls the rate at which the tarnish forms.

Upon substituting for Δt_R in Eq. [8] we obtain

$$r = \frac{Bc^2}{\Delta l_T} \qquad [9]$$

From the data on the rate of formation of the film, c^2 is equal to 1.2×10^{-8} in.^{2}/hr, assuming that a bulk measurement can be extended to the thin tarnish layer at a crack tip.[2] For a value of B close to unity, the rate of advance of the crack is given by

$$r = \frac{1.2 \times 10^{-8}}{\Delta l_T} \text{ in./hr} \qquad [10]$$

If the distance between the main markings in Fig. 11 is taken as the thickness of the tarnish film at the time it ruptures a calculation of the rate of crack advance can be made using Eq. [10]. This leads to rates of cracking of 0.0025 in./hr at a gross stress of 67,000 psi and 0.0006 in./hr at a gross stress of 30,900 psi. These replicas were taken close to the crack origin where the corresponding experimentally determined rates are about 0.017 and 0.004 in./hr, respectively. The observed and calculated rates could be brought into closer agreement if approximately one-half of the distance between markings were attributed to the advance due to plastic blunting. Because of uncertainties in the tarnishing process at the tip of a crack and in making measurements from the replicas it does not seem possible to make a more rigorous calculation of these rates at present.

From the experimental findings it has been shown that the rate of growth is proportional to $\sigma_g{}^2 l$. This indicates that the advance of the crack front is related to Eq. [7], and can be expressed as

$$\sigma_g{}^2 l \propto \frac{1}{\Delta l_T}\left(1 + \frac{\Delta l_B}{\Delta l_T}\right) \qquad [11]$$

If the advance due to blunting is linearly related to the advance due to tarnish rupture, then the above proportionality can be reduced to

$$\sigma_g{}^2 l \propto \frac{1}{\Delta l_T} \qquad [12]$$

A rationalization of this empirical relationship is not straightforward in that the factors responsible for the rupture of the film at the tip of a crack are quite complex. It is known, however, that the radius of a crack tip is directly related to the quantity $\sigma_g{}^2 l$ (26). The smaller the size of the radius the more the stress state will approach one of plane strain, a condition which would tend to cause a rapid decrease in shear stress immediately ahead of the curved crack front. Since tensile fracture usually is the result of shear deformation, fracture of the tarnish and the advance of the crack front may also depend on the magnitude of the shear stresses encountered as the film thickens and its fracture resistance decreases. The lower the value of $\sigma_g{}^2 l$, the greater will be the thickness attained before rupture because of the lower magnitude of shear stresses involved.

[2] Since the grain boundaries in annealed brass are replicated in the oxide (Fig. 4), enhanced diffusion along these oxide grain boundaries may be associated with the intergranular cracking mode in annealed brass. Heavy cold work would tend to reduce the structural difference between matrix and boundaries.

Concluding Remarks

1. It is concluded that both the initiation and propagation of stress corrosion cracking in tarnished α-brass involves the formation and rupture of a weak, protective film, and that cracking occurs because rupture of the film localizes the effects of stress and environment. This localized cracking process is avoided if the film is not sufficiently protective to restrict general corrosion. For example, we have observed this to be the case for copper in the ammoniacal copper sulfate solution. It can also be avoided if the film is strong enough to sustain the applied stress without rupturing.

2. The process of film rupture does not require massive plastic deformation of the substrate. This finding does not preclude the possibility that dislocation motion within the tarnish or on a microscale at the tarnish-brass interface occurs and is involved in the rupture process.

3. The rate of growth of stress corrosion cracks for a wide range of crack growth rates is a single valued function of the parameter $\sigma_g{}^2\sqrt{l}$, and the rate is proportional to $\sigma_g{}^2 l$. From this relationship it follows that the time to rupture varies inversely as the square of the applied stress level. σ_g.

Acknowledgment

The authors express their appreciation to Drs. T. L. Johnston, A. S. Tetelman, and G. F. Bolling for helpful discussions during the course of this investigation. The capable assistance of Mrs. P. McAlpine, Mr. R. Benoit, and Mr. J. Ingall is also acknowledged.

Manuscript received Aug. 10, 1964.

Any discussion of this paper will appear in a Discussion Section to be published in the December 1965 JOURNAL.

REFERENCES

1. H. L. Logan, *J. Research Natl. Bureau Standards*, **48**, 99 (1952).
2. R. Bakish and W. D. Robertson, *Acta Met.*, **4**, 342 (1956).
3. W. D. Robertson and A. S. Tetelman, "Strengthening Mechanisms in Solids," ASM, Metals Park, Ohio (1962).
4. H. W. Pickering and P. R. Swann, *Corrosion*, **19**, 373t (1963)
5. D. Tromans and J. Nutting, "Fracture of Solids," p. 637, Gilman and Drucker, Editors, Interscience Publishers, New York (1963).
6. A. J. Forty, "Physical Metallurgy of Stress Corrosion Fracture," T. N. Rhodin, Editor, Interscience Publishers, New York (1959).
7. D. L. Douglass, G. Thomas, and W. R. Roser, *Corrosion*, **20**, 15t (1964).
8. T. P. Hoar, *ibid.*, **19**, 331t (1963).
9. J. G. Hines, *Corrosion Sci.*, **1**, 21 (1961).
10. H. H. Uhlig, "Physical Metallurgy of Stress Corrosion Fracture," T. N. Rhodin, Editor, Interscience Publishers, New York (1959).
11. L. Graf, "Stress Corrosion Cracking and Embrittlement," W. D. Robertson, Editor, John Wiley & Sons, Inc., New York (1956).
12. A. J. Forty and P. Humble, *Phil. Mag.*, **8**, 247 (1963).
13. E. Mattson, *Electrochim. Acta*, **3**, 279 (1961).
14. A. R. Bailey, *Met. Rev.*, **6**, 101 (1961).
15. G. Edmunds, Symposium on Stress Corrosion Cracking of Metals, ASTM-AIME (1944).
16. A. J. Forty, "Recent Advances in Stress Corrosion," A. Bresle, Editor, Bulletin 25, Corrosion Committee, Royal Swedish Academy of Engineering Sciences, 22 (1961).
17. R. Feder, A. S. Nowick, and D. B. Rosenblatt, *J. Appl. Phys.*, **29**, 984 (1958).
18. A. J. McEvily, Jr. and W. Illg, U. S. National Advisory Committee for Aeronutronics, T. N. 4394 (1958).
19. P. C. Paris, M. P. Gomez, and W. E. Anderson, *Trend in Engineering*, **13**, 9 (1961).

20. H. F. Hardrath and A. J. McEvily, Jr., Proceedings of the Crack Propagation Symposium, Cranfield, College of Aeronutronics, **1**, 231 (1963).
21. H. W. Liu, Private communication.
22. H. J. Engell and A. Bäumel, "Physical Metallurgy of Stress Corrosion Fracture," T. N. Rhodin, Editor, Interscience Publishers, New York (1959).
23. J. W. Menter and D. W. Pashley, "Structure and Properties of Thin Films," Neugebauer, Newkirk, and Vermilyea, Editors, John Wiley & Sons, New York, p. 111 (1959).
24. J. W. Beams, *ibid.*, p. 183.
25. B. E. Conway and J. O'M Bockris, *Plating*, **46**, 321 (1959)
26. B. A. Bilby, A. H. Cottrell, and K. H. Swinden, *Proc. Roy. Soc.*, **A272**, 304 (1963).

Adsorption of Monomeric and Polymeric Amino Corrosion Inhibitors on Steel

R. R. Annand[1] and R. M. Hurd[2]
TRACOR, Inc., Austin, Texas
and Norman Hackerman
Department of Chemistry, The University of Texas, Austin, Texas

ABSTRACT

The adsorption of 4-ethylpyridine, 4-ethylpiperidine, and very low molecular weight poly(4-vinylpyridines) was studied in cyclohexane solutions containing hydrogen reduced steel powder. Isotherms were obtained for the monomers at 30°C. They show that an amount equivalent to monolayer formation is adsorbed at equilibrium concentrations in the range 2.5 to 5.0 x 10^{-3}M. The polymer was adsorbed to a much greater extent. Using a specially designed chromatographic method, the heat of adsorption of the piperidine derivative from cyclohexane was determined. Simultaneous measurements of the adsorption of the polymer and the corrosion of the steel in aqueous hydrochloric acid have shown that the corrosion rate decreases by 80% as the polymer adsorbs to form a very incomplete layer. From these results, it is concluded that these compounds chemisorb to the steel surface and that the 4-ethylpiperidine is bonded at the nitrogen atom but that the 4-ethylpyridine is adsorbed in a position with the plane of the ring parallel to the steel surface. Attachment of polymer is at multiple sites in the molecule, but appreciable portions of the chains are left in the solution phase. The area which is deactivated toward corrosion by adsorption of poly(4-vinylpyridine) from HCl is considerably greater in extent than that which is physically covered by the adsorbed molecules, *i.e.*, a large neighboring area of steel surface is ennobled by the adsorbed polymer molecules.

In corrosion inhibitor research, it has long been recognized that preferential adsorption of organic inhibitors interferes with the reaction between the corrodant species and the metal surface. At first, this interference was believed to result from electrostatic attraction between cations and cathodic areas, or between anions and anodic areas. This concept alone has since been shown to be untenable (1), and other types of adsorption have had to be considered. In 1954 Hackerman and Makrides proposed a chemisorption mechanism of inhibitor action (2), and Finley and Hackerman showed that a persistent, inhibiting adsorption of amines could be obtained in benzene (3). Other investigators have discussed various other types of adsorption or combinations of types to account for the observed results (4, 5). Recently radiochemical and spectrophotometric measurements of the adsorption of thiourea derivatives have been reported (6, 7). However, solution adsorption measurements on steel surfaces for inhibitor amines with similar molecular character but dissimilar inhibitor action have been lacking.

The work reported here was undertaken in conjunction with an inhibition study (8) to examine the adsorption behavior of amine inhibitors and to elaborate the relationship between adsorption and inhibition. A dual approach was chosen: (i) a study of two simple compounds, 4-ethylpiperidine and 4-ethylpyridine, which are similar in size, base strength, solubility, and chemical nature, but which are not so similar as might be expected in their inhibitor effectiveness; and (ii) a study of the relative adsorbabilities of a monomer amine, 4-ethylpyridine, and a polymer, poly(4-vinylpyridine), which had very short chains and whose repeating units had the same structure as the monomer. To keep the reactions at the steel surface simple and therefore to focus attention on the adsorption, the adsorption experiments were carried out in cyclohexane on steel powder which was carefully freed of oxide by reduction in a hydrogen atmosphere.

[1] Present address: Petrolite Corporation, St. Louis, Missouri.

[2] Present address: Continental Oil Company, Ponca City, Oklahoma.

Experimental Procedures

Static adsorption measurements.—These experiments were designed to study adsorption from cyclohexane solutions onto reduced steel powder in the absence of oxygen. The steel powder was reduced in hydrogen, weighed, and then introduced to the thermostated adsorption cell under the surface of the cyclohexane without exposure to air. In some cases, the adsorbable amine was present in the solution before the steel powder was added; in others, the amine was added later. There was no observable difference in the equilibrium amount adsorbed due to the different procedures. The adsorption cell was provided with a paddle stirrer and was maintained under a positive nitrogen pressure of 3 or 4 lb by means of a mercury columun on the exit line. Tank nitrogen was bubbled through a zinc-vanadyl sulfate tower to remove oxygen, then through a sulfuric acid scrubber to remove any water spray, and finally a Drierite tower to remove any acid spray. The nitrogen was then passed through a cyclohexane bubbler which was kept in the thermostated water bath with the adsorption cell. All of the connections between the bubbler and the adsorption cell were made of glass. Teflon sleeves were used to seal

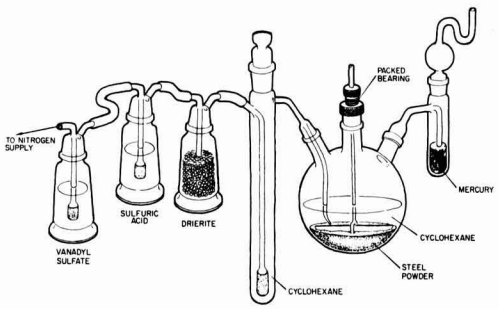

Fig. 1. Adsorption cell and gas train

the ground-glass joints. The arrangement of this equipment is shown in Fig. 1.

The adsorption cell was assembled from a one-liter, three-neck Morton flask with a Trubore packed stirrer bearing assembly[3] combined with a shop modified lubricant trap. When connected to a Waco stirrer motor to complete the apparatus, it could be kept sealed and operating continuously for at least as long as 30 days without a net loss of cyclohexane and without contamination of the solvent with lubricant or chemicals from the gas train.

The bubbler and the adsorption cell were immersed in a stirred water bath maintained at 30° ± 0.005°C by a Sargent Thermonitor, with water level in the bath maintained by a simple float valve arrangement. In the usual case, samples of the solution for analysis were taken systematically over a period of about 10 days and were used to determine the course of the adsorption process. Samples from a portion of the thermally equilibrated initial solution, taken before introduction of the steel, were used as standards for this comparison.

The steel powder used for these experiments was obtained from the Vanadium-Alloys Steel Corporation, Latrobe, Pennsylvania. Chemical analysis supplied by the manufacturer was in the typical range for the SAE 1020 composition. Sieve analysis produced 85.0% of the particles in the range 140-200 mesh or 74-105μ. BET determination showed 0.0571 m^2/g for the specific surface of the reduced powder. This indicates a surface roughness factor of 5.8.

The powder, contained in a Vycor tube, was prepared for the adsorption experiments by reducing it with hydrogen at 650°C maintained in a controlled temperature furnace, Completeness of reduction was determined by absorbing the water formed in a Drierite tower and weighing. Hydrogen, predried with Drierite, was used for the reduction. This procedure was adopted after several trials to determine the best compromise between absence of sintering and rapid reduction. Following reduction, the hydrogen flow was replaced with oxygen-free, dry argon, and the steel was maintained at temperature for several hours to allow any absorbed hydrogen to escape. Any oxidation was detected by the change in color of the powder.

Oxygen was removed from the argon by passage through a purification train similar to that used for the nitrogen in the adsorption system. For added insurance, before introduction to the powder samples, it was also passed through a steel powder bed held at temperature. The steel powder was transferred to the adsorption cell by means of a purified nitrogen stream which blew it out of the reduction tube and through a glass tube inserted into the adsorption cell under the surface of the cyclohexane. The weight of powder transferred was determined by weighing the reduction tube before and after transfer.

Spectrophotometric analysis was the method chosen for concentration determination. By appropriate adjustment of sample size and light-path length, a wide range of concentrations could be covered accurately. In some cases in which only a small relative concentration change occurred, the differential technique was applied. In general, the adsorption cell was filled with 200 ml of solution and a pipetted 4 ml sample was taken each time. This was split into triplicate 1 ml samples which were carried through the analysis scheme. Before contact with the steel, a portion of the amine solution was reserved to furnish the triplicate standards which were run concurrently with the samples.

For the experiments with 4-ethylpyridine and poly(vinylpyridine), spectrophotometric measurements were made on the diluted samples using the pyridine absorbance peak at 225 mμ and a prepared standard calibration curve.

For the experiments with 4-ethylpiperidine, it was necessary to introduce a chromophore into the molecules before the spectrophotometric measurements could be made. For this purpose, 2,4-dinitrofluorobenzene was used as a reagent to introduce a dinitrobenzene moiety at the nitrogen site (9). Contrary to the usual procedure, the reaction was carried out in cyclohexane held in a water bath at 60°C.

After the appropriate time for maximum color development and cooling to room temperature, spectrophotometric measurements were made at 352 mμ on the reacted solution without further treatment except to dilute to a known volume. The absorptivity of the unreacted 2,4-dinitrofluorobenzene is small enough at 352 mμ, and the reaction is sufficiently complete that, by using an excess of reagent, the background absorbance could be reliably blanked out using the same amount of reagent in the blank as in the sample. The concentration of piperidine in the measured volume was determined from a standard calibration curve.

From the analytical concentration, the sample volume, and the volume contained in the adsorption cell combined with the weight of steel contained in the cell, the amount adsorbed was calculated in terms of micromoles of amine per gram of steel. For the polymer, these calculations were in terms of micromoles of r-mer per gram of steel, since the analytical method produced this result. The number of micromoles of polymer per gram of steel were obtained from the molecular weight.

Measurement of adsorption from HCl.—Use of the spectrophotometric procedure for poly(vinylpyridine) in acid solutions is complicated by the general absorbance of the iron at the wavelengths of interest. Since corrosion of the steel continuously increased the iron concentration over the time period in which the polymer was adsorbing, a problem developed. However, by using the criteria cited by Mellon (10) for choosing the best wavelengths for measurement, a simultaneous method was developed for determining both iron and poly(vinylpyridine) concentrations by measuring at two wavelengths, 255 and 239 mμ. It was necessary to combine the spectrophotometric cell and adsorption cell because of the rapidity of the adsorption and corrosion phenomena. Also, because of the interrelationships between such factors as HCl concentration, rate of corrosion, solubility of poly(vinylpyridine) hydrochloride, and inhibitor effectiveness, it was found that an acid concentration of 0.01*N* gave the best compromise between time available for data taking and optimum range of concentrations measured.

The procedure was to start with a known volume of the uninhibited acid and a known weight of steel powder in a regular spectrophotometric cell and to take enough data to determine the corrosion rate. Then a known volume of a concentrated solution of the poly(vinylpyridine) hydrochloride in 0.01*N* HCl was added and the solution thoroughly agitated before spectrophotometric measurements (now including the simultaneous determination of the inhibitor) were resumed. These measurements were continued at short intervals over about an hour and were only terminated

[3] Obtained from Ace Glass Company, Vineland, New Jersey.

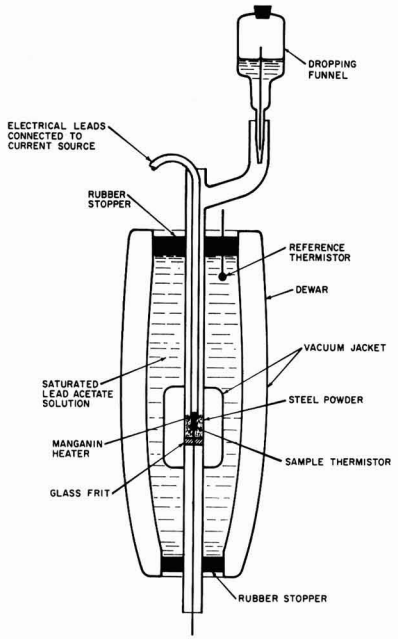

Fig. 2. Apparatus for dynamic adsorption measurements

when the absorbance increase due to iron dissolution pushed the total absorbance out of the range of the spectrophotometer. The concentrations of iron and of pyridine r-mers were determined by substituting the absorbance data into a set of simultaneous equations and solving in the usual way (11). The equations were derived and checked with standard solutions and mixtures.

Heat of adsorption measurements.—These experiments, based on a modification of the procedure of Groszek (12), were carried out in the flow calorimeter schematically outlined in Fig. 2. A known weight of steel powder rests on a glass frit with a glass-jacketed thermistor[4] inserted through a small hole drilled in its center. The steel was placed in the center of a double-walled bulb which was about halfway down a glass column. The thermistor was placed in the center of the mass of steel powder. A small coil of manganin heater wire was put in the steel on the same axis as the thermistor and slightly above. The heater was connected to a constant-current source. The column passed down the axis of a double-walled outer container, and the bulb was centered in this volume. The space between the walls of both the double-walled structures was evacuated. The large vessel was filled with a concentrated lead acetate solution to increase its heat capacity, and a second matching thermistor was located in this solution close to the outside wall of the column.

The thermistors were made part of a Wheatstone bridge circuit in combination with a set of mercury cells and with a Helipot which formed the third and fourth legs. The balance condition of the bridge was detected by a 5 mv stripchart recorder. A specially designed dropping funnel (which completes the apparatus) was used to obtain the slow flow rates required. In use, pure solvent was allowed to flow down the walls and adjusted to a rate of about 0.25 ml/min. The bridge, which was balanced initially, registered a large unbalance in the hot direction as the solvent reached the steel powder. Flow was continued until the balance condition was again obtained indicating that the heat released by solvent wetting had been removed from the inner bulb by the flowing solvent. At this time, the solvent funnel was quickly exchanged for a similar funnel containing a solution of the adsorbate in the same solvent and flowing at the same rate.

When this solution, temperature equilibrated by its contact with the thermostated column walls, reached the steel powder, a positive temperature excursion due to the heat of adsorption was registered by the recorder. It was followed by a somewhat slower fall in temperature as the continuing flow carried this heat out of the steel sample bulb. For calibration, a known constant-current pulse was then sent through the heater for a predetermined time, and a similar curve was traced by the recorder. Empirical adjustment of the geometrical arrangement of the heater wires and of the pulse time and magnitude were required to obtain a curve comparable to that produced by the amine solution so that the areas under the curves could be compared. This procedure gives a value which is the difference between the heat of adsorption of adsorbate and the heat of desorption of solvent.

Synthesis and characterization of the compounds used.—The 4-ethylpyridine was obtained from Reilly Tar and Chemical Company and was distilled immediately before use through a vacuum-jacketed, highly efficient column under a nitrogen atmosphere.

The poly(4-vinylpyridine) was prepared from freshly distilled 4-vinylpyridine (obtained from the same source) by polymerization in ethanol under nitrogen. A specially designed, high-dilution method was used in which the initiator, 2,2′-azoisobutyronitrile, and methanol solution were each added slowly to a large volume of an ethanol solution of the monomer held under nitrogen just below the reflux temperature. The resulting solution was then allowed to stand at temperature and under nitrogen for several days. Using this method, only slightly disperse samples of polymer were obtained. By properly adjusting the ratio of initiator to monomer and the over-all concentration of each, the molecular weights obtained could be controlled to give samples ranging from five r-mer units up to about one hundred. Molecular weights were determined with a Mechrolab Vapor Osmometer. Because the isolation procedures produced a partially hydrated polymer, it was necessary to use a dehydration procedure to obtain cyclohexane solutions. This procedure involved refluxing a solution of the polymer in methanol over calcium hydride followed by addition of cyclohexane and elimination of the methanol by repeated exhaustive distillation. The resulting cyclohexane solution was separated from the insoluble dehydration products (from hydrolysis of the hydride) by decantation.

Cyclohexane obtained from Phillips Petroleum Company (99 mole % minimum) was used for all of the experiments. It was distilled under nitrogen before use. A similar grade of n-heptane was used in some of the experiments.

The 4-ethylpiperidine used in the experiments was obtained by catalytic hydrogenation of purified 4-ethylpyridine in a Parr apparatus over palladium charcoal. It was purified by distillation in the vacuum-jacketed still, and the absence of the pyridine was verified by ultraviolet spectrophotometric analysis.

Results

Static adsorption experiments.—Adsorption-time curves illustrating the results of the adsorption experiments conducted in cyclohexane are presented in Fig. 3 for samples of poly(4-vinylpyridine) and for 4-ethylpyridine. The curves for 4-ethylpiperidine were similar. In the adsorption-time runs for the 4-ethylpyridine and 4-ethylpiperidine, the initial concentration of adsorbate was varied over a range sufficient to produce a change in the final, equilibrium concentration covering the range 5-50 x 10^{-4}M. These limits were estab-

[4] Obtained from Victory Engineering Corporation, Springfield, New Jersey.

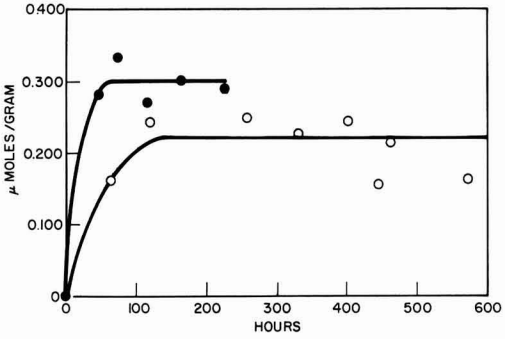

Fig. 3. Adsorption-time curves: ●, poly(vinylpyridine), MW = 3200; ○, 4-ethylpyridine.

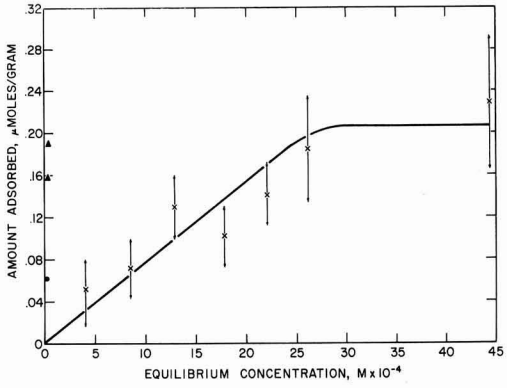

Fig. 4. Composite adsorption isotherm for 4-ethylpyridine solutions in cyclohexane: △, polymer 512 MW; ●, polymer 1200 MW; X, monomer.

lished by the limitations of the spectrophotometric analysis. In the case of the polymer solutions, it was not possible to cover so wide a range because of added limitations posed by the low solubility and high adsorbability of the polymers. Each point on the curves is the average of the differences between triplicate samples and triplicate standards. The standards were obtained from that portion of the original solution which was removed prior to introduction of the steel powder. No difference in the adsorption was observed between hydrogen-saturated steel and steel which had been outgassed in argon.

The adsorption levels indicated by the plateaus in the individual adsorption-time curves were used to define the isotherms for 30°C shown in Fig. 4 and 5. The average value for all of the points on the plateaus of the adsorption-time curves were used for the points on the isotherms. The points plotted in Fig. 4 are derived from at least two determinations of the adsorption-time curve, and the arrows reflect the composite standard derivation of the averages. The individual points from each of three polymer runs are included in Fig. 4 to show greater extent of adsorption at low concentrations.

Using the BET area of the steel powder and the amount adsorbed on the plateaus of the isotherms, the surface area available to each adsorbed molecule was calculated. These data are contained in Table I, along with a summary tabulation of the amount adsorbed, the projected area covered by each molecule, and the resulting number of layers of adsorbate.

The area/molecule figures in the table were obtained by arranging scale models of the molecules in the appropriate adsorption position using a flat surface to represent the steel surface. Several photographs of

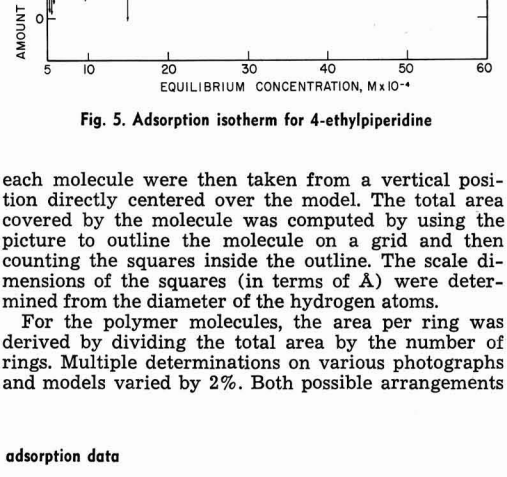

Fig. 5. Adsorption isotherm for 4-ethylpiperidine

each molecule were then taken from a vertical position directly centered over the model. The total area covered by the molecule was computed by using the picture to outline the molecule on a grid and then counting the squares inside the outline. The scale dimensions of the squares (in terms of Å) were determined from the diameter of the hydrogen atoms.

For the polymer molecules, the area per ring was derived by dividing the total area by the number of rings. Multiple determinations on various photographs and models varied by 2%. Both possible arrangements

Table I. Summary of adsorption data

Compound	Amount adsorbed, μmoles/g	Area/molecule, Å²				No. of layers
		Experimental[a]		Model[b]		
4-Ethylpiperidine	0.24 ± 0.08	39 ± 13		33		0.84 ± 0.28
4-Ethylpyridine	0.21 ± 0.07	46 ± 15		49		1.1 ± 0.4
				21[c]		0.46 ± 0.15[c]
		Calculated in terms of				
Poly(4-vinylpyridine)	Rings	Molecules	Rings	Molecules	Rings	Molecules	
MW 512 (4 units)	0.19 ± 0.02	0.048 ± 0.006	54 ± 6	216 ± 24	45	180	0.83 ± 0.09
MW 1160 (10 units)	0.42 ± 0.03	0.042 ± 0.003	31 ± 3	310 ± 31	45	450	1.45 ± 0.14
MW 3200 (30 units)	1.05 ± 0.06	0.035 ± 0.002	9.5 ± 0.6	284 ± 18	45	1395	4.74 ± 0.30

[a] Calculated using the number of amine rings removed from solution and the BET area of the steel powder.
[b] Projected area calculated from scale models: Assuming flat orientation for the pyridine rings in both monomer and polymer; assuming chain form for the piperidine rings.
[c] Calculated assuming perpendicular orientation of the pyridine ring.
NOTE: The values under the columns headed "Rings" are calculated on the basis of the pyridine ring concentrations; the values in the columns headed "Molecules" are calculated on the basis of polymer molecule concentrations. These values were not obtained from isotherms, but instead for individual adsorption-time runs.

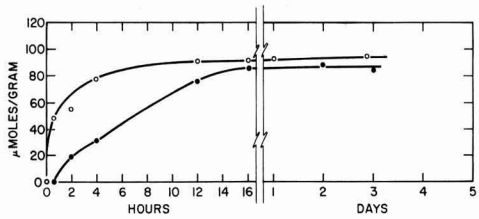

Fig. 6. Adsorption-time curves for 4-ethylpyridine on completely reduced (○) and lightly oxidized (●) steel powders.

for the pyridine, *i.e.*, with the plane of the ring perpendicular to the surface and parallel to the surface, are quoted in the table. For 4-ethylpiperidine, the chair form was assumed in the table, although all of the possible arrangements in either configuration covered essentially the same area within experimental error.

As an incidental observation, the adsorption behavior of 4-ethylpyridine was observed on a sample of steel powder which had been slightly oxidized by a brief exposure to a small amount of air while the steel was still hot, which resulted in a slight discoloration. The adsorption-time curve shown for this material is compared in Fig. 6 to the usual adsorption-time curve obtained on carefully protected (unoxidized) steel powder. It may be seen that the total amount of adsorption has not been affected (within experimental error), but that the rate of adsorption on the oxidized surface was appreciably slower.

Both of the analytical procedures for these experiments produced triplicate analyses (on the same sample) which were within the precision range of good analytical practice. In addition, the analyses of the standard solutions were consistent throughout the course of an experiment and conformed to Beer's law in experiments with different concentrations. The pooled standard deviations (representing the dispersion of the triplicates) over the course of a run in all these cases were in the range of 0.5-1.5% of the average. Triplicate analyses which were run on duplicate samples taken from the cell at the same time were also comparable to the over-all precision. In view of the good precision of the measurements of the individual points, the scatter exhibited in the adsorption-time curves is greater than expected, and it is concluded that the scatter must originate from the adsorption process itself. The deviations among multiple runs at

Table II. Adsorption of poly(vinylpyridine) (MW 1160) from aqueous 0.01*N* HCl

Grams steel	Adsorption, μmoles/g	% Inhibition
2.0	0.014	n.d.
4.0	0.017	80
4.0	0.016	80
8.0	0.020	80

low concentration as shown in Fig. 5 also reflect this cause.

Adsorption of poly(vinylpyridine) from HCl.—Typical curves obtained in these experiments are presented in Fig. 7, and the results of four experiments are summarized in Table II. Curve A in Fig. 7 has been normalized by subtracting the amount of iron present at the time the polymer solution was added. Zero time, therefore, corresponds to the time at which the polymer solution was added. The data points in curve B were derived from the absorbance measurements by the procedure previously described for the cyclohexane solutions. The level portion of the adsorption curve (B) corresponds to 0.016 μmoles of polymer adsorbed per gram of steel. This amount is less than one-tenth monolayer (calculating as for Table I and assuming no appreciable area change).

The results from all of the experiments are summarized in Table II. The figures quoted in Table II in the column headed % Inhibition were derived from the equation

$$\% \text{ Inhibition} = \left(1 - \frac{\text{Rate inhibited}}{\text{Rate-uninhibited}}\right) \times 100$$

The corrosion rates used in this equation were derived from the slopes of the iron curves, in inhibited and uninhibited solution. In all cases, the initial polymer concentration was 3.9×10^{-5}M in terms of pyridine rings or 3.9×10^{-6}M in polymer molecules. Because the uninhibited rate falls off after a long time compared to the experimental interval, it is concluded that diffusion eventually limits both reactions.

Heat of adsorption experiments.—These experiments are briefly included here primarily to demonstrate further evidence for the chemisorption of 4-ethylpiperidine. Typical curves for the amine in cyclohexane and for a calibration experiment are reproduced in Fig. 8. In successive experiments using in-

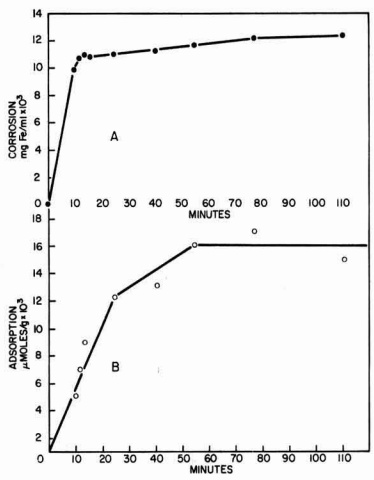

Fig. 7. Comparison of adsorption and corrosion in polypyridine inhibited 0.01*N* HCl.

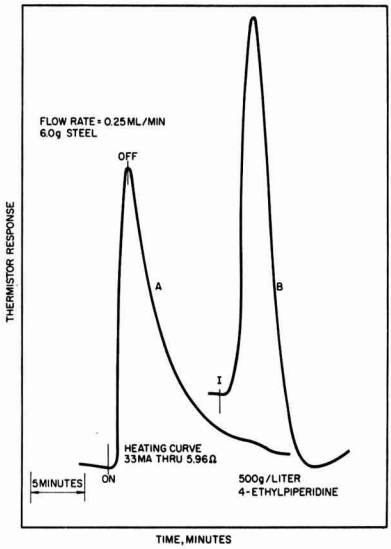

Fig. 8. Heat of adsorption curves for steel powder in cyclohexane

creasing concentrations of amine, the curves observed gradually became narrower and peaked at higher and higher temperatures until at 400 g/l, and thereafter their shape and height stabilized at that shown in Fig. 8. Above 400 g/l concentration, saturation is achieved and the coverage is assumed to be that obtained in the static experiments (Table I).

The calibration curve shown was developed empirically by adjusting the geometrical relationship between the heater and thermistor and by adjusting the magnitude and interval of current flow. The same amount of steel and the same rate of solvent flow were used as in the experiment with 4-ethylpiperidine. The current used to produce the calibration curve corresponds to 16.8 millicalories. Using this figure and assuming saturation of the steel at 0.24 μmoles of 4-ethylpiperidine adsorbed per gram of steel, the heat of differential adsorption is calculated to be 13 kcal per mole. This value was shown to be substantially free of heat-of-solution effects in an experiment using solvent only in the sample chamber. In this experiment 300 μl of the amine in one slug were injected into the solvent stream flowing into a 3.0 ml volume of the same solvent surrounding the thermistor. A small negative heat of solution was observed. However, this amount of heat is insignificant because the total quantity of amine available for adsorption is 3000 times the amount adsorbed at equilibrium.

In other experiments, a small positive heat of adsorption was observed for cyclohexane adsorbed onto steel from n-heptane (99 mole% minimum), and both benzene and 4-ethylpyridine were found to adsorb exothermically onto steel from cyclohexane. When n-heptane was used as solute in cyclohexane, its adsorption on steel is endothermic.

Discussion

From the data collected in Table I, it is concluded that both 4-ethylpiperidine and 4-ethylpyridine are adsorbed to the extent of an essentially complete monolayer.

It is concluded that the pyridine rings are adsorbed with the plane of the rings parallel to the local plane of the metal surface, primarily because the isotherm for 4-ethylpyridine shows monolayer formation when this position is assumed. The alternative vertical position would require participation of solvent molecules in the adsorbed layer which, in turn, would seem to require a close solvent-solute association, a conclusion which belies the closer association expected between the structurally similar cyclohexane and 4-ethylpiperidine molecules. Finally, both benzene and 4-ethylpyridine adsorb exothermically from cyclohexane, indicating that participation of the π-electron system does occur in adsorption bond formation.

The possibility that the apparent adsorption was really due to hydrogenation of the pyridine chromophore by hydrogen absorbed in the steel was investigated by treating samples from one run with the piperidine reagent (which will react with any primary or secondary nitrogen). There was no detectable reaction. Furthermore, there was no difference between adsorption runs with hydrogen-saturated steel and those with argon-degassed steel. Finally, it was observed during the synthesis work that pyridine ring reductions are difficult even with platinum metal catalysts and much higher temperatures and hydrogen pressures. For these reasons, it is concluded that the decrease in solution concentration during an adsorption run is truly the result of accumulation of pyridine molecules at the iron surface.

In the case of 4-ethylpiperidine adsorption the difference in projected areas covered by different orientations and different steric arrangements of the molecule are much smaller than experimental error due to the ball-like shape of the molecule. From the heat of adsorption data, it is concluded that the nitrogen atom participates strongly in the formation of the adsorption bond, and therefore the molecules at the surface are arranged with the nitrogen in close proximity to the surface and not with the ethyl tail down. This conclusion is supported by the recent observation by other investigators of a charge-transfer type spectrum for a long-chain amine adsorbed on chromium (13). Dehydrogenation reactions are ruled out in this case also because of the dual experiments with hydrogen-saturated and argon-degassed steel.

Even short poly(vinylpyridine) chains (4 units) are much more strongly adsorbed than the monomer. This is shown by the individual points included in Fig. 4 and by the data in Table I. There is a definite tendency for the adsorption to increase with time on the plateau portion of the adsorption-time curves. In addition, increasing the length of the chains greatly increases the adsorption tendency. Apparently, the polymer molecules all adsorb to about the same extent, as shown by the consistent values for amount adsorbed calculated in Table I in terms of molecules. This means that the number of rings removed from the solution by adsorption increases with chain length. It also means that all of the rings on a chain are not adsorbed, but some of them remain partly in the solution phase. However, adsorption of the polymers at more than one point in the molecule makes them very difficult to displace and accounts for the greatly increased inhibition by these molecules.

The aqueous solution measurements show that a considerable portion of the metal surface in excess of the amount covered is deactivated toward corrosion because adsorption of less than one-tenth monolayer produced 80% inhibition. This is probably the result of overlapping of domains of ennoblement when more than one ring is absorbed from a molecule in which they are close together.

Conclusions

1. Molecules of 4-ethylpiperidine are strongly chemisorbed on a steel surface to form a monolayer of molecules adsorbed in the chair configuration and bonded at nitrogen.
2. Molecules of 4-ethylpyridine are chemisorbed on steel in a monolayer and in a position with the plane of the ring parallel to the metal surface.
3. Adsorption of poly(vinylpyridine) molecules is by attachment at several of the adsorbable chain members so that strong adsorption is rapid and desorption is difficult even from solution in aqueous hydrochloric acid.
4. Adsorption of the polymers from acid solutions produces ennoblement of a much greater area of the steel surface than that which is physically covered.

Acknowledgment

The authors gratefully acknowledge the able assistance of Dr. J. S. Payne, Jr., and Mr. R. N. Foote, who carried out the syntheses and of Messrs. J. W. Dooley and D. H. McLendon and Mrs. Peggy Glass, who made many of the measurements. In addition, they thank Drs. P. D. Gardner and R. M. Roberts for their advice and constructive criticisms of the organic portions of the work. The work was done under Contract No. DA-23-072-ORD-1590 for the Army Research Office, Department of the Army. One of the authors (NH) expresses his appreciation of the support by the Robert A. Welch Foundation of Houston, Texas, and of the Office of Naval Research of the work in his laboratory which led in part to this research.

Manuscript received Sept. 3, 1964.

Any discussion of this paper will appear in a Discussion Section to be published in the December 1965 JOURNAL.

REFERENCES

1. M. Stern and A. L. Geary, *This Journal*, **104**, 56 (1957).
2. N. Hackerman and A. C. Makrides, *Ind. and Eng. Chem.*, **46**, 523 (1954).
3. H. F. Finley and N. Hackerman, *This Journal*, **107**, 259 (1960).

4. H. Fischer, Symposium Europeen sur Les Inhibiteurs De Corrosion, Xeme Manifestation de la Federation Europeeme de la Corrosion, Ferrara (italie) 1960, (Universita Degli) Studi Di Ferrara, 1961, p. 1-71.
5. L. I. Antropov, "Kinetics of Electrode Processes and Null Points of Metals," Ranchi, India, Catholic Press (1960).
6. T. K. Ross and D. H. Jones, Symposium Europeen sur Les Inhibiteurs De Corrosion, Xeme Manifestation de la Federation Europeeme de la Corrosion, Ferrara, (italie) 1960, (Universita Degli) Studi Di Ferrara, 1961, pp. 163-182.
7. L. Cavallaro, L. Felloni, and G. Trabanelli, Symposium Europeen sur Les Inhibiteurs De Corrosion, Xeme Manifestation de la Federation Europeeme de la Corrosion, Ferrara (italie) 1960, (Universita Degli) Studi Di Ferrara, 1961, pp. 111-135.
8. R. R. Annand, R. M. Hurd, and N. Hackerman, *This Journal*, **112**, 144 (1965).
9. F. C. McIntire, L. M. Clements, and M. Sproull, *Anal. Chem.*, **25**, 1757 (1953).
10. M. G. Mellon, "Analytical Absorption Spectroscopy," pp. 369-373, John Wiley & Sons, Inc., New York (1950).
11. M. G. Mellon, "Analytical Absorption Spectroscopy," pp. 374-376, John Wiley & Sons, Inc., New York (1950).
12. A. Groszek, *J. Chromatog.*, **3**, 454 (1960).
13. D. Churchill and L. S. Bartell, *J. Phys. Chem.*, **67**, 2518 (1963).

Inhibition of Acid Corrosion by Soluble Monomer and Polymer Amines Containing Identical Functional Groups

R. R. Annand,[1] and R. M. Hurd,[2]
TRACOR, Inc., Austin, Texas
and Norman Hackerman
Department of Chemistry, The University of Texas, Austin, Texas

ABSTRACT

Samples of three kinds of very low polymer amines were examined in aqueous HCl solutions to determine their inhibitor effectiveness. The results show that soluble molecules containing multiple repeating units which are identical in functionality are more efficient corrosion inhibitors than the corresponding monomers, presumably because of multiple adsorption bonding. The compounds used in these experiments are (i) poly(4-vinylpyridine), (ii) poly(4-vinylpiperidine), and (iii) polyethyleneamines. Chains four units in length and longer produce inhibition equivalent to monomer at concentrations which are nearly four orders of magnitude lower than those required for the monomer. This effect is due to the increased stability of the adsorption bonding and also to some overlapping of ennobled micro areas. In the high ranges, the inhibition is not linearly related to coverage. The differences in inhibitor effectiveness among the three monomers are retained in parallel by the polymers.

The experiments reported here are part of a study of the influence of molecular structure on inhibitor effectiveness. Previous work (1) has shown that in a series of saturated cyclic amines which have a progression in the orbital character of the secondary nitrogen atom, both the adsorption bonding and inhibitor effectiveness progressed in parallel. The present work sought to test the hypothesis that soluble molecules containing multiple repeating units with identical functionality would be more efficient corrosion inhibitors than the corresponding monomers because of multiple adsorption bonding. Accordingly, three series of compounds were examined for inhibitor effectiveness in hydrochloric acid: (i) 4-vinylpyridine polymers with 4-ethylpyridine as monomer, (ii) 4-vinylpiperidine polymers with 4-ethylpiperidine as monomer, and (iii) polyethyleneamines with ethylenediamine as monomer.

The experimental procedures were designed to give the best reproducibility of the data and to spread the results from the individual compounds so that reliable comparisons of their individual behavior could be made. They were so chosen that the comparisons among compounds would be valid, *i.e.*, so that identical conditions of solubility, H^+ concentration, etc., were obtained. In general, this required working in strong mineral acid solutions. A wide range of inhibitor concentration was investigated, and the three different polymer systems were tested to check the general applicability of the individual results.

[1] Present address: Petrolite Corporation, St. Louis, Missouri.

[2] Present address: Continental Oil Company, Ponca City, Oklahoma.

Experimental Procedure

Weight-loss experiments.—Both belt polished SAE 1010 steel coupons with an area of about 15 cm^2 and hand polished low carbon shim steel coupons with much larger areas were corroded in 3*N* HCl for periods of time long enough to give an easily determined weight change even in highly inhibited solutions. The usual length of time was 2-4 hr for the small coupons and 1-2 hr for the large ones. Inhibition results were the same for both types of coupons. All coupons were run twelve at a time with at least triplicates of each concentration of inhibitor. Triplicate blanks always took up three out of the twelve coupons. In this manner, a large body of blank runs was collected during the course of the experiments, and any significant deviation of the blanks in a set of twelve coupons [determined statistically by the t-test (2)] was taken as cause for a rerun of that set of experiments.

Reproducibility was aided by running the experiments with the coupons and solutions contained in individual test tubes which were immersed in a controlled temperature bath. Gasometric checks of both the inhibited and uninhibited solution were performed by connecting the tube to a gas buret and measuring the volume of hydrogen evolved as a function of time over the course of the experiment. These plots were all linear and passed through the origin. The volume of gas evolved corresponded to the weight of metal lost according to stoichiometry.

Experiments were run in which the concentration of inhibitor[3] was changed from the order of 1*N* to

[3] Concentrations throughout this paper are expressed in terms of nitrogen atoms, *e.g.*, the equivalent weight of a molecule containing four nitrogen atoms = MW/4.

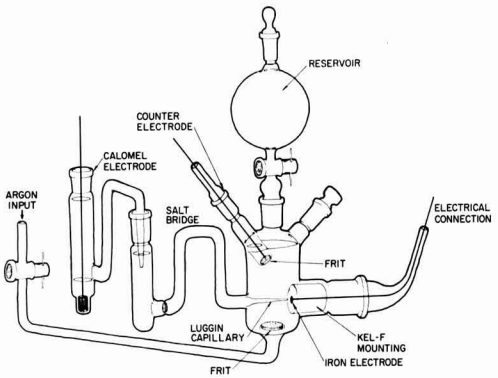

Fig. 1. Polarization cell

about $10^{-6}N$, or until acceleration of the corrosion reaction was observed. In the experiments with significant amounts of basic inhibitor present, the acid concentration was adjusted to maintain it at 3.0*N* in the inhibited solutions. All of the inhibitors were completely soluble under the conditions of the experiments.

Polarization experiments.—Polarization experiments were performed using the cell design shown in Fig. 1. The steel samples used were obtained by punching circular disks out of some of the small SAE 1020 coupons. A length of iron wire was spot welded to one face of each disk. A premolded Kel-F cylinder drilled axially to accept the wire was used to mount the iron disk electrode. The disk was mounted in the Kel-F and bonded to it by reheating and pressing in the original mold. Finally the wire end of the cylinder was turned on a lathe to a standard taper and the electrode face was polished uniformly with emery paper. The whole Kel-F electrode assembly was mounted in the cell by firmly seating it in the female portion of a demountable female-male double TS joint section.

Polarization curves were taken in the usual way using a platinum counterelectrode in a separate compartment and a calomel reference electrode connected through a salt bridge to a Luggin capillary. Placement of the bridge capillary was not extremely critical because the solutions were highly conducting. However, by adjustment of the over-all length of the Kel-F mounting, a distance of a few millimeters was maintained. Electric current was supplied by a parallel pair of 90v radio batteries operated through a variable high resistance to make them a constant-current source. Electrode potentials were measured with a potentiometer, and currents were measured by the IR drop through a standard resistance.

The usual procedure was to insert the polished electrode into the empty cell, fill it with degassed 1.0*N* HCl, and then wait to allow the open-circuit potential to stabilize while the solution was further degassed and stirred with argon. Polarization data were first taken in the cathodic (hydrogen evolution) direction, and then after rechecking the open-circuit potential, in the anodic (iron dissolution) direction. In most experiments with inhibitor, a weighed amount of inhibitor was added after the open-circuit potential had stabilized with a fresh electrode and then the polarization curves were taken. In some cases, uninhibited polarization curves were taken first and then the inhibitor added and the inhibited polarization curves taken. Repetitive experiments agreed well when a freshly polished electrode and a fresh solution bath were used each time a set of experiments was run. Changes in ferrous ion concentration throughout a run were not large enough to affect the potentials. After periods of continuous or consecutive exposure to the acid of several days' duration, the electrodes showed evidence of preferential corrosion around the edge of the metal. This corrosion proceeded from the flat side of the edge and not from the curved side which was effectively bonded to the Kel-F. The presence of these areas was indicated by distortions in the polarization curves.

Synthesis and purification of compounds used.—The polyethyleneamines were obtained from Distillation Products Industries and were distilled before use. The 4-ethylpyridine was obtained from Reilly Tar and Chemical Corporation, and before use it was distilled in a nitrogen atmosphere through a highly efficient, vacuum-jacketed still. It was also stored under nitrogen. The poly(4-vinylpyridine), poly(4-vinylpiperidine), and 4-ethylpiperidine were synthesized in the laboratory. The monopiperidine was obtained by catalytic hydrogenation in a Parr apparatus using a palladium-charcoal catalyst. After distillation in a nitrogen atmosphere, the product was checked spectrophotometrically for absence of the pyridine. This product was also stored under nitrogen.

After many trials, a procedure was designed for obtaining very low molecular weight poly(vinylpyridines) by polymerizing 4-vinylpyridine (obtained from Reilly Tar and Chemical Corporation and freshly distilled before use) using 2,2′-azoisobutyronitrile as initiator. The procedure finally adopted consisted in polymerizing in a very dilute ethanol solution which was kept under nitrogen almost at the reflux temperature. By properly adjusting the extent of dilution in the polymerization media and the ratio of monomer to initiator, polymer samples could be obtained which ranged in chain length from four to about one hundred units. Number average molecular weights were determined using a Mechrolab Vapor Osmometer. The number of initiator fragments per chain was determined by infrared spectral analysis. This indicated two fragments per chain.

The 4-vinylpiperidine polymers were obtained from the corresponding polypyridine by catalytic reduction in a high-pressure stainless steel autoclave. During the course of a great many trial reductions using different catalysts and at various operating temperatures and pressures, it was found that the necessary catalytic function was the ability to cause reduction at the lowest possible temperature so that degradation was a minimum. Using ruthenium on carbon and the highest hydrogen pressure safely obtainable in the autoclave at 250°C, a satisfactory reduction was obtained with only slight degradation. Only a very small percentage of unreduced pyridine units remained, but a

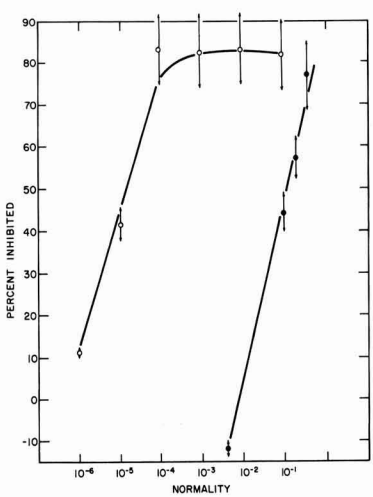

Fig. 2. Per cent inhibition *vs.* log concentration for mild steel at 40°C in 3.0*N* HCl; ○, poly(vinylpyridine) (MW 160); ●, 4-ethylpyridine.

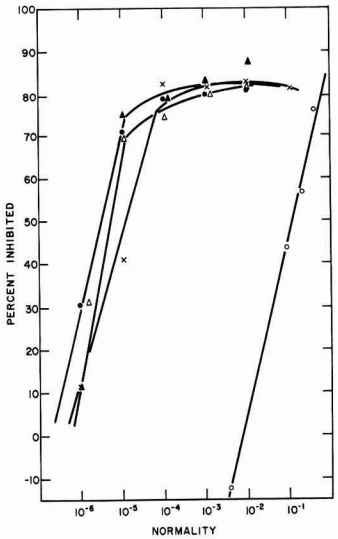

Fig. 3. Effect of polymer chain length on inhibitor effectiveness for mild steel polypyridines in 3.0*N* HCl at 40°C. Chain length: ○, 1 unit; ●, 4 units; X, 10 units; ▲, 14 units; △, 67 units.

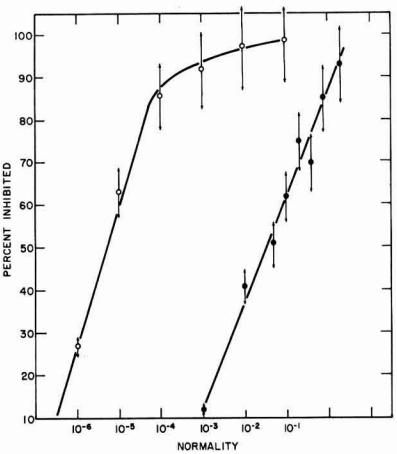

Fig. 4. Per cent inhibition *vs.* log concentration for mild steel at 40°C in 3.0*N* HCl; ●, 4-ethylpiperidine; ○, poly(vinylpiperidine) (MW 400).

ruthenium-polymer complex was formed in the autoclave reaction. It was necessary to wash out the ruthenium by extraction into n-butanol from an acidic aqueous solution. Dicyclohexylthiourea was added to the butanol to force the extraction by competitive complexation of the ruthenium. The complex thus formed had a distinctive blue color and therefore could be used as its own indicator to signal complete removal of the ruthenium. The purified polymer was then recovered by making the solution basic, filtering, washing and vacuum drying.

Discussion of the Results

The curves obtained from the weight loss experiments for the three series of compounds are shown in Fig. 2, 3, 4, and 5. From these, it is readily seen that the hypothesis which was tested is indeed valid. Polymer chains above 3 to 4 units in length produce the same inhibition as the monomer at concentrations up to four

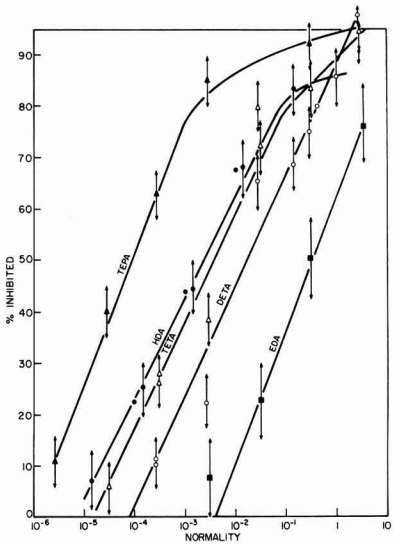

Fig. 5. Per cent inhibition *vs.* log concentration for mild steel at 40°C in 3.0*N* HCl; ●, hexamethylenediamine; ○, diethylenetriamine; ■, ethylenediamine; △, triethylenetetramine; ▲, tetraethylenepentamine.

powers of ten lower in magnitude. In all of the experiments, the inhibitor was completely soluble; no emulsions were used.

Because two and three unit polypyridines and polypiperidines were not available, one of the reasons for the work with the polyethyleneamine series was to determine whether the increase in inhibitor effectiveness of polymers is progressive from one up to four or five units. The data of Fig. 5 show that it is progressive up to four units, but the data of Fig. 3 show that this progression ceases above four units. These data show that the stability of the adsorption bonding to the metal determines the inhibitor effectiveness. That is, a soluble species which adsorbs readily and which is not easily removed when once adsorbed will be most effective. It is interesting to note that among the three types of compounds, the same trends in inhibitor effectiveness (in terms of the position of the curves on the log axis) exhibited by the monomers on the rising portion of the curve are retained by the polymers. This suggests that adsorption of polymers provides a multiplying effect to the relationships between the kind of individual adsorption bonds and the inhibitor effectiveness of that bond.

A possible alternative mechanism for the effectiveness of the polymers is the precipitation of a metal polymer complex in the immediate vicinity of the metal surface. This is rejected on the following grounds: (i) Complexes of hexamethylenediamine would be expected to be much less soluble (and therefore more effective) than those of either diethylenetriamine or triethylenetetramine, yet they all have nearly the same inhibition effect; (ii) in no case has a complex containing precipitate been observed in the presence of excess iron(II) or iron(III); (iii) a continuous tendency to precipitate and therefore to inhibit would be expected as the chain length is increased, particularly for very long chains and when several iron atoms are complexed by one chain; no such tendency was observed with the polypyridines or polypiperidines above the level of four units (Fig. 3); and (iv) no visible film was formed on the coupons under any inhibited conditions.

An unexpected feature of the results is the existence of the log-linear portion which extends over about two decades on the log concentration axis. This feature has

been found to be a general one for a wide variety of compounds tested in this laboratory. As shown in the 4-ethylpyridine curve (Fig. 2), even points which represent an increase in corrosion rate lie on the line when plotted in terms of negative inhibition. The negative numbers are derived on the same basis as the others, *i.e.*, from the equation

$$\% \text{ Inhibited} = \left(1 - \frac{\text{Rate inhibited}}{\text{Rate uninhibited}}\right) \times 100$$

where the rate terms are in the same units, *e.g.*, mg lost/hr/cm^2.

The fact that the curves for per cent inhibition as a function of log concentration are linear over an appreciable range for the polyethyleneamines, the polypiperidines, polypyridines, and other compounds indictate a linear relation between adsorption from acid solution and log concentration. Such a relationship is found in the Temkin isotherm (3, 4),

$$\theta = -\frac{RT}{\beta \Delta H_o} \ln AC$$

In this expression, β is a constant; A is a complex function of ΔH_o and other parameters; and ΔH_o is the heat of adsorption for very low coverage, (θ). For adsorption from dilute aqueous solution, ΔH_o will be influenced by contributions from the heats of desorption of solvent and of neutralization of the inhibitor conjugate acid.

The ionization constants for all of the polyethyleneamines have been published (5-8). Using these values, the normalities of amine, and the concentration of HCl, it can be shown that at the highest concentration plotted for tetraethylenepentamine, only 0.74% of the molecules are not fully protonated. The free amine (completely unprotonated) is present at a concentration of the order of $10^{-36}N$ at an analytical concentration (*i.e.*, amount of amine added per unit volume of solution) corresponding to good inhibition. Furthermore, under the experimental conditions of high, constant H^+ ion concentration, the concentration of any of the possible species, *i.e.*, from completely unprotonated to completely protonated, is a linear function of the analytical concentration. The base strengths in the polyethyleneamine series range upward from tetraethylenepentamine. The polypyridines and piperidines are expected to be quite similar for comparable chain-length. On this basis, if it can be assumed that per cent inhibition is proportional to per cent coverage (θ), then

$$\%I = K\theta = -\frac{KRT}{\beta \Delta H_o} \ln A - \frac{KRT}{\beta \Delta H_o} \ln C$$
$$= m \log C + \text{Constant}$$

where K is the proportionality constant. That is, the slope of the line, $\%I = F(\log C)$, is proportional to the reciprocal of the net heat of adsorption. Furthermore, since β is an independent constant, if the ΔH_o's, the K's, and the β's are similar, the slopes of the lines, $\%I = F(\log C)$, should be the same.

The data in Table I were obtained by a statistical treatment of the data shown graphically in Fig. 5 to get average values of the slopes of the rising portion of the individual curves. It can be seen that the slopes are very nearly uniform for all of the polyethyleneamines. This must mean that only small differences occur in the ΔH_o's and β's due to the different ratios

Table I. Slopes of the curves of Fig. 5

Compound	Slope, %I per log cycle
EDA	17.9
HDA	17.2
DETA	18.5
TETA	17.5
TEPA	18.9
Average	18.0

Table II. Slopes of the curves of Fig. 2, 3, and 4

Compound	Slope, %I per log cycle
Ethylpyridine	42.0
Polypyridine (MW 514)	40.0
Polypyridine (MW 1160)	32.0
Polypyridine (MW 1549)	44.2
Polypyridine (MW 6954)	58.8
Ethylpiperidine	25.5
Polypiperidine (MW 400)	32.5

of the number of primary to secondary amino nitrogens. However, it may represent large contributions by the heats of neutralization and desorption of solvent which are the same for all the compounds. These may be masking the relatively smaller differences in the heat of formation of the chemisorption bond among the different compounds.

For comparison, the slopes of the curves from Fig. 2, 3, and 4 are included in Table II for polymer and monomer pyridines and piperidines. The higher slopes of these curves are consistent with either a large solvent contribution to the heats of reaction or with a difference of a factor of about two in either β or K, because the inhibitor effectiveness at saturation is not appreciably different for the two kinds of polymers. There is, however, a greater spread in the data of Table II, indicating a greater difference between monomer and polymer.

The factor, K, in the above discussion is used because adsorption experiments from acid solutions (9) have shown that in 0.01N HCl polypyridines are capable of producing 80% inhibition under conditions where less than one-tenth monolayer coverage is obtained. Furthermore, polarization curves taken with and without both monomer and polymer show that the metal is ennobled by 20 mv or more due to the adsorption of these inhibitors (10). An example of this is presented in Fig. 6. These observations strongly suggest that in the plateau portion of the polymer curves where θ ceases to be proportional to the per cent inhibition efficiency, the proportionality breaks down because the ennobled areas of the surface begin to overlap as θ increases, and thus K is no longer constant.

Conclusions

1. Very short chains of adsorbable groups improve inhibitor effectiveness by orders of magnitude compared to monomeric species.

2. This effect is interpreted in terms of a greatly increased stability of the net total adsorption bonding

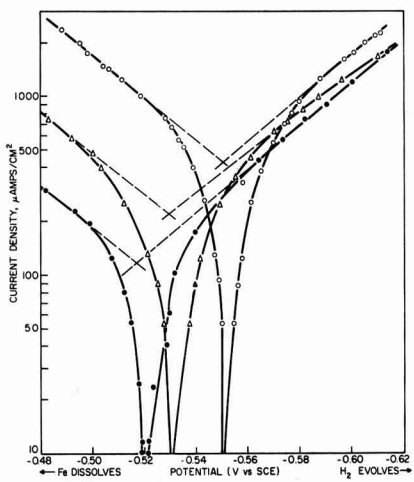

Fig. 6. Polarization curves for uninhibited monomer and polymer solutions; △—△, 0.1M 4-ethylpyridine in 1N HCl; ○—○, 1N HCl uninhibited; ●—●, 0.031M poly(vinylpyridine) 512 MW in 1N HCl.

in the polymer species, *i.e.*, a high tendency to adsorb, to stay adsorbed, and to form strong metal/inhibitor bonds which contribute an enhanced ennobling effect.

3. In the case of adsorption which ennobles the metal surface, the inhibition is not linearly related to coverage in the high inhibition ranges.

4. In agreement with 3, the variations in effectiveness of the individual adsorbable groups (exemplified by the monomers) are retained in the polymer.

Acknowledgment

The authors gratefully acknowledge the assistance of Dr. J. S. Payne, Jr., and Mr. R. N. Foote, who carried out the organic syntheses and of Dr. I. Y. Chang, who took the polarization data. This work was carried out under Contract No. DA-23-072-ORD-1590 for the Army Research Office, Department of the Army. One of the authors (NH) also expresses his appreciation to the Robert A. Welch Foundation of Houston, Texas, and to the Office of Naval Research for support of research in his laboratory over the years which in part led to this work.

Manuscript received Sept. 3, 1964. This paper was presented in part at the 20th Annual NACE Conference, March 1964, Chicago, Illinois.

Any discussion of this paper will appear in a Discussion Section to be published in the December 1965 JOURNAL.

REFERENCES

1. N. Hackerman, R. M. Hurd, and R. R. Annand, *Corrosion*, **18**, 37t (1962).
2. W. J. Youden, "Statistical Methods for Chemists," pp. 24-28, John Wiley & Son, New York (1959).
3. S. Brunauer, K. S. Lore, and R. G. Keenan, *J. Am. Chem. Soc.*, **64**, 751 (1942).
4. A. Frumkin and A. Slygin, *Acta Physicochim. URSS*, **3**, 791 (1935).
5. Alexander Gevo, *J. Am. Chem. Soc.*, **76**, 5159 (1954).
6. H. B. Jonassen, F. W. Frey, and A. Schaefsma, *J. Phys. Chem.*, **61**, 504 (1957).
7. H. B. Jonassen, R. B. LeBlanc, A. W. Meibohm, and R. M. Rogan, *J. Am. Chem. Soc.*, **72**, 2430 (1950).
8. R. Rometsch, A. Marxer, and K. Miescher, *Helv. Chim. Acta*, **34**, 1611 (1951).
9. R. R. Annand, R. M. Hurd, and N. Hackerman, *This Journal*, **112**, 138 (1965).
10. R. R. Annand and N. Hackerman, "Corrosion Inhibition," in "Encyclopedia of Electrochemistry," C. A. Hampel, Editor, Reinhold Publishing Co., New York (1964).

The Influence of Crystal Orientation on the Oxidation of Tungsten

R. W. Bartlett and J. W. McCamont

Philco Research Laboratories, Newport Beach, California

ABSTRACT

The oxidation of tungsten above 1800°C is described in terms of deviations from gas collision theory (Hertz-Knudsen equation). The probability that a colliding oxygen molecule will react with tungsten is strongly dependent on crystal orientation. Of the crystal faces examined, (100) surfaces oxidize most rapidly with a reaction probability of 0.4. (111) and (110) surfaces oxidize at approximately the same rate as polycrystalline tungsten. The morphology of oxidized (100) surfaces is smooth with the exception of occasional stepped octahedral pyramids each bound by {111} faces. The morphology of (111) surfaces is smooth except for numerous stepped tetrahedral pyramids each bound by {100} faces. Initiation of these shapes is not associated with dislocations or detectable impurities. However, dislocations subsequently cluster at mature octahedral pyramids. The morphology of oxidized (110) tungsten surfaces consists of extremely irregular surfaces and macroscopic ledges, but shapes clearly related to crystal geometry were not identified.

Oxidation of tungsten at temperatures above 1300°C involves collision, chemisorption of oxygen on the tungsten surface, chemical reaction, and evaporation of tungsten oxides. Oxidation rates are linear and have been determined from pressure measurements (1-4) and by measurements of sample dimension changes (5-7) taken during oxidation. Below approximately 1800°C the oxidation rate increases with temperature in an exponential manner characteristic of activated chemical processes. Above 1800°C the rate is independent of temperature except at very low pressures and high temperatures. There is evidence that oxygen atoms chemisorb in two distinct monolayers with different binding energies (2, 8). Oxide polymers, particularly $(WO_3)_3$ and $(WO_2)_3$, have been shown to be the predominant vapor species in equilibrium with tungsten oxides (9). However, a recent mass spectrometric study (10) indicates that monomers are the species evaporated from oxidizing tungsten surfaces. Polymerization evidently occurs later as a result of collisions in the gas phase. Above 2000°C the WO_2 monomer is produced in greater abundance than WO_3 (10).

The nonactivated oxidation rate behavior of tungsten has been explained in terms of deviations from the rate at which oxygen molecules collide with the tungsten surface, since this is the maximum possible rate. Using gas kinetic theory (Hertz-Knudsen equation)

$$J = \epsilon P_{O_2}/(2\pi mkT)^{1/2} \qquad [1]$$

Where J is the number of oxygen molecules which react each second and ϵ is the probability that each O_2 molecule striking the surface will react; $\epsilon \leq 1$. Since the rate is not limited by a prior or subsequent activated step or endothermic step, the reaction probability is equivalent to the sticking probability (condensation coefficient) of oxygen. In a previous study (7), with polycrystalline tungsten, rate data at oxygen pressures from 10^{-6} atm to 1 atm were described with a constant value of the reaction probability, $\epsilon = 0.06$. This correlation included an independent correction for the lowered oxygen pressure at the surface caused by the tungsten oxide gas boundary layer which is present at high pressures. This correction was based on free convection theory.

A study of the effect of metal crystal orientation on oxidation rates at temperatures where condensed oxides form has been made for tungsten (11) and several other metals (12). Similar studies at high temperatures where the oxide products vaporize are rare in general and have not been made for tungsten. The purpose of this study was to determine the reaction probabilities and observe variations in tungsten morphology during oxidation of low index faces.

Experimental

One half inch diameter single crystals of known [hkl] orientation were wafered to produce short cylindrical samples each bound by parallel (hkl) faces. Using a 2% NaOH electrolyte, these surfaces were electropolished, and some were electroetched to develop etch marks and to outline subgrain boundaries. The oxidation procedure is described below. Samples were set on a thin tungsten pedestal located in a vacuum chamber. A stable mounting was accomplished using an insertion hole drilled in the side of the sample. The chamber was evacuated and backfilled with dry oxygen to 1 x 10^{-6} atm. Pressure was maintained by controlling the flow of oxygen through the system. This oxygen pressure was chosen and used exclusively because of several advantages. First, this pressure was high enough to permit removal of considerable tungsten. This allows full development of morphological changes and insures accurate rate measurements. Second, although this pressure is higher than typical condensation-evaporation experiments in metal systems, it is lower than required to form a gas boundary film sufficient to affect the rate of oxidation. Third, at this pressure, there is comparative rate data for polycrystalline tungsten from two sources (4, 7). All samples were oxidized at 2050° ± 50°C using an R.F. induction coil. Temperature was measured with a calibrated disappearing filament pyrometer using corrections for the spectral emissivity of tungsten and calibrated window absorptivity. The oxidation rate was determined by measuring the decrease in distance between opposite (hkl) faces with micrometer calipers accurate to ±0.0001 in. These measurements were made on samples which had been oxidized 420 min, and the decrease in interface distance varied between 0.0195 and 0.045 in.

The tungsten crystals used as samples were grown by the Linde Company using a plasma arc Verneuil technique, Table I. In all cases misorientation of crystal faces with the surface was less than 5°.

Since the orientation and appearance of etch marks generated in aqueous solutions were used to correlate the morphological results of high-temperature oxidation, a brief introductory discussion of wet etch marks on tungsten is necessary. Etch pits in tungsten have been studied extensively by Schadler (13) using a $CuSO_4 \cdot NH_4OH$ solution and by Berlec (14) using both a $CuSO_4 \cdot NH_4OH$ solution and a 2% NaOH solution. The results using either etchant are identical. Square etch pits are developed on (100) surfaces, and elongated triangular pits develop on (112) surfaces of tungsten. In both cases, the defining sides of the etch pits are {110} planes. Plastic deformation experiments and matched etch pit patterns in cleaved surfaces indicate that the etch pits coincide with dislocations intersecting the surface. Berlec (14) has observed small oriented etch hillocks with a triangular outline on heavily etched (111) surfaces of tungsten. Neither etch pits nor hillocks occur on (110) surfaces of tungsten. All of these results were confirmed during the present study. We have also found that the wet etch pyramids on (111) surfaces cluster at subgrain boundaries, suggesting an association with dislocations.

Table I. Nominal composition tungsten crystals

C	6 ppm	Fe	0.01%
O	5 ppm	Mg	0.001
Al	0.01%	Mn	0.01
Co	0.003	Mo	0.1
Cu	0.001	Ni	0.01
Cr	0.01	Si	0.01

Table II. Measured reaction probabilities based on an oxidation period of 420 min at 2050°C and: $W + O_2 \rightleftharpoons WO_2(g)$

$P_{O_2} = 1 \times 10^{-6}$ atm, T = 300°K;

$$\epsilon = (\text{rate}) \left(\frac{\rho_W N_O}{M_W P_{O_2}} \right) (2\pi mkT)^{1/2}, \quad \epsilon = 9.84 \times 10^8 \ (\text{rate})$$

Sample	Face	Avg. face recession	Recession rate, in./min	ϵ
W-12	(100)	0.0176	4.2×10^{-5}	0.41
W-13	(100)	0.0172	4.1×10^{-5}	0.40
W-20	(100)	0.0186	4.3×10^{-5}	0.42
W-4	(110)	0.0032	7.7×10^{-6}	0.076
W-7	(110)	0.0032	7.6×10^{-6}	0.075
W-8	(110)	0.00295	7.0×10^{-6}	0.069
W-31	(111)	0.0040	9.5×10^{-6}	0.093
W-32	(111)	0.0040	9.5×10^{-6}	0.093
W-33	(111)	0.00395	9.4×10^{-6}	0.092

Vicinal surfaces composing the faces of structural anomalies, hillocks and pits, formed on tungsten were identified from (*a*) the height or depth of the structure measured by oil emersion microscopy, (*b*) the projected geometry of the structure, and (*c*) the orientation of the crystal with respect to the orientation of the hillock or pit. Crystal orientation was determined by x-ray diffraction.

Results

The measured values for reaction probabilities on (100), (110), and (111) faces are shown in Table II. These data are also shown in graphical form and compared with polycrystalline data at the same pressures in Fig. 1. The values for (110) and (111) faces are similar to the polycrystalline values, but the reaction probability on the (100) face was much faster, approaching half of the total collision rate.

The differences in morphology of the tungsten surface were more striking, but the results were equally reproducible. Polished (100) and (111) surfaces tended to remain smooth while (110) surfaces were jagged. Grooving of subgrain boundaries occurs on (100) and (111) surfaces. Etch pits or other indications of accelerated oxidation at dislocations were not observed on any of the crystal faces as a result of oxidation. Wet etch pits introduced before oxidation lost definition as a result of oxidation but did not change otherwise.

(100) Surface.—Examination of the 90-min oxidation micrographs reveals occasional marks similar to the wet etch pits. These hillocks are the initial appearance of growth anomalies on (100) surfaces which remain for extended periods of oxidation and eventually become octahedral pyramids. These growth forms also appear as small rounded craters in their early stages.

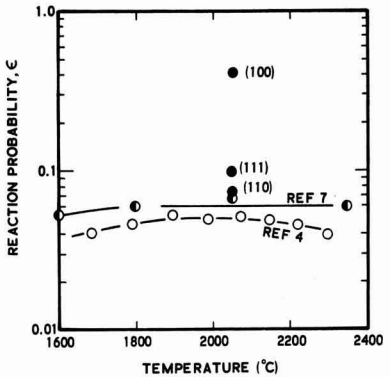

Fig. 1. Reaction probability for polycrystalline tungsten wire (4) and rod (7) and single crystal low index faces at 1 x 10^{-6} atmospheres oxygen pressure.

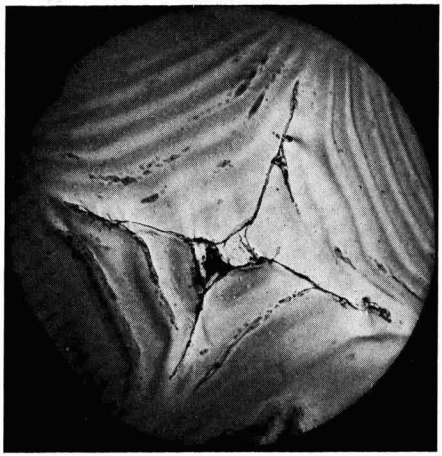

Fig. 2. Carbon replica of stepped pyramid on (100) tungsten surface. Magnification 1500X.

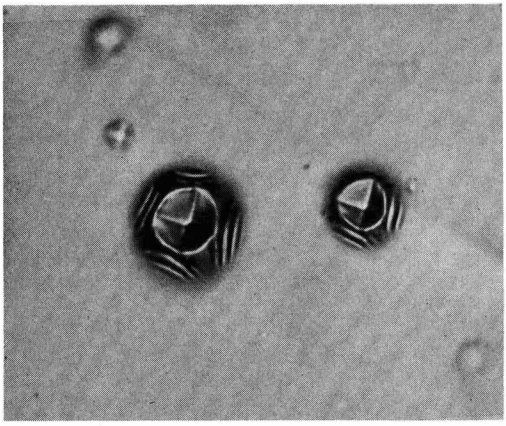

Fig. 3. Octahedral pyramids on (100) surface with cores having the shape of shallow polyps. Small craters slightly out of focus can be seen in the background; oxidation 7 hr at 2070°C. Magnification approximately 500X.

Sometimes they appear as shallow polyp structures containing fourfold symmetry. An electron micrograph replica of a mature octahedral pyramid is shown in Fig. 2. It is considerably larger than a wet etch pit. Its sides are {111} faces rather than the {110} faces observed for wet etch pits. The octahedral faces are stepped to provide for a flatter total pyramid shape without sacrificing the exposure of low index faces at the surface. However, the edges of each pyramid, where the {111} planes intersect, are not stepped. This shape leads to the appearance of fourfold inverted rings in optical micrographs. The center of these pyramids may simply be a continuation of the pyramid structure or contain the shallow polyps. Two examples of the latter are shown in Fig. 3.

The mature stepped pyramid structures are slow to develop. Those shown in Fig. 2 and 3 were formed by an oxidation period of 7 hr. There were comparatively few of these structures on the (100) surface, but they were observed on all samples oxidized more than 3 hr. They have been seen at subgrain boundaries, but there was no preference for this location and little tendency to cluster at any location. Their orientation is fixed by their {111} faces and the orientation of the crystal, Fig. 4. Small misorientations between adjacent subgrains were indicated by small changes in orientation of the stepped pyramids contained within them. As with wet etch pits, slight misorientation of the surface with respect to the (100) plane caused distortions of the symmetrical shape of the pyramids.

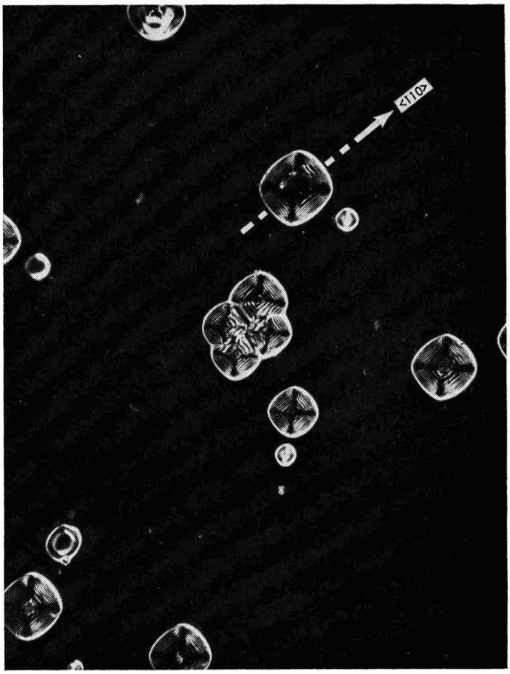

Fig. 4. Orientation of stepped octahedral pyramids on (100) tungsten surface; darkfield illumination. Magnification approximately 130X.

Extensive oxidation after dislocation etching has shown that octahedral pyramids are not initiated at dislocations. However, mature pyramids subsequently act as traps for dislocations. A polished (100) surface was oxidized 7 hr and later marked with a referencing hardness indentation near two octahedral pyramids. The sample was then etched in 2% NaOH to develop wet etch pits. This is shown in the second micrograph of Fig. 5. Dislocations clustered within the strain hardened area around the indentation mark as expected. However, equally dense dislocation clustering has occurred within the octahedral pyramid. Because the wet etch pits are bound by {110} faces their outline is rotated 45° with respect to the square outline of the octahedral pyramids.

Electron microprobe analysis of the tungsten surface at the stepped pyramids was undertaken to determine if impurities were influencing this behavior. Elements other than tungsten were not present in detectable amounts. Furthermore, the tungsten x-ray emission intensity was not diminished at octahedral pyramids relative to the rest of the sample. If tungsten oxides, borides, carbides, or nitrides were present in appreciable quantities, a measurable reduction in tungsten x-ray intensity would have been detected.

(111) Surface.—The morphology development on (111) surfaces was similar to the (100) surfaces. The surface remained smooth; but gradually stepped tetrahedral pyramids matured, Fig. 6. They were more numerous than the octahedral pyramids observed on the (100) surface. Electron micrographs show the steps more clearly than light micrographs. In many instances the hillocks are rounded and only approximate tetrahedral shape. These oxidation pyramids are oriented differently than the wet etch pyramids. This is shown

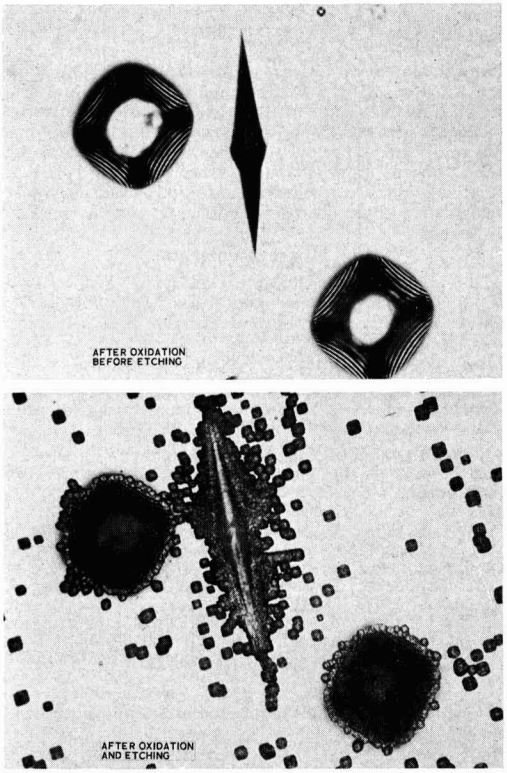

Fig. 5. Post oxidation wet etching treatment shows accumulation of dislocations at stepped pyramids on (100) tungsten surface. Magnification approximately 260X.

in Fig. 7. Both micrographs were taken in the same area and identified by hardness indentations, not shown. The sample was wet etched prior to oxidation, left micrograph. The triangles formed by the intersection of the wet etch pyramids with the (111) surface are pointing down and to the left. The results of a 1-hr oxidation treatment are shown in the right micrograph. A stepped pyramid has formed at the top of the photographed surface, but its triangular outline on the surface is pointing upward and to the right. Oxidation has rounded the wet etch pyramids and is tending to reorient them as triangles pointing in the opposite direction of their original orientation. From a comparison of crystal orientation, as determined from x-ray diffraction studies, with pyramid orientation on the (111) surface we determined that the wet etch pyramids are bound by {110} faces while the stepped oxidation pyramids are bound by {100} faces. The apparent change in orientation of the wet etch pyramids during high temperature oxidation is caused by the preference for {100} faces rather than {110} faces under these conditions. Consequently, the {100} faces advance and the {110} faces recede as defining surfaces for the hillocks.

(110) Surface.—Pyramids or other definite crystallographic shapes do not form on the (110) surface. Grooving of subgrain boundaries also does not occur although these boundaries usually can be detected and followed in a microscope field because of slight differences in shading which occur at the boundaries. The mature morphology developed after a 7-hr oxidation treatment consists of: (*a*) long serrated ridges; (*b*) triangular shapes with saw-tooth edges pointing toward shallow depressed areas and all oriented in a common direction; and (*c*) numerous parallel striations. These are shown in Fig. 8. Rare examples of isolated dodecahedral (110) faces occurred as small

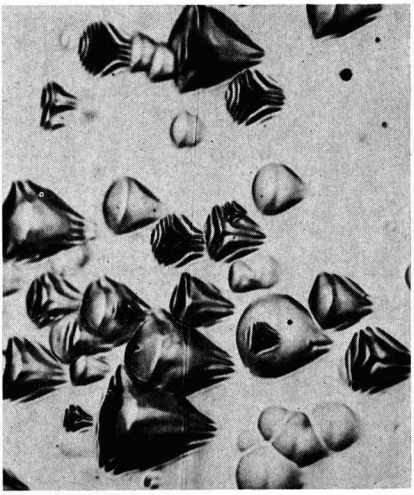

Fig. 6. Mature tetrahedral pyramids on the (111) surface of tungsten oxidized 7 hr at 2050°C. The photograph is bisected by a subgrain boundary.

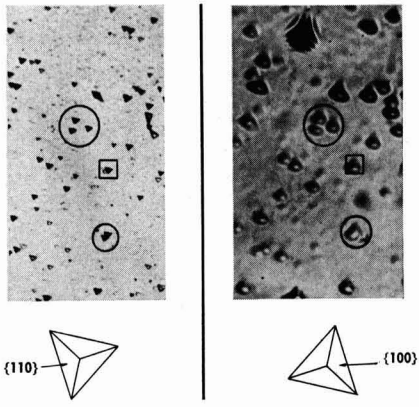

Fig. 7. Orientation of wet etch pyramids on (111) before oxidation, left; reverse orientation of oxidation triangular pyramid developed during a 1-hr oxidation period at 2050°C in the same area, right. Photographs were matched with indentation marks. Magnification approximately 375X.

sections of the tungsten crystal projecting outward from the surface.

Discussion

The results of this study are not easily explained by other published data or models for evaporation and condensation. The order of oxidation rates measured in this study, (100) > (111) > (110>, is different from the rates of formation of thin oxide films on tungsten measured by Metrofanov (11) at 400°-450°C. The order of the latter study was (111) > (100) > (110), and rate increases were correlated with reductions in electronic work functions. The oxidation mechanisms are different, and agreement is not necessarily expected.

Batterman (5) studied faceted hillocks and pits formed during the etching of germanium in a H_2O_2-HF solution. He reasoned that a stable hillock required that the recession rate of the hillock face be less than the product of the recession rate of the base plane and cosine of their angle of intersection. Batterman's results were generally consistent with this rule, but not consistent in all cases. The prevalent formation of

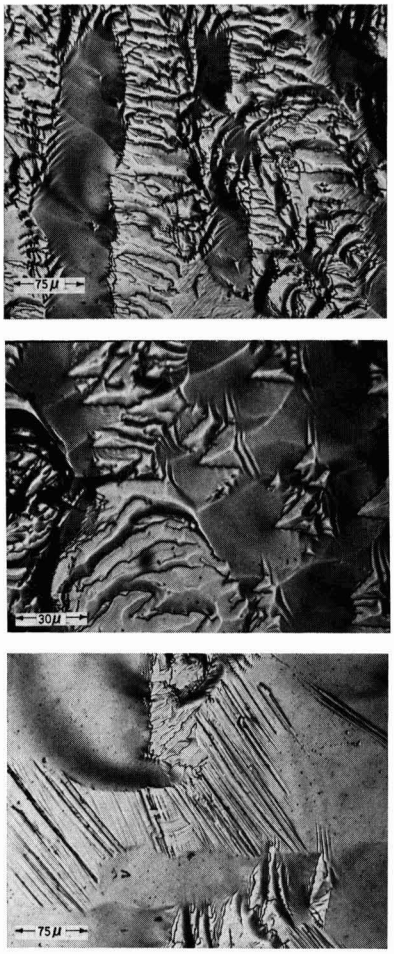

Fig. 8. Characteristic patterns on the (110) tungsten surface resulting from oxidation.

tetrahedral pyramids with {100} faces on a (111) base plane of tungsten does not conform with Batterman's rule.

Sticking coefficients of diatomic molecules have been attributed to entropy decreases involved in transforming from the gas phase to the chemisorbed state. In particular, hindered rotation of the molecule in the chemisorbed state appears to be a plausible cause of a sticking coefficient less than unity (16). On this basis, the sticking coefficient is the ratio of the partition functions for the chemisorbed state and gas state. Since vibration frequencies cannot be evaluated, the approximation that vibrational partition functions have values of unity is taken, and the sticking coefficient is reduced to the reciprocal of the rotational partition function for oxygen

$$\epsilon = \frac{\sigma h^2}{8\pi^2 IkT} \qquad [2]$$

The calculated value for ϵ at 300°K is 0.014. This does not conform with the experimental results, and the model fails to account for the observed rate anisotropy.

When entropy effects are absent, evaporation coefficients are expected to be high and macroscopic ledges absent unless impurities are present (17). Impurities may be contributing to the observed morphologies, but without positive evidence no conclusions can be drawn.

Acknowledgments

The authors are grateful to Mr. R. W. Walker and Mr. J. P. Pope for experimental assistance and to Dr. W. M. Fassell for his helpful discussions. This study was sponsored by Aeronautical Systems Division, U. S. Air Force under Contract AF 33(657)-8654.

Manuscript received June 15, 1964; revised manuscript received Aug. 24, 1964. This paper was presented at the Washington Meeting, Oct. 11-15, 1964.

Any discussion of this paper will appear in a Discussion Section to be published in the December 1965 JOURNAL.

REFERENCES

1. I. Langmuir, *J. Am. Chem. Soc.*, **105**, 35 (1913); *ibid.*, **37**, 1139 (1915).
2. J. Eisinger, *J. Chem. Phys.*, **30**, 412 (1959).
3. J. A. Becker, E. J. Becker, and R. G. Brandes, *J. Appl. Phys.*, **32**, 411 (1961).
4. H. U. Anderson, "Kinetic Studies of the Reactions Occurring Between Tungsten and Gases at Low Pressures and High Temperatures," (Ph.D. Thesis, University of California 1962); UCRL 10135, April 1962.
5. R. A. Perkins and D. D. Crooks, *J. Metals*, **13**, 490 (1961).
6. R. A. Perkins, W. L. Price, and D. D. Crooks, "Oxidation of Tungsten at Ultra-High Temperatures," Lockheed Report 6-90-62-98, November 1962, Sunnyvale, Calif.
7. R. W. Bartlett, *Trans. AIME*, **230**, 1097 (1964).
8. J. A. Becker in "Solid State Physics," Vol. 7, p. 379-424, F. Seitz and D. Turnbull, Editors, Academic Press, New York (1958).
9. J. Berkowitz, W. A. Chupka, and M. G. Inghram, *J. Chem. Phys.*, **27**, 85 (1957).
10. Joan Berkowitz-Mattuck, A. Buchler, J. L. Engelke, and S. N. Goldstein, *J. Chem. Phys.*, **39**, 2722 (1963).
11. O. V. Mitrofanov, "Soviet Physics-Crystallography," **8**, No 2, 229-231 (Trans) (1963).
12. A. T. Gwathmey and K. R. Lawless, "The Influence of Crystal Orientation on the Oxidation of Metals," in "The Surface Chemistry of Metals and Semiconductors," pp. 483-521, H. C. Gatos, Editor, John Wiley & Sons, New York (1960).
13. H. W. Schadler, "Correlation of Etch Pits and Dislocations in Tungsten," in "Direct Observations of Imperfections in Crystals," pp. 593-608, J. B. Newkirk and J. H. Wernick, Editors, Interscience Publishers, New York (1962).
14. I. Berlec, *J. Appl. Phys.*, **33**, 197 (1962).
15. B. W. Batterman, *J. Appl. Phys.*, **28**, 1236 (1957).
16. F. M. Wanlass and H. Eyring, "Sticking Coefficients," in "Advances in Chemistry Series No. 33," p. 140, American Chemical Society (1961).
17. J. P. Hirth and G. M. Pound, "Condensation and Evaporation Progress in Materials Science," Vol. XI. Chap. D., The MacMillan Co., New York (1963).

Low-Pressure Oxidation of Niobium at 1200°-1700°C

Per Kofstad and Svein Espevik

Central Institute for Industrial Research, Blindern, Oslo, Norway

ABSTRACT

The oxidation behavior of niobium has been studied at 1200°-1700°C at oxygen pressures ranging from 2 x 10^{-4} to 0.5 Torr. The oxidation involves dissolution of oxygen in the metal, formation of NbO, NbO_2, and Nb_2O_5. The oxidation may be divided into 3 main stages: (*a*) an initial linear oxidation which is followed by (*b*) a parabolic oxidation which, in turn, transforms into (*c*) a final linear oxidation. The initial linear oxidation involves dissolution of oxygen in the metal and the oxidation is governed by the rate of chemisorption on the metal surface. The parabolic oxidation is due to formation of protective NbO_2, which is further oxidized to porous nonprotective Nb_2O_5 at a linear rate. The oxidation is affected by the presence of liquid Nb_2O_5 at and above 1500°C, and at higher temperatures evaporation of Nb_2O_5 becomes an increasingly important part-process.

A major shortcoming of refractory metals is their poor high-temperature oxidation resistance. When considering applications of these metals or their alloys at elevated temperatures, even under "vacuum" conditions, a knowledge of their oxidation behavior is required. Also for applications of these metals in coated condition, such knowledge is desirable as it provides the margin of safety in case of coating failure.

Inouye (1) studied the oxidation of niobium at 850°, 1000°, and 1200°C at oxygen pressures ranging from 3 x 10^{-5} to 5 x 10^{-3} Torr. The initial oxidation was found to proceed principally by dissolution of oxygen in the metal, and this was followed subsequently by formation of NbO, NbO_2, and Nb_2O_5. NbO_2 was shown to form a protective scale, which was further oxidized to a nonprotective layer of Nb_2O_5. Other investigators have studied the oxidation behavior of niobium at higher oxygen pressures at temperatures up to 1200°C (2-6). Close to 1 atm O_2 the oxidation has been found to involve primarily the dissolution of oxygen in the metal and the formation of Nb_2O_5. However, on the basis of Inouye's work (1) it seems safe to conclude that NbO and NbO_2 are formed as intermediate reaction products also at higher oxygen pressures, although they may only be present in small amounts.

No detailed studies of oxidation of niobium at temperatures in excess of 1200°C appear to have been reported previously in the literature.

Experimental Methods

Materials.—The niobium metal sheet was obtained from Murex Ltd., England. Estimates of metallic impurities were as follows: Fe and Al, each 0.05%; Si, 0.02%; Cr, Pb, and Hg, each 0.01%, and C_T 0.1%. The hardness of the as-received sheet was VHN 75 (10 kg load).

Prior to oxidation the specimens were polished with alumina, rinsed in distilled water and acetone. The metal was recrystallized in high vacuum ($<10^{-5}$ Torr) in the oxidation apparatus prior to the start of the oxidation run. Commercial tank oxygen dried over phosphorus pentoxide was used.

Methods.—Rates of oxidation were measured thermogravimetrically with a Cahn automatic recording balance. The specimens were suspended in a Pt-13% Rh wire ($d = 0.2$ mm). Above 1600°C the Pt/Rh-wire became alloyed with niobium, probably through the formation of liquid alloy phase, and under these conditions a thin niobium wire was used to suspend the specimen in the hotter part of the furnace. The surface area of the niobium wire was small compared to that of the specimen.

The furnace is shown schematically in Fig. 1. An alumina tube (Morgan recrystallized alumina) served as reaction chamber, and it was mounted directly on the baffle valve of an Edwards F203 oil diffusion pump which has an unbaffled pumping speed of 70-80 liters/sec and a speed through the baffle valve of 50-55 l/sec. The alumina tube had an inner diameter of 33 mm and a length of 50 cm. A small alumina bucket was placed in the lower end of the tube to catch any specimens which might fall down due to breaking of the suspending wire. The reaction temperature was measured with Pt-5% Rh/Pt-20% Rh or Ir/Ir-60% Rh thermocouples located inside the reaction chamber next to the specimen.

The complete furnace system consisted of two separate high-vacuum systems serving, respectively, the reaction chamber and the heating element chamber. The latter contained the molybdenum heating element (wire with a diameter of 1 mm wound directly on the alumina tube and embedded in alundum cement) and three molybdenum and tantalum heat shields. The outer wall of the reaction chamber consisted of a Pyrex tube which was cooled by a tight-fitting, water-cooled copper shell. High vacuum was always maintained in the heating element chamber.

The specimens were introduced at room temperature and the system was evacuated to $<10^{-5}$ Torr. The temperature was subsequently raised and equilibrated. Due to outgassing of the furnace during the heating period, the temperature was slowly increased to the desired level, and 3-4 hr was used to raise the temperature to 1500°C. The outgassing and small unavailable leaks in a furnace system of this type unquestionably cause some contamination in addition to the original impurities in the niobium specimens. On the other

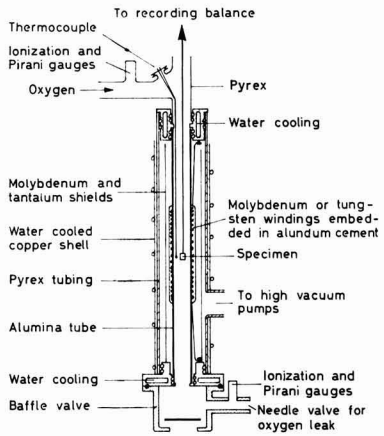

Fig. 1. Schematic illustration of the furnace system

hand oxygen impurities at temperatures above 1600°-1700°C may to some extent be removed through oxide evaporation. In a later improvement of the system a vacuum lock has been incorporated which permits an introduction of the specimens into the furnace after outgassing and temperature equilibration of the system.

The oxidation run was started by introducing oxygen in the system, and up to 1 min was necessary before establishing the correct oxygen pressure. During oxidation at the lower pressures the baffle valve was kept open, and oxygen was continuously pumped through the reaction chamber. The oxygen pressure was monitored at both ends of the reaction chamber by means of calibrated Pirani (LKB) and ionization (Leybold) gauges. Below approximately 0.01 Torr a pressure drop developed along the reaction chamber. Under these conditions the desired pressure was first established at the top of the chamber, and a small oxygen leak was subsequently introduced in the baffle valve to equalize the pressures. During oxidation the same oxygen pressure was maintained at both ends of the reaction chamber.

When the reaction rate measurements were completed, the specimens were cooled slowly in high vacuum in the oxidation apparatus. As this procedure could cause changes in the appearance of the reacted specimens, specimens for metallographic examinations were also oxidized in another furnace system and quenched from the reaction temperature by dropping them onto niobium metal ships in quartz tube beneath the furnace. The quartz tube, which was also part of the high vacuum system, was precooled in liquid nitrogen.

The x-ray diffraction studies were made with a GE-XRD-3 recording x-ray diffractometer. The metallographic studies were performed with a Reichert universal camera microscope (Model MeF).

Experimental Results

Reaction rate measurements.—Rates of oxidation of niobium were measured at temperatures from 1000° to 1700°C at oxygen pressures ranging from 2 x 10^{-4} to 0.5 Torr O_2. The initial studies were made on specimens measuring approximately 11 x 11 x 1.9 mm (total surface area of about 3.3 cm^2), but as will be discussed below, it was also later necessary to study oxidation rates as a function of sample size.

Results of the thermogravimetric studies on 3.3 cm^2 specimens are presented in Fig. 2-5, in which the weight change (in mg/cm^2) is plotted as a function of time (in minutes). The weight change was evaluated using the original geometrical dimensions of the specimens. No attempts were made to study reaction rates at oxygen pressures lower than 2 x 10^{-4} Torr O_2 due to possible effects of degassing of walls, etc., on the oxidation. No measurable weight changes were observed during heating of the specimens provided the pressure in the system was $<10^{-5}$ Torr. If the pressure rose to 10^{-4} Torr during the heating period, small weight gains could result prior to the run, but such contamination (<0.02 mg) were not found to affect the subsequent oxidation within the reproducibility, which could be estimated to be within 15%.

Figures 2 and 3 show the effect of oxygen pressure on the rate of oxidation at 1400° and 1600°C, respectively. In Fig. 4 and 5 is shown the effect of tempera-

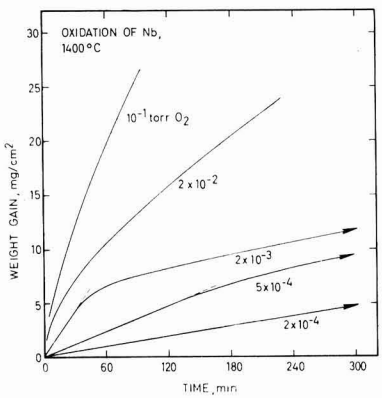

Fig. 2. Effect of oxygen pressure on oxidation of niobium at 1400°C

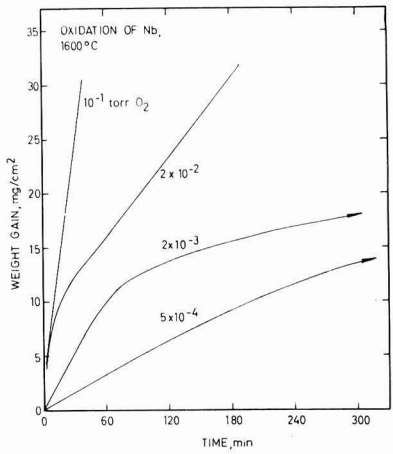

Fig. 3. Effect of oxygen pressure on oxidation of niobium at 1600°C

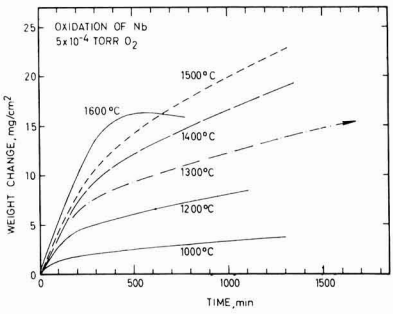

Fig. 4. Effect of temperature on oxidation of niobium at an oxygen pressure of 5 x 10^{-4} Torr.

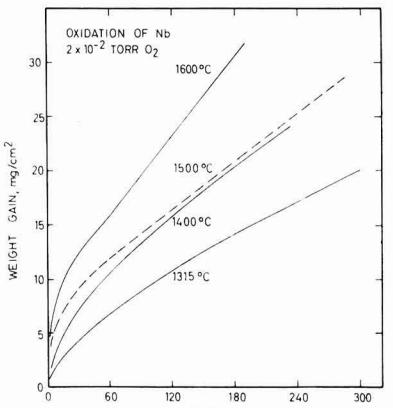

Fig. 5. Effect of temperature on oxidation of niobium at an oxygen pressure of 2 x 10^{-2} Torr.

ture on the rate of oxidation at oxygen pressures of 5×10^{-4} and 2×10^{-2} Torr.

The reaction rate measurements show that the oxidation may be divided into three main stages: (i) an initial linear rate of oxidation which is followed by (ii) a parabolic stage (<1500°C), which in turn after longer periods of oxidation transforms into (iii) a final linear rate of oxidation. The rate of oxidation during all three stages exhibits a large oxygen pressure dependence. The duration of the two first stages is a function of oxygen pressure and becomes shorter the higher the oxygen pressure. At 2×10^{-2} Torr O_2 the duration of the initial linear stage is a few minutes at most.

Between 1400° and 1500°C a change in the temperature dependence of the oxidation during the final linear oxidation is observed (Fig. 5). This change is concluded to be associated with the transition from solid to liquid Nb_2O_5. The melting point of Nb_2O_5 is about 1490°C (7, 8).

Above 1500°C oxide evaporation also becomes an important part-process as evidenced by the weight loss observed during later stages of oxidation at and above 1600°C (Fig. 4). Rates of oxide evaporation into vacuum ($\sim 2 \times 10^{-5}$ Torr) from oxidized specimens were measured at 1550°, 1600°, and 1650°C.

Studies on oxidized specimens.—When oxidation was stopped during the initial linear stage, no visible changes of the specimen could be observed, and no oxide phase could be identified either by x-ray diffraction or metallographic studies. However, x-ray diffraction studies showed that the lattice parameter of the niobium metal had increased during oxidation. From this it is concluded that oxygen dissolves in the metal during the linear stage (9, 13).

X-ray diffraction studies on the surface of specimens oxidized into the parabolic stage only gave reflections due to NbO_2. At 1700°C an additional, unidentified reflection with $d = 2.21$Å was observed. The color of the surface oxide was black, and the oxide adhered extremely well to the substrate. Metallographic cross sections closely resembled those previously published by Inouye (1). The scales were often broken up, but this is concluded to be a result of the cooling of the specimens and the resultant stresses which are built up due to the difference in thermal expansion of the oxide and the substrate. It was also difficult to preserve the scales during polishing.

NbO was present beneath the NbO_2 scales, and the metallographic cross section shows that it is preferentially formed at grain boundaries and that it grows as irregularly shaped crystals in the niobium metal. Examples of cross sections of niobium specimens oxidized at 1500° and 1600°C are shown in Fig. 6a and b. The amount of the NbO phase present in a specimen appeared to be larger the higher the temperature.

The final linear stage of the oxidation was found to be associated with formation of Nb_2O_5 on the NbO_2 scale. After cooling to room temperature, the pentoxide was identified as the high-temperature modification, α-Nb_2O_5. The oxide was in the form of a porous and voluminous scale which easily detached at room temperature. The color was gray.

When liquid Nb_2O_5 was formed, sudden weight losses were observed during the thermogravimetric measurements, and this was probably due to a dripping off of the liquid oxide. After oxidation most of the pentoxide was also found, in one case in the form of a drop, at the lower end of the specimen.

Discussion

The oxidation behavior of niobium at 1200°-1700°C exhibits the same general features as described by Inouye (1) for the temperature range 850°-1200°C. The oxidation involves three main stages: (i) an initial linear oxidation, (ii) a subsequent parabolic stage, and (iii) a final linear oxidation. Above the melting point of Nb_2O_5 the oxidation is affected by the presence of the liquid oxide phase, and above 1500°C evaporation of

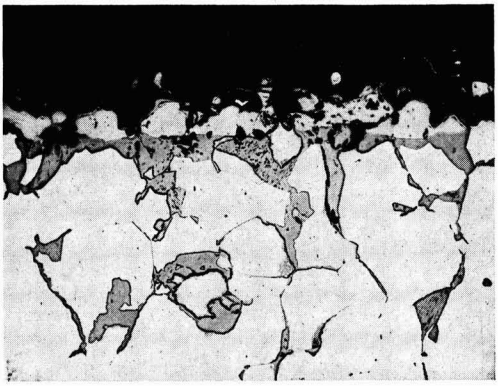

Fig. 6. Metallographic cross section of specimen oxidized for 4100 min at 1500°C and 2×10^{-4} Torr O_2. The gray oxide is NbO. Magnification 80X.

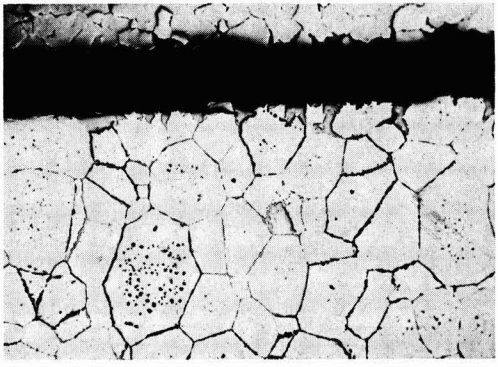

Fig. 6b. Metallographic cross section of specimen oxidized for 60 min at 1600°C and 5×10^{-3} Torr O_2. Magnification 80X.

Nb_2O_5 also becomes important during the later stages of the reaction. In the following the various stages and the associated mechanisms and rate-determining processes will be discussed.

The Initial Linear Oxidation

Oxygen dissolution.—During the initial linear oxidation oxygen dissolves in the metal. During later stages and during the transition to the subsequent parabolic oxidation it is concluded that oxidation also comprises formation of NbO at the metal surface.

The initial linear oxidation shows a large oxygen pressure dependence, and the shorter duration of this stage with increasing oxygen pressure partly reflects that the niobium becomes more rapidly saturated with oxygen. However, at higher oxygen pressures a competing oxide formation on the surface also tends to shorten the linear stage, and above about 10^{-2} Torr O_2 the initial linear oxidation becomes too short to be evaluated accurately from the thermogravimetric studies. Under these conditions a simultaneous oxygen dissolution and oxide formation take place.

At sufficiently low oxygen pressures the duration of the initial linear stage will be determined by the solubility of oxygen in niobium, and thus on the size and thickness of the specimens. In this respect a knowledge of the solubility of oxygen in niobium is important.

The solubility of oxygen in niobium in equilibrium with NbO has been studied by Seybolt (9), Elliot (10), Pemsler (11), Bryant (12), and Gebhardt and Rothenbacher (13). A summary of their results is shown in Fig. 7. Both the heat of solution and the solubilities at 1000° and 1100°C reported by Seybolt may be too high, as an extrapolation leads to unreasonably high solu-

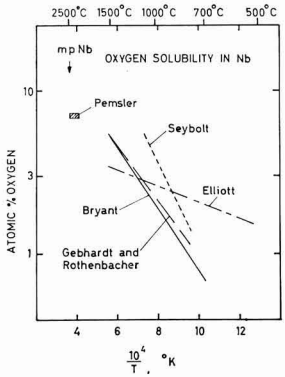

Fig. 7. Solid solubility of oxygen in niobium in equilibrium with NbO as a function of the reciprocal absolute temperature.

bilities at temperatures close to the melting point of niobium. At low temperatures one may fail to reach equilibrium between NbO and the niobium-oxygen solid solution due to slow kinetics. Below 700°C the formation of suboxides of niobium (18-20), which are probably metastable, may also yield too high apparent solubilities. Pemsler reports a solubility of about 7 at. % in the temperature range 2170°-2470°C. There is good agreement between the results of Bryant and of Gebhardt and Rothenbacher, and it is believed that these results represent the better values for the oxygen solubility in niobium.

Using Bryant's values the maximum weight gain due to oxygen dissolution for specimens measuring 11 x 11 x 1.9 mm amounts to about 3.8 mg/cm² at 1300°C, 5.15 mg/cm² at 1500°C, and 6.45 at 1700°C. At the lower oxygen pressures employed in this work (2×10^{-4} and 5×10^{-4} Torr O_2), the initial linear rate persists until the specimens become close to saturated before appreciable oxide formation begins to take place.

Temperature and oxygen pressure dependence.—Figure 8 shows the initial linear rate of oxidation as a function of oxygen pressure. Both the results of this work and those of Inouye are included. The results suggest that the initial linear rate is proportional to the oxygen pressure at low oxygen pressures and that a transition to a gradually smaller pressure dependence occurs with decreasing pressure.

In considering the initial oxidation it is found, as described below, that a large fraction of the impinging oxygen molecules reacts with the metal. Under such conditions the danger exists that the measured rate of reaction may be partially or completely governed by the rate of transport of oxygen through the reaction tube to the specimen. This will be a function of the dimensions of the tube, the reaction rate, and the total

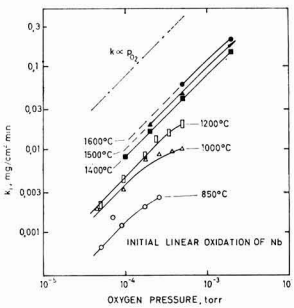

Fig. 8. The rate constant for the observed initial linear oxidation, k_i, as a function of oxygen pressure. The open points show Inouye's results (1) while the filled points represent this work.

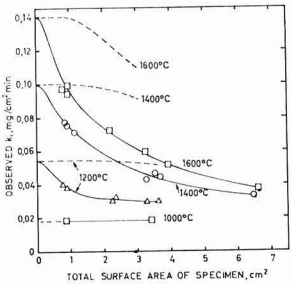

Fig. 9. Observed initial linear rate of oxidation as a function of total surface area of specimen.

surface area of the specimens. In order to test and thus possibly correct for such an effect, the rate of oxidation was measured as a function of specimen size. The results of such measurements are illustrated in Fig. 9, which shows the initial linear rate as a function of the total surface area of the specimen. As seen the observed reaction rate above 1200°C was found to increase markedly with decreasing surface area, thus indicating that the oxidation was in fact partially governed by transport of oxygen in the reaction chamber.

At sufficiently small rates of total oxygen consumption of the specimens the rate should be independent of specimen surface area, and thus an extrapolation of the curves in Fig. 9 to zero surface area should give the rate of reaction of the metal. From the results in Fig. 9 it is seen that an exact extrapolation is difficult to make at the higher temperatures. In the present case the reaction rates at zero surface area was estimated by comparing with rates measured in another apparatus for which a rate-limiting transport of oxygen was not equally critical. The latter values are indicated by the broken lines. Below 1200°C, at which transport limiting effects are not important, both apparatus gave the same rates of oxidation. It may also be noted that during subsequent parabolic oxidation below 1500°C and during the final linear oxidation the reaction rates become slow enough that transport-limiting factors are of no importance.

Although the observed reaction rates above 1200°C are partly limited by transport of oxygen in the reaction chamber, it may still be concluded that the reaction is proportional to the oxygen pressure as the results in Fig. 8 represent relative values at the same surface area. The same pressure dependence is also suggested by Inouye's results below about 2×10^{-4} Torr O_2. This pressure dependence suggests that adsorption of oxygen on the surface is an important rate-limiting factor.

In considering adsorption on metals we shall follow Ehrlich's (14) treatment and assume that oxygen molecules first become physically adsorbed on the surface and that subsequent chemisorption occurs on specific surface sites from the reservoir of physically adsorbed molecules. Accordingly the adsorption is written as

$$O_{2(g)} \underset{k_{-1}}{\overset{k_1}{\rightleftharpoons}} O_2 \text{ phys. ads.} \qquad \text{phys. ads.} \quad [1]$$

$$2 \text{ sites} + O_2 \text{ phys} \xrightarrow{k_2} O_{\text{chem}} + O_{\text{chem}} \quad \text{chemisorption} \quad [2]$$

If adsorption of oxygen limits the rate of oxidation, the subsequent steps in the reaction, which may involve incorporation of the chemisorbed oxygen atoms and subsequent diffusion into the metal, are relatively rapid processes, and the oxidation mechanism is described by Eq. [1] and [2].

$k_1 p_{O_2}$ denotes the rate of adsorption of physically adsorbed molecules. When assuming a condensation coefficient of unity (15), $k_1 p_{O_2}$ is equal to the rate of

impingement of oxygen molecules, which from the kinetic gas theory is given by

$$k_1 p_{O_2} = \frac{p_{O_2}}{(2\pi mkT)^{1/2}} \quad [3]$$

k_{-1} and k_2 represent the rate constant for desorption and chemisorption of physically adsorbed molecules. The temperature dependence of k_{-1} and k_2 may be given the general formula

$$k_n = \alpha_n \exp(-E_n/RT) \quad [4]$$

where E_n is the activation energy and α_n accounts for the frequency and probability factors associated with the process.

The above model neglects effects due to interactions of physically adsorbed molecules and desorption of chemisorbed oxygen molecules.

During linear oxidation one may further assume that the concentration of the intermediate species, *i.e*, the physically adsorbed molecules, does not change with time and that the condition of stationary states may be applied. This leads to the following expression for the initial linear rate of oxidation, k_l

$$k_l = k_1 p_{O_2} \frac{k_2(1-\theta)^2}{k_{-1} + k_2(1-\theta)^2} \quad [5]$$

where θ represents the fraction of chemisorption sites occupied by chemisorbed oxygen.

From Eq. [5] it is seen that $k_l \propto p_{O_2}$ at sufficiently low oxygen pressures, *i.e.*, when $1-\theta \cong 1$, while a transition to a gradually smaller oxygen pressure dependence will be observed with increasing oxygen pressure, *i.e.*, when θ can no longer be neglected. As seen in Fig. 8 this is in agreement with Inouye's results. It should furthermore be noted that the deviation from $k_l \propto p_{O_2}$ probably occurs at lower oxygen pressures the lower the temperature.

When $k_l \propto p_{O_2}$ the temperature dependence is given by

$$k_l = \frac{p_{O_2}}{(2\pi mkT)^{1/2}} \cdot \frac{\alpha_2 \exp(-E_2/RT)}{\alpha_2 \exp(-E_2/RT) + \alpha_{-1}\exp(-E_{-1}/RT)} \quad [6]$$

and accordingly an Arrhenius plot of k_l should not give a straight line relationship. This is also suggested by the experimental results as shown in Fig. 10, where the logarithm of k_l has been plotted as a function of the reciprocal absolute temperature under conditions where $k_l \propto p_{O_2}$, *e.g.*, at 10^{-4} Torr O_2. The values of k_l represent extrapolated values at zero surface area

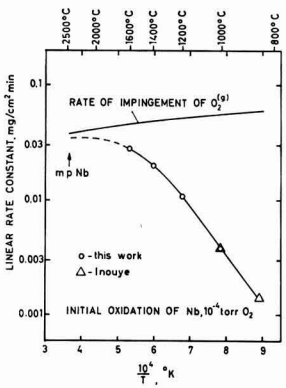

Fig. 10. Logarithm of k_l (extrapolated values at zero surface area of specimen) as a function of the reciprocal absolute temperature.

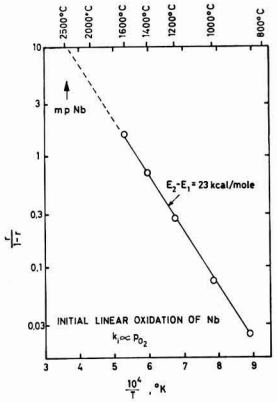

Fig. 11. Logarithm of the quantity $r/1-r$ as a function of the reciprocal absolute temperature; r is the reaction coefficient.

(Fig. 9), and the values have furthermore been extrapolated from 5 x 10^{-4} to 10^{-4} Torr O_2 in order to allow a comparison with Inouye's results under conditions where $k_l \propto p_{O_2}$. Equation [6] does, of course, also apply at other oxygen pressures as long as $k_l \propto p_{O_2}$. The calculated weight gain if all oxygen molecules which impinge at 10^{-4} Torr O_2 were to react with the metal is also shown in Fig. 10.

In order to confirm the above mechanism (Eq. [1] and [2]) one may introduce the term reaction coefficient, $r = k_l/k_1 p_{O_2}$, which denotes the fraction of the impinging molecules that react with the metal. The term $r/1-r$ is given by

$$\frac{r}{1-r} = \frac{k_2}{k_{-1}} = \frac{\alpha_2}{\alpha_{-1}} \exp\{-(E_2 - E_{-1})/RT\} \quad [7]$$

and a plot of log $r/1-r$ as a function of $1/T$ should thus give a straight line relationship where the slope is determined by the difference in activation energies between that of chemisorption and that of desorption of physically adsorbed molecules. Figure 11 shows that the initial linear oxidation of niobium obeys Eq. [7] under conditions when $k_l \propto p_{O_2}$ and that $E_2 - E_{-1} = 23$ kcal/mole.

It may be noted that the value of r increases from 0.024 to 0.61 from 850° to 1600°C, and at the latter temperature about 60% of the impinging oxygen molecules react with the metal. Tantalum exhibits a closely similar oxidation behavior under corresponding conditions (15), but for this metal the reaction coefficient r is about half of that for niobium. Both metals have therefore excellent gettering properties at high temperatures.

In Fig. 11 the value of $r/1-r$ has been extrapolated to the melting point of niobium. Corresponding values of k_l have been evaluated and these are indicated by the broken part of the curve in Fig. 10, and these thus represent estimated values if the mechanism is valid up to the melting point. It may be possible, however, that a direct desorption of chemisorbed oxygen to the gas phase becomes significant at temperatures near the melting point of niobium, and this could cause a larger decrease in the "apparent" activation energy k_l with increasing temperature than indicated by the extrapolated values in Fig. 10. Depending on the associated activation energies an appreciable desorption of molecules could even cause a reversal in temperature dependence. Niobium metal may also be deoxidized by high-vacuum treatment at very high temperatures, probably through the evaporation of niobium oxides, and such effects would further be expected to influence the oxidation behavior of niobium. At low partial pressures of oxygen near the melting point of niobium the oxygen solubility will also be a function of the

oxygen pressure (11) and the duration of linear stage will be correspondingly limited.

Parabolic Oxidation

During the transition from the initial linear to the parabolic oxidation, it is concluded that the oxidation *mainly results in formation of NbO.* This does not occur as a plane-parallel film or scale on the metal, but as a growth of NbO crystals into the metal from the surface. The NbO crystals are irregularly shaped and often show large variations in size. It is reasonable to conclude that the growth of NbO depends on the orientation of the individual grains in the metal. The growth and penetration of NbO into the metal is also favored at grain boundaries. Qualitatively it appears that NbO formation is governed by the crystal growth in the solid phase, but from this work it is not possible to evaluate specific details of this process or its temperature dependence. Qualitatively it may, however, be concluded that the amount of NbO becomes relatively larger the higher the temperature.

The parabolic oxidation itself is concluded to be associated with NbO_2 formation. Metallographic examinations after cooling to room temperature show in places a broken-up scale, but this is probably a result of cooling as in the places where the NbO_2 scale is intact, it exhibits excellent adherence to the substrate. NbO_2 probably forms a compact, protective scale during the oxidation, as is also previously found by Inouye (1), and the parabolic rate is concluded to reflect a Wagner-type mechanism with a rate-determining diffusion through NbO_2.

For a further evaluation of the diffusion process associated with the parabolic oxidation the oxygen-pressure dependence of the parabolic rate constant, k_p, has been evaluated, and the results are shown in Fig. 12. *In estimating the rate constant it was assumed that* the amount of NbO in the metal beneath the scale remained unchanged during the oxidation. Below 1500°C $k_p \propto p^{1/2}{}_{O_2}$, while at 1500°C the results indicate a smaller and also a varying oxygen pressure dependence. At 1600° and 1700°C the reaction rate measurements did not permit an evaluation of the parabolic rate constant. This may possibly be due to an increased importance of NbO formation, to the presence of liquid Nb_2O_5, or to effects of oxide evaporation (see below).

Judging from the growth of the oxide scale on niobium, a rate-determining transport of oxygen in NbO_2 appears probable. If the Wagner mechanism applies, an oxygen pressure dependence of $k_p \propto p^{1/2}{}_{O_2}$ is unusually large. It also rules out a defect structure involving oxygen vacancies. However, a possible explanation could be that the defects in NbO_2 involve interstitial oxygen according to the relationship

$$1/2\ O_2(g) \rightleftharpoons O_i^{z-} + ze^+ \qquad [8]$$

and that diffusion of oxygen takes place through an interstitially mechanism. A pressure dependence of $p^{1/2}{}_{O_2}$ could in principle be obtained either if the electron holes, e^+, are associated with the interstitial oxygen ion or if intrinsic ionization of electrons from the conduction to the valence band ($\text{nil} \overset{K_e}{\rightleftharpoons} e^+ + e^-$) yields an electron hole concentration which is very much larger than that produced from Eq. [8], *i.e.*, if $\{e^+\} = K_e^{1/2} >> O_i^{z-}$.

According to Eq. [8] NbO_2 is proposed to contain excess oxygen relative to the stoichiometric oxide. NbO_2 has possibly a small homogeneity range (17), but otherwise little is known about its defect structure. The above considerations (Eq. [8]) are therefore at this stage purely speculative and are put forth solely to explain the oxygen pressure dependence of the parabolic oxidation.

In the temperature range 1200°-1400°C the parabolic oxidation has an activation energy of $E = 44$ kcal/mole. In view of the lack of knowledge of the defect structure of NbO_2 a detailed interpretation of this value is not possible.

NbO_2 is further oxidized to Nb_2O_5, and the growth of the latter oxide is, at least during the later stages of the reaction, linear with time. During the parabolic growth of NbO_2 traces of Nb_2O_5 may be present on the surface although it is not detected in the x-ray diffraction studies. The fact that the parabolic oxidation does exhibit an oxygen pressure dependence shows that Nb_2O_5 has no protective properties. This is also suggested by the appearance and by the metallographic cross sections of oxidized specimens which show porous scales of Nb_2O_5. The growth of NbO_2 + solid Nb_2O_5 thus probably involves a Loriers-type mechanism (17).

Final Linear Oxidation

Growth of solid Nb_2O_5.—As mentioned above the solid Nb_2O_5 has no protective properties and forms a voluminous and porous scale. When this stage is reached during the oxidation, the thickness of the NbO_2 *scale will, according to a* Loriers-type mechanism, approach a limiting thickness, and the final linear rate essentially represent formation of Nb_2O_5.

The rate of formation of Nb_2O_5, k_f, also shows a large oxygen pressure dependence. This is shown in Fig. 13 where log k_f is plotted as a function of log p_{O_2}. Results from ref. (4) are also included, and these are represented by the open points. At 1000°C k_f is proportional to $p^{1/2}{}_{O_2}$ over the whole oxygen pressure range studied. The same applies to the higher oxygen pressure at 1200° and 1300°C.

An oxygen pressure dependence of $k_f \propto p^{1/2}{}_{O_2}$ suggests that a dissociative adsorption equilibrium is established on the surface (14, 15). Following Eq. [1] and [2] the reaction may in this case be written

$$O_2 \overset{K_1}{\rightleftharpoons} O_2 \text{ phys. ads.}$$

$$2 \text{ sites} + O_2 \text{ phys. ads.} \overset{K_2}{\rightleftharpoons} O_{\text{chem}} + O_{\text{chem}} \qquad [9]$$

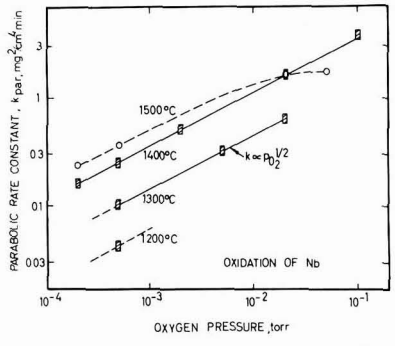

Fig. 12. Parabolic rate constant for formation of NbO_2 as a function of oxygen pressure.

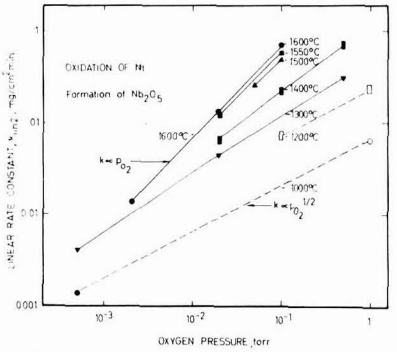

Fig. 13. Rate constant for the final linear oxidation, k_f, as a function of oxygen pressure.

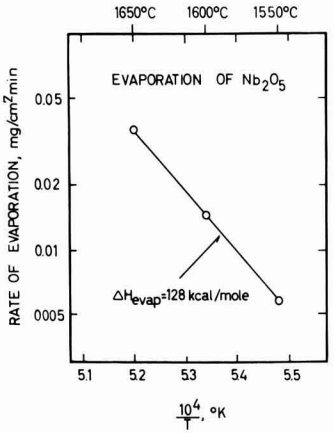

Fig. 14. Logarithm of the rate of evaporation from liquid Nb_2O_5 on oxidized Nb specimens as a function of the reciprocal absolute temperature.

$$O_{chem} \xrightarrow{k_3} \text{products} \qquad [10]$$

where $K_1 = \frac{k_1}{k_1}$ and K_2 represent the equilibrium constants. The rate of oxidation is accordingly given by

$$k_f = k_3 [O_{chem}] = k_3 K^{1/2}{}_{12} (1-\theta) p^{1/2}{}_{O_2} \qquad [11]$$

where $K_{12} = K_1 K_2$. At low coverage, *i.e.*, when $1-\theta \cong 1$, the rate of oxidation will be proportional to $p^{1/2}{}_{O_2}$ as observed for k_f. It should also be noted that at sufficiently high oxygen pressures, the rate of oxidation will as a limit become independent of oxygen pressure.

At very low oxygen pressures the assumption of chemisorption equilibrium will no longer be valid, and at sufficiently low oxygen pressures the rate of adsorption will become rate-determining. As a limit the rate of oxidation will become proportional to p_{O_2} as described above for the initial oxidation. The change to a somewhat larger oxygen pressure dependence at the lower pressures at 1300° and at 1400°C is believed to reflect such a transition in the rate-determining process.

When $k_f \propto p^{1/2}{}_{O_2}$ the activation energy amounts to about 24 kcal/mole. In this connection it should be noted that the value of k_3 increases while that of K_{12} decreases with increasing temperature, and the activation energy associated with k_f (when proportional to $p^{1/2}{}_{O_2}$) represents the difference between the activation energy associated with k_3 and the "enthalpy of chemisorption" associated with K_{12} (Eq. [11]).

Formation of liquid Nb_2O_5.—The rate of formation liquid Nb_2O_5 shows a different dependence on oxygen pressure and temperature than that of the growth of solid Nb_2O_5. As seen in Fig. 13 $k_f \propto p_{O_2}$ for the formation of $Nb_2O_{5\,liq}$. At low oxygen pressures this difference in pressure dependence leads to a smaller rate of formation of Nb_2O_5 when it is in liquid form (*e.g.*, 1600°C) than when it is solid (*e.g.*, 1300°C).

From the relationship $k_f \propto p_{O_2}$ it is concluded that the rate of chemisorption is the rate-determining process. When liquid Nb_2O_5 is formed, the whole specimen surface is probably always covered by a continuous layer of liquid oxide. When relatively large amounts are formed the oxide also drips off the specimen. The rate-determining chemisorption takes place on the liquid oxide surface, and the oxygen rapidly diffuses through the liquid phase to the solid oxide phase where it reacts to form Nb_2O_5.

The apparent activation energy for the formation of $Nb_2O_{5\,liq}$ as determined from the results at 1500°, 1550°, 1600°C amounts to 16 kcal/mole. Following the treatment for the initial linear oxidation this value approximately corresponds to the difference in activation for the chemisorption and the desorption of the molecules physically adsorbed on liquid Nb_2O_5.

Oxide evaporation.—Above 1550°C an appreciable evaporation of Nb_2O_5 takes place, and at 1600°C, for instance, a resultant weight loss of the specimen occurs during later stages of the oxidation at the lower oxygen pressure (Fig. 4).

The rates of evaporation in vacuum ($\sim 2 \times 10^{-5}$ Torr) was measured at 1550°, 1600°, and 1650°C and the results are presented in Fig. 14. The evaporation rates per unit surface area were evaluated using the original geometrical dimensions of the unoxidized specimens. Corrections due to the increase in surface area resulting from oxide formation would be small.

The enthalpy of evaporation is 128 kcal/mole. As this value is much larger than the activation energy for the formation of liquid Nb_2O_5 (~ 16 kcal/mole), the oxide evaporation will become increasingly important the higher the temperature. The rate of oxide evaporation may be considered to be approximately independent of oxygen pressure at oxygen pressures employed in this work, while the rate of formation is proportional to p_{O_2}. The amount of liquid Nb_2O_5 on the surface or whether it evaporates as soon as it is formed, will consequently at a specific temperature be determined by the oxygen pressure.

The rate of evaporation from a free surface into a vacuum is related to the pressure of the evaporation species by the Hertz-Langmuir equation

$$z_i = \alpha_i p_i / (2\pi m_i kT)^{1/2} \qquad [12]$$

z_i is the number of molecules evaporating per unit time per unit area, m_i is the molecular weight of the gas molecule, p_i is the equilibrium pressure, and α_i is the evaporation coefficient. When the molecule in the condensed phase is the same as the vapor species, the value of α_i has been found to be close to unity. In this work the liquid Nb_2O_5 may be expected to be deficient in oxygen relative to stoichiometric composition, but the exact composition is not known.

No mass-spectrometric analysis has been made of the evaporating species, but, assuming an evaporation coefficient equal to unity and that the molecules are Nb_2O_5, the observed evaporation rates give (Eq. [12]) the following values for the equilibrium pressure of Nb_2O_5: 4.3×10^{-6} Torr at 1550°C, 9.5×10^{-6} Torr at 1600°C, and 2.8×10^{-5} Torr at 1650°C.

Acknowledgment

This work has in part been sponsored by the Air Force Materials Laboratory, Research and Technology Division, AFSC, through the European Office of Aerospace Research, United States Air Force.

The authors are indebted to the members of the staff at the Central Institute for Industrial Research who have participated in the experimental work.

Manuscript received Feb. 14, 1964; revised manuscript received Sept. 8, 1964.

Any discussion of this paper will appear in a Discussion Section to be published in the December 1965 JOURNAL.

REFERENCES

1. H. Inouye, "The Oxidation of Columbium at Low Oxygen Pressures," in "Columbium Metallurgy," AIME Metallurgical Society Conferences, Vol. 10, D. L. Douglass and F. W. Kunz, Editors, Interscience Publishers, New York (1961).
2. H. Inouye, "Scaling of Columbium in Air," Reactive Metals Proceedings, (MD) Special Report Series No. 5, Met. Soc., AIME (1956).
3. W. D. Klopp, C. T. Sims, and R. I. Jaffee, Battelle Memorial Institute, BMI-1170, 1957.

4. P. Kofstad and H. Kjøllesdal, *Trans. AIME.*, **221**, 285 (1961).
5. V. I. Arkhorov, A. F. Gerasimov, and T. V. Ushkova, *Fiz. metal. metalloved.*, **12**, 761 (1961).
6. T. Kolski, *Trans. Quart.*, **55**, 119 (1962).
7. A. J. Pollard, *J. Am. Ceram. Soc.*, **44**, 630 (1961).
8. J. J. Diamond and S. J. Scheider, *ibid.*, **43**, 1 (1960).
9. A. U. Seybolt, *J. Metals*, **6**, 774 (1954).
10. R. P. Elliott, *Trans. AIME.*, **200**, 990 (1954).
11. J. P. Pemsler, *This Journal*, **108**, 744 (1961).
12. R. T. Bryant, *J. Less-Common Metals*, **4**, 62 (1962).
13. E. Gebhardt and R. Rothenbocher, *Z. Metallkunde*, **54**, 623 (1963).
14. G. Ehrlich, *J. Phys. Chem.*, **59**, 473 (1955).
15. P. Kofstad, *J. Less-Common Metals*, **7**, 241 (1964).
16. G. Brauer, *Z. anorg. u allgem. Chem.*, **248** (1941); *Naturwiss.*, **28**, 30 (1940).
17. J. Loriers, *Compt. rend.*, **229**, 547 (1949).
18. N. Norman, *J. Less-Common Metals*, **4**, 52 (1962).
19. N. Norman, P. Kofstad, and O. J. Krudtaa, *ibid.*, **4**, 124 (1962).
20. G. Brauer, H. Müller, and G. Kühner, *ibid.*, **4**, 533 (1962).

Electrical Behavior of Passive Iron

J. L. Ord[1] and J. H. Bartlett

Department of Physics, University of Illinois, Urbana, Illinois

ABSTRACT

From a study of the steady-state and of galvanostatic transients, it is concluded, in agreement with Vetter and Weil, (i) that there exists a layer on iron when it is passive, (ii) that an electric field drives ions through this layer, and (iii) that the resistance to the flow of these ions is nonohmic. In the steady state, the thickness of this layer varies linearly with passivating potential from about 8Å to about 68Å. Transition from the steady passive state to the active state can occur slowly (probably by uniform thinning) for anodic current constant and less than the steady-state value, or rapidly (probably without thinning) for cathodic currents. The results indicate that, when the system is in a nonsteady state, there is a nonzero charge distribution within the layer. Even if the steady-state current be restored, it may take a long time for this charge distribution to relax back to the neutral steady state.

The nature of passivity, as exemplified by the electrical behavior of a passive iron electrode, has been the subject of much debate. Interest has centered around such questions as: (i) Is there a thin monolayer or a layer of appreciable thickness on the surface? (ii) What are the mechanisms for formation and removal of such layers? (iii) What is responsible for the large (600 mv) overpotential necessary to maintain iron in the passive state?

Previous studies of the electrical properties of passive iron have not been very extensive. Some work has been done in alkaline solutions, but the most information has been obtained with acid solutions. Some early investigations were made using nitric acid (1) but this is a rather complicated system, and later studies (2-4), including those reported here, are all with sulfuric acid. Franck and Weil (2) demonstrated the existence of a nonzero steady current, which is called the corrosion current and which is just sufficient to form new layer at a rate which balances the loss rate due to dissolution by the acid. Vetter (4) recorded galvanostatic transients from the steady state, measuring the rise of potential as a function of net charge added. He suggested the existence of an electrical field across a passive layer of appreciable thickness. His potentiostatic measurements also indicated that current through the layer is an exponential function of this field. Weil (3) repeated these measurements with more refined techniques, and concluded that "it is correct to assume that particle transport through the passive layer occurs by ions moving in an electric field." Vetter later (5) speculated that the layer is a composite oxide, the part nearest the metal being Fe_3O_4 and the outer part being Fe_2O_3.

The present work, using entirely different methods of analysis, confirms the essential ideas of Vetter and of Weil that there is an electric field driving ions through the layer and that the resistance offered to their flow is nonohmic in nature. In addition, it indicates that there is a nonzero charge density within the layer during the course of a galvanostatic charging process. The system is not then in a steady state, and it takes a considerable time, even when the steady-state current has been restored, for the system to relax back to normal. Reliable estimates of the thickness can as yet be made only for the steady state, where the thickness varies linearly with passivating potential from about 8Å to around 68Å.

Activation comes about in two different ways. For large cathodic current, the process is independent of layer thickness, so that activation corresponds to a rapid breakdown of protection at the metal-layer interface. On the other hand, when an anodic current of less than steady-state value flows, activation does depend on the initial thickness, which is taken to mean that the acid must eat away the layer until finally there is a breakthrough with consequent disruption.

Experimental

Transients were recorded by photographing an oscilloscope trace. This technique enables very fast transients to be recorded and is convenient also for transients of several minutes duration. Slow transients were recorded by setting the sweep rate at 5 sec/cm and adjusting the sweep length to 10 cm. The dead time between sweeps is negligible at this setting. An example of a slow transient recorded in this manner is given in Fig. 5.

The circuitry used is shown schematically in Fig. 1. The potentiostat consists of a 10-turn Helipot placed across a bank of 2v batteries. The galvanostat consists of a variable resistor in series with a 180v battery bank. These simple arrangements offer a number of advantages over more sophisticated electronic circuitry. (*A*) The galvanostat and potentiostat can be placed in series, and switching from one to the other can be accomplished by shorting or opening the galvanostat output. (*B*) Complex transients can be applied using a relay bank with calibrated time intervals between the closing of the relays. For example, one can switch in succession from constant potential to one constant current to open circuit to another constant current, with all switching controlled by the relay bank. (*C*) Auxiliary electrodes are not needed in the cell. The galvano-

[1] Present address: Department of Physics, University of Waterloo, Waterloo, Ontario, Canada.

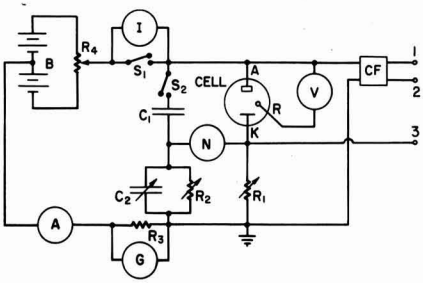

Fig. 1. Circuit diagram: A, anode; K, cathode, R, reference electrode; V, VTVM; CF, cathode follower; N, null detector; G, signal generator; I, constant current source; B, battery bank; A, microammeter.

stat kept the current constant to within 0.5% for all potential transients of interest. When the Helipot was replaced by fixed resistors for potentiostatic transients, the potential stayed constant to within 1 mv for current changes of 100 μa.

The Schering impedance bridge, consisting of R_1, R_2, C_1, and C_2 along with the cell, is shown in Fig. 1 (it does not affect the potentiostatic circuitry). The a-c signal was introduced by connecting a 5-ohm resistor in series with the potentiostat, and connecting a low-frequency oscillator across it. A high-gain null detector allowed the bridge to be operated with 10 mv a-c across the cell.

The measuring and recording circuitry is more critical than the cell supply circuitry. A VTVM with 100 megohm input impedance and a 20 μa panel meter can be used for most simple measurements. For more critical measurements a Keithley d.c. VTVM Model 200B (input impedance greater than 10^{14} ohms) was used to measure potential, and a Keithley Micro-microammeter Model 414 to measure current. A low-noise cathode follower with bandwidth greater than 100 kc is needed to operate the oscilloscope, especially for open-circuit transients. Either a conventional triode (6F5, grid current 6 x 10^{-9} amp) or a triode-connected electrometer tube (CK 5886, grid current less than 10^{-14} amp) can be used in a battery-operated cathode-follower circuit to achieve this performance.

The electrolyte used for all experiments except those studying the effect of pH was 2*N* H_2SO_4. The behavior of a passive iron electrode in this electrolyte does not appear sensitive to dissolved gases; oxygen-saturated, nitrogen-saturated, and hydrogen-saturated electrolytes yield identical results. Since a platinized-platinum electrode was made the cathode, hydrogen-saturated electrolyte was usually used to stabilize the potential of the cathode. Measurements were normally made at room temperature (22°C). A mercurous sulfate (0.1*N* $K_2SO_4/Hg_2SO_4/Hg$) electrode was used as reference. All potentials are given with respect to this reference. At room temperature in 2*N* H_2SO_4 this electrode has a potential of approximately 0.725v with respect to a reversible hydrogen electrode.

The anodes were prepared from a polycrystalline iron rod of 99.99% purity. An anode consisted of a ½ in. segment of this rod machined to a cross-sectional area of 0.2 cm² and mounted on a copper rod covered by glass tubing. The iron was first coated with a compound such as WD-4 shellac or Cenco Sealstix. After the coating had been removed from the end, the rod was mechanically polished. The anode surface was mounted so as to be vertical in the cell. It is usually desirable to work with a mildly etched surface whose roughness factor does not change rapidly. With the anode geometry described above (even after deep etching) a nominally plane surface of 0.2 cm² area can be restored by mechanical polishing. To enable data obtained using anodes of different roughness factors to be compared, the assumption has been made here that at

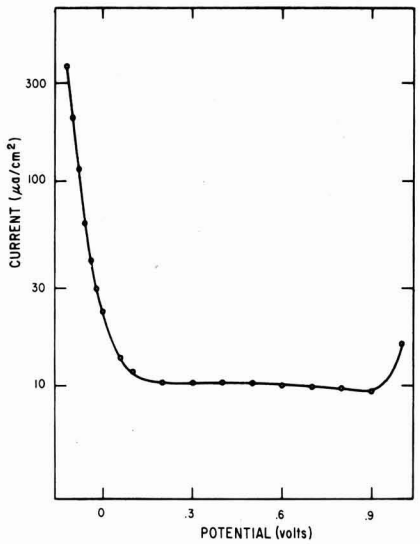

Fig. 2. Steady-state current *vs.* potential

room temperature (22°C) in 2*N* H_2SO_4 the current density at potentials in the middle of the passive region is 10 μa/cm². An electrode which exhibits this current density probably has a roughness factor near 1.5. (No measurement of the roughness factor was made.)

Results

Potentiostatic measurements.—If an iron electrode is placed in solution and a constant potential is applied, the current is found to reach a steady state after a certain interval, and the dependence of steady-state current on potential is represented by a so-called current *vs.* potential curve. The shape of this curve in the active region was given by Bartlett and Stephenson (6), and in the passive region by Franck and Weil (2). In the present measurements, where the electrode was passivated at constant potential, the current reached the steady state within 30 min and then stayed constant for at least 10 hr. Figure 2 shows the steady-state current density as a function of potential for the passive region. (The active-state corrosion potential is located at −1.03v on the potential scale, *vs.* mercurous sulfate, used in Fig. 2.) Franck and Weil (2) have reported longer times to reach the steady state, but they passivated at constant current and reached oxygen evolution, where there is presumably a fairly thick oxide layer, before switching to constant potential. (The longer times would be expected because of the fact that the oxide layer must become thinner to correspond to a steady state of a lower potential, and both thinning and readjustment take place slowly.)

As is seen from Fig. 2, the current density is approximately constant in the passive region between about 0.2v and 0.9v. Above 0.9v, it rises steeply with increasing potential due to oxygen evolution, and below 0.2v it also rises rapidly with decreasing potential, which represents an increase in rate of dissolution of the electrode.

The steady-state current density depends strongly on temperature and pH. The temperature dependence[2] is consistent with an activation-controlled process with energy of about 17 kcal/mole, as reported by Vetter (4). The pH range from 0 to 3 was studied using mixtures of H_2SO_4 and K_2SO_4, and it was found that the logarithm of the current density decreases linearly with increasing pH over this range. The current density changes by a factor of 10 for a pH change of 3.

[2] This measurement has been made for the range of 5°-70°C, at a potential of 0.4v, by D. DeSmet (private communication).

Only a limited amount of information about the electrode can be obtained from potentiostatic transients. When the potential is switched from one constant value to a higher one, the current density has an initial (infinite) discontinuous rise, because of the relation $i = C\ dV/dt$, which is followed by a slower decline to its initial value (7). If one measures the value of the current density just subsequent to the above capacitive transient, the indications are that it depends exponentially, not linearly, on the potential. For a quantitative study of this dependence, it is more convenient to use galvanostatic transients.

Measurements of a-c impedance were made in conjunction with the steady-state potentiostatic measurements. The a-c impedance, corrected for electrolyte resistance, may be expressed in terms of an equivalent parallel resistance, R_p, and capacitance, C_p. Both resistance and capacitance decrease with increasing frequency. The capacitance changes by a factor of 2 and the resistance by a factor of 10^3 over the frequency range from 1 to 10^4 cps. The resistance and capacitance are plotted against steady-state potential in Fig. 3 and Fig. 4 for a frequency of 100 cps.

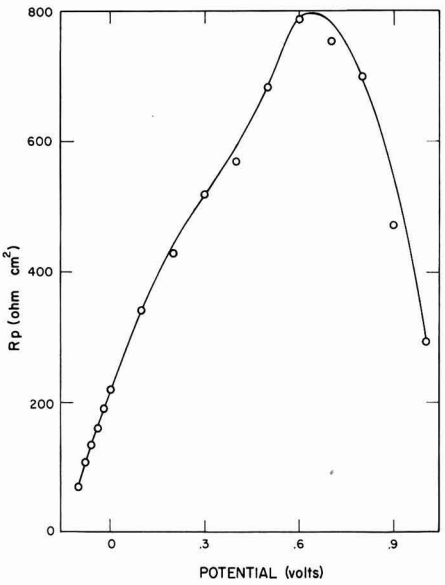

Fig. 3. Parallel resistance vs. potential; frequency, 100 cps

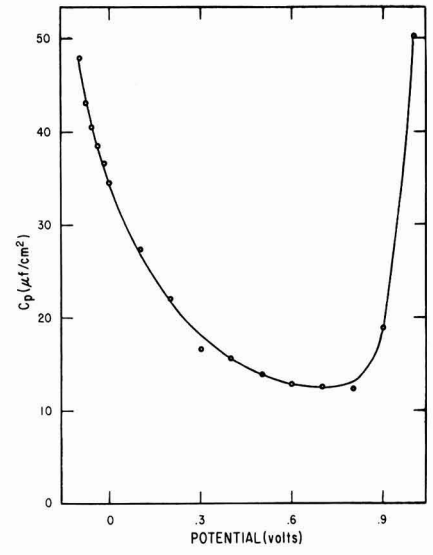

Fig. 4. Parallel capacitance vs. potential; frequency, 100 cps

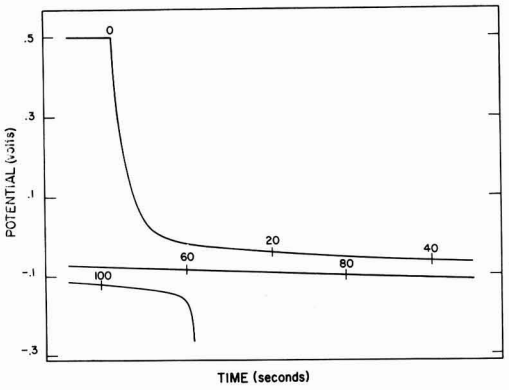

Fig. 5. Open-circuit potential transient. The corrosion potential (—1.03v) is not shown.

Galvanostatic measurements.—Figure 5 shows the potential transient observed when a steady state is interrupted by opening the circuit. This galvanostatic transient can be divided roughly into three parts: an initial capacitive transient, a sloping plateau,[3] and a sharp transition to the corrosion potential (not shown in the figure). Transients starting from different steady-state potentials differ mainly in the height of the capacitive transient.

An examination of the variation with current of the initial slope of a galvanostatic transient shows that the electrode does have a definite capacitance C which is given by the equation

$$i = C\ dV/dt + i_{ss} \qquad [1]$$

where i_{ss} is the steady-state current. The dependence of the reciprocal capacitance on the initial steady-state potential is shown in Fig. 7. Also shown is the reciprocal a-c equivalent capacitance at 100 cps.

In experiments such as the above, the times are so short that the potential V cannot change appreciably. To describe the behavior for longer times, let us assume that the potential is given by

$$i = C\ dv/dt + f(v) \qquad [2]$$

where v is the overpotential measured from a zero to be defined below. Since the observed transient is not a linear function of the time, the quantity $f(v)$ cannot be a constant. Furthermore, although the transient appears roughly exponential, the fit to a single exponential curve is not close, and so we cannot assume $f(v) = v/R$ (equivalent circuit as a resistance in parallel with a capacitance). However, if the parallel leakage current $f(v)$ be assumed to depend exponentially on v (as might be expected if activation processes control), then the transient can be fitted reasonably well. Accordingly, let us assume that

$$f(v) = i_o \exp\ (v/v_o) \qquad [3]$$

where i_o and v_o are constants.

When $i = 0$ (open circuit), the differential equation of the capacitive transient is, from [2] and [3],

$$C\ dv/dt + i_o \exp\ (v/v_o) = 0 \qquad [4]$$

and the solution is

[3] Attempts to define precisely a "Flade potential" at the end of this plateau meet the difficulty that the plateau itself curves downward well before the sudden transition to the active state.

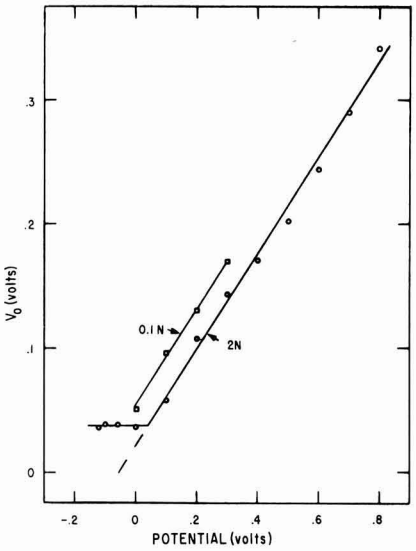

Fig. 6. v_o vs. potential

$$v = v_o \ln(Cv_o/i_o) - v_o \ln(t + Cv_o/i_I) \qquad [5]$$

where i_I is the current prior to opening the circuit. An equation of this form has been derived by Grahame (8), and applied to a study of the anodic oxidation of cadmium (8a). By choosing θ suitably, one can fit the initial two-thirds of the capacitive transient by a straight line

$$v = \text{const} - v_o \ln(t + \theta) \qquad [6]$$

The slope of this straight line is v_o, and it is a well-defined experimental parameter.

Figure 6 shows the values of v_o which are obtained when the circuit is opened from a definite steady-state potential, as a function of that potential. This function is linear in the region where the current density is constant, and is constant (and equal to 37 mv) at lower potentials (below about 0.05v for $2N$ H_2SO_4).

In order to calculate the parameter i_o, it is necessary to determine the zero of overpotential. Since the overpotential under consideration is associated with the capacitive transient, it will be zero when that transient has died out. However, there is another much slower process occurring which causes the plateau to slope. Accordingly, it is natural to suppose that the above overpotential is zero on the plateau extrapolated backwards. When this is done, it turns out that i_o is approximately constant over the potential region where the steady-state current i_{ss} is constant. Because the plateau is not exactly linear, this extrapolation is difficult. However, one can obtain a well-defined zero of overpotential by assuming i_o is constant when i_{ss} is, and extrapolating as in Fig. 6. The zero is located at -0.055v, and $i_o = 0.75$ μa/cm^2 when $i_{ss} = 10$ μa/cm^2, and the acid is $2N$ H_2SO_4.

Since the exponential nature of $f(v)$ has been established, and since the steady-state current density has a temperature dependence indicating the existence of an activation energy, it is now in order to discuss the theoretical equation relating current density to overpotential across an activation barrier. This, according to various authors (9), is of the form

$$i/i_o = \exp(\alpha\lambda\eta/kT) - \exp(-(1-\alpha)\lambda\eta/kT) \qquad [7]$$

where η is the overpotential measured from the reversible potential, α is the fraction of the overpotential which aids the forward current, λ is the valence of the charge carriers, and i_o is the exchange current at zero overpotential. If η is large, the last term may be neglected and this equation has the same form as Eq. [3]. If η is small, however, Eq. [3] and its consequence Eq. [5] are no longer valid, and this may account in part for the fact that the bottom third of the capacitive transient deviates from the curve of Eq. [6].

Assuming temporarily that η is large, let us try to correlate it with the measured overpotential v. If we should equate v to η, then it folows that $v_o = kT/a\lambda$, a constant independent of v. This result is not consistent with Fig. 6, where v_o depends linearly on v, and hence the entire overpotential cannot appear across the activation barrier.

It seems more reasonable to assume (10) that a layer of thickness D is present at the interface and that only a fraction of the overpotential appears across the activation barrier. In this event, we can relate $\alpha\eta$ to the field E by the equation $\alpha\eta = aE$, where a defines a "jump distance" for forward motion of particles across the activation barrier. Then, from Eq. [7] and [3], we have

$$E = (kT/a\lambda)(v/v_o) \qquad [8]$$

for the field across the barrier. If there were no charge within the layer, then (by Gauss' theorem) the field would be constant across the layer, $v = ED$, and the thickness

$$D = (a\lambda/kT)v_o \qquad [9]$$

If we assume that in the steady state the layer is neutral, then its thickness will be proportional to v_o, which can be determined experimentally. Figure 6 then indicates that (i) the layer has a limiting thickness below which it does not decrease and (ii) that the thickness increases linearly with steady-state potential up to about ten times this minimum thickness.

As mentioned above, the steady-state current density depends strongly on pH. Comparison of the two curves in Fig. 6, representing $0.1N$ H_2SO_4 and $2N$ H_2SO_4, respectively, shows that v_o depends only on v and not on pH.

In reaching the steady state, for a given overpotential, the system parameter i_o somehow adjusts itself so that the final value is in accordance with Eq. [3], where the current density i is itself equivalent to the rate at which the acid removes the layer, this rate depending on pH and temperature.

A comparison of Fig. 6 with Fig. 7 shows that the reciprocal capacitance is a linear function of v_o in the steady state. Apparently the capacity is related to the

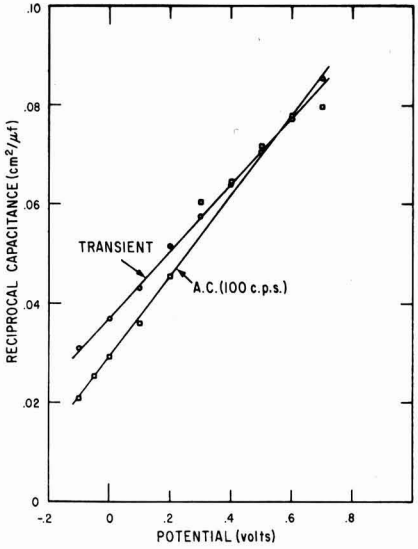

Fig. 7. Reciprocal capacitance vs. potential

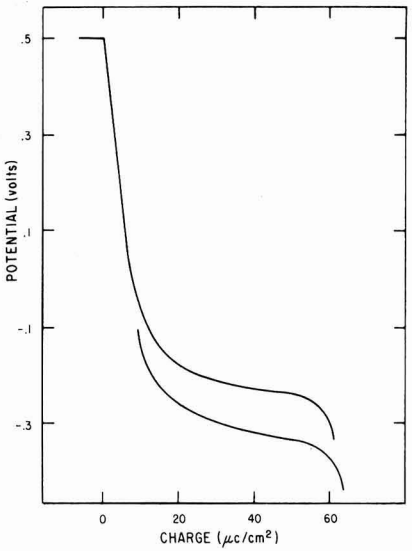

Fig. 8. Cathodic potential transients. Cathodic current: upper curve, 0.256 ma/cm²; lower curve, 2.56 ma/cm².

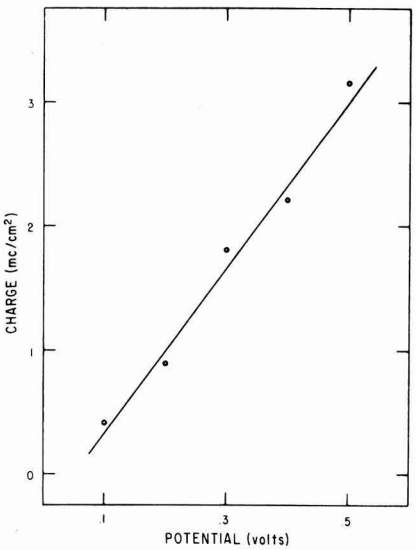

Fig. 9. Charge to activate vs. potential. Anodic current 3μa/cm²

thickness of the layer. The discussion section below shows that this is to be expected if one adopts a rather general model for the layer.

Transition to the Active State

If the electrode is initially passive and in a steady state with anodic current i_{ss}, a transition to the active state may be effected if one applies a constant current $i < i_{ss}$. This current can be anodic or cathodic.

The case where the current is cathodic and large with respect to the corrosion current is illustrated by Fig. 8, where potential has been plotted *vs. it*, with t the time the current i has flowed. The two curves are for two different values of the current, and it is seen that the length of the plateau[4] depends only on the charge and not on the current density. (Strictly speaking, activation might be expected to depend on $(i_{ss} - i)t$, but $|i_{ss}| < i$ and hence one may use it for the charge involved, without causing appreciable error.) The amount of charge required, before the transition to the active state occurs, is equivalent to a fraction of a monolayer. Other authors (3) have observed this, and have suggested that a "hole" is created in the layer. But then the charge to make a hole should depend on the layer thickness (as measured by the initial potential) and this is not found. An alternative explanation is that large cathodic currents cause disruption of a monolayer, followed by a general breakdown and a transition to the active state.

Activation with anodic current $i < i_{ss}$ is different from that with large cathodic current, because the initial thickness is important in the former case. In Fig. 9, for an anodic current density of 3 μa/cm², the activation charge is shown as a function of initial steady-state potential. This charge is greater than that for cathodic activation, and it increases linearly with the thickness of the surface layer. During anodic activation, the erosion of the layer by the acid may be assumed to continue at the rate i_{ss}, while formation occurs at the rate i. As long as there is an anodic current, this will tend to flow where the layer is thinnest and thus automatically keep the thickness of the layer uniform. However, continued erosion will eventually make the layer so thin that disruption must occur. With this picture, the anodic activation charge corresponds to a layer at least several atoms thick, and so will be greater than the cathodic activation charge, which seems to involve less than a monolayer.

If the current is zero or cathodic and small, the transition to the active state is intermediate in behavior between the above types of activation. Presumably the erosion culminates in the formation of a hole through the layer, there being nothing to prevent it. For zero applied current (open circuit) the time to activate is not entirely reproducible, which apparently is due to the thinning being nonuniform, or in other words to the existence of "local action currents."

Layer Growth

To study the increase in thickness of a passive layer, we have recorded galvanostatic transients with anodic currents greater than the steady-state current, and a typical one is shown in Fig. 10. Starting from the steady state, there is at first a capacitive rise in potential, which may be regarded as a rapid adjustment to the increased current. The potential goes through a maximum, decreases slightly to a plateau and then rises linearly with time. (The experiments of Weil (3) were such that the maximum and plateau were not recorded.) At higher passivating potentials, the length of

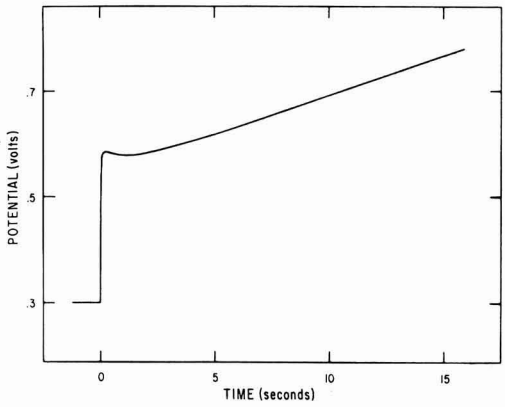

Fig. 10. Galvanostatic potential transient. Anodic current, 183 μa/cm².

[4] The plateau itself shifts to more negative potentials as the cathodic current is increased, according to $\Delta V = 0.04 \ln i$, which relation is practically independent of thickness.

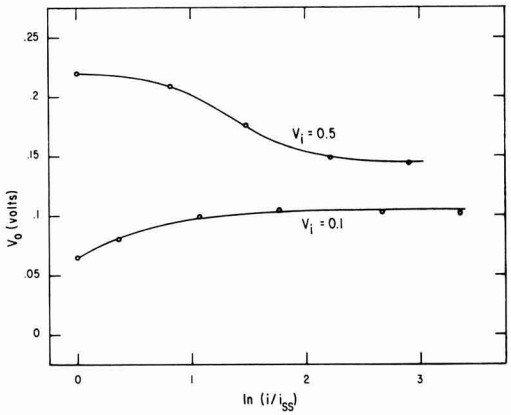

Fig. 11. Dependence of v_o on current. Initial steady-state potential: upper curve, 0.5v; lower curve, 0.1v.

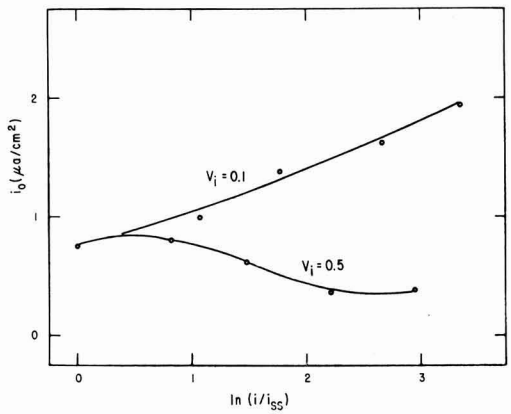

Fig. 12. Dependence of i_o on current. Initial steady-state potential: upper curve, 0.1v; lower curve, 0.5v.

the plateau shows little potential dependence, but does vary approximately inversely with excess current, indicating that a constant amount of charge is required to reach the end of the plateau. The slope of the linear potential rise is approximately proportional to $i - i_{ss}$, as would be expected if the layer is thickening.

Closer investigation reveals that a point on the above linear rise does not correspond to a steady state, for the field is not constant across the layer. If the circuit be opened when an excess charge of 0.05 mc/cm^2 (enough to complete the capacitive transient and arrive on the plateau, without appreciably changing the layer thickness) has passed, then it is found that the field across the activation barrier has changed from its steady-state value. [The open-circuit transient can be fitted by a $\ln(t + \theta)$ function over a wide range of potential, and so one can obtain good parameters v_o and i_o. These are shown in Fig. 11 and 12, for 2 different values of the initial steady-state potential v_i, as a function of the applied current i.] Now with a given potential v and a thickness D, the average field is v/D, which will be the actual field in the steady state. If the field across the activation barrier is different from this average, so must the field in the remainder of the layer be different, and the field cannot be constant. By Gauss' theorem, $\partial E/\partial x = 4\pi\rho$, so the interior of the layer has a nonzero charge density at the end of the plateau (and on the linear rise as well).

Relaxation from the charged condition to the neutral steady state can be followed by switching down to the

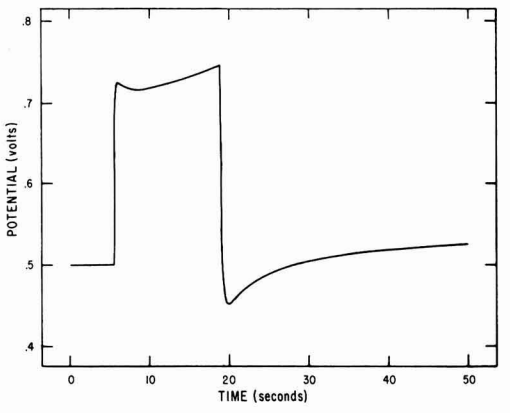

Fig. 13. Galvanostatic potential transient. Current switched from 10 to 73 μa/cm^2, then back to 10 μa/cm^2.

corrosion current, at any point of the linear rise. Figure 13 shows the resulting behavior. The rapid drop of potential (capacitive transient) is followed by a slow rise. After about a half a minute, i_o and v_o return to their steady-state values, which are consistent with the final potential. But an open-circuit transient from the linear rise drops very rapidly, so that i_o and v_o can be expected to be nearly constant during the drop, which is in fact found.

In general, then, i_o and v_o can change rapidly if a large change of current is made, but quite slowly if redistribution of charge over the whole layer is involved. If, for instance, the solution be changed from 0.1N H_2SO_4 to 2N H_2SO_4, keeping the potential constant, the quantity v_o takes about 2.5 min, and i_o as long as 10 min, to reach new steady values (unpublished experiments by D. DeSmet). Apparently i_o and v_o serve to describe local conditions at an activation barrier, which conditions adjust rapidly to electron flow, but only slowly to motion of ions.

The thickness of the layer can be estimated by indirect methods in a manner similar to that used by Vetter and Weil (1), and our results are roughly the same. If excess charge ΔQ is given to the layer, and relaxation at $i = i_{ss}$ is allowed to proceed to completion, then the increase of potential ΔV is related to ΔQ in a linear fashion, as shown in Fig. 14. If this charge ΔQ all goes to build layer, the increase in thickness ΔD is given by the equation $\Delta D = M(\Delta Q/\sigma A)/s\lambda F$, where M is the molecular weight, σ the roughness factor, A area, s specific gravity, and λ the valence of ion. Thus we can relate ΔD to ΔV if we make assumptions about M, σ, s, and λ. But since Fig. 6 shows a linear connection between v_o and V, ΔD will be proportional to Δv_o. This is in agreement with Eq. [9], the factor of proportionality being $a\lambda/kT$. Assuming that the layer is composed of Fe_2O_3, that $\sigma = 1.5$ and $\lambda = 3$, and that $D = (a\lambda/kT)v_o$ from Eq. [9], the minimum thickness is calculated to be 8Å. the thickness at $v = 800$ mv is 68Å, and the jump distance a is 1.9Å. [A somewhat similar dependence of thickness on potential was found in the anodic oxidation of platinum (11, 12)].

Discussion

Now that the evidence indicates the existence of a nonzero charge within the layer, it becomes natural to inquire how this charge builds up, relaxes, and causes the layer to change in thickness. One can obtain at least partial answers by considering the behavior of a layer with an arbitrary distribution of charge.

If the charge density is ρ and the dielectric constant is ϵ, then Gauss' theorem states that

$$\epsilon E = 4\pi \int \rho dx \qquad [10]$$

The drop in potential across the layer is

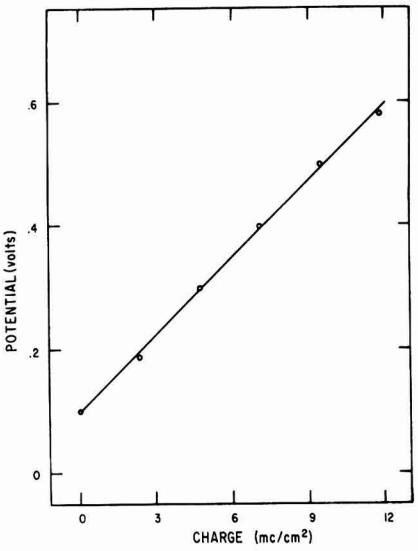

Fig. 14. Steady-state potential *vs.* charge. Potential measured 100 sec after switching down to steady-state current. Charge = $(i - i_{ss})t$.

$$v = -\int_0^D E\,dx \qquad [11]$$

This may change because the charge density changes, or because the layer increases in thickness. The total amount will be

$$\Delta v = \int_0^D \Delta E\,dx + E\Delta D \qquad [12]$$

Furthermore, by continuity, the time rate of change of charge density is given by

$$\frac{\partial \rho}{\partial t} = -\frac{\partial i}{\partial x} \qquad [13]$$

where i is the current density.

Now let us discuss a galvanostatic charging process, using the above equations. When the current is increased at $t = 0$, electrons flow without delay, leaving ionized iron atoms behind, ready to migrate in the opposite direction under the influence of the field E. Suppose that these ions are contained in a small length Δx. Then, from [13]

$$\Delta\rho\,\Delta x = \Delta i\,\Delta t$$

By [10], $\epsilon\Delta E = 4\pi\,\Delta\rho\,\Delta x = 4\pi\,\Delta i\,\Delta t$.

If the region Δx is at the metal interface and $\Delta x << D$,

$$\Delta v = -D\Delta E = \frac{4\pi}{\epsilon}\Delta i\,\Delta t\,D \qquad [14]$$

Since capacity is defined in general by the equation $C = -i/(dV/dt)$, we see that our system behaves as if there were a capacitative element (in parallel with the normal resistance) through which the current Δi flows. Its capacity is, from [14],

$$C = \epsilon/4\pi D \qquad [15]$$

This equation is consistent with our experimental observations that the reciprocal capacity in the steady state varies linearly with the potential (and thus with the thickness). Since there is nothing in the above derivation which restricts the system to be in the steady state, we should be able to find the thickness by measuring the capacity and applying Eq. [15].

To proceed further, let us attempt to describe the thickening process, making what seem to be natural assumptions. Vetter (4) has suggested that at the layer-electrolyte interface negative oxygen ions are produced and that these can migrate through the layer toward the metal. Exactly where they combine with positive ions to produce added layer has been left open, so let us suppose that this occurs somewhere in the middle of the layer, the position being determined by the relative mobilities of the various types of ion. If, except where the ions are combining, the charge density is steady, then $\Delta E = 0$ and Eq. [12] results in $\Delta v/\Delta t = E_c(\Delta D/\Delta t)$, E_c being the field at the site of combination. If the thickening (thinning) occurs at a constant rate, then the potential will rise (fall) linearly with time. For a galvanostatic transient with $i > i_{ss}$, we do observe a linear rise, and for $i > i_{ss}$ a linear fall, during the latter part of the transient.

More quantitative statements about changes in thickness and about the factors governing the exchange current and electric field seem to demand further experimentation, especially in connection with the relaxation process. Qualitatively, however, the above model does tie together phenomena which are otherwise inexplicable, and thus furnishes guidelines toward further progress in understanding the structure of a passive layer.

Acknowledgment

This work was supported by the U.S. Army Research Office (Durham) under contracts DA-11-022-ORD-2525 and DA-11-022-ORD-3442, and by the University of Illinois Research Board.

Mr. W. P. Perkins rendered invaluable assistance both in performing the experiments and in analyzing the data. Mr. L. D. Ferguson assisted with studies of capacitance and of concentration dependence. Mr. J. E. Orme helped with the a.c. measurements, and Mr. P. O. Schemmel and Mr. W. H. Trester with the data analysis.

For all this support and assistance, we are deeply appreciative.

Manuscript received May 7, 1962; revised manuscript received Oct. 14, 1964. This paper was presented at the 2nd International Passivity Conference, Toronto, September 1962.

Any discussion of this paper will appear in a Discussion Section to be published in the December 1965 JOURNAL.

REFERENCES

1. K. J. Vetter, *Z. Elektrochem.*, **55**, 274 (1951).
2. U. F. Franck and K. G. Weil, *ibid.*, **56**, 814 (1952).
3. K. G Weil, *ibid.*, **59**, 711 (1955).
4. K. J. Vetter, *ibid.*, **58**, 230 (1954).
5. K. J. Vetter, *ibid.*, **62**, 642 (1958).
6. J. H. Bartlett and L. Stephenson, *This Journal*, **99**, 504 (1952).
7. Ya. M. Kolotyrkin, *Z. Elektrochem.*, **62**, 664 (1958).
8. D. C. Grahame, *J. Phys. Chem.*, **57**, 257 (1953).

8a. P. E. Lake and E. J. Casey, *ibid.*, **106**, 913 (1959).

9. J. O'M. Bockris and E. C. Potter, *This Journal*, **99**, 169 (1952).
10. N. Cabrera and N. F. Mott, *Repts. Progr. Phys.*, **12**, 163 (1948-49).
11. J. Giner, *Z. Elektrochem.*, **63**, 386 (1959).
12. H. A. Laitinen and C. G. Enke, *This Journal*, **107**, 773 (1960).

The Structure of Electrodeposited Copper Examined by X-Ray Diffraction Techniques

E. M. Hofer[1] and H. E. Hintermann

Laboratoire Suisse de Recherches Horlogères, Neuchâtel, Switzerland

ABSTRACT

X-ray diffraction line profiles of copper, electrodeposited from an acid plating bath in the presence of thiourea, have been analyzed by Fourier techniques. From the coefficients data on microstrains, crystallite size, twin fault, and stacking fault densities were obtained. The stored energy and the dislocation density have been derived from the value of the rms strains. The sums of the determination of the Fourier coefficients of the various diffraction peaks were calculated with a computer. The particle size as determined by the Fourier analysis varies between 1350 and 180Å. The smallest particle size is obtained in a plating bath with a thiourea concentration of 20 mg/l. The deposits contain no stacking faults; the microtwin density is high. The microstrains are strong, indicating high values for the stored energy, ≈0.25 cal/g, and the dislocation density, ≈2 x 10^{11}/cm^2. A relationship was established between hardness and strain. X-ray results were compared with those obtained from electron microscopical observations on the same specimens.

The mechanical properties of electrodeposits have been the subject of many studies (1). The properties are due to definite microstructural features comparable to those produced by cold-work, such as small grain size and strong internal tensions. Fischer (2) explained that strong inhibition can entirely block a crystal's active growth sites during deposition and thus cause a notable decrease in the grain size with increasing amounts of the additive. Vermilyea and co-workers proved quantitatively that the rate of electrodeposition of metal whiskers is controlled by this mechanism (3), and that the formation of polycrystalline electrodeposits can be explained by the same mechanism (4).

Strains in galvanic deposits are similar to those produced by cold-work. Their presence has been known for almost a century (5, 6). They are the result of distortions in the mosaic structure influenced by the deposition parameters (7, 8). Strain can result from the transformation of atomic hydrogen enclosed in the crystalline body of the metallic deposit into molecular hydrogen (9-11), the retaining and releasing of atomic hydrogen during electrodeposition (10, 11), and the presence of dislocations created by growth accidents (9, 12). Steinemann and Hintermann (13) measured dislocation densities in copper deposits of 10^8 to 10^{11} dislocations/cm^2. Another reason for the presence of strains is the inclusion of the additive or a reaction product thereof in the deposit (13). By electron microscopical techniques an occlusion density of 10^{17}/cm^3 was determined (13). Jan (14) measured the occlusion density by x-ray small angle scattering and obtained similar results. The pinning of dislocations between inclusions, as observed in copper sheets electroplated in the presence of gelatine, is still another cause for the improved mechanical properties of electrodeposited metals (13, 15).

An accurate and extended knowledge of the microstructure of electrodeposits was necessary if a relation between certain deposition parameters and the resulting mechanical properties of the electrodeposits were to be found. One possible and promising method of investigation was a Fourier analysis of the x-ray diffraction peaks obtained from electrodeposits (16, 17). This method renders a better statistical value for the crystallite size than does the electron microscope, since the examined surface of the specimen is much larger. Moreover, from the analysis of the diffraction peaks by Fourier techniques, additional data on the magnitude of microstrains and the density of growth faults can be obtained. This technique has the further advantage of being nondestructive. Its results combined with hardness measurements contribute to a better understanding of the structural defects and their influence on the mechanical properties of electrodeposited metals.

Experimental

Sample preparation.—Copper deposits of 30μ thickness were produced on laminated and annealed copper sheets of 50μ thickness. The electrolytic cell was of cylindrical shape with a rotating cathode and a stable concentric anode of the following dimensions: cathode, diameter 40 mm, height 100 mm, effective height[2] 82 mm; anode, diameter 80 mm, height 100 mm. This cell was constructed for good reproductibility of the following parameters: (*a*) current density *i*, (*b*) temperature *T*, (*c*) geometry *G*, (*d*) agitation *A*. These parameters were kept constant for all depositions.

Seven deposits were made. Analytical grade thiourea[3] was used as an additive. The initial composition of the plating bath was 1*N* $CuSO_4$, 1*N* H_2SO_4, prepared as described by Fischer and co-workers (18, 19). A fresh solution was used for each plating. The thiourea was added in quantities of 5, 10, 15, 20, 25, 40, and 100 mg/l solution immediately before the electrodeposition. The other deposition parameters were: $i = 28$ ma/cm^2 and $T = 22° \pm 1°$C. The samples were chosen from an area exhibiting the least of preferred crystallite orientation, usually from the central region of the cathode. In order to prevent recovery at room temperature, the specimens were held under liquid nitrogen until investigated by x-ray diffraction.

Heat treatments were made for 1 hr at temperatures of 100°, 175°, 250°, 350°, 450°, and 550°C, respectively.

X-ray methods.—The x-ray diffraction patterns were recorded with a Philips proportional counter diffractometer. Filtered Co Kα radiation (voltage 30 kv, current 10 ma, Fe filter) was used, thus eliminating the copper fluorescent radiation from the sample. The width of the divergence slit was 1°, that of the receiving slit 0.2 mm. The scanning speed was ¼ degree 2θ/min, the chart speed 800 mm/hr.

The electrodeposits were mounted in a stainless steel specimen holder in order to provide reproducible experimental conditions during the recording of the various diffraction patterns. The heat-treatment was performed while the specimen was kept in the holder. The background was determined from a sample annealed at 550°C and substracted from each diffraction pattern of the samples to be analyzed.

[1] Present address: Central Research Laboratory, American-Standard, New Brunswick, New Jersey.

[2] Height of the sheet on which the copper actually was deposited.

[3] Merck p.a.

If a fcc metal is considered to be composed of a stacking of (111) layers whose normal sequence would be ABCABCABC . . ., a stacking fault is a break in this sequence ABC↓BCABC . . ., whereas a reversal in the sequence ABCACBA represents a twin fault. The probability α of finding a stacking fault between two (111) layers can be determined from the relative positions of the 111 and 200 reflections of the sample as deposited and the annealed standard (20, 21), *i.e.*

$$(2\theta_{200} - 2\theta_{111})_{\text{untreated}} - (2\theta_{200} - 2\theta_{111})_{\text{annealed}} = -\left(\tan\theta_{200} + \frac{1}{2}\tan\theta_{111}\right)\frac{45\sqrt{3}\,\alpha}{\pi^2} \quad [1]$$

The Fourier analysis of the recorded diffraction peaks was carried out with an electronic computer, IBM 1620. The program was established in such a way that, after the function to be analyzed had been introduced in form of discrete values P'_ν spaced in regular intervals θ_ν, the Fourier coefficients and the position of the center of gravity with regard to the peak maximum, ΔCG, of each peak were obtained (17). For the calculation of the Fourier transform and ΔCG, intervals equal to 2 sin θ/λ were used. The ordinates were previously divided by $f^2(1 + \cos^2 2\theta)/\sin^2\theta$, f being the atomic scattering factor. Once the ΔCG value was known, the probability β of finding a twin fault between two (111) layers could be determined by the method of Cohen and Wagner (22)

$$\Delta\text{CG}(^\circ 2\theta)_{111} - \Delta\text{CG}(^\circ 2\theta)_{200} = \beta\,(11\tan\theta_{111} + 14.6\tan\theta_{200}) \quad [2]$$

The cosine Fourier coefficient A_L, for which the line broadening due to instrumental effects (23) is corrected by the method of Stokes (24), can be considered as the product of two coefficients A_L^S and A_L^D. L is the real distance in the crystal normal to the diffracting planes, equal to na_3; n is the harmonic number, and a_3 is the unit cell dimension in the direction perpendicular to the diffracting planes. A_L^S is due to the particle size, A_L^D to the rms strain averaged over the distance L : $\langle\epsilon_L^2\rangle^{1/2}$

$$\ln A_L = \ln A_L^S - 2\pi^2(L/a_o)^2 h_o^2 \langle\epsilon_L^2\rangle \quad [3]$$

where $h_o^2 = (h^2 + k^2 + l^2)$ is the order of the reflection and a_o is the true lattice parameter. Only the term due to the strain is a function of h_o^2. Thus, if A_L is plotted as a function of different orders of reflection $(h_1^2 + k_1^2 + l_1^2)$ a straight line is obtained, whose intersection with the ordinate furnishes the value of A_L^S. This value, a function of L, renders $\langle D\rangle_{\text{eff }hkl}$, the size of the coherently diffracting domains. This effective dimension of the particles includes the effects of grain boundaries, small angle boundaries, stacking faults, and twin faults

$$\frac{1}{\langle D\rangle_{\text{eff }hkl}} = -\left[\frac{dA_L^S}{dL}\right]_{L\to o} = \frac{1}{\langle D\rangle} + \frac{1.5\alpha + \beta}{a_o} c_{hkl} \quad [4]$$

c_{hkl} is a coefficient which depends on the reflection under study. In this work the orders 111 and 222 have been used for which c_{hkl} is equal to $\sqrt{3}/4$. The expression $[(1.5\alpha + \beta)/a_o]\ 3/4 = \langle D\rangle^{-1}_{F\,111}$. The term $\langle D\rangle_{F\,111}$ is the calculated particle size due to the presence of faults only.

The diffraction peaks of all seven samples with and without heat treatment at different temperatures were analyzed by Fourier techniques. To apply the correction of Stokes for the instrumental line broadening, a sample annealed at 550°C was used as a standard. Moreover, to check if there was any annealing effect on freshly deposited coatings at ambient temperature, these samples were stored after deposition under liquid nitrogen and their x-ray diffraction patterns recorded at a sample temperature of —160°C. For this purpose a low-temperature goniometer head analogous to the one described by Wagner (25) was used. It was experimentally verified that neither the width nor the form of the diffraction peaks were influenced by the use of this goniometer attachment.

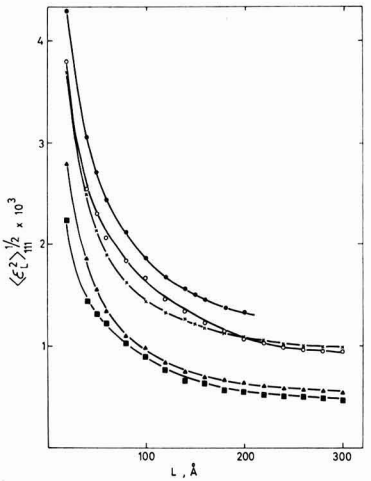

Fig. 1. rms strain $\langle\epsilon^2_L\rangle^{1/2}$ vs. the averaging distance normal to the diffracting planes L, for copper deposited from 1N H_2SO_4, 1N $CuSO_4$ with 40 mg/l thiourea and for different annealing temperatures: ●, —160°C; ○, 25°C; X, 100°C; ▲, 175°C; ■, 250°C; 40 mg/l.

Results

Strains.—The rms strains of the seven specimens were calculated as a function of L (example in Fig. 1). If it is assumed that the distribution of the strains within the crystal is random, it is possible to calculate the stored energy due to the elastic distortions in the lattice with the formula of Faulkner (26)

$$V = \frac{15\,E}{2(3 - 4\nu + 8\nu^2)}\langle\epsilon^2\rangle$$

where E is Young's modulus in the direction $[hkl]$ of the deformation and ν is Poisson's ratio.

The rms strain $\langle\epsilon_L^2\rangle^{1/2}$ is a component normal to the reflecting planes, averaged over a column length L, then squared and averaged over all sample regions. According to McKeehan and Warren (27), the true value of the strain is only obtained at small values of L. Therefore V has been chosen to be calculated for $L = 20$Å, a value which seemed sufficiently small to satisfy this condition, yet sufficiently great that $\langle\epsilon_L^2\rangle^{1/2}$ could be determined precisely. Values of V were calculated for each annealing temperature T_a at various thiourea concentrations (Fig. 2 a-g). Also listed in Fig. 2 are the size of coherently diffracting domains, rms strain, and Vickers DPH values. The curves were drawn taking into account for the maximum deviation from V, as indicated in the appendix. The point at —160°C indicates that the sample was actually kept at this temperature during the recording of the diffraction pattern. From the plotted curves it is evident that the release of the stored energy with increasing temperature does not proceed in a parallel manner for the seven specimens. Hence the recovery mechanism depends on the concentration of the additive which itself influences the structure, the number of occluded impurities, and the number of faults in the plate. Several authors (28-30) have studied the recovery of pure copper after irradiation or cold-work and have distinguished five recovery stages. Although the numerous publications on this subject agree on the activation energy of the different stages and also on the

temperature ranges within which the transitions are supposed to occur, they disagree somewhat on the interpretation of the kinetics of these phenomenons.

The first recovery stage, between —240° and —225°C, is attributed to close-pair annihilation by the motion of interstitials immediately adjacent to a vacancy (28-30), or to a local rearrangement process occurring in displacement spikes (29). The second stage, between —160° and —60°C, is associated with di-interstitial (30) or interstitial (28) migration or with the migration of divacancies or "wide" pair recombination (29). The third stage, between —60° and +40°C, is characterized by divacancy migration (28), diffusion of interstitials, and their recombination with vacancies (29), vacancy migration, or the breaking up of interstitial clusters (30). All the authors attribute the fourth stage, from

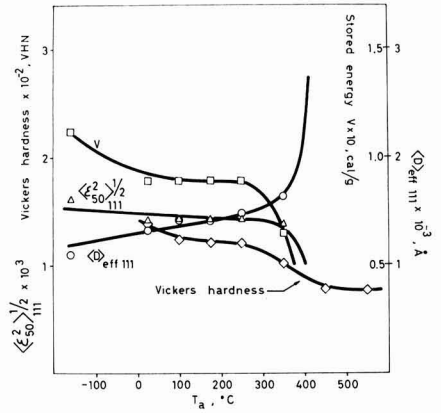

Fig. 2. Size of the coherently diffracting domains $\langle D \rangle_{\text{eff } 111}$, rms strain $\langle \epsilon^2_{50} \rangle^{1/2}_{111}$, stored energy V and Vickers hardness number VHN for 20g load as function of the annealing temperature T_a. (*a*) 5 mg/l thiourea.

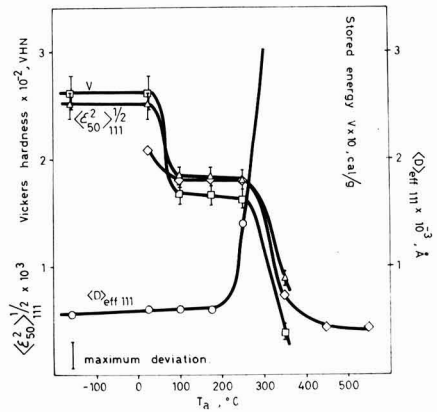

Fig. 2b. 10 mg/l thiourea

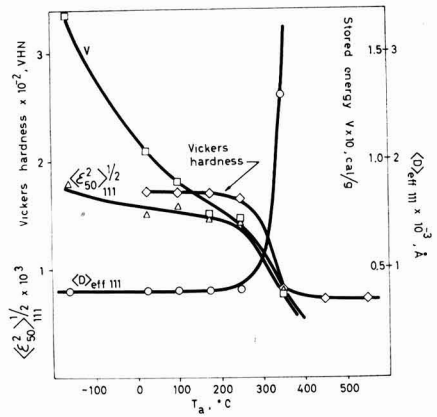

Fig. 2c. 15 mg/l thiourea

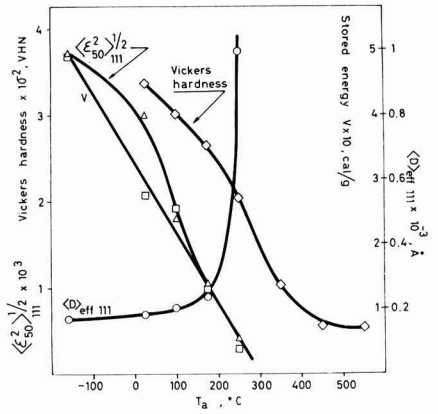

Fig. 2d. 20 mg/l thiourea

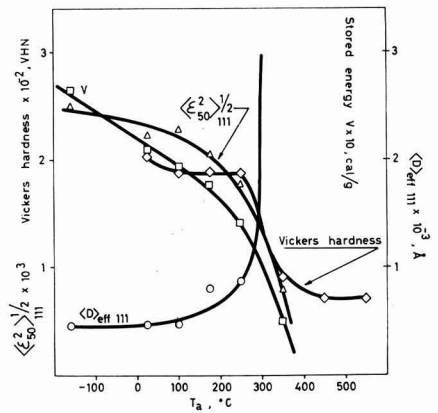

Fig. 2e. 25 mg/l thiourea

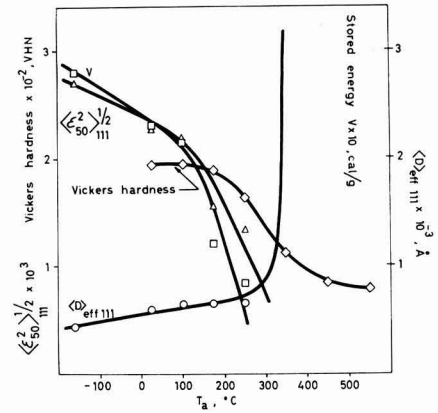

Fig. 2f. 40 mg/l thiourea

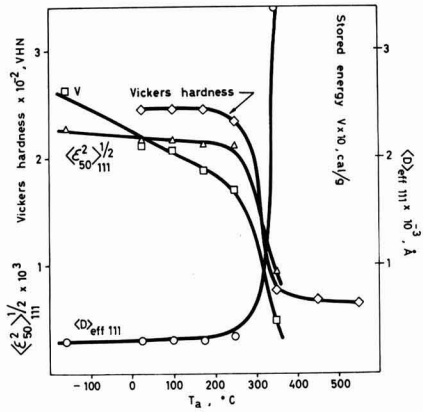

Fig. 2g. 100 mg/l thiourea

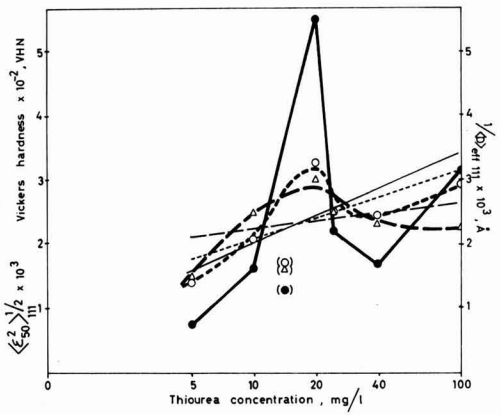

Fig. 3. rms strain $\langle\epsilon^2_{50}\rangle^{1/2}_{111}$, inverse of the size of the coherently diffracting domains $1/\langle D\rangle_{eff\ 111}$ and Vickers hardness number VHN vs. thiourea concentration in the bath: —— •, $1/\langle D\rangle_{eff\ 111}$; — — △, $\langle\epsilon^2_{50}\rangle^{1/2}_{111}$; - - - - ○, Vicker's hardness.

100° to 200°C, to the migration of isolated vacancies and to their disappearance at grain boundaries or dislocations. The fifth stage, at about 240°C, is unanimously considered as the stage of reorganization of the crystal by self-diffusion and migration of dislocations occurring before the recrystallization or simultaneously with it.

This information is summarized in Table I. An attempt was made to compare the recovery behavior of the copper electrodeposits of this study to samples of pure copper processed in a different manner as described in the literature.

In the case of the electrodeposits only the stages III, IV, and V could be observed, because the bath temperature at the time of the deposition was 22°C. The only purpose of the diffraction under liquid nitrogen was to prevent a recovery of the deposit at ambient temperature. From Fig. 2 it is evident that the three later recovery stages could generally be observed on all deposits. The different stages have been separated by taking into account (i) the limiting temperature as stated in Table I, (ii) the course of the curves as indicated by the measured points, and (iii) for stage V also the onset of the rapid grain growth. The percentages of recovery were calculated from the curves representing V as a function of T_a (Fig. 2), assuming that 50% of the entire stored energy is represented by the latter three recovery stages, as is actually the case for irradiated and cold-worked metals. However, two remarks must be made: (*A*) The presence of a rather high number of impurities occluded in the crystalline structure of the deposits retards the different recovery steps so that the processes succeeding one another become less pronounced and tend to overlap. (*B*) It is more the secondary effects of the recovery stages III and IV which can be observed by x-ray diffraction methods, namely the vacancy migrations. Their occurrence makes a rearrangement of the dislocation network within the crystal lattice possible and thus diminishes the microstrains. Results are reported in Table I. Those obtained from the deposits produced at low and medium thiourea concentrations compare reasonably well with the values given by the literature, those deposits produced at high thiourea concentrations do not. But rather than to look for a good agreement between literature and experimental results this comparison reveals the complexity of the structure and the recovery behavior of these electrodeposits.

Crystallite size and recrystallization.—The crystallite size varies as a function of the additive's concentration in the plating solution. The inverse of the crystallite size, $1/\langle D\rangle_{eff\ 111}$, was plotted as a function of the initial thiourea concentration in the bath (Fig. 3). As a maximum had previously been found for the strains at 20-25 mg/l thiourea, a minimum of the grain size was observed in the same concentration range.

The average diameter $\overline{D}$ as obtained from an electron microscopical study of these electrodeposits was determined by the method of Braun (31) which relates the average volume $\overline{v}$ of the grains to its average linear dimension $\overline{\mathfrak{L}}$ measured on the micrographs,

Table I. Release of stored energy in copper electrodeposits compared to the release of stored energy in cold-worked and irradiated copper

		Stage I	Stage II	Stage III	Stage IV	Stage V
Activation energy	(29)	0.1 ev	0.2-0.5 ev	0.72 ev	1.19 ev	2.1 ev
Temperature interval	(28)	−245° to −230°C	−180° to −70°C	−60° to 50°C	130°C	230°C
Values admitted for this work		−240° to −225°C	−160° to −60°C	−60° to 40°C	100°-200°C	240°C
Model	(28) (29)	close-pair annihilation id. + rearrangement in spikes	interstitial migration migration of vacancy clusters	di-vacancy migration interstitial migration	vacancy migration id.	self-diffusion id.
Release of stored energy after cold-work	(28)	0%	40%	30%	10%	10%
Release of stored energy after irradiation	(28)	25%	25%	30%	10%	10%
Release of stored energy in the electrodeposits	additive: mg/l					
	5			25%	25%	
	10			20%	30%	
	15			30%	10%	10%
	20			25%	15%	10%
	25			15%	15%	20%
	40			15%	20%	15%
	100			12%	10%	28%

Table II. Copper-thiourea, principal results of the structural analysis

Thiourea concentration, mg/l	$\overline{D}$ Electron microscope, Å	$<D>_{eff\ 111}$, Å	$<D>_{F\ 111}$, Å	Stored energy, v, cal/g	Twin fault density, β	ρ_{WS}, cm^{-2}	ρ_c, cm^{-2}	$<\epsilon^2_{50}>^{1/2}_{111}$, %	Hardness, VHN
5	1500	1350	1640	0.09	0.005	0.50×10^{11}	0.50×10^{11}	0.15	139
10	620	620	780	0.26	0.011	1.55×10^{11}	1.65×10^{11}	0.25	206
15	990	780	1640	0.11	0.005	0.65×10^{11}	0.75×10^{11}	0.16	170
20	250	180	400	0.28	0.021	2.20×10^{11}	2.30×10^{11}	0.30	335
25	470	450	1050	0.21	0.008	1.55×10^{11}	2.30×10^{11}	0.25	205
40	615	600	870	0.23	0.009	1.30×10^{11}	1.50×10^{11}	0.23	197
100	350	310	700	0.21	0.012	1.20×10^{11}	3.00×10^{11}	0.22	245

i.e., $\overline{v} = 2.57\ (\overline{\mathcal{L}})^3$. The values in Table II indicate an excellent concordance between $<D>_{eff\ 111}$ and $\overline{D}$.

The results from the electron microscopical study on the various electrodeposits are summarized in Table III.

A minimum grain size is observed at an original thiourea content of 20-25 mg/l solution.

The growth of the coherently diffracting domains with the annealing time and temperature is different for each specimen (Fig. 2). By observing the curves relating the crystallite growth to the annealing temperature at constant annealing time, a slow increase of the grain size is noticed, previous to the fast raise which gives evidence of the actual recrystallization. This slow grain growth is perhaps induced by the diffusion of vacancies from sites of high local strain toward grain boundaries and dislocations. The absorption of vacancies by dislocations leads to a complete rearrangement of the dislocation network within the lattice, thus causing an increase in crystallite size $<D>_{eff\ 111}$ as measured by Fourier techniques. These mechanisms have been described and discussed by van Bueren and Hornstra (32).

Twin faults.—No shifts of the 111 and 200 reflections were found on the x-ray diffraction patterns of the electrodeposits. This indicates a low stability or a very small number of stacking faults in the plates. The same findings were obtained from the electron microscopical study of these deposits. On the other hand the microtwin faults are numerous and easily detectable. Different interpretations exist concerning their formation in a metal electrodeposited in the presence of an additive. Most theories explain them as caused by a blocking of one of the crystal's growth directions by the additive (9). Hinton, Schwartz, and Cohen (16) explain the formation of the twin faults on the basis of a particular stacking mechanism of the (111) layers. The arrival of an additive molecule or a molecule of a reaction product thereof can have either of two effects on the structure of the crystallite: (*A*) An adsorbed foreign molecule, if similar in size to the metal atom to be deposited, may let pass an advancing growth step and permit the crystal layers to pile up continuously in a correct stacking sequence. The region around the molecule may be strained, causing dislocations, but no faults will be produced. (*B*) If the adsorbed foreign molecule is considerably larger than the metal atoms of the deposit, an advancing growth step is forced by this obstacle to change its growth direction, and the growth layers continue to pile up in a stacking sequence in reverse to the former until the molecule is covered. Thus a fault is created. In most cases the plating solution does not contain the additive dissolved in a simple molecular form but rather in

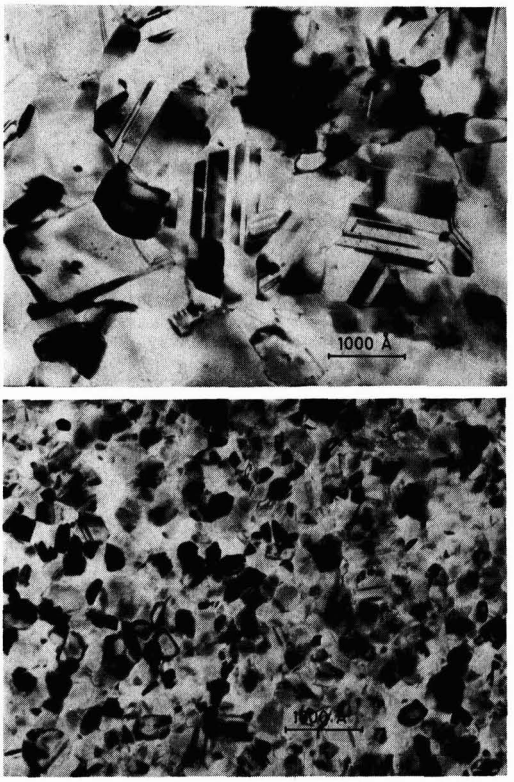

Fig. 4. Electron micrographs of copper deposits. Conditions: 1*N* H_2SO_4, 1*N* $CuSO_4$, 28 ma/cm^2, room temperature. (*a*) (*top*) solution containing 10 mg/l thiourea; (b) (bottom) solution containing 20 mg/l thiourea.

Table III. Evaluation of the electron micrographs

Additive conc, mg/l	Average grain size $\overline{D}$, Å	Appearance
5	1500	Large grains, broken up in subgrains by small angle boundaries and microtwins. Occlusions preferentially arranged in chains.
10	620	Grains of rounded shapes; occlusions more numerous and more randomly distributed than in the former deposit (Fig. 4a).
15	990	Structure different from the structure of the other deposits. Elongated grains in preferential directions. Chains of occlusions arranged in the direction of the longer axis of the crystallites. Microtwins not uniformly distributed over the plate.
20	250	Very small grains of rounded shapes and homogeneous in size (Fig. 4b).
25	470	Similar to the preceding deposit but with larger grains.
40	615	Similar to the plating deposited in the presence of 10 mg/l thiourea, but less uniform.
100	350	Needle-like structure. Small grain size. Boundaries faded and difficult to estimate.

Table IV. Reproductibility of the Fourier analysis

	$<D>_{eff\ 111}$ %	$<\epsilon^2_{20}>^{1/2}_{111}$ %	$<\epsilon^2_{50}>^{1/2}_{111}$ %	$<\epsilon^2_{100}>^{1/2}_{111}$ %	$<D>_{F\ 111}$ %
Maximum deviation	±5	±3	±5	±6	±5
Standard deviation	±2.5	±1.3	±1.7	±2.4	±2.6

complex compounds with the metal ions, the formation parameters and exact stoichiometric composition of which are not yet well understood. It is very possible that these complex compounds present themselves, according to the experimental conditions, in a form more or less favorable for the formation of microtwin faults. However, since these phenomena occur either as chemical or electrochemical reactions in the bulk of the plating solution or in the diffusion and double layer immediately adjacent to the electrode surface during electrodeposition, they do not come within the scope of this paper.

The probability of finding a twin or growth fault, *i.e.*, of finding two or more layers in an incorrect sequence, was calculated by the method of Cohen and Wagner. The influence of the instrumental line broadening and the $K\alpha_1\alpha_2$ doublet was minimized by an appropriate choice of the slits in the pathway of the incident and diffracted beams, respectively. Furthermore, a recent study by Witt and Schoening (33) makes it evident that the $K\alpha_1\alpha_2$ doublet introduces a negligible error in the determination of β, if the asymmetry of the peak is measured over the entire line profile, as is actually done in this study by means of an IBM 1620 electronic computer.

Table II reports the calculated β values of the seven plates as deposited. β varies between 0.005 and 0.021. With these probability values it is possible to calculate $\langle D\rangle_{F\,111}$, *i.e.*, the crystallite size due only to the presence of faults. The absolute value for the twin fault density as such is perhaps of little significance. What seems to be more important is the comparison between $\langle D\rangle_{\text{eff }111}$ and $\langle D\rangle_{F\,111}$. There are in fact samples with high β-values for which $\langle D\rangle_{F\,111}$ is much larger than $\langle D\rangle_{\text{eff }111}$ (20 mg/l and 25 mg/l thiourea). This indicates that the relative twin fault density in the deposit is low. Yet, for other samples (5, 10, and 40 mg/l thiourea) this difference between $\langle D\rangle_{F\,111}$ and $\langle D\rangle_{\text{eff }111}$ is small. Hence the grains of the deposit are divided by a great number of twin faults, which is also confirmed by the electron microscopical study. Thus, the investigated samples may be classified in two groups: (*a*) deposits with predominant influence of the twin faults, $\langle D\rangle_F/\langle D\rangle_{\text{eff}} < 2$ (5, 10, and 40 mg/l thiourea), and (*b*) deposits for which the smallness of the coherently diffracting domains is due to other causes, $\langle D\rangle_F/\langle D\rangle_{\text{eff}} > 2$ (20 and 25 mg/l thiourea).

Dislocations.—Considering the fact that local strains caused by occlusions of impurities fall off with $1/r^3$, and the strains due to dislocations with only $1/r$, it can be concluded that $\langle\epsilon_{50}^2\rangle^{1/2}$ is mainly due to dislocations. Furthermore, knowing the values for the rms strains and postulating a maximal separation and a minimal interaction of the dislocations as a working hypothesis, it is possible to calculate the dislocation density in the sample with the formula of Williamson and Smallman (34)

$$\rho_{WS} = \frac{16\langle\epsilon_{50}^2\rangle}{b^2}$$

where b is the Burgers vector of the dislocation ($a_o/2$ [110]). Admitting moreover the hypothesis that the recovery stages are due only to mechanisms anticipated by the literature, and also assuming that the entire energy remaining in the metal lattice in recovery stage V is the sum of the energies of individual dislocations only, and finally knowing the energy of a simple dislocation, it is possible to calculate the dislocation density. According to Cottrell (35) the energy of a single dislocation is 1.5×10^{-4} erg/cm. The dislocation densities were calculated according to both methods, the results of which are reported and compared in Table II. A good agreement between the results of the two methods was observed, the value ρ_c generally being slightly higher than ρ_{WS}. The accuracy of this method depends on the estimation of the onset of recovery stage V, which is rather hazardous at certain instances. The differences between the two methods are small indeed. In the former, it is postulated that only in the recovery stage V the energy due to dislocations alone is released. Thus it is possible to separate the strains caused by dislocations from those due to other causes. In the latter, the strains due to dislocations are separated from those of other origins, considering that they fall off with $1/r$. In both methods the hypothesis of the maximal separation and the minimal interaction between the dislocations is made. No consideration is given, however, to annexed effects as, *e.g.*, the pinning of dislocations by occlusions.

Hardness.—Microhardness measurements were made on the deposits using a Zeiss D 30 Hardness Tester, type Hanemann. All hardness values reported here, expressed in Vickers hardness number (VHN), were determined using a load of 20g. Test samples were chosen from the same area of the cathode as those used for the x-ray investigation.

Three factors seem to influence the hardness: (i) the fineness of the grain, (ii) the dislocation density, and (iii) the pinning of the dislocations by impurities. The fineness of the grain and a high dislocation density restrict the mobility of the dislocations. For this reason, the Vickers hardness number (VHN) was reported as a function of the annealing temperature T_a, together with the rms strains $\langle\epsilon_{50}^2\rangle^{1/2}{}_{111}$ and the crystallite size as determined by the Fourier analysis of the diffraction peaks, $\langle D\rangle_{\text{eff }111}$. All are variables of the same function (Fig. 2). An excellent agreement is noticed in the behavior of these quantities with the temperature, which proves that the hardness depends on $\langle D\rangle_{\text{eff }111}$ and $\langle\epsilon_{50}^2\rangle^{1/2}{}_{111}$. Furthermore it may be noted (Fig. 3) that the deposits presenting the smallest grain size and the highest strains are also those with the highest hardness number. Thus again one observes a concurrent behavior of the hardness, the inverse of the crystallite size, and the rms strains of the deposits.

Conclusions

Figure 3 could serve as a summary of the structural study carried out on the copper-thiourea system. Based on a least square calculation straight lines have been drawn between the points of measurement of the inverse of the grain size, the microstrains, and the Vickers hardness. These lines show the trend of these parameters to increase with the logarithm of the concentration of thiourea, indicating a direct action of the quantity of the additive on the structure and mechanical properties of the deposit.

The same points[4] have been connected also by curves, all of which indicate a maximum in the region of 20 mg/l thiourea. This may be interpreted as follows:

1. The region between 5 and 10 mg/l thiourea. This could be designated as the "region of normal interaction," meaning that the additive produces the expected effects on the electrodeposits, such as small grain size, strong preferred orientation,[5] and numerous twin faults. These are all effects which can be explained by relatively simple mechanisms, for example the blocking of certain growth layers by the additive.

2. The region between 15 and 30 mg/l thiourea. It could be called the "region of strong interaction." The high number of additive molecules can block all growth directions of the crystallite, thus causing large strains and producing structures of small grain sizes. For the same reason the relative twin fault density decreases and the preferred orientation of the crystallites disappears. The deposit is very homogeneous, the mechanical properties are optimal. It is the region of the additive's highest power.

3. The region between 30 and 100 mg/l thiourea. This region could be designated as the "region of complex interaction" because the effects are diverse. They seem to have a recurrent tendency, the grain size and the

[4] Except those for 15 mg/l thiourea, for which the authors feel that the measurements are not reliable enough to influence the trend of the curve.

[5] This preferred orientation was measured using a Schultz goniometer (36).

relative twin fault density increase, the preferred orientation of the crystallites reappears and the hardness number decreases. The molecules of the additive are too numerous; hence they either disturb one another in their action of blocking the growth centers, or they form less inhibitive complex compounds with the copper ions. These deposits contain within themselves areas which strongly resemble deposits of the first type of this classification (large number of twin faults, preferred crystallite orientation) and areas which resemble deposits of the second type (small grains of homogeneous size and shape).

A more detailed study of the copper-thiourea system is imperative. It should explain which one of the two interpretations: linear increase of the parameters with the logarithm of the thiourea concentration or maximum at a certain well-defined value of the additive's concentration is correct. However, our mastery of certain electrochemical problems is incomplete, and our knowledge of the reciprocal actions between electrolyte and additive in the bulk of the solution and at the electrode-electrolyte interface is fragmentary. A better understanding of these reactions is necessary before the present study can be refined and extended.

Acknowledgments

The authors are grateful to Professors P. Dinichert and J. Rossel for helpful discussions. They thank Ph. Javet for the preparation of the deposits, J. Béguin for taking the electronmicrographs, Dr. A. Braun for the hardness measurements, and E. Saurer for assistance in the numerical computations.

Manuscript received April 30, 1964; revised manuscript received Oct. 8, 1964.

Any discussion of this paper will appear in a Discussion Section to be published in the December 1965 JOURNAL.

APPENDIX

The limits of reproductibility of the Fourier analytical treatment of the profiles of x-ray diffraction lines have been determined on a coper electrodeposit by performing the following operations five succeeding times: (*a*) mounting the specimen in the specimen holder, performing the diffraction; (*b*) measuring the ordinates P'_ν according to equal intervals with a pantograph; (*c*) calculating the Fourier transforms and applying the correction of Stokes, on an electronic computer IBM 1620; (*d*) separating graphically the grain size effect from the effect of the microstrains; (*e*) calculating the quantities $<D>_{\text{eff }111}$ (size of the coherently diffracting domains), $<\epsilon_L^2>^{1/2}_{111}$ (rms strains) and $<D>_{F\,111}$ (crystallite size due only to the presence of faults).

The maximum deviation and the standard deviation have been calculated for these different quantities and are reported in Table IV.

From the maximum deviation on $<\epsilon_{20}^2>^{1/2}_{111}$ of $\pm 3\%$ the maximum deviation on V was calculated to be $\pm 6\%$.

In one case it was shown that the results obtained from two different deposits, produced under identical electrochemical conditions, strayed less than 10%. However, further investigations of this sort are needed to assert this value.

REFERENCES

1. S. Steinemann, J. P. Renaud, H. E. Hintermann, and A. Braun, *Bull. Soc. Suisse Chronométrie*, **4**, 230 (1958).
2. H. Fischer, *C.I.T.C.E.* CR. 4 Réunion Cambridge, London (1952).
3. P. B. Price, D. A. Vermilyea, and M. B. Webb, *Acta Met.*, **6**, 524 (1958).
4. D. A. Vermilyea, *This Journal*, **106**, 66 (1959).
5. B. Mills, *Proc. Roy. Soc. (London)*, **26**, 504 (1877).
6. Bouty, *Compt. rend.*, **88**, 714 (1879).
7. L. G. Palatnik, E. L. Gebstein, and J. S. Lukoz, *J. Tech. Phys. (USSR)*, **10**, 1756 (1940).
8. H. Fischer, P. Huhse, and F. Pawlek, *Z. Metallkunde*, **47**, 43 (1956).
9. H. Fischer, "Elektrolytische Abscheidung und Elektrokristallisation von Metallen," Springer-Verlag, Berlin (1954).
10. M. R. J. Wyllie, *J. Cem. Phys.*, **16**, 52 (1948).
11. R. M. Bozorth, *Phys. Rev.*, **26**, 390 (1925).
12. N. Cabrera and D. A. Vermilyea, "Growth and Perfection of Crystals," John Wiley & Sons, Inc., New York (1958).
13. S. Steinemann and H. E. Hintermann, *Schweiz. Arch. angew. Wiss. Techn.*, **26**, 202 (1960).
14. J. P. Jan, *Z. angew. Math. Phys.*, **14**, 1 (1963).
15. E. M. Hofer and P. Javet, *Bull. Soc. Suisse Chronométrie*, **4**, 779 (1962).
16. R. W. Hinton, L. H. Schwartz, and J. B. Cohen, *This Journal*, **110**, 103 (1963).
17. E. M. Hofer and P. Javet, *Helv. Phys. Acta*, **35**, 369 (1962).
18. H. Binder and H. Fischer, *Z. Metallkunde*, **53**, 161 (1962).
19. H. Seiter and H. Fischer, *Z. Elektrochem.*, **63**, 249 (1959).
20. M. S. Paterson, *J. Appl. Phys.*, **23**, 805 (1952).
21. B. E. Warren, "Progress in Metal Physics," Vol. 8, p. 147, Pergamon Press, New York (1959).
22. J. B. Cohen and C. N. J. Wagner, *J. Appl. Phys.*, **33**, 2073 (1962).
23. L. Alexander, *ibid.*, **21**, 126 (1950); **25**, 155 (1954).
24. A. R. Stokes, *Proc. Phys. Soc.*, **361**, 382 (1948).
25. C. N. J. Wagner, Thesis, Saarbrücken University (1957).
26. E. A. Faulkner, *Phil. Mag.*, **5**, 519 (1960).
27. M. McKeehan and B. E. Warren, *J. Appl. Phys.*, **24**, 52 (1953).
28. H. G. van Bueren, "Imperfections in Crystals," North-Holland Publishing Company, Amsterdam (1960).
29. A. Seeger, in "Handbuch der Physik," Vol. 7/1, S. Flügge, Editor, Springer-Verlag, Berlin (1955).
30. J. M. Corbett and R. M. Walker, *Phys. Rev.*, **110**, 767 (1958).
31. A. Braun, *Rev. mét.*, **52**, 676 (1955).
32. H. G. van Bueren and J. Hornstra, "Proc. 4th Symp. Reactivity of Solids," Elsevier, Amsterdam (1960).
33. F. Witt and F. R. L. Schoening, *J. Appl. Phys.*, **33**, 2464 (1962).
34. G. K. Williamson and R. E. Smallman, *Phil. Mag.*, **1**, 34 (1956).
35. A. H. Cottrell, "Dislocations and Plastic Flow in Crystals," p. 38, The Clarendon Press, Oxford (1963).
36. L. G. Schultz, *J. Appl. Phys.*, **20**, 1030 (1949).

Preparation and Properties of Electrodeposited Cylindrical Magnetic Films

M. W. Sagal

Bell Telephone Laboratories, Incorporated, Murray Hill, New Jersey

ABSTRACT

A process is described for the electrodeposition of cylindrical permalloy films with near zero magnetostriction. The design of a plating cell intended to achieve good uniformity of electrolyte agitation over the plating region is given. The steps used in the preparation of the wire substrate are discussed. Results showing the dependence of average alloy composition on electrolyte flow rate and *p*H are given, along with typical magnetic characteristics of the plated wire.

Most of the work described in the literature on the preparation and characteristics of magnetic thin films for memory applications has been concerned with films evaporated or electrodeposited on flat insulating or metallic substrates (1, 2). An alternative configuration, an anisotropic film deposited on the surface of a small diameter wire, offers a number of advantages from the device point of view (3). A process for the fabrication of this material by a continuous electrodeposition process using high agitation conditions for achieving high current densities and compositional uniformity has been described previously (4, 5). In this earlier work the importance of proper substrate preparation, including the use of a copper preplate, was pointed out. This paper describes an advanced design of a continuous plating system in some detail, including a sequence of substrate cleaning and preplate steps which has been found to give a satisfactory surface for the subsequent plating of a nickel-iron film with desirable magnetic properties. Further, the degree of composition control that can be routinely achieved by proper regulation of the plating parameters is discussed, along with typical data showing the dependence of average film composition on electrolyte flow rate and *p*H. Finally, values of magnetic parameters closely related to the ultimate performance of the material as a memory device are given.

The process is shown schematically in Fig. 1. The substrate is a 0.005 in. diameter hardened Be-Cu wire which is carefully drawn in order to minimize scratches caused by dirt particles collecting on the dies. It is pulled through the apparatus at 6 in./min. The wire is protected from the laboratory atmosphere by a nitrogen blanket between each process step. An electrolytic alkaline cleaner removes organic soil and loose dirt, and an acid dip removes surface oxide. The wire surface at this state, although superior to that of ordinary commercially drawn wire, still shows (Fig. 2a) a large number of pits and small scratches under high magnification. In general, 1μ magnetic films plated onto this surface with no further preparation do not have satisfactory properties. The wire is then plated with 1μ of copper from a commercial plating bath.[1] Figure 2b shows the appearance of the wire surface after copper plating. This copper plate may serve to smooth the surface although it clearly does not eliminate the surface imperfections completely. The omission of the copper plating step in the process has the effect of raising the values of dispersion and minimum bit writing current (see discussion of magnetic properties for definitions) by a factor of from 2 to 4, depending on the local surface roughness of the substrate. The wire is rinsed in ultrasonically agitated deionized water between each of these preparatory steps.

[1] Unichrome copper plating process of M and T Chemicals, Inc.

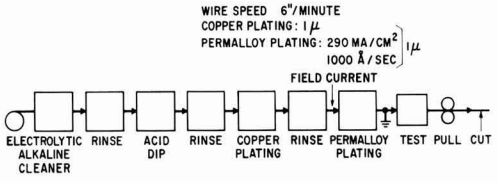

Fig. 1. Schematic view of plating process

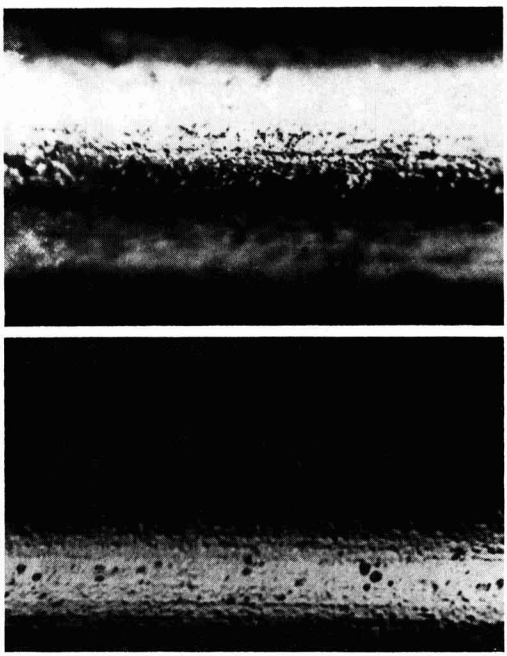

Fig. 2. Photomicrographs of Be-Cu wire surface with Nomarski type interference microscope (560X): (a) (top) after cleaning and acid dip; (b) (bottom) after copper plating.

Electrical contact is made to the wire by means of a gold plated brass wheel following the last rinse tank to permit the introduction of direct current into the wire while the permalloy film is being deposited. The circumferential magnetic field from this current results in a circumferential easy axis in the film where the application requires it. Alternatively, if an easy axis along the wire length is desired, a field is applied by means of Helmholtz coils mounted outside the permalloy plating chamber.

In the high current density-high agitation permalloy plating process used here, the composition of the plated

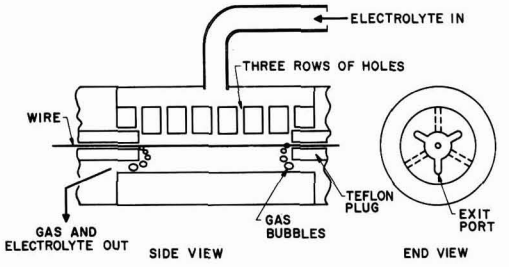

Fig. 3. Plating cell

alloy is a sensitive function of the electrolyte agitation at the wire surface. The permalloy plating chamber is designed to give uniformly high agitation along the entire length of wire being plated in order to reduce the possibility of composition gradients in the film. A centrifugal pump forces the electrolyte through the cell. Provision is made for regulating the electrolyte temperature, pH, and flow rate. The heart of the plating chamber is a Lucite tube with three staggered rows of holes drilled through the wall (shown schematically in Fig. 3). The electrolyte is forced through these holes and impinges on the surface of the moving wire at high velocity. It is removed through low impedance exit ports at both ends of the chamber. The wire passes in and out of this Lucite tube through Teflon plugs which extend into the region of high electrolyte agitation. Nitrogen gas is bubbled through the Teflon plugs to establish a plating region whose length is determined by the maximum penetration of gas bubbles into the Lucite tube. The bubbles penetrate past the Teflon tips by about one bubble diameter, which is approximately equal to the hole diameter of the Teflon plugs. The gas is swept out through the low impedance exit ports at each end by the high velocity electrolyte. This bubble seals serves two purposes. It prevents leakage of the electrolyte from the plating chamber into the rest of the apparatus, and it insures that the electrolyte agitation at the entrance and exit points of the wire is very nearly the same as the agitation in the central portion of the plating cell.

The nitrogen gas swept out from the plating region leaves the system through a tube in the outer part of the plating chamber. Since the electrolyte is not sealed off from air, a gradual drop of Fe^{2+} concentration is observed. This oxidation problem has not been serious since a change in electrolyte composition can be compensated by an adjustment in another process variable.

The importance of a near-zero magnetostriction composition in uniaxial magnetic films has been generally recognized (1). The stresses in evaporated or electrodeposited films cause severe degradation in uniaxial properties if the film is very far from the zero magnetostriction composition. For the plated wire, the composition requirements are even more severe because of the bending and twisting of the small diameter wire substrate which occurs during handling. It has been found that the average composition of the film should be held to within about $\pm$ 0.2% of the zero magnetostriction composition to avoid difficulties from strain-induced skew during memory assembly. In contrast, a detectable increase in dispersion of the film in an unstressed wire (resulting from internal stresses in the film) occurs when the film composition deviates from the zero magnetostriction composition by more than about $\pm$ 1%.

The required control of composition can be obtained by proper control of plating parameters. The composition of the plated alloy depends on bulk bath composition, temperature, pH, agitation, and plating current density. Electrolyte agitation affects the composition of the plated film through its effects on depletion layer

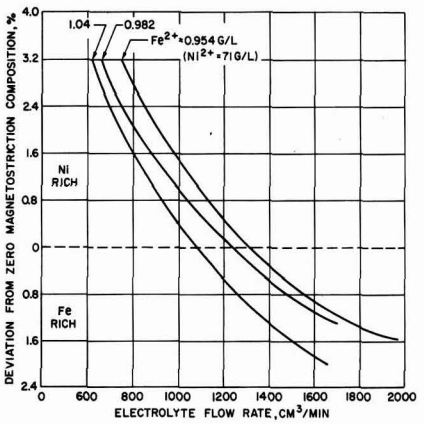

Fig. 4. Dependence of film composition on electrolyte flow rate (sulfamate bath). The zero on the ordinate corresponds to about 20% Fe. A composition "0.8% Fe rich" is therefore 20.8% Fe.

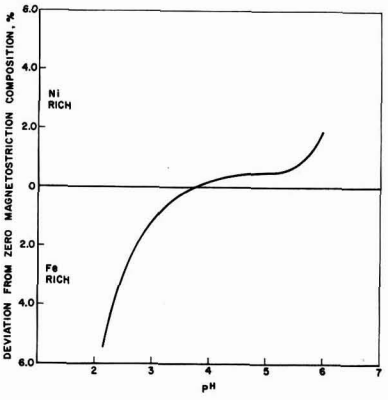

Fig. 5. Dependence of film composition on electrolyte pH (sulfate-chloride bath).

thickness and the composition of the electrolyte next to the substrate (which is in general different from the bulk composition). For a fixed plating cell geometry, agitation is dependent on the electrolyte flow rate. Figure 4 shows how the composition of the film, determined by x-ray fluorescence, depends on electrolyte flow rate with other parameters held constant. The probable effect of a change in plating cell geometry will be to move the curves of Fig. 4 along the flow rate axis. The increase in Fe content of the film with increasing flow rate (*i.e.*, increasing agitation) is in accord with the expected effect of decreased depletion layer thickness on the deposition rate of the more readily deposited metal (6) (Fe in this case).

Figure 5 illustrates the dependence of film composition on bath pH with other parameters held constant. The increase in Fe content below pH = 4 may be associated with a slight drop in cathode efficiency at low pH. This would increase the proportion of the more readily deposited metal in the alloy in a way similar to a decrease in current density (6).

In routine operation, the composition is measured indirectly by a magnetostriction measurement. One end of a plated wire is clamped and the other end twisted through a known angle. The resultant helical stress in the film introduces an easy axis skew, which is measured by the method of Belson (7). The sense and magnitude of the induced skew is a measure of

Table I. Magnetic characteristics

	$I_{b_{MIN}}$, ma	$I_{b_{MAX}}$, ma (with $H_\perp = 0$)
$H_{\perp_{WRITE}}$ = 9 oe:	4	35
6 oe:	8	38
4 oe:	14	48
3 oe:	23	57

Belson α_{90} = 1.2°
Belson skew = 0.3°
H_K (loop tracer) = 3 oe

the deviation of the average film composition from the zero magnetostriction alloy.[2]

The plating conditions are then adjusted until the magnetostriction is as close to zero as possible (corresponding to a composition of about 20% Fe, balance Ni). For example, the electrolyte flow rate or pH can be changed to modify the alloy composition, as indicated in Figs. 4 and 5. The average film composition can be controlled to ± 0.1%.

X-ray fluorescence composition measurements are based on an average over 3 feet of plated wire. The magnetostriction test provides a measurement of average composition over 1 in. lengths of wire. Measurements of magnetostriction over a series of adjacent 1 in. segments give the same result which shows that any composition variations along the wire length must be on a scale << 1 in. Further, the absence of bad bits resulting from magnetostriction effects when the wire is incorporated into experimental memory planes with approximately 0.05 in. bit centers (3) indicates that significant compositional variations along the wire are absent. Although the type of plating cell described here is designed to minimize agitation inhomogeneities along the plating length, experiments have not yet been carried out to measure composition gradients through the film thickness. In principle, one source of composition gradient often found in plated films because of the build-up of a depletion layer (8) should be absent here, since wire entering the plating cell encounters a steady state depletion layer.

Both sulfate-chloride (2) and sulfamate (4) baths have been used successfully.

Magnetic Properties

The most significant magnetic characteristics of the plated wire, as determined by an on-line pulse test, are given in Table I. The on-line test permits continuous monitoring of memory characteristics as the wire is produced. Only properties of films with the easy axis around the wire circumference are described here, since this type of film has been most thoroughly studied. Some of the characteristics of these films have been previously given (3).

A ½ in. long coil which supplies a hard direction field is mounted at the end of the plating apparatus. This coil defines the length of wire under test, and is long enough to effectively eliminate the geometry-dependent demagnetizing field in the hard direction. The pulse program is shown in Fig. 6. The parameters of primary interest are:

1. $I_{b_{min}}$, the bit writing current (*i.e.*, the current producing the easy direction field) needed to switch 90% of the available flux at a particular value of hard direction writing field $H_\perp$; and
2. $I_{b_{max}}$, the bit disturb current (with $H_\perp = 0$) which reduces the 90% written-in bit to 81% of full flux on the application of 100 disturbs. (For a 0.005 in. diameter wire, 1 ma ≡ 0.032 oe.)

[2] This technique is due to T. R. Long (to be published).

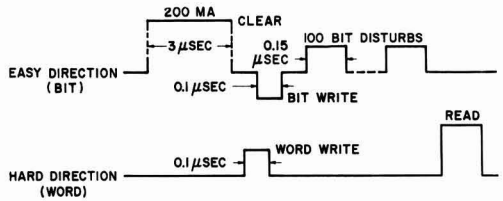

Fig. 6. Pulse program for on-line test of wire with circumferential easy axis.

Values of $I_{b_{min}}$ and $I_{b_{max}}$ for a typical film are given in Table I. Since variations of about ±20% in bit current amplitude and pulse width should be anticipated in actual memory operation, a good criterion for acceptable film quality is $I_{b_{max}} \geq 1.5\ I_{b_{min}}$. In addition, in order to be conservative, the measurements are made using a disturb pulse width 1.5 times the bit write pulse width since the disturb effect increases with pulse width (3).

The increase of $I_{b_{max}}$ with an increase in $I_{b_{min}}$ is a general phenomenon in these films. This result implies that the specification of an undisturbed read signal equal to 90% of available flux is not a complete description of the state of the film before the application of disturb pulses. The particular combination of $H_{\perp_{WRITE}}$ and bit writing current which is chosen to switch 90% of available flux affects the resistance to domain wall motion when easy axis disturb pulses are subsequently applied.

The effects of a larger number of disturb pulses and the simultaneous application of easy and hard direction disturb pulses are measured off-line, and have been discussed elsewhere (3).

Table I also contains values of α_{90} (dispersion) and skew as measured by the Belson technique (7), as well as the anisotropy field H_K measured by a loop tracer method. These measurements are of some use in qualitatively evaluating film samples, but are a poor means of quantitatively predicting performance under pulse switching conditions.

Acknowledgments

It is a pleasure to acknowledge the contributions of J. T. Chang, I. Danylchuk, U. F. Gianola, C. E. Johnson, T. R. Long, and A. J. Perneski. The author would also like to thank K. M. Olsen and R. F. Jack for samples of Be-Cu wire and Miss S. M. Vincent and J. E. Kessler for x-ray fluorescence analysis of the films.

Manuscript received June 30, 1964; revised manuscript received October 1, 1964.

Any discussion of this paper will appear in a Discussion Section to be published in the December 1965 JOURNAL.

REFERENCES

1. E. W. Pugh, "Magnetic Films of Nickel-Iron," in "Physics of Thin Films," Vol. 1, George Hass, Editor; Academic Press, New York (1963).
2. I. W. Wolf, *J. Appl. Phys.*, **33**, 1152 (1962).
3. I. Danylchuk, A. J. Perneski, and M. W. Sagal, Proc. of the 1964 Conference on Nonlinear Magnetics, Washington, D. C.
4. T. R. Long, *J. Appl. Phys.*, **31**, 123S (1960).
5. T. R. Long, Paper presented at the Detroit Meeting of the Society, Oct. 1-5, 1961.
6. "Electrodeposition of Alloys," Vol. I, Chap. 6 and 11, Abner Brenner, Academic Press, New York (1963).
7. H. Belson, Proc. of the 1963 Conference on Nonlinear Magnetics, Washington, D. C.
8. G. H. Cockett and E. S. Spenser-Timms, *This Journal*, **108**, 906 (1961).

Fluorescent Emission Spectra in II-VI Compounds

R. E. Halsted, M. Aven, and H. D. Coghill

Research Laboratory, General Electric Company, Schenectady, New York

ABSTRACT

Fluorescent emission spectra in "pure" and variously doped single crystals of CdTe, ZnTe, and to a lesser extent CdSe and ZnSe, have been recorded at temperatures of 25°K or below. These data have been tabulated and graphically presented along with prior low-temperature data on these materials, CdS, and ZnS. The pattern of results provides evidence for the existence of analogous defects throughout the II-VI family of compounds.

The fluorescent emission properties of the large band-gap II-VI compounds, particularly ZnS and CdS, have been investigated extensively in the past. Preparative procedures for maximizing specific emission bands in these materials in powder form have been established. Much attention has been given to models which at least provided a conceptual basis for organizing the results (1). Currently considerable attention is being given to the development of improved techniques for the preparation and purification of single crystals of II-VI compounds (2-4). Much progress has been made. One can therefore anticipate increasing application in the near future of diverse optical and electrical measurements to the determination of the position and nature of defect levels in these materials.

This work should be significantly expedited by making maximum use of evidence that analogous defect levels may exist in the various members of a given class of compounds. Similarities in preparative procedures, experimental behavior, and interpretation of results can thus be exploited. Prior studies of the ZnCdS phosphor system have provided a nice illustration of the utility of fluorescent emission data for establishing such analogs. With improved preparative control, it was established that the emission bands attributable to a given impurity exhibit a systematic shift in wavelength with host lattice variation from ZnS to CdS (5-7). Comparatively limited attention has been given to an extension of this evidence for analogous emission bands from the sulfides into the selenides and tellurides of zinc and cadmium (8-10).

In the course of investigations of II-VI compounds at this Laboratory, we have recorded emission spectra in "pure" and doped single crystals of these materials, generally at ~25°K. Data on the compounds CdTe and ZnTe provide a substantial addition to prior work. Emission due both to near-band-edge radiative recombination processes and deep impurity levels has been observed. Because of the survey nature of this work, these results will eventually be extended and perhaps some cases of inaccurate identification established.

We have noted, however, that the results do indeed provide a rather convincing extension of the evidence for analogous emission processes found in the ZnCdS system. A compilation of these data with prior work has been found to have current value in suggesting probable analogs between the transitions in different compounds. For example, it has provided a basis for appraising the relevance of electrical transport and optical measurements in p-type ZnTe and CdTe to a general understanding of acceptor defects in this class of materials. For this reason we have prepared the following tabulation of our data and selected prior published data on the positions of fluorescent emission bands for impurities from columns I, III, and VII of the periodic table in the sulfides, selenides, and tellurides of zinc and cadmium. Column V and other impurities were not included because of the limited amount of data now available for more than one II-VI compound. The information is also presented graphically. In addition to cataloging the new results, this form of presentation dramatizes the evidence suggested by the order in the data for probable analogs in the fluorescent emission processes in these materials. Some questions arising from these correlations are noted. However, no attempt is made to provide a critical examination of the evidence for the nature of the various recombination processes involved.

Experimental Procedure

Our method for taking fluorescent emission data has been conventional in nature. For data at liquid hydrogen temperature, samples were mounted with an adhesive varnish (G.E. 7031) on a coolable copper substrate in an evacuated housing. They were masked, except for an observation slit, with indium foil. A thermocouple, cemented in pressure contact with the edge of the crystal but shielded from exposure to the excitation radiation by the foil, was generally used to monitor the temperature of the sample. Samples were immersed in liquid helium for 4°K data. A 1000-w filtered high-pressure mercury arc (G.E. AH-6) was used as an excitation source. Both LiF prism and grating spectrometers were employed as dictated by resolution and wavelength range requirements. Spectrometer output was measured with either cooled PbS, infrared sensitive photomultiplier (RCA 7102), or 1P21 photomultiplier detectors. Spectrometer and detector combinations were calibrated in wavelength and response with standard sources.

Our results have been obtained primarily on single crystal material prepared at this Laboratory. Single crystals of all materials except CdTe have been grown from the vapor (11). CdTe crystals were grown from the melt (3). Samples of commercially available vapor-grown CdS and CdSe were also employed (12, 13). Data on material doped both before crystal growth and by diffusion after crystal growth have been recorded. Cleaved surfaces were preferably employed for observations of fluorescence. In order to obtain comparable results on chemically etched surfaces, some experimentation with etching procedures for each material was generally required.

Compilation Procedure

Tables I through VI present a compilation of our emission data and prior published data for the compounds ZnS, CdS, ZnSe, CdSe, ZnTe, and CdTe, respectively. For convenient reference we have also cited the low temperature band gap, E_g; the energy for exciton formation, E_{ex}; and the longitudinal optical phonon energy, $E_p(\mathrm{LO})$. E_g is established by adding to E_{ex} the exciton binding energy determined by observation of both ground and first excited states. Our somewhat arbitrary selection of prior data was prompted by considerations such as the following.

Data taken at 80°K or below have been cited wherever possible for several reasons. The position of low-temperature emission peaks can be related to well-defined band-gap energies for estimates of the binding energy of the defect levels involved. The emis-

sion peaks are also narrower and their maxima better defined. In some cases LO phonon structure can be resolved providing a measure of the transition energy unobscured by LO phonon emission. Between 0° and 80°K the band gap decreases in energy only ~0.01 ev. References were also favored which were concerned with tracing a given emission band through a variation in host lattice composition. Some recent references are cited to supply an entry into the literature concerned with providing a detailed description of specific recombination mechanisms. In some cases our data have been tabulated and prior references also listed. In most such cases we are assuming responsibility for some difference in detail, *e.g.*, temperature, but the results are regarded as being in agreement.

The peak positions given for emission bands with unresolved LO phonon structure are the energy equivalent of the wavelength of maximum emission on an energy per unit wavelength ($E/\Delta\lambda$) *vs.* wavelength plot. Most published data on these compounds are so plotted. The use of the physically more significant photons per unit photon energy ($P/\Delta E_p$) *vs.* photon energy plot would shift the position of broad peaks to somewhat lower energies since $(P/\Delta E_p) \propto \lambda^3(E/\Delta\lambda)$. Widths at half-height of these broad emission peaks are tabulated in parentheses after the peak position to provide an approximate description of the emission band. Evidence for small variations in the position of these spectra with crystal structure and identity of compensating defects have been omitted even though well established (5). However, some cases of extreme variation are noted.

Fluorescent emission of near-band-gap energy in II-VI compounds at low temperatures occurs as resolved sets of equally spaced emission lines formed by the simultaneous emission of photons and 0,1,2,--LO phonons (14). The relative intensities of lines within a set have been described by a relation of the form $I_n = I_0 N^n/n'$ (15). I_n is the relative intensity of the $(n+1)$th line involving the emission of a photon plus n LO phonons. N is the mean number of emitted phonons. Although the accuracy of this description appears to be poor when applied to experimental results with sufficiently small N, we have used it as a basis for characterizing spectra with resolved LO phonon structure. We have tabulated the position of

Table I. Data on fluorescent emission spectra in ZnS

E_g(14°K) = 3.84 ev (cubic), 3.91 ev (hexagonal).
E_{ex}(14°K) = 3.800 ev (cubic), 3.873 ev (hexagonal) (18).
E_p(LO) = 0.044 ev (14).

Dopant	Peak position [N] or (W/2)	Temp, °K	References
U, Cl	3.782* ev	10	(19)
U, Cl	3.76*	10	(19)
U, Cl	3.64* [1.0]	10	(19, 16)
U, Cl	3.00 (~0.25)	80	(19, 5)
U, D	2.63-2.75 (0.30)	80	(19, 20)
Ag > D	3.20 (0.25)	80	(5)
Ag ≈ D	2.86 (0.25)	80	(5)
Ag, Ag-D	2.0 (0.6)	80	(5, 21, 22)
Cu > D	2.85 (0.25)	80	(20)
Cu ≈ D	2.38 (0.28)	80	(20)
Cu	1.83 (0.50)	80	(21)
Cu-In	1.55 (0.50)	80	(23, 5)
Cu	0.84 (structured)	80	(24, 25)
Au-D	2.64 (0.28)	80	(6, 26)
Au-D	2.34 (0.26)	80	(6)
Au-In, Au-Ga	1.5 (0.5)	80	(5)

Table II. Data on fluorescent emission spectra in CdS

E_g(4.2°K) = 2.583 ev.
E_{ex}(4.2°K) = 2.554 ev (27).
E_p(LO) = 0.038 ev (14).

Dopant	Peak position [N] or (W/2)	Temp, °K	References
U	2.554* ev	1.6	(27, 42)
U	2.547* [3 × 10⁻⁴]	1.6	(27, 42)
U	2.536* [8 × 10⁻³]	1.6	(27, 42)
U	2.39*-2.42* [0.8]	25	(16)
U, D	1.70 (0.25)	80	(23, 28)
U, D	1.40 (0.36)	80	(23)
Ag	2.00 (0.20)	80	(5)
Ag	1.68 (0.25)	80	(5)
Au	1.94 (0.22)	80	(6, 29)
Au	1.55 (0.4)	300	(6)
Au	1.05 (0.28)	80	(6, 29)
Cu	1.57 (0.23)	80	(29)
Cu	1.18 (0.24)	80	(29)
Cu	0.75 (structured)	80	(24, 25)

Table III. Data on fluorescent emission spectra in ZnSe

E_g(4°K) = 2.820 ev (cubic).
E_{ex}(4°K) = 2.800 ev (cubic) (30).
E_p(LO) = 0.031 ev (14).

Dopant	Peak position [N] or (W/2)	Temp, °K	References
U, Cl	2.802*	4	(23)
U, Cl	2.797* [1 × 10⁻²]	4	(23)
U	2.793* [5 × 10⁻²]	4	(23, 32)
U	2.783* [0.3]	4	(23, 32)
U	2.69*-2.75* [0.6]	25	(23, 32, 16)
U	2.53 (0.15)	25	(23, 32)
U, D	2.07 (0.25)	25	(23, 32, 33)
Ag	2.61 (0.16)	25	(23)
Ag	2.22 (0.22)	25	(23)
Cu	2.34 (0.18)	25	(23, 8)
Cu	1.95 (0.18)	25	(23, 8, 33, 34)
Cu	1.25 (0.21)	25	(23, 35)
Au	1.78 (0.36)	170	(34)
U	1.45 (0.20)	25	(23)
U	0.78 (0.2)	25	(23, 35)
U	0.63 (0.2)	25	(23, 35)
U	0.56 (0.2)	25	(23, 35)

Table IV. Data on fluorescent emission spectra in CdSe

E_g(1.8°K) = 1.840 ev.
E_{ex}(1.8°K) = 1.824 ev (36).
E_p(LO) = 0.027 ev (14)

Dopant	Peak position [N] or (W/2)	Temp, °K	References
U	1.82*	25	(23)
U	1.81*	25	(23)
U	1.74*	25	(23, 16)
U	1.53 (0.15)	25	(23)
U	1.44 (0.15)	25	(23)
Ag-D	1.35 (0.20)	80	(29)
Cu-D	1.03 (0.20)	80	(28, 23)
Au-D	0.85 (0.20)	80	(29)

Table V. Data on fluorescent emission spectra in ZnTe

E_g(4°K) = 2.39 ev.
E_{ex}(4°K) = 2.382 ev (37).
E_p(LO) = 0.026 ev (14).

Dopant	Peak position [N] or (W/2)	Temp, °K	References
U	2.381*	25	(23)
U	2.375* [1 × 10⁻²]	25	(23)
U	2.31*-2.35* [0.23]	25	(23, 16)
U, Cu	2.24*, 2.21 (0.07)	25	(23)
Ga, In	2.11 (0.12)	25	(23)
U	1.88 (1.986*)	25	(38, 23)
U, Ga	1.65, 1.56 (0.25)	25	(23)
U	1.05 (0.12)	25	(23)
U	0.98 (0.12)	25	(23)
Ag	2.28*	25	(23)
Ag	1.92 (0.19)	25	(23)
Cu	1.97 (0.13)	25	(23)
Cu	1.47 (0.18)	25	(23)
Au	1.33 (0.2)	25	(23)
Ga	0.67 (0.16)	25	(23)

Table VI. Data on fluorescent emission spectra in CdTe

E_g(2.1°K) = 1.605 ev.
E_{ex}(2.1°K) = 1.595 ev (39, 40).
E_p(LO) = 0.021 ev (14).

Dopant	Peak position [N] or (W/2)	Temp, °K	References
U	1.595*	25	(14)
U	1.593* [1 × 10⁻²]	25	(14)
U	1.589* [4 × 10⁻²]	25	(14)
U	1.52*-1.56* [0.3]	25	(16)
U	1.45*	25	(14)
D	1.40-1.44 (0.08)	25	(14)
U	1.10-1.15 (0.11)	25	(23)
D	1.05-1.11 (0.11)	25	(23)
Ag	1.49*	25	(14)
Ag	1.19 (0.15)	25	(23)
Cu	1.23 (0.14)	25	(23)
Cu	0.88 (0.18)	25	(23)
Cu	≤0.55 (0.08)	25	(23)
Au	1.27 (0.11)	80	(41)
Au	0.72 (0.10)	25	(23)

the highest energy peak of the series and identified such energies with an asterisk. $N(\equiv I_1/I_0)$ is given in square brackets for a number of cases where the peaks were reasonably well resolved. We have attempted to select those band-edge spectra which appear to be dominant in pure materials. Some variability has been observed in the position of the exciton absorption line, and hence in the band gap in nominally pure materials (30). We have therefore tabulated band-edge emission data from one source for each compound, although citing other references. This procedure should permit a more significant determination of the energy differences between the various transitions listed.

Emission bands are identified with the addition of specific dopants. Generally speaking, there remains uncertainty in II-VI compounds as to the specific nature of the defect at which an emission process originates. Compensating native defects, isolated or associated, may be involved as well as the dopant. The specified impurity addition is therefore indicative of preparative procedure, but cannot be regarded as identifying the origin of the emission in any precise way. In presenting the data some abbreviations were introduced. The symbols for specific elements are generally employed with the exceptions of U and D denoting "undoped" (but not necessarily pure) and "donor" impurity, respectively. The use of D indicates that essentially the same result has been obtained with several impurities from columns III or VII of the periodic table. If D is linked to another element by other than a comma, *e.g.*, Ag > D, Ag ≈ D, Ag — D, the presence of both impurities is believed to be required. In some compounds the results have been shown to be dependent on the relative proportion of impurities; hence, *e.g.*, Ag > D.

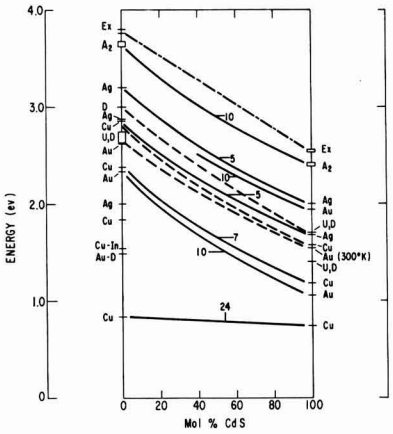

Fig. 1. Fluorescent emission energies in ZnCdS system

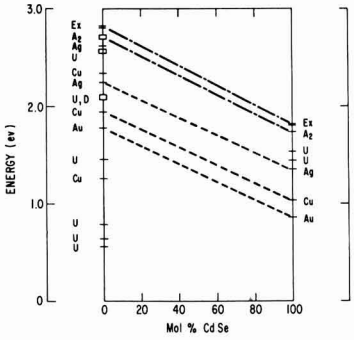

Fig. 2. Fluorescent emission energies in ZnCdSe system

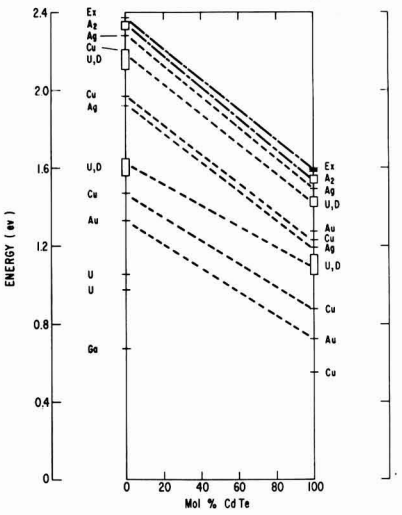

Fig. 3. Fluorescent emission energies in ZnCdTe system

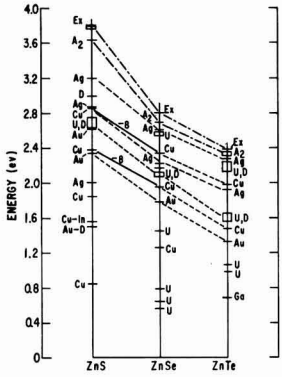

Fig. 4. Fluorescent emission energies in ZnSSeTe system

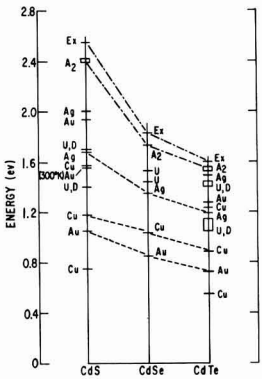

Fig. 5. Fluorescent emission energies in CdSSeTe system

This information is presented graphically in Fig. 1 to 5. The pattern of analogous emission processes suggested by the data is indicated by the connecting lines. Solid lines are employed where correlations have been previously established by a study of the relevant ternary compounds through a range of compositions. A reference is cited for each case of this type. Broken lines are used in two cases where the validity of the correlation appears assured even though their position

in compounds of intermediate composition has not been ascertained. Emission attributed to bound or free excitons is termed "exciton" emission and identified by its proximity in energy with exciton absorption or reflectance data. The energy scale of Fig. 1 to 5 does not permit an indication of the detail observable with high resolution in this region. Analogs of the "green edge emission" or "A_2" emission of CdS are identified by the unique characteristics of their spectra (16). Dashed lines are employed where the correlations are suggested by the pattern of results but have not otherwise been confirmed. If the correlations prove generally valid, one might expect the connecting lines to approximate the positions of emission bands in intermediate compounds. The curvature of these lines can, however, be substantial. It may perhaps be extreme in the case of ZnSeTe compounds where the band gap has been reported to go through a minimum at a composition $ZnSe_{0.35}Te_{0.65}$ (17).

Discussion

The data presented in Fig. 1 through 5 demonstrate that there exists a general regularity in the way the positions of the levels belonging to the different luminescence centers vary from compound to compound. Examination of the data for the more detailed features of such correlative relationships, however, generates many questions which at present have no simple or unambiguous answers. Some examples are illustrative.

Emission attributed to the recombination of excitons bound to various defects gives rise to quite complex spectra at liquid helium temperatures. Some prominent examples are included in Tables I and VI, although not resolved in Fig. 1 to 5. In the case of CdS, Zeeman effect studies of these emission and associated absorption spectra have identified three types of transitions present as: (*a*) exciton bound to a neutral donor defect, (*b*) exciton bound to an ionized donor, and (*c*) exciton bound to a neutral acceptor (27, 42). Free exciton recombination is also observed and identified by its coincidence in energy with exciton absorption. It becomes relatively more prominent at higher temperatures where the binding energy of an exciton to the above defects is small compared to kT. Analogous recombination processes occur in other compounds (43-45). Tentative identification of bound exciton processes in II-VI compounds other than CdS may be feasible by assuming that the energy by which the exciton is bound to a defect, E_{ex}-E_{exd}, is approximately a constant fraction, F, of the defect binding energy, E_d, for a given type of shallow defect. Here E_{exd} is the formation or recombination energy for an exciton bound to the defect. If the nature of a transition becomes known from magneto-optical studies, a knowledge of F should conversely permit an estimate of the position of the defect level involved. In silicon $F \approx 0.1$ for excitons bound to either donors or acceptors with defect binding energies up to 0.15 ev (43). The applicability of this relationship to the II-VI class of compounds requires the approximate validity of the effective mass approximation and a relatively constant ratio of hole-to-electron masses. For an exciton bound to a neutral donor in CdS a value for F of $0.0066/0.033 = 0.20$ was found (27). Comparable ratios for the dominant emission in the exciton region for n-type CdTe and ZnSe are indicated. The magnitude of F for the exciton bound to a neutral acceptor is uncertain in CdS since the depth of the active acceptor level is not known. Since the effective mass of electrons is smaller than the effective mass of holes in II-VI compounds, F may be smaller for acceptor defects than for donor defects (46).

Analogs of the green edge emission in CdS have been identified by their unique doublet structure. Currently two types of defect levels observed in electrical transport measurements could provide recombination transitions of appropriate energy. A correlation has recently been made between these spectra and the presence of double-acceptor levels near the conduction band in II-VI compounds (47). An explanation of the emission energy and structure, the temperature dependent characteristics, and the variability of the spectra with crystal doping appears possible on this basis (16). However, electrical measurements have also shown the presence of acceptor levels approximately 0.05 ev from the valence band in CdTe and ZnTe (48-50). Analogs of these levels in the selenides and sulfides would permit donor-acceptor-pair emission (51) in the energy ranges of interest. It remains to be determined whether one or both of these mechanisms are operative.

Figures 1 to 5 suggest that the pattern of "high" and "low" energy emission bands identified in the literatube for Cu, Ag, Au, and "self-activated" ZnCdS phosphors exists for the entire II-VI family of compounds. Thus the extensive effort which has been devoted to the identification of such emission processes as those occurring at 2.85 and 2.38 ev for ZnS:Cu, 2.7 ev for self-activated ZnS and 2.00 ev for CdS:Ag has immediate relevance in other compounds if the correlations are valid (52). Discrepancies remain to be resolved. For example, the "high energy Ag" band occurring at 2.00 ev in CdS:Ag has been attributed to a transition between a level near the conduction band and the valence band (53). The suggested analog in ZnTe, however, appears to involve a transition between the conduction band and a relatively shallow acceptor level which can be seen electrically (50).

In ZnS and CdS a structured emission band can be observed at ~0.8 ev. The structure is attributed to internal Cu transitions that are relatively uninfluenced by host lattice composition. Other transitions occur in the red and near infrared in ZnS which appear to depend strongly on the identity of both donor and acceptor impurity. ZnSe and ZnTe samples generally are found to exhibit infrared emission at photon energies below those discussed above. Further investigation may establish analogs among these.

Acknowledgments

The authors gratefully acknowledge contributions by their colleagues at the Research Laboratory, both by way of informative discussions and material for spectral analysis. L. H. Esmann provided skillful assistance with much of the experimental work.

This investigation has been supported in part by the U.S. Army Engineer Research and Development Laboratories, Fort Belvoir, Virginia, and in part by the Aerospace Research Laboratory, Office of Aerospace Research, U.S. Air Force.

Manuscript received Sept. 11, 1964. This paper was presented at the Toronto Meeting, May 3-7, 1964.

Any discussion of this paper will appear in a Discussion Section to be published in the December 1965 JOURNAL.

REFERENCES

1. See, *e.g.*, H. W. Leverenz, "Luminescence of Solids," John Wiley & Sons, Inc., New York (1950), or the more recent work D. Curie, "Luminescence in Crystals," John Wiley & Sons, Inc., New York (1963).
2. M. Aven and H. H. Woodbury, *Appl. Phys. Letters*, **1**, 53 (1962).
3. M. R. Lorenz and R. E. Halsted, *This Journal*, **110**, 343 (1963).
4. L. R. Shiozawa, J. L. Barrett, G. P. Chotkevys, S. S. Devlin, and J. M. Jost, Aeronautical Research Laboratory Contract No. AF33(616)-6865, Final Report, Period January 1960-December 1961 (unpublished).
5. W. van Gool, *Philips Research Repts.*, **13**, 157 (1958); Philips Research Repts. Suppl. No. 3 (1961).
6. M. Avinor, *This Journal*, **107**, 608 (1960).
7. H. Ortmann and H. Treptow, *Z. Naturforsch*, **16a**, 910 (1961).
8. F. F. Morehead, *J. Phys. Chem. Solids*, **24**, 37 (1963).

9. A. A. Bundel, Z. I. Guratskaya, and M. N. Noskova, *Optics and Spectroscopy*, **11**, 352 (1961).
10. M. Avinor and G. Meijer, *J. Chem. Phys.*, **32**, 1456 (1960).
11. W. W. Piper and S. J. Polich, *J. Appl. Phys.*, **32**, 1278 (1961).
12. Eagle-Picher Company, 1948 American Building, Cincinnati, Ohio.
13. Harshaw Chemical Company, 10064 Chester Ave., Cleveland, Ohio.
14. R. E. Halsted, M. R. Lorenz, and B. Segall, *J. Phys. Chem. Solids*, **22**, 109 (1961).
15. J. J. Hopfield, *ibid.*, **10**, 110 (1959).
16. R. E. Halsted and B. Segall, *Phys. Rev. Letters*, **10**, 392 (1963).
17. S. Larach, R. E. Shrader, and C. F. Stocker, *Phys. Rev.*, **108**, 587 (1957).
18. J. L. Birman, H. Samelson, and A. Lempicki, *General Telephone and Electronics Research and Development Journal*, **1**, 2 (1961). Exciton binding energy of 0.04 ev estimated.
19. H. Samelson and A. Lempicki, *Phys. Rev.*, **125**, 901 (1962) reports data on cubic ZnS. Other data are on hexagonal ZnS.
20. W. van Gool and A. P. Cleiren, *Philips Research Repts.*, **15**, 238 (1960).
21. M. H. Aven and R. M. Potter, *This Journal*, **105**, 134 (1958). Data converted to energy/$\Delta\lambda$ *vs.* λ plot to give tabulated λ_{max}(ev).
22. E. F. Apple and F. E. Williams, *ibid.*, **106**, 224 (1959).
23. Our data.
24. P. F. Browne, *J. Electronics*, **2**, 1 (1956). Position given for highest energy peak of structured emission band.
25. I. Broser, R. Broser-Warminsky, H. J. Schulz, Proc. Internat'l Conf. on Semiconductor Physics, Prague, 1960, p. 771.
26. S. T. Henderson, P. W. Ramby, and M. B. Halstead, *This Journal*, **106**, 27 (1959).
27. D. G. Thomas and J. J. Hopfield, *Phys. Rev.*, **128**, 2135 (1962); *ibid.*, **122**, 35 (1961).
28. B. A. Kulp, *ibid.*, **125**, 1865 (1962); B. A. Kulp and R. H. Kelley, *J. Appl. Phys.*, **31**, 1057 (1960).
29. See ref. (10). Absence of high energy Ag, Cu, or Au bands with excess activator is noted in CdSe.
30. M. Aven, D. T. F. Marple, and B. Segall, *J. Appl. Phys.*, **32S**, 2261 (1961). This reference notes a variability between samples which is believed due to variable content of sulfur impurity in General Electric ZnSe. Band edge data cited are from cubic crystals grown from high purity Eagle Picher ZnSe powder. (See M. Aven and P. R. Kennicott, Scientific Report No. 8, Contract No. AF19(628)-329, August 1964). Data on hexagonal ZnSe have also been reported (31).
31. E. F. Gross and L. G. Suslina, *Soviet Phys.-Solid State*, **4**, 2689 (1963).
32. D. C. Reynolds, L. S. Pedrotti, and O. W. Larson, *J. Appl. Phys.*, **32S**, 2250 (1961) enumerates additional emission bands in this energy region.
33. S. Larach, *J. Chem. Phys.*, **21**, 756 (1953).
34. L. Ya. Markovskii and R. I. Smirnova, *Optics and Spectroscopy*, **10**, 98 (1961).
35. B. A. Kulp and R. M. Detweiler, *Phys. Rev.*, **129**, 2422 (1963).
36. J. O. Dimmock and R. G. Wheeler, *J. Appl. Phys.*, **32S**, 2271 (1961).
37. A. C. Aten, C. Z. van Doorn, and A. T. Vink, Proc. Internat'l Conf. on Semiconductor Physics, Exeter, 1962, p. 696.
38. R. E. Dietz, D. G. Thomas, and J. J. Hopfield, *Phys. Rev. Letters*, **8**, 391 (1962).
39. D. T. F. Marple and B. Segall, To be published.
40. D. G. Thomas, *J. Appl. Phys.*, **32S**, 2298 (1961).
41. D. de Nobel, *Philips Research Repts.*, **14**, 361 (1959).
42. D. C. Reynolds and C. W. Litton, *Phys. Rev.*, **132**, 1023 (1963).
43. J. R. Haynes, *Phys. Rev. Letters*, **4**, 361 (1960).
44. D. G. Thomas, M. Gershenzon, and J. J. Hopfield, *Phys. Rev.*, **131**, 2397 (1963).
45. D. R. Hamilton, W. J. Choyke, and Lyle Patrick, *ibid.*, **131**, 127 (1963).
46. W. Kohn, footnote ref. (43).
47. M. R. Lorenz, B. Segall, and H. H. Woodbury, *Phys. Rev.*, **134**, A751 (1964).
48. M. R. Lorenz and B. Segall, *Phys. Rev. Letters*, **7**, 18 (1963).
49. D. G. Thomas and E. A. Sadowski, *J. Phys. Chem. Solids*, **25**, 395 (1964).
50. M. Aven and B. Segall, *Phys. Rev.*, **130**, 81 (1963).
51. D. G. Thomas, M. Gershenzon, and F. A. Trumbore, *ibid.*, **133**, A269 (1964).
52. See, *e.g.*, S. Shionoya, T. Koda, K. Eraand, and H. Fijiwara, *J. Phys. Soc. Japan*, **19**, 1157 (1964).
53. C. C. Klick, *Phys. Rev. Letters*, **2**, 418 (1959).

Luminescence of Europium in the Ternary System: La_2O_3-Gd_2O_3-Y_2O_3

R. C. Ropp[1]

Sylvania Electric Products Inc., Towanda, Pennsylvania

ABSTRACT

A detailed study of a rare-earth oxide ternary system activated by Eu^{+3} has shown that these phosphors are host-sensitized. There are matrix excitation bands present as well as a band attributed to perturbation of excited states of Eu^{+3}. An exciton mechanism is believed responsible for the matrix band and the field perturbation of the excited Eu^{+3} state.

The broad field of phosphors comprising rare-earth oxides activated by rare earths has been neglected in the past, primarily because of availability and purity of rare-earth materials. Recently, however, there has been a renaissance of interest in the fluorescence of rare earths, chiefly because of their applicability to the field of lasers. The earliest work by Urbain (1) stressed the cathodoluminescent properties of Gd_2O_3 and Y_2O_3 activated by small amounts of Eu, Er, Sm, or Tb. Subsequent investigations included description of the ultraviolet properties of La_2O_3:Pr (2), as well as Lu_2O_3, Sc_2O_3, or Y_2O_3, all activated by Sm (3). Later studies concentrated on Y_2O_3. Rosenberger (4) studied Y_2O_3:Er and La_2O_3:Er, and the spectroscopic transitions associated with Er^{+3} luminescence. Chang (5) studied conditions necessary for laser action of Eu^{+3} in Y_2O_3. Wickersheim and Lefever (6) gave general properties of luminescence of phosphors based on Y_2O_3 and La_2O_3, while in the most recent work, Axe and Weller (7) studied the effect of other rare-earth impurities on the luminescence of Eu^{+3} in Y_2O_3.

In an earlier work by the author (8), it was established that only three rare-earth oxides were effective as matrices in promoting rare-earth fluorescence: La_2O_3, Gd_2O_3, and Y_2O_3.[2] Of the rare-earth ions, only Sm^{+3}, Eu^{+3}, Tb^{+3}, and Dy^{+3} gave appreciable room-temperature luminescence. A study of the ternary system was conducted to define some of the mechanisms which produce luminescence in rare-earth oxide phos-

[1] Present address: Westinghouse Electric Corporation, Bloomfield, N. J.

[2] Here we designate Y_2O_3 and La_2O_3 as rare-earth compounds, although they contain no 4f electrons as does Gd_2O_3 [$4f^7$]. They do have similar chemical behavior.

phors, and to determine the energy processes which occur during the luminescent transitions. Compound formation in the ternary system is limited to the monoclinic $LaYO_3$ and to the hexagonal compound La_3YO_6 (9). Presumably, similar gadolinium compounds form.

Experimental Methods

The nitrates (or the oxides dissolved in concentrated nitric acid) of the requisite rare earths were dissolved to form 0.40M solutions. Mixtures of the ions in solution were made so that the required volumes totaled one liter before precipitation. The activator content was maintained at 2.5 mole % of the total cation content. Oxalic acid as a 10% solution was used as the precipitant, knowing the reaction to be quantitative in the presence of 5 mole % excess acid (10).

$$2M^{+3} + 3(C_2O_4)^{=} \rightarrow M_2(C_2O_4)_2 \cdot xH_2O$$

where $x = 2$ to 6 when the precipitation is carried out at 80°C. The precipitate was dried overnight at 110°C and fired in air at temperatures ranging between 500° and 1100°C to form the phosphor, using open silica crucibles.

La_2O_3 is unstable in air, spontaneously forming the hydroxide $La(OH)_3$ which is nonluminescent. Appropriate precautions to prevent hydrolysis are required prior to measurement of spectral properties.

The optical spectra were obtained with the aid of a commercial instrument (11) having two monochromators. The excitation monochromator provided a constant energy excitation beam over the range of 46,000 to 20,000 cm^{-1}. Either monochromator may be programmed separately to provide excitation or fluorescence spectra. The spectra are automatically compensated for wavelength energy but not for relative intensity. Resolution in the instrument varies from a few angstroms in the ultraviolet to about 10Å in the red region of the spectrum.

Experimental Results

Single-oxide systems.—All three single oxides are activated by Eu^{+3}, as shown in Fig. 1. The excitation properties differ, while the emission occurs in the same spectral region, the strongest line being a red emission line close to 6100Å.

La_2O_3 has the hexagonal A-type structure, while Y_2O_3 and Gd_2O_3 form the cubic C-type structure, both typical of the rare-earth oxides, depending on the atomic number and firing temperature (12). Table I lists published data found for these oxides as well as cell constants determined in this work.

The most intense emission line for Eu^{+3} in La_2O_3 is positioned at 16,100 cm^{-1}, while those for Gd_2O_3 and

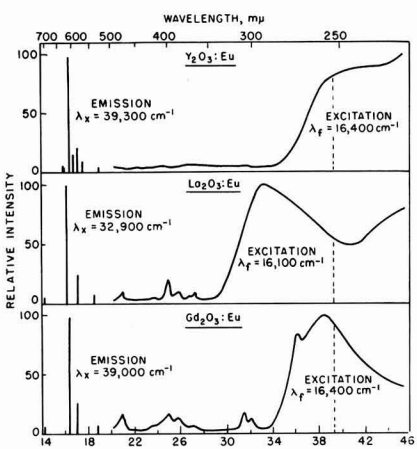

Fig. 1. Excitation-emission of Eu^{+3} in rare-earth oxide matrices

Table I.

Oxide	Firing temp, °C	Structure	a_o	c_o	Cation site symmetry	Number of oxide neighbors
La_2O_3	1000	Hexagonal	3.937Å	6.130Å	Distorted octahedral	7
Y_2O_3	1000	Cubic	10.604	—	Distorted cubic	6
Gd_2O_3	1000	Cubic	10.8	—	Distorted cubic	6
Gd_2O_3	1400	Monoclinic	Not determined		Distorted trigonal	7

Y_2O_3 are positioned at 16,400 cm^{-1}. These differences are attributed to symmetry changes at the cationic site where Eu^{+3} in Gd_2O_3 or Y_2O_3 can substitute in either of two sites having C_{2v} or S_6 symmetry. The site in La_2O_3 involves a peculiar sevenfold coordination having C_3 symmetry (13).

There are three distinct features in the excitation spectra. The low-intensity narrow bands are probably 4f → 4f transitions between levels of the activator atoms. There are two broad, intense excitation bands, one of which always appears at the same wavelength, regardless of activator (8). These are probably matrix excitation bands. The position and intensity of the other broad excitation band (thought to be an activator excitation band) are dependent on both the matrix and the incorporated activator (8).

The matrix excitation band of Y_2O_3:Eu occurs at about 2000Å. Those phosphors based on La_2O_3 all show the same broad matrix excitation band at 2200Å. The rather narrow excitation band in Gd_2O_3:Eu found at 36,000 cm^{-1} (2780Å) is caused by an excitation transition in the Gd^{+3} ion ($^8S_{7/2} \rightarrow {}^6I_J$). There is a broad excitation band peaking at about 47,600 cm^{-1} for Gd_2O_3:Eu because of matrix excitation.

The nature of the activator excitation band is more obscure. The bands might be attributed to 4f → 5d transitions or to a perturbed 4f → 4f transition in the Eu^{+3} activator center. Previous authors have favored the former, primarily because it is difficult to visualize or justify a mechanism involving perturbation of the "shielded" 4f electronic states.

The effect of structure on excitation.—The three matrices, La_2O_3, Y_2O_3, and Gd_2O_3, offer an ideal group for studies of matrix-activator interactions and the effect of site symmetry of fluorescent properties. Referring to Table I, it may be seen that all structures involve sites in which a departure from a regular symmetry is prevalent.

In a phosphor where host sensitization plays a primary role, long-range energy transport mechanisms would be expected to occur only in those matrices having a high degree of lattice-ordering. In noncrystalline materials, host sensitization (matrix excitation) does not generally occur.

Thus, the differences in excitation band position observed for the three systems would lead to the expectation that the matrix bands should be dependent on structure. The fact that Gd_2O_3 is dimorphic offers a method for determining the effect of structure on excitation bands. It would be expected that the intensity of the matrix excitation band would be highly dependent on the crystallinity of the matrix, and its position perhaps dependent on structure. Substantiating experimental data are presented in Fig. 2. Note that the monoclinic form has a broad peak apparent at 42,000 cm^{-1} (as well as the band due to Eu^{+3}). The cubic form, identified by x-ray analysis, also has two peaks whose relative intensities depend on firing temperature. The material fired at 600°C has one main peak at 39,400 cm^{-1}; another band appears at 44,000 cm^{-1}. The difference in intensity of this latter band is due to differences in crystallinity of the materials. Thus, according to x-ray diffraction analysis, the 600°C-fired material is much less crystalline and the matrix excitation band is much less intense than the

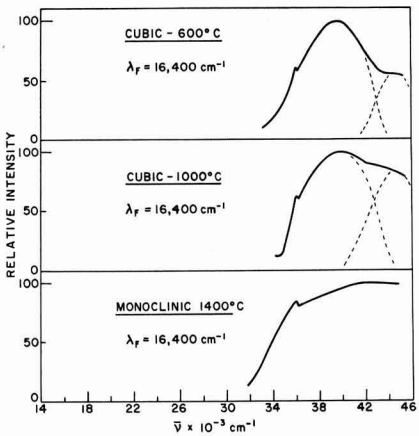

Fig. 2. Effect of structure on Gd_2O_3 : Eu excitation spectra

material fired at 1000°C. A previous paper (14) has shown that decomposition of the oxalates begins at 400°C and is complete at 600°C if given enough time for reaction. The materials were identified, by x-ray analysis, as cubic Gd_2O_3. The chief difference was in crystallite size (*i.e.*, crystallinity). Thus, the matrix excitation band intensity is a function of the degree of lattice-ordering.

There is one energy transfer process which occurs in the Gd_2O_3 phosphor, but not in Y_2O_3 or La_2O_3. This is the excitation transfer process corresponding to absorption within the Gd^{+3} ion (2780Å) by a transition within the 4f shell, with subsequent excitation of Eu^{+3}. This process is a separate excitation mechanism from the activator or matrix excitation processes.

The ternary system.—The ternary system forms only four compounds: $LaYO_3$ is monoclinic (9), and presumably $LaGdO_3$ has the same structure; La_3YO_6 is hexagonal, and likewise its conjugate, La_3GdO_6. No other compounds are known. Figure 3 shows a phase diagram found for the ternary system fired at 1000°C. Three separate single-phase regions were found: cubic, monoclinic, and hexagonal. Two-phase regions connect each with the other. The phase diagram must be regarded as approximate, since no specific effort was made to determine composition after firing. The data represent the initial cation ratios of ions in solution before oxalate precipitation and subsequent firing. Since these steps are essentially quantitative, no serious error is believed to have resulted (7). At 1400°C, the phase diagram changes so that the area of the cubic phase is reduced and the monoclinic region expands to include monoclinic Gd_2O_3.

It was found that the ultraviolet plaque response (2537Å irradiation) was a function of structure and not of composition (see Fig. 4). Thus, the hexagonal and monoclinic regions can produce 65% of standard manganese-activated cadmium-borate phosphor brightness. In the mixture having the cubic structure,

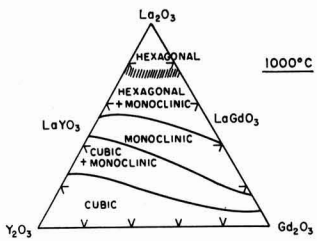

Fig. 3. Phase diagram of the ternary system La_2O_3-Gd_2O_3-Y_2O_3

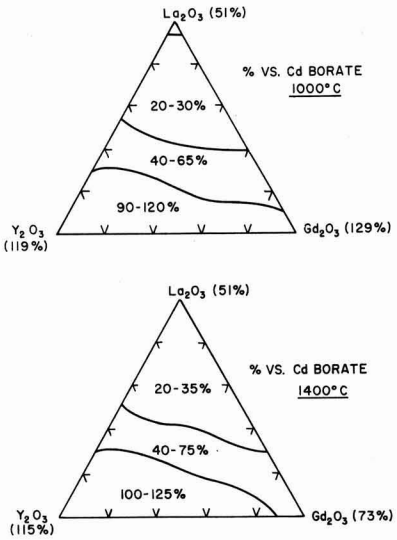

Fig. 4. Plaque brightness as a function of composition

those compositions containing no La have the highest brightness. Of these, the ultraviolet response seems to increase with Gd_2O_3 content, which would be predicted since the excitation-band maximum of Gd_2O_3:Eu is closer to 2537Å than that of Y_2O_3:Eu. The experimental data, accordingly, indicate simple solid-solution formation between Y_2O_3 and Gd_2O_3. However, the systems fired at 1400°C show decreased ultraviolet response as the transition from cubic to monoclinic symmetry occurs. Consequently, high ultraviolet response is found only in compositions having cubic symmetry.

In the ternary system, the differences in the excitation bands attributed to Eu^{+3} were determined as a function of composition. Since these excitation bands appear at widely separated points in the spectra, it is possible to classify the bands as to type. These data are given in Table II. Note that these are the excitation bands attributed to perturbation of excited states of the Eu^{+3} cation incorporated within the matrix.

It is readily seen that the excitation peak observed is not a function of structure but is due to the presence or absence of La. When La is present, the excitation is typical of the La_2O_3 spectrum, regardless of structure.

Discussion of Results

It has been demonstrated that there are two broad, intense excitation bands present in Eu^{+3}-activated rare-earth oxide phosphors. Of these, the band peaking at the higher energies has been shown, by correlation of x-ray and excitation data, to be associated with

Table II. Excitation as a function of composition

Composition La	Y	Gd	Structure	Excitation peak, cm^{-1}	Type of Eu^{+3} band
1.0	—	—	Hexagonal	33,600	La
—	1.0	—	Cubic	40,200	Y
—	—	1.0	Cubic	38,600	Gd
0.8	0.2	—	Hexagonal	34,600	La
0.7	—	0.3	Monoclinic + hexagonal	34,000	La
0.6	—	0.4	Monoclinic + hexagonal	33,700	La
0.5	0.4	0.1	Monoclinic	34,200	La
0.4	0.4	0.2	Cubic + monoclinic	34,500	La
0.4	0.6	—	Cubic + monoclinic	34,200	La
0.4	0.2	0.4	Cubic + monoclinic	34,100	La
0.2	—	0.8	Cubic + monoclinic	34,900	La
0.2	0.8	—	Cubic	34,700	La
0.1	0.1	0.8	Cubic + monoclinic	35,500	La + Gd
0.1	0.8	0.1	Cubic	37,500	Gd + Y
—	0.4	0.6	Cubic	38,000	Gd + Y
—	0.6	0.4	Cubic	38,200	Y + Gd
—	0.2	0.8	Cubic	37,700	Gd
—	0.8	0.2	Cubic	38,500	Y + Gd

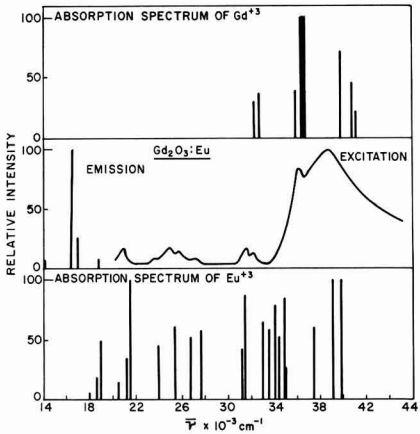

Fig. 5. Comparison of absorption spectra of Eu^{+3} and Gd^{+3}

matrix excitation, at least in Gd_2O_3:Eu. Because the matrix band intensity is dependent on lattice-ordering, one is led to the conclusion that this band is the result of exciton processes (excited states of the lattice). There are at least two possibilities of exciton formation. In one process, the exciton formation involves an oxygen p^6 electron in analogy to the alkali halides (15). In the other, cation exciton states in the lattice are involved. Such behavior has been observed also in the alkali halides, particularly KCl (16). Of the two mechanisms, the latter is preferred because of the behavior of the excitation bands in the ternary system. In the ternary system, the matrix excitation may occur by formation of "bound-states" in which a cation p^6 electron is excited to a p^5d or p^5s state, and the wave is propagated throughout the lattice (17). Such a mechanism gives rise to host sensitization and requires high lattice perfection. Experimental evidence supports these conclusions because of the fact that there are "typical" matrix excitation bands for all three compounds. Such bands are a function of the cation, not of the structure.

As mentioned previously, the nature of the activator excitation band is not at all clear. The broad, intense excitation bands found at lower energies might be attributed to one of three causes: (i) the matrix, (ii) the isolated activator center, or (iii) the interaction of matrix with activator center. Case (i) can be shown to be improbable by consideration of the energy levels of Gd^{+3} and Eu^{+3}, as shown in Fig. 5. The energy levels were determined by absorption measurements (18) of Gd^{+3} and Eu^{+3} in solution. Although the triplet absorption of Gd^{+3} appears shifted in Gd_2O_3:Eu, the main excitation band cannot be attributed to Gd^{+3}, but must be due to Eu^{+3} energy levels perturbed by the crystal field or some other factor.

Case (ii) must be eliminated because only narrow bands would be expected for $f^n \rightarrow f^{n-1}f^*$ transitions (and perturbation of the $f^n \rightarrow f^{n-1}d^*$ excited state would involve the crystal field interaction).

Case (iii) can be subdivided into two possibilities: (a) where the interaction arises between cation pairs M^{+3}-Eu^{+3}, and (b) where the perturbation is due to the interaction of a field on the activator center, *i.e.*, the perturbation of the excited state is dependent on crystal structure. In the ternary system, if (a) proved to be true, we would expect La_2O_3:Eu, which has poor response to 2537Å, to improve in brightness when small amounts of Gd, Y, or both, were present. Experimental results, given previously, eliminate this possibility.

Thus, one is left with the conclusion that the broad excitation band is due to perturbed excited states of the activator, Eu^{+3}. A possible explanation is that perturbation is caused by the exciton field. The exact nature of the perturbation mechanism, whether field-interaction or vibronic coupling, is unknown. However, the experimental evidence shows that the La_2O_3 matrix possesses the lowest energy exciton states, so that even a cubic structure containing but 20% La still possesses an excitation spectrum typical of La_2O_3 containing Eu^{+3}. With this mechanism, one would expect the position of the band (*i.e.*, the minimum energy required for excitation) to be a function of composition, not of structure, as observed.

Correlation (19) of the published values of the energy levels of Eu^{+3} (20) to the emission spectra shows that in La_2O_3 emission occurs from the $^5D_1$ level, whereas in the other cubic oxides, emission occurs from the $^5D_0$ state. This difference is attributed to the local site symmetry of the Eu^{+3} activator in the oxide structures.

It has been observed that a mechanism, in which $4f \rightarrow 4f$ transitions can possess high oscillator strengths with strong transition probabilities, can exist (21) and that such a transition would involve an enforced dipole type of transition at the C_{2v} site in the cubic crystal because of the lack of a center of inversion. Polarization of emission along the $\bar{1}\bar{1}\bar{1}$ plane would then be expected. It remains for more direct measurements to demonstrate the accuracy of the proposed mechanism.

Acknowledgment

The author is indebted to Dr. C. W. W. Hoffman for the x-ray powder diffraction measurements, to H. D. Layman for preparation of the samples, and to Dr. R. W. Mooney, M. A. Aia, and Dr. H. J. Borchardt for helpful discussions.

Manuscript received April 1, 1964.

Any discussion of this paper will appear in a Discussion Section to be published in the December 1965 JOURNAL.

REFERENCES

1. G. Urbain, *Ann. Chim. Phys.*, **18**, 293 (1909).
2. H. Gobrecht and R. Tomaschek, *Ann. Phys.*, **29**, 324 (1937).
3. F. A. Kröger, "Some Aspects of The Luminescence of Solids," Elsevier Publishing Co., New York (1948).
4. F. Rosenberger, *Z. Phys.*, **167**, 349, 360 (1962).
5. N. C. Chang, *J. Appl. Phys.*, **34**, 3500 (1963).
6. K. A. Wickersheim and R. A. Lefever, *This Journal*, **111**, 47 (1964).
7. J. D. Axe and P. F. Weller, *J. Chem Phys.*, **40**, 3066 (1964).
8. R. C. Ropp, *This Journal*, **111**, 311 (1964).
9. J. Cassedanne and H. Forestier, *Compt. rend.*, **253**, 2953 (1961).
10. K. G. Broadhead and H. H. Heady, *Anal. Chem.*, **32**, 1603 (1960).
11. W. Slavin, R. W. Mooney, and D. T. Palumbo, *J. Amer. Opt. Soc.*, **51**, 93 (1961).
12. I. Warshaw and R. Roy, *J. Phys. Chem.*, **65**, 2048 (1961).
13. L. Pauling, *Z. Krist.*, **69**, 415 (1928).
14. R. C. Ropp and E. E. Gritz, "Proceedings of the Fourth Rare Earth Conference," Gordon and Breach, New York, To be published (1964).
15. R. S. Knox and N. Inchaupe, *Phys. Rev.*, **116**, 1093 (1959).
16. F. Fischer, *Z. Phys.*, **160**, 194 (1960); see also: E. Ilmas, R. Kink, G. Liidja, and Ch. B. Lushchik, *Tr. Inst. Fiz. i Astron. Akad. Nauk. Est*, **23**, 221 (1963); V. L. Broude, A. F. Prikhot'ko, and E. I. Rashba, *Uspekhi fiz. Nauk (USSR)*, **67**, 99 (1959).
17. M. Trlifaz, *Czech. J. Phys.*, **13**, 631 (1963).
18. R. Prandtl and W. Scheiner, *Z. anorg. allgem. Chem.*, **220**, 107 (1934).
19. R. C. Ropp, Unpublished data.
20. G. S. Ofelt, *J. Chem. Phys.*, **38**, 2171 (1963).
21. B. R. Judd, *Phys. Rev.*, **127**, 750 (1962).

Diffusion-Induced Imperfections in Silicon

M. L. Joshi and F. Wilhelm

Components Division, International Business Machines Corporation, Poughkeepsie, New York

ABSTRACT

Diffusion-induced dislocations and precipitates have been studied through electron microscopy as a function of the diffusion depth. High concentrations of phosphorus and arsenic were diffused in (111) Si wafers to a shallow depth under the condition of constant solute surface concentration. Extensive dislocation networks were observed in phosphorus diffused wafers, whereas only a few single dislocations were detected in arsenic-diffused wafers. The results are shown to be in general agreement with Prussin's model of dislocation generation by relief of the stress due to solute lattice contraction of P and As.

The generation of dislocations in crystals by solute concentration gradients is well known (1-3). Such gradients can, for instance, be set up by fluctuations of the freezing rate during solidification. The solute concentration gradients imposed by shallow diffusion of large dopant concentration have been shown to cause the generation of dislocations in silicon (4-6). Queisser (4) found regular arrays of line patterns following crystal symmetry on silicon diffused with a high concentration of boron into a shallow surface layer and etched subsequently. These patterns were interpreted as slip lines due to the stress introduced into silicon lattice by the nonuniformly distributed, undersized, substitutional boron impurity. Prussin (5) produced etch pits marking dislocation sites on cleavage planes normal to the plane of diffusion in (111) silicon wafers symmetrically diffused with boron and phosphorus. It was shown that the stresses introduced by the solute lattice contraction were sufficient to produce dislocations. X-ray microscopy (6) and electron probe analysis (7) using essentially the reverse current of an irradiated diode as a read-out have given support to these findings. Jaccodine (8) reported the observation of individual dislocations forming networks in a phosphorous-diffused (111) silicon slice by transmission electron microscopy.

In this article, we present a study of diffusion induced dislocations as a function of the impurity diffusion depth in a (111) silicon wafer by the technique of transmission electron microscopy. Transmission electron micrographs were also obtained at the surface and near the junction in an arsenic-diffused wafer with surface concentration $\approx 5 \times 10^{20}$ cm^{-3}. This was done to explore the influence of the atomic size factor in the generation of defects by diffusion. On the basis of Pauling's tetrahedral covalent radii, P is undersized in Si, whereas As is almost the same size.

There is a considerable interest in regard to the diffusion-induced imperfections, other than dislocations. The detailed analysis of thin phosphorus-diffused layers in p-type silicon by Tannenbaum (9) has shown that at high concentrations of phosphorus ($>10^{20}$/cm^3) there is a significant difference between the profiles determined by sheet resistivity (corrected for ionization) and by radio tracer measurements. Tannenbaum interpreted this difference by postulating that part of the phosphorus is present not in the substitutional sites, but in the interstices or as precipitates. The detection of phosphorus precipitation by transmission electron microscopy in the diffused profile should be very informative in the light of the above consideration.

Experimental

Diffusion.—Three slices 10-mil thick and ~1 in. in diameter were cut parallel to (111) from a Czochralski-grown boron-doped ($\sim 10^{15}$ cm^{-3}) silicon crystal. The dislocation density of the crystal section from which the slices were cut was found by the etch pit technique to be less than 500/cm^2. The silicon wafers were lapped and chemically polished to remove any surface damage. Two of the wafers were symmetrically diffused on both sides with phosphorus in an open tube configuration at a temperature of 1150°C from a P_2O_5 source that was held at 300°C. The wafers were removed from the diffusion furnace and allowed to cool in room air on the quartz platform.

The third nondiffused wafer annealed at 1150°C served as a control to detect any possible defects introduced during specimen preparation. Both the etch pit technique and the electron microscopy revealed no such defects.

One of the diffused wafers was used for the determination of the solute profile, and the other for the study of the diffusion-induced imperfections. The surface impurity concentration was greater than 10^{21}/cm^3, as determined from the sheet resistance measurements and Irvin's curves (10). The p-n junction depth was about 2μ. The phosphorus-diffusion profile as obtained by the anodization-sectioning technique (9) in conjunction with the sheet resistivity measurements is shown in Fig. 1. This profile represents the ionized phosphorus distribution. The diffusion-induced imperfections were examined at the surface and at the depths 1/4, 1/3, 1/2, 1 and 1 1/2μ in the solute profile, as indicated in Fig. 1.

Specimen preparation.—The diffused wafer was cut by diamond-scribing into strips ⅛ in. wide. These strips were subjected to anodic oxidation, on the side to be studied. By successive removal of the oxide layers with HF, the appropriate depth in the solute profile was reached. The thickness of the removed silicon

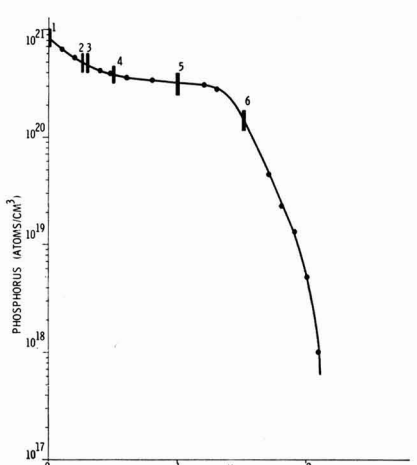

Fig. 1. Diffusion profile indicating levels of depth in the specimen where imperfections were studied; electron micrographs at point 1 to 6; four-point probe profile; diffusion: silicon 1150°C, P_2O_5 300°C.

layer per sectioning strip was determined from a comparison of the silicon oxide color to a standard film thickness gauge. The accuracy of this measurement is about ±50Å in 1000Å. Each strip was cut into ⅛ x ⅛ in. samples.

In order to obtain transparency to the electron beam in the microscope, the specimen had to be thinned to a few thousand angstroms. The samples were chemically polished down from the other side of the diffused surface under study by chemical polishing, using the solution: 300 cc of HNO_3 (70%), 200 cc of CH_3COOH (glacial), 100 cc of HF (47%), and 3g of iodine crystals. The surface to be studied was well protected from the chemical attack. Occasionally, samples were thinned by the electrolytic jet etch technique using a mixture of isopropyl alcohol and HF.

Electron Microscopic Observations

A Philips electron microscope (100B) was used for diffraction electron microscopy of the specimens. Individual dislocations are found in all investigated layers of the P-diffused wafer, down to a depth of 1½μ in the diffusion profile. At the surface (0μ depth) and at the depth of ¼μ (Fig. 2 and 3), rather complete networks were seen. Many threefold nodes are observed, joined by sections of almost straight dislocations. The network cells are of dimensions ½ to 1μ across. Dislocation densities up to 10^9 cm/cm^3 were measured. At the depth of 1/3μ into the diffused layer (Fig. 4), the dislocation networks appeared to be broken into smaller patches, sparingly connected with each other. At still greater depths (½ to 1½μ), the networks have practically disappeared (Fig. 5 and 6) and individual dislocations, some straight and some branched with one or two threefold nodes, are present.

The spreading of the network and the length of the component dislocations indicate that the dislocations lie in the plane of observation, *i.e.*, in the (111) plane. In many cases, where dislocations leave the (111) plane to terminate at the specimen surface, an abrupt change of direction takes place, revealed by the wavy appearance of the dislocations. The waviness [explained by the dynamical theory of diffraction contrast (11)] is due to inclination of the dislocation line with respect to the foil.

No stringent regularity exists in the network studied. Whenever small range regularity is detected, network cells tend to be hexagonal (Fig. 3), with dislocations joining in nodes under angles of 120°. Straight disloca-

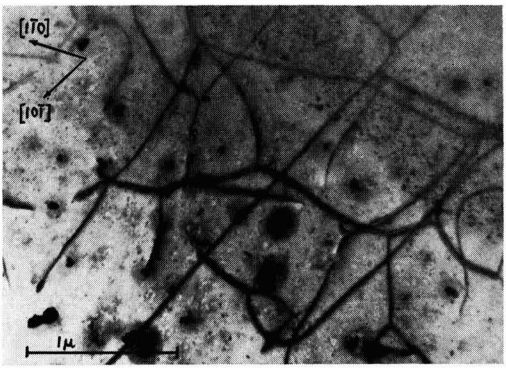

Fig. 2. Dislocation structure near the surface (depth 0μ)

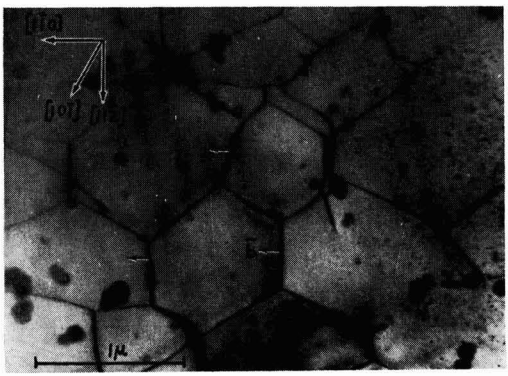

Fig. 3. Network of dislocations at depth ¼μ in the diffusion profile; arrows indicate Burgers vector.

Fig. 4. Breaking-up of dislocation network at depth 1/3μ

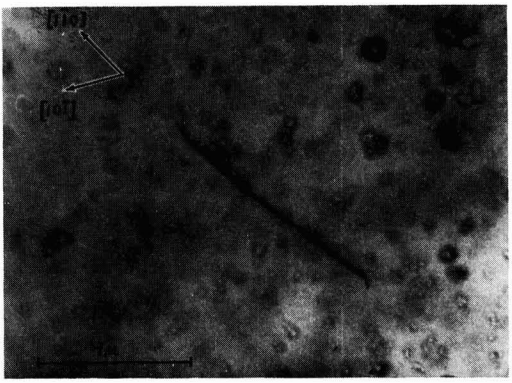

Fig. 5. Single dislocation at depth ½μ; only a few dislocations are found at this and at deeper levels.

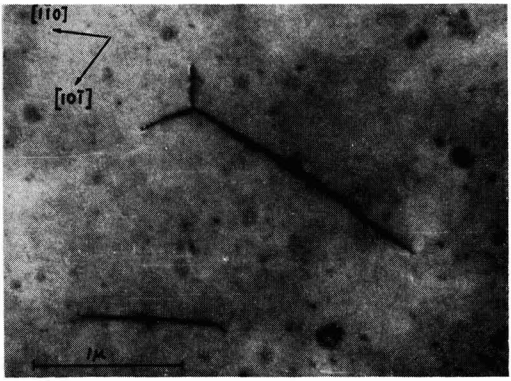

Fig. 6. Single dislocations at the 1½μ level; note wavy appearance at the ends of the dislocations, indicating tilt of these dislocation parts out of the plane of observation.

tions often lie in <112> directions. Isolated nodes, however, are occasionally found with their dislocations lying in a <110> direction.

The Burgers vector was determined on some of the dislocations (Fig. 3) by darkfield observation under illumination from a selected diffracted beam, indicating the edge character of the dislocations. They are of $a/2$ <110> type, in agreement with the findings of other researchers (6, 8).

Tilt of the specimen in the electron microscope revealed no other dislocations other than those shown in Fig. 3. The threefold nodes of the dislocation networks observed were contracted; no indication of extension is present. Figure 7 represents several groups of almost-straight parallel dislocations at $1/3\mu$ depth at the magnification of 12,000X. They seem to form a triangular pattern, with dislocations lying in <110> directions—interpreted as lying on {111} planes other than the plane of the specimen.

Dislocations in the specimen studied are rather immobile. No dislocation motion under the stress of the electron beam was observed in the electron microscope. Occasionally microcracks are observed in the material, created during the specimen preparation.

A (111) silicon wafer from a pulled silicon crystal doped with P ($>5 \times 10^{20}/cm^3$) was investigated for comparison with the diffusion-induced defects. Only very few dislocations inclined to the plane of observation were found in these specimens (Fig. 8). No other defects than dislocations were found.

On the magnification scale employed (30,000X), the dislocation distribution is considerably inhomogeneous.

Fig. 7. Low-magnification micrograph reveals traces of dislocations lying in the three {111} planes, projected upon the plane of observation. In this micrograph (taken at a depth of $1/3\mu$), an unusually high dislocation density (for this depth) is found, not characteristic for this level when compared to many other observations.

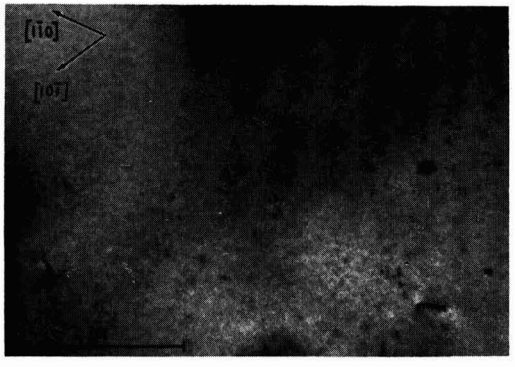

Fig. 8. Phosphorus-doped sample ($\sim 10^{21}$ at./cm^3); only a few short dislocations are present.

Frequently, particles of crystalline shapes (Fig. 9) are found in the diffused specimen throughout the diffusion profile studied herein. Their distribution also varies considerably in the different areas investigated. There are square, hexagonal and elongated particles of various apearances, with sizes ranging from 500Å to about 1μ. It is strongly suspected that these particles are phosphorus precipitates. Dark-field imaging did not give any indication of coherence of these particles with the parent lattice. The particles retain their shapes even in very fine detail when the specimen is washed in concentrated HNO_3 and subsequently in concentrated HF. They appear, however, to be lightened in contrast after the acid treatment.[1]

Arsenic diffused (surface concentration, $5 \times 10^{20}/cm^3$) boron-doped ($\sim 1.5 \times 10^{16}/cm^3$) silicon samples were examined at the surface and near the junction. Only a few single dislocations were observed; they often seem to lie almost perpendicular to the plane of observation (Fig. 10). Needle-type precipitates were observed at some places near the surface. No precipitation was detected near the junction.

Discussion

The electron microscope investigation gives evidence of the presence of dislocations and precipitates in silicon specimens, with a diffusion gradient of a high concentration of phosphorus. The absence of any significant amount of dislocations in the uniformly doped phosphorus ($> 5 \times 10^{20}/cm^3$) specimen should indicate that it is not necessarily the high solute concentration that induces dislocations. The small distribution coefficient ($k_0 = 0.35$) in phosphorus doping of single crystals could cause local concentration fluctuations, giving rise to the few dislocations seen in Fig. 9. The extensive dislocation networks seen in the diffused-phosphorus specimens are the result of relief of the stress gradient introduced by the solute lattice contraction of phosphorus diffused in silicon. Incidentally, the origin of the diffuse regions of extra x-ray scattering power observed on the glide plane traces in the case of silicon grown by floating-zone process has been suggested by other researchers to be these dislocation networks (12, 8). In addition, the regular arrays of the line markings (4) revealed by etching seem to be slip lines caused by glide on {111} planes, which our observations on dislocation networks corroborate.

The determination of the Burgers vectors in some experiments (Fig. 2), indicates that these particular dislocations seem to possess almost-pure edge character. These dislocations are oriented very closely in a <112> direction. The pure-edge dislocation on the (111) plane with a/2 <110> Burgers vector in the case of a diamond lattice is a composite dislocation which

[1] In a similar investigation, Schmidt and Stickler (14) have recently reported the identification of a silicon phosphide phase by transmission electron microscopy.

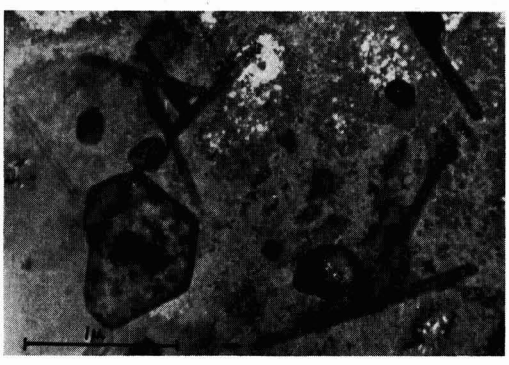

Fig. 9. Photo shows particles found in many areas throughout the diffused profile.

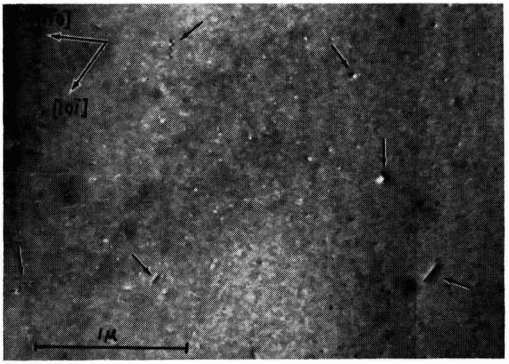

Fig. 10. Small dislocations in an As-diffused specimen; some are pointed out by arrows; micrograph taken near the surface.

occurs when the axis of a simple 60° Read's dislocation (with 1.4 broken bonds per lattice constant) changes alternately from one <110> orientation to another (13). Under the conditions of diffusion and solute lattice contraction such a dislocation (which requires 1.63 broken bonds per lattice constant) could be energetically possible.

The dislocation networks in the (111) plane of observation give credence to Prussin's concept of the stress relief by diffusion-induced dislocations. Since the dislocations must lie in the diffusion plane for the stress relief, only the six {111} slip systems with Burgers vectors a/2 <110> lying in {111} planes other than the plane of diffusion can be activated (according to Prussin). Only the edge components of these Burgers vectors contribute to the strain relief in the diffusion plane. The generation of the dislocations with predominant edge character is also consistent with this model. In the case of diffusion from a constant solute surface concentration (*i.e.*, for a strictly erfc distribution), Prussin derived a Gaussian dislocation distribution from the surface to a point in the diffused layer where the dislocation density drops to zero. The etch-pit density distribution on the cleaved plane extended half way into the diffusion profile in Prussin's own experiment (of deep diffusion of phosphorus in silicon). The significant feature of our study is that a dislocation density of 10^9 cm/cm^3 extends from the surface to about 1/3μ depth and then begins to drop very rapidly and is negligible beyond a quarter of the way into the profile.

The surface dislocation density (according to Prussin's model on the basis of the solute lattice contraction coefficient $\beta \approx 10^{-24}$ cm^3/atom) is $\approx 3 \times 10^8$ cm, which is within one order of magnitude of our experimental observation. However, the dislocation penetration into the interior in our experiment seems shallower than expected. Considering the inhomogeneity of dislocation distribution on the scale of observation, it is not possible to compare the distribution actually obtained by electron microscopy to the expected one. The total number of dislocations created at the beginning of the diffusion process is dispersed into the interior of the sample during transport of the solute. This dispersion is likely to be restricted because of the nodes tending to anchor the dislocation networks.

It is also invariably observed that solute profiles are not erfc-type when high amounts of impurities are diffused into very shallow depths. Both of these considerations (anchoring and solute profiles) may be responsible for the deviations of the dislocation distributions-based strictly on the erfc distribution of the solute. The likely effect of dense dislocation networks in the diffused surface affecting the sheet resistivity measurements should not be neglected in estimating impurity concentration from Irvin's curves.

The absence of dislocation networks in the case of a large amount of arsenic diffusion indicates the importance of the degree of atomic misfit. The misfit ratio r/r_o (where r and r_o are Pauling's tetrahedral covalent radii of the solute and silicon) for P and As is 0.932 and 1.0, respectively. The incorporation of As in Si, consequently, would involve very little strain. The high surface concentration of P ($> 10^{20}$/cm^3) in comparison with that of B ($\approx 3 \times 10^{19}$/cm^3) needed for observation of slip patterns (4) is another example of the solute lattice contraction effect ($r/r_o = 0.746$ for B).

The observation of particles believed to be phosphorus precipitates indicates that the strains introduced into the diffused samples are locally inhomogeneous. The origin of the precipitates lies in the diffusion process, and well-defined shapes imply crystallinity (14). The incorporation of such particles may contribute to the deviation of the diffusion profile from the expected one. It should not be surprising if these precipitates, which extend almost to the p-n junction, affect the electrical behavior of the devices containing large amount of P diffusant.

Acknowledgments

The authors wish to express their gratitude to E. S. Wajda for suggesting the problem and helpful discussions. They also wish to thank F. W. Schneider, J. N. Ramsey, J. G. Christ, and G. A. Silvey for their valuable help and encouragement. They are grateful to S. Mader for his helpful comments.

Manuscript received June 5, 1964.

Any discussion of this paper will appear in a Discussion Section to be published in the December 1965 JOURNAL.

REFERENCES

1. A. J. Goss, K. E. Benson, and W. G. Pfann, *Acta. Met.*, **4**, 332 (1956).
2. F. C. Frank, *Advances in Phys.*, **1**, 91 (1952).
3. W. A. Tiller, *J. Appl. Phys.*, **29**, 611, (1958).
4. H. J. Queisser, *ibid.*, **32**, 1176 (1961).
5. S. Prussin, *ibid.*, **32**, 1876 (1961).
6. G. H. Schwuttke and H. J. Queisser, *ibid.*, **33**, 1540 (1962).
7. J. J. Lander, H. Schreiber, Jr., T. M. Buck, and J. R. Mathews, *Appl. Phys. Letters*, **3**, 206 (1963).
8. R. J. Jaccodine, *ibid.*, **4**, 114 (1964).
9. E. Tannenbaum. *Solid State Elect.*, **2**, 123 (1961).
10. J. C. Irvin, *Bell System Tech. J.*, **41**, 387 (1962).
11. A. Howie and M. J. Whelan, *Proc. Roy. Soc.*, **A267**, 206 (1962).
12. A. E. Jenkinson and A. R. Lang, "Direct Observations of Imperfections in Crystals," p. 471, Interscience Publishers, New York (1962).
13. J. Hornstra, *J. Phys. Chem. Solids*, **5**, 129 (1958).
14. P. F. Schmidt and R. Stickler, Recent News Paper presented at the Toronto Meeting of the Society, May 3-7, 1964.

TriPyramid Growth of Epitaxial Silicon

Morio Inoue

Research Laboratory, Matsushita Electronics Corporation, Takatsuki, Osaka, Japan

ABSTRACT

The tripyramids in vapor grown epitaxial silicon on substrates of (111) orientation were examined by chemical etching and x-ray diffraction techniques. The growth patterns of the tripyramids were brought out clearly by etching the epitaxial layer with the Sailer etch and the iodine etch successively. The tripyramids consist of twinned crystallites of [511] orientations. They originate at the interface between the substrate and the epitaxial layer. The cause of twinning was proved to be the formation of silicon carbide on the surface of the substrate. A crystallographic model was derived from the experimental results.

Epitaxial silicon films grown on single crystal substrates by the vapor decomposition method often contain stacking faults and tripyramids. The stacking faults have been investigated by many authors using chemical etching (1) and electron transmission techniques (2). It has been shown that the number of the stacking faults depends on both the physical perfection and amount of surface contamination of the substrate (3).

In addition to the stacking faults, growth hillocks, called tripyramids (4), have been observed on {111} substrates (5, 6). Batsford *et al.* reported that the residual water and organic solvents during chemical polishing induce the stacking faults and the tripyramids (3). Those were produced during the film growth, and they have been often found to be associated with the stacking faults. The tripyramids seen on epitaxial silicon layers obtained by reduction of silicon halide have also been observed on some germanium layers deposited by cathodic sputtering (7). Miller *et al.* (5) proposed a crystallographic model and a formation mechanism for the pyramids. However their model does not seem satisfactory to explain our geometrical observation by chemical etching and x-ray diffraction. A new model is proposed and the geometry and origin of the tripyramid growth are discussed in this paper.[1]

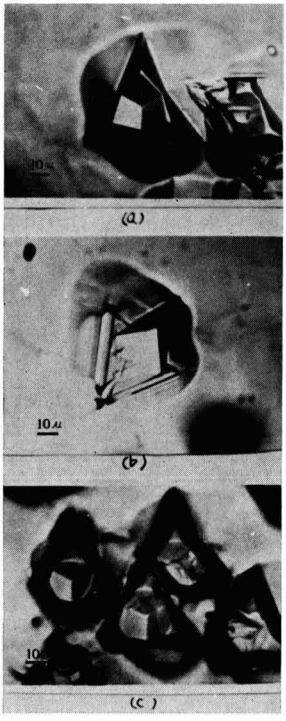

Fig. 1. Microphotographs of tripyramid growth on Si (111): (a) a typical tripyramid, (b) a monopyramid, (c) modified tripyramids.

Experiments

Epitaxial growth.—The epitaxial layers were prepared by silicon tetrachloride vapor decomposition at 1250°C in a hydrogen atmosphere (8). Chemically etched silicon wafers of (111) orientations were used as substrates. A substrate was placed on a graphite susceptor and heated by induction. The final removal of oxide was carried out in a hydrogen stream for 15 min at a temperature of 1260°C. The growth rate was approximately 1μ min^{-1}. The grown layers were usually $10 \sim 1000\mu$ in thickness.

Figure 1 shows a starlike hillock on the epitaxial layer called a tripyramid. The size and height of the tripyramid hillocks vary proportionally to the deposition thickness of the layer. They originate at the interface between the substrate and the epitaxial layer. Usually they exhibit figures similar to the one shown in Fig. 1a, but in a particular case monopyramids (Fig. 1b) and modified tripyramids (Fig. 1c) were observed. The geometry of the tripyramids were clarified by measuring the height and length under the optical microscope (Fig. 7).

Chemical etching study.—The internal crystallographic structure of the growth pyramids has been investigated by chemical etching techniques. The Sailer

[1] After this work was completed, a paper on the tripyramid imperfections was published by T. L. Chu and J. R. Gavaler, *Phil. Mag.*, 9, 993 (1964). They had studied the structure of tripyramids by chemical etching and optical microscope techniques. Their crystallographic analysis is similar to that of this work. However, their work does not contain the nucleation mechanism of the tripyramid.

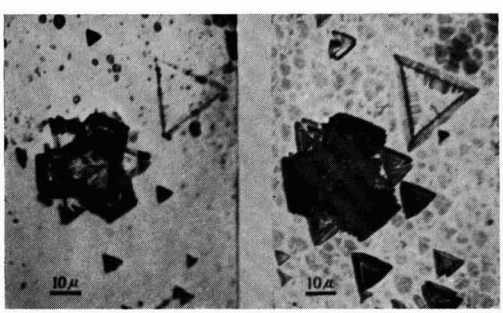

Fig. 2. Etch figure of tripyramid etched with Sailer etch: (a) (left) 2 hr, (b) (right) 3 hr. Dislocation etch pits and triangular etch figures of the stacking faults are revealed simultaneously.

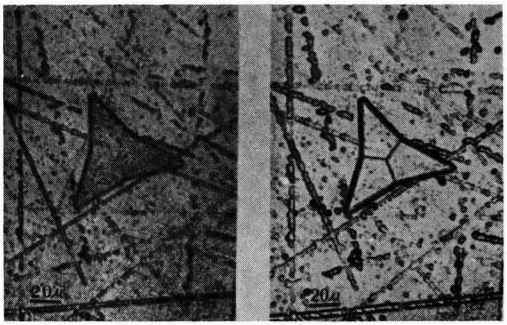

Fig. 3. Etch figure of tripyramids: (a) (left) etched with Sailer etch for 1 hr after partial removing of the hillock; (b) (right) the same samples were etched successively with iodine etch for 10 sec.

etch[2] and the iodine etch[3] were used in this work to bring out clearly the growth pattern of the pyramids. Figure 2 shows an etch figure of a tripyramid etch with the Sailer etch for 2 ~ 3 hr at room temperature. The copper deposited on the surface during Sailer etching was removed with nitric acid. Triangular defect boundaries associated with the tripyramids and isolated stacking faults were definitely revealed. As the Sailer etch shows clearly the area of a tripyramid, but does not reveal its inner structure, a modified etching was tried.

The samples were subjected to the Sailer etch for 1 hr and to the iodine etch for about 10 sec after hillocks were removed by lapping the surface with alundum powder and diamond paste. Whereas etching with the Sailer etch for 1 hr only reveals outlined boundaries (Fig. 3a), a following short period of iodine etching definitely etches the Y-shaped inner boundary between three incoherent crystallites (Fig. 3b). The angle at the tip of the starlike figure is 43°. Surrounding defect boundaries exhibit faster etch rates than inner Y-shaped boundaries. Besides these outer and inner boundaries, stacking faults and twin boundaries are also etched definitely by this technique as shown in Fig. 4. Figure 4 shows the etch figure after the double etching described above. Growth pyramids often associate with stacking faults (Fig. 2a and Fig. 4). It is noted that the stacking faults and the tripyramids are concentric in their configuration and are rotated 60° to each other.

In Fig. 4 the length of an equilateral triangle due to a stacking fault is equal to the distance between two adjacent tips of a starlike tripyramid configura-

[2] 3000 ml NHO_3 + 600 ml HF + 2 ml Br_2 + 23g Cu $(NO_3)_2$ dilute 10:1 with deionized water before use.

[3] 110 ml glacial CH_3COOH + 100 ml HNO_3 + 50 ml HF + 0.3g I_2.

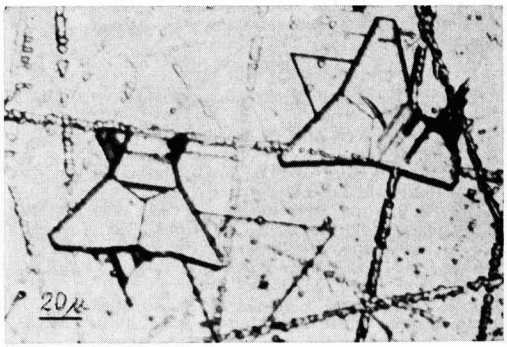

Fig. 4. Etch figure of tripyramids and stacking faults. Etched with Sailer etch for 1 hr and iodine etch for 10 sec.

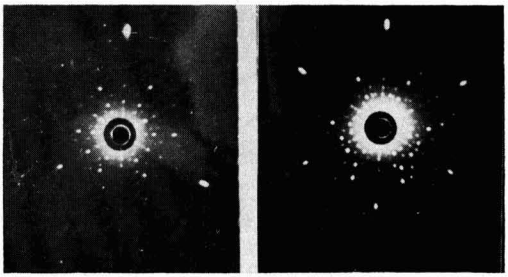

Fig. 5. X-ray back Laue reflection photograph: (a) (left) substrate silicon of [111] orientation; (b) (right) tripyramid hillock region of an epitaxial layer.

tion. This shows that the tripyramids originate at the substrate-epitaxial layer interface and grow in a similar way to the stacking faults. Moreover, it was proved by etching the cross section, that in the presence of stacking faults, the tripyramids originate at the same point as the stacking faults.

However, a tripyramid as shown in Fig. 3b, not associated with the triangular defects of a stacking fault, is often observed. This figure suggests that stacking faults are not essential to the growth of tripyramids.

X-ray back reflection.—The orientation of the crystallite can be shown up by x-ray back reflection. Laue photographs were taken on epitaxial layers with a 80μ growth thickness. A grown layer whose density of tripyramids was more than 5 x 10^4 cm^{-2} showed the following mixed Laue spot pattern (Fig. 5b). (On the sample, whose tripyramid density was less than 1 x 10^3 cm^{-2}, the spot pattern due to only the [111] orientation was observed.)

(I) [111] substrate
(II) [111] 180° rotated twin
(III) [511] due to the rotation about $[\bar{1}11]$ as twin axis.
(IV) [151] due to the rotation about $[1\bar{1}1]$ as twin axis.
(V) [115] due to the rotation about $[11\bar{1}]$ as twin axis.

(I) is the substrate orientation and the epitaxial area free from the tripyramids which has substantially a [111] orientation (Fig. 5a). (II) is 180° rotated twins about the [111] substrate orientation. (III), (IV), and (V) are also twin orientations to the substrate crystal, although their axes are not parallel to the substrate [111] direction. Above five axes gave nearly the same intensities, but sometimes one of the intensities of (III), (IV), and (V) became predominantly when one of the three crystallites of the tripyramid grew exclusively as shown in Fig. 1b.

The crystallite orientations of the tripyramids were clarified by the correspondence between the boundary figure of etching and the results of x-ray diffraction (described in detail in the discussion).

Electron diffraction study.—In order to know the origin of four kinds of twins, substrate surfaces were examined by electron diffraction. It was proposed that the overgrowth of SiC on silicon originate twinning of the crystal (5). A silicon wafer of (111) orientation on which carbon of a few angstrom in thickness was deposited in vacuum, was heated at a temperature of 1175°C for 15 min in a hydrogen stream. Electron diffraction showed that the carbon coated silicon surface reacted with the carbon to form silicon carbide (α-SiC). When carbon-coated silicon wafers were used as substrates, the epitaxial layer inevitably produced many tripyramids. Figure 6 shows the effect of carbon deposition on tripyramid nucleation. On the left half

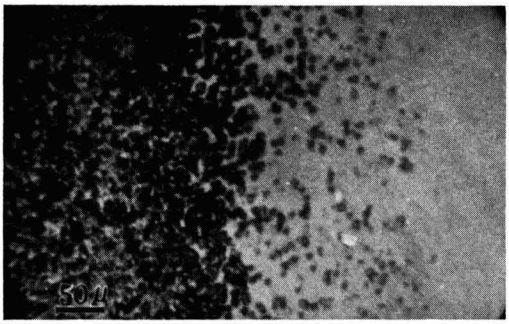

Fig. 6. Effect of carbon deposition on tripyramid nucleation. A carbon film was deposited on the left half region before epitaxial growth.

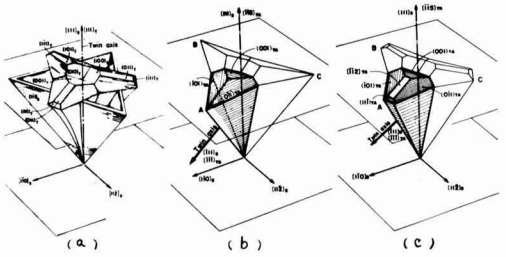

Fig. 7. Three-dimensional diagram illustrating the geometry of the tripyramid: (a) Miller's model, (b) and (c) author's model.

region, a carbon film was deposited before epitaxial growth. In the growth system, a graphite pedestal used as RF heater is the active source of carbon contamination. However in an all silicon-quartz system where no carbon is present, the tripyramid growth was very rare or not observed.

Discussion

Miller *et al.* proposed a crystallographic model and a formation mechanism for the pyramids (5). After their model the tripyramid associates with the twin lamella as shown in Fig. 7a. Tripyramids are 60° twinned to the substrate resulting from overgrowth of the silicon carbide.

From the experimental results of the etching and the x-ray reflection the author derived a model different from that by Miller (5). The schematic diagrams are shown in Fig. 7b and 7c. In the following paragraphs the crystallographic models are discussed in comparison to the Miller model (Fig. 7a).

The orientations of the crystallites in a tripyramid were [511], [151], and [115]. Three crystallites A, B, and C in Fig. 7c are incoherent to each other and were connected through the Y-shaped boundary as shown in Fig. 3b. Since the tripyramids have [511] orientations, they exhibit faster etch rates with the Sailer etch than the surrounding (111) region in Fig. 2. It was shown by partial removing and etching that the tip of the starlike tripyramid grows rectilinearly as shown in Fig. 7b.

The crystallographic indices of the exposed planes of the tripyramid were (110) and (100) (Fig. 7b). The modified form of Fig. 1c exposed (211) and (111) planes too (Fig. 7c). These indices were determined by measuring the height and length under the optical microscope on the basis of the criteria of the [511] and [111] orientations which were established by x-ray diffraction. The results do not agree with the model in Fig. 7a. The interfaces in the layer marked by oblique lines in Fig. 7b were determined in the same way and they appear to be (221) planes to the twinned crystallite.

The tripyramid and the substrate silicon are combined by multiple and complicated twinnings. In a diamond structure 60° twinning axes <111> exist in four ways, [111], [$\bar{1}$11], [1$\bar{1}$1], and [11$\bar{1}$]. All of the twinnings were detected by x-ray diffraction. Twinnings [$\bar{1}$11], [1$\bar{1}$1] and [11$\bar{1}$] correspond to the crystallites A, B, and C, respectively, in Fig. 7b (cf. Fig. 2c).

Although a crystallite A combines with a surrounding (111) layer by twinning about the [$\bar{1}$11] axis, the interfaces between them are not ($\bar{1}$11) plane but have a more complicated boundary. The striped bands in Fig. 4 correspond to the [111] 180° rotation twins. In fact these twins are always present in x-ray diffraction patterns. Because tripyramids without stacking faults are observed (Fig. 3), stacking faults are not essential to growth mechanism.

The cause of twinning was proved to be the formation of silicon carbide by Miller *et al* (5). After their results, the formation of α-SiC (hexagonal) layers on the silicon surface brings forth the twinning by the packing effect. SiC (0001) is parallel to the Si (111). The twin in the diamond lattice is produced when two extra SiC (0001) planes are inserted into a crystal. SiC nucleates at sites along the steps bounded by the (111) planes (5). These steps are produced by the thermal etching or by a reaction of $SiCl_4$ and H_2. Twinning about each of three ($\bar{1}$11) planes of the steps or etch pits on the (111) substrate surface introduces the crystallite of [511] orientation as shown in Fig. 7b. The effect of carbon or silicon carbide on tripyramid nucleation was experimentally proved (Fig. 6). In practical growth conditions, there are some origins which appear to be capable of depositing silicon carbide on the substrate surface beside the carbon pedestal. They are the small quantities of organic solvents such as methane, carbon tetrachloride, etc. (3, 9, 10). Vapor transport reactions of the carbon and silicon have been proposed (5).

It has been concluded that the tripyramid is introduced into the vapor-grown silicon layer through a few atomic layers of silicon carbide formed at the substrate interface. The graphite pedestal and the organic solvents are the active source of carbon contamination. To produce highly perfect epitaxial layers free from the tripyramids, it is necessary to clean the substrate and to remove carbon from the reaction system.

Acknowledgments

The author wishes to thank Dr. S. Takayanagi and Dr. I. Teramoto for their helpful discussions.

Manuscript received July 31, 1964.

Any discussion of this paper will appear in a Discussion Section to be published in the December 1965 JOURNAL.

REFERENCES

1. T. L. Chu and J. R. Gavaler, *This Journal*, **110**, 388 (1963).
2. G. R. Booker and R. Stickler, *J. Appl. Phys.*, **33**, 3281 (1963).
3. K. O. Batsford and D. J. D. Thomas, *Elec. Commun.*, **38**, 354 (1963).
4. T. B. Light, "Metallurgy of Semiconductor Materials," Metallurgical Soc. Conf., Vol. 15, p. 137, Interscience Publishers, New York (1962).
5. D. P. Miller, S. B. Watelski, and C. R. Moore, *J. Appl. Phys.*, **34**, 2813 (1963).
6. T. L. Chu and J. R. Gavaler, "Metallurgy of Advanced Electronic Materials," Metallurgical Soc. Conf., Vol. 19, p. 209, Interscience Publishers, New York (1963).
7. E. Reizman and H. Basseches, "Metallurgy of

Semiconductor Materials," Metallurgical Soc. Conf., Vol. 15, p. 169, Interscience Publishers, New York (1962).
8. H. C. Theuerer, *This Journal*, **108**, 649 (1961).
9. K. Sato, *Oyo Buturi*, **32**, 777 (1963).
10. R. C. Newman and J. Wakefield, "Solid State Physics in Electronics Telecommunications, Proceedings of an International Conference, Brussels," Vol. 1, pt. 1, p. 318, Academic Press Inc., New York (1960).

Vapor Phase Transport and Epitaxial Growth of $GaAs_{1-x}P_x$ Using Water Vapor

G. E. Gottlieb

RCA Laboratories, Princeton, New Jersey

ABSTRACT

It was found that $GaAs_{1-x}P_x$:Te doped layers can be homogenously transported by a vapor phase technique using water vapor. Epitaxial layers of the same As-P ratio as the melt-grown source wafers were grown onto [111] and [100] GaAs substrates. The reaction proceeds via the following equation

$$2GaAs_{1-x}P_x + H_2O \rightleftarrows Ga_2O + (1-x)\,As_2 + (x)\,P_2 + H_2$$

Ga_2O is the actual transporting species. At a water vapor pressure of 0.286 mm (ice at −30°C) an activation energy of 85 kcal/mole was calculated. The amount of material transported was found to be a function of (*a*) $\sqrt{P_{H_2O}}$ entering the system, (*b*) the temperature difference between source and substrate, (*c*) the composition of the source material, and of course (*d*) the absolute source temperature. The transport of GaAs with water vapor was found to have an activation energy that is nonconcentration dependent within the range of water vapor pressures studied. Certain aspects of Te doping were studied; the oxygen content of the epitaxial layers was studied via mass spectrographic techniques.

The useful and interesting electrical characteristics of GaAs and GaP are well known. A logical extension of the work on these compounds is a study of the properties of the alloys $GaAs_{1-x}P_x$. As in the case with the pure compounds (especially GaP) the alloys are difficult to prepare by normal melt growth techniques. The usual problems encountered in the melt-growth of high melting point materials are concerned with purity and crystallinity. The alloys present the additional problem of homogeneity, *i.e.*, a constant ratio of As to P throughout the matrix.

This paper will discuss the growth of $GaAs_{1-x}P_x$:Te doped layers by a vapor phase technique. This work was instituted in order to obtain a compound having a band gap of 1.72 ev, so that by injection luminescence it emits at 7200Å and thereby stimulates a $CaF_2:Dy^{+2}$ laser. This experiment was performed (1), and it was found that the light emitted by the $GaAs_{1-x}P_x$ diodes was sufficient to stimulate the above-mentioned laser. The difficulties inherent in the melt-growth technique, just mentioned, suggested that vapor phase growth should be used as a preparative technique. Schäfer (2) discussed various aspects of vapor phase transport, the preparation of high melting point materials via volatile intermediates. Antell and Effer (3) applied the technique to III-V compounds, using iodine and chlorine as the transporting agent. Pizzarello (4) synthesized large polycrystalline boules of $GaAs_xP_{1-x}$, using GaAs and P or GaAs and GaP as starting materials and iodine as the transporting agent. Holonyak (5) reported the epitaxial growth of GaAs and GaP, using various chlorides as transporting agent. In the present work oxygen transport was utilized, in contrast to the above worker's use of halide transport. Gershenzon and Mikulyak (6) have also reported the growth of GaP, via a Ga_2O transport mechanism. Previous experience (7) with the transport of GaAs via Ga_2O, in a close-spaced system, indicated that Ga compounds can be transported successfully in this manner. Therefore, the close-spaced system with water vapor as the source of oxygen seemed the logical choice of method.

Frosch (8) has reported the growth of GaP and $GaAs_{1-x}P_x$ utilizing a Ga_2O vapor transport mechanism in an open tube apparatus, with the bulk of the paper devoted to GaP. In contrast to the above, the present paper is largely concerned with the growth of $GaAs_{1-x}P_x$ in the close-spaced system, via Ga_2O. Some of the topics discussed in the above paper are common to those reported in the present work, for example, growth rates, doping, crystal morphology, and usable growth parameters. However, the work reported here is devoted solely to $GaAs_{1-x}P_x$, presenting quantitative data on (a) the effects of temperature, (b) the $\sqrt{P_{H_2O}}$ relationship, (c) the homogeneity of the grown layers, and (d) incorporation of the transport agent into the grown layer.

Experimental

The close-spaced system of Nicoll (9) was used. The source and substrate wafer temperatures were each controlled by separate heaters. To insure an equal temperature over the entire wafer heavy molybdenum disks were placed between the wafers and their respective heaters. Temperature measurement and control were achieved by thermocouples placed in small holes in the molybdenum disks. A spacing of 10 mils was used between the source and substrate. Palladium diffused hydrogen, at a flow rate of 6 cc/min, was passed over ice at −20° to −30°C; the ice temperature was maintained by a salt-ice bath, or by an ethylene glycol-water bath. This technique controlled the amount of water vapor admitted to the system. The various growth parameters were studied by observing the weight loss of the source wafer as a function of the parameter of interest. A detailed description of the apparatus and of the experimental procedure has been given previously (7).

The $GaAs_{1-x}P_x$:Te source wafers were cut from melt-grown ingots. These source wafers were polycrystalline, with a varying As-P ratio. Mechanically polished (111) and (100) GaAs wafers, etched in 1:1:10 $H_2O:H_2O_2:H_2SO_4$ prior to growth were used as substrates.

Results and Discussion

The actual transport is assumed to proceed as follows

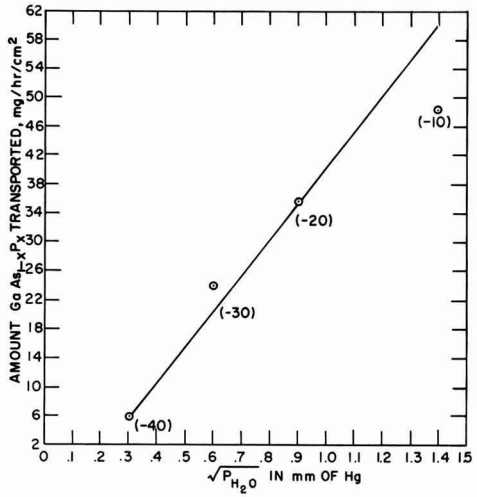

Fig. 1. Amount of $GaAs_{1-x}P_x$ transported as a function of water-vapor pressure. Figures in the parenthesis are the temperatures corresponding to the indicated vapor pressures. T_H, 935°C; T_C, 920°C.

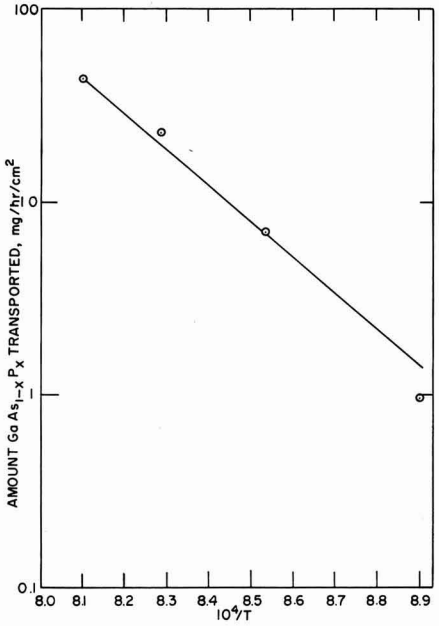

Fig. 2. Temperature dependence of the transport rate plotted as the amount of $GaAs_{1-x}P_x$ transported *vs.* $10^4/T$.

$$2GaAs_{1-x}P_x + H_2O \rightleftarrows Ga_2O + (1-x)\,As_2 + (x)\,P_2 + H_2 \qquad [1]$$

Ga_2O is the transporting species, as demonstrated by several authors (10, 11). It was previously found (7) that the transport of GaAs by H_2O is proportional to $\sqrt{P_{H2O}}$; this study shows that the amount of $GaAs_{1-x}P_x$ transported (Fig. 1) is also dependent on $\sqrt{P_{H2O}}$, with some deviation at higher H_2O concentrations. This deviation from the expected relationship could be due to the formation of Ga_2O_3, which was observed in this work at higher water vapor concentrations; (P_{H2O} above 9 mm). Previous work (12) on the Ga_2O-Ga_2O_3 system is in agreement with the above.

Figure 2 shows a plot of the reciprocal temperature *vs.* the log of the amount of $GaAs_{1-x}P_x$ transported. The activation energy for the reaction, calculated from this graph is 85 kcal/mole, at a water vapor pressure of 0.286 mm (ice at −30°C). Comparative activation energies are 74 kcal/mole, for GaP, at a water vapor pressure of 0.286 mm, and 49 kcal/mole, for GaAs at a water vapor pressure of 4.58 mm (ice at 0°C) (7). The closeness of the activation energies indicates that essentially the reaction is "Ga transport," via Ga_2O.

It was found that the GaAs-H_2O transport reaction has a non-concentration dependent activation energy, within the range of water vapor pressures studied. At 4.58 mm H_2O pressure, the activation energy is 49 kcal/mole and at 0.77 mm the activation energy is 47.4 kcal/mole. This indicates that within the above mentioned limits there are no competing source reactions, ruling out the formation of Ga_2O_3 as represented by the following equation

$$2GaAs + 3H_2O \rightarrow Ga_2O_3 + H_2 + As_2$$

The formation of Ga_2O_3 would also lower the efficiency of the reaction by 1/3 putting an upper limit of 67% on the deposition efficiency. In the present study 80-90% of the weight loss of the source was gained on the substrate.

This lack of dependence of the activation energy on the H_2O concentration is in direct contrast to the GaAs-HCl (13) situation, in which the activation energy is very dependent on the HCl concentration (pressure).

The layers of $GaAs_{1-x}P_x$ obtained in this study were single-phase, single-crystal solid solutions of the above material. A completely mirror-like layer was usually obtained, at a growth rate of one-four mils/hour. Among the factors influencing growth rate are source composition, temperature of source and substrate, temperature difference, and wafer geometry. A good growth rate is not in itself sufficient to produce useful layers. Other factors of importance to be discussed, are substrate perfection, doping and impurities in the films.

It was found that the growth rate varied significantly with the source composition. As shown in Fig. 3, growth rate increased as the percentage of GaP increased. A possible reason for these results is the effect of the reverse reaction. GaAs can be transported at much lower temperatures than GaP. Therefore, at higher temperatures the reverse reaction becomes appreciable, and tends to limit the amount of material transported with a small temperature difference. These results are at temperatures of 935°-920°C (935° hot zone, or source, 920° cold zone, or substrate).

Small changes in the temperature difference have striking effects on the appearance of the grown layers. A $GaAs_{1-x}P_x$ layer grown at 950°-900°C, (900°-cold zone, or substrate), is usually very rough, 940-900 improves the appearance somewhat, but a startling change occurs when 940-920 is used. Under these con-

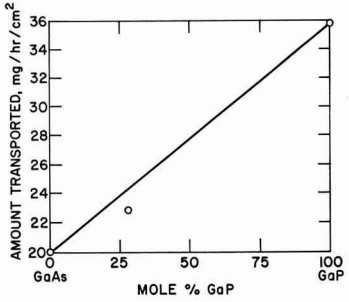

Fig. 3. Dependence of the amount of material transported on source composition. T_H, 935°C; H_2O, at 30°C; flow rate, 6 cc/min.

ditions the layer is mirror-like, with only occasional growth defects. This strong temperature dependence is in direct contrast to the GaAs situation, in which a variation of 50°C in the temperature difference between source and substrate produced hardly discernible changes in the grown layers.

The above facts are partially explained by Fig. 4. This shows that as the temperature difference between source and substrate is decreased, the amount transported also decreases. Although the concentration of Ga_2O in the gas phase is determined by the source temperature, the rate of removal of Ga_2O is determined by the substrate temperature. The same amount of material is therefore arriving at the substrate, but the "sticking probability" is lowered, due to the higher substrate temperature. For this reason, less material is deposited per unit area per unit time. Furthermore, the higher substrate temperature produces an increased surface mobility; this along with the lower deposition rate explains the improved crystallinity observed with small temperature differences. The effect of the temperature difference on the amount of material transported is demonstrated by two experiments performed at a source temperature of 980°C. In the first experiment the substrate temperature was 965°C, and 33 mg/cm²/hr were transported. In the second experiment, all the conditions were the same except that the substrate temperature was decreased to 930°C. In this case 110 mg/cm²/hr were transported.

The dependence of the amount of $GaAs_{1-x}P_x$ transported on the substrate temperature is due to the close-spacing, and the resultant interaction between source and substrate parameters. The close-spaced system approaches the behavior of a sealed system, in which the substrate temperature, by affecting the concentration of Ga_2O in the gas phase, has a profound effect on the amount of $GaAs_{1-x}P_x$ transported, as shown in Fig. 4.

Most of the source wafers were Te doped in the 1-5 x 10^{18} atoms/cm³ range; however, 10^{17} Te/cm³ doping was also studied. Both mass spectroscopic and electrical measurements indicated that in the range 10-100 ppm (2 x 10^{17}-2 x 10^{18}), the Te concentration in the epitaxial layer is the same as that in the source wafer. However, source wafers with up to 300 ppm of Te produced epitaxial layers containing only 100 ppm. This data is shown in Table I. Since the vapor pressure of elemental Te is large, it is not clear whether the Te transports as Te or as TeO_2.

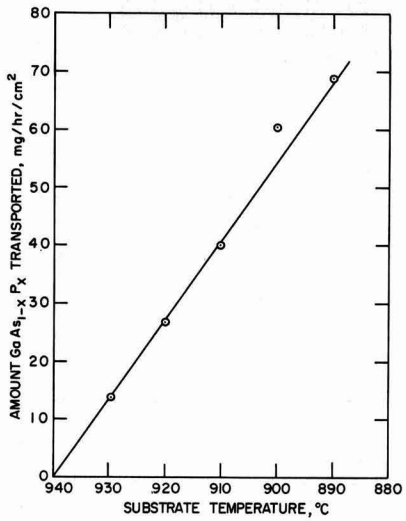

Fig. 4. Amount of $GaAs_{1-x}P_x$ transported as a function of the substrate temperature, at a constant source temperature. T_H, 940°C; H_2O, at 30°C.

Table I.

Number	Oxygen content of source, at. ppm†	Oxygen content of grown layer, at. ppm	Tellurium content of source, at. ppm	Tellurium content of grown layer, at. ppm	Growth rate, mg/hr/cm²
32	—	330	100	100	100
84	3	135	10	10	38.4
97	3	1350	10	10	16.9
116	—	1300	100	100	23.3
122	—	—	7.5 × 10^{17}*	2 × 10^{18}*	24.8
124	—	135	—	10	29.7
126	10	400	—	29	—
143	30	—	300	100	20.4
150	30	330	300	100	20.4

* Determined by Hall measurements.
† At. ppm = atomic parts per million.

The uniformity of the grown layers was studied by ultrasonically cutting small disks (0.040 in. diameter) from an epitaxial layer and corresponding source wafer, and then analyzing the composition of these disks via lattice constant measurements. The results of one such analysis are shown in Fig. 5. The grown layer had a maximum over-all variation in composition of 2%; the diffraction lines were sharp, indicating a variation within each disk of less than ±0.5%. Both the internal variation, and the over-all variation are much less in the grown layer than in the source. The As-P variation in the source is usually about 15%.

The layer shown in Fig. 5 was grown at a rate of ~12 mils/hr. A similar analysis (not shown) was performed on a layer grown at ~1.6 mils/hr. It was found that the maximum over-all compositional variation was also ~2% in this layer. However, the point to point variation was much less in the layer grown slowly, than in that grown more rapidly. Most of the slowly grown layer was one composition, with a single point deviating from this composition by ~2%. This indicates that the compositional variation within the grown layer is dependent on the growth rate. As would be expected, regrowth of a wafer further reduces compositional variation.

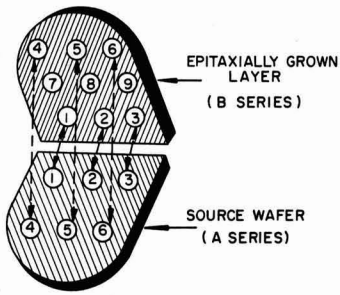

Fig. 5. The relationship between the source composition (A series) and the epitaxial layer composition (B series) is shown. Identical numbers from each series indicate areas adjacent to each other during growth. The substrate in this case was [100] GaAs wafer, grown at 920°C (substrate temperature).

Sample	Lattice Constant Å	Mole % GaAs	Mole % GaP
B_1	5.592	69.9	30.1
B_2	5.596	71.7	28.3
B_4	5.596	71.7	28.3
B_5	5.591	69.3	30.7
B_6	5.596	71.8	28.2
B_7	5.593	70.5	29.5
B_8	5.595	71.0	29.0
A_1	5.586-5.607	67.0-77.2	33.0-22.8
A_2	5.580-5.598	64.0-72.6	36.0-27.3
A_5	5.584-5.609	66.0-78.0	34.0-22.0
A_6	5.581-5.603	64.4-75.2	35.6-24.8

A very few layers had areas of smeared Laue patterns, indicating some type of crystalline imperfection. In order to determine whether these irregularities are already present in the substrate wafers, or whether they are originating in the epitaxial layers, GaAs substrate wafers were etched in 1:1:10 $H_2O:H_2O_2:H_2SO_4$. Of a large number of substrate wafers etched in this manner, only a few showed any type of defect; the majority of the wafers polished in the above etch. The defective wafers were used as substrates, and the layers grown on these wafers had areas of smeared Laue patterns. Correlating these areas with the corresponding substrate areas showed that the substrate irregularity has propagated into the grown layers, manifesting itself as a "smeared" Laue pattern. Microphotographs of this effect are shown in Fig. 6.

Three separate areas on an individual [$\bar{1}\bar{1}\bar{1}$] GaAs substrate were photographed. Each area is shown prior to growth and after growth of the epitaxial layer; the Laue pattern of the layer in each area is also shown. The substrate and layer photos are magnified 150X. The layer was grown at a substrate temperature of 920°C and a growth rate of 4.6 mg/hr/cm² (0.37 mils or 9 μ/hr). Figure 6(a) shows a severely distorted area. The irregularities are already evident in the substrate and are manifested as a dark area on the deposit photo. The Laue pattern shows broken dots, and the start of ring formation. In Fig. 6(b) the disturbances are less severe. The dots in the Laue pattern are somewhat distorted and broken. Figure 6(c) shows a nondistorted area, with nonbroken dots, essentially defect free single crystal material. Layers grown on the (100) plane were found by visual and microscopic examination to have fewer crystalline defects than (111) growth.

Typical wafer surfaces are shown in Fig. 7. Figure 7(a) exhibits an epitaxial layer grown on a [100] GaAs substrate. The layer was grown at 920°C at a growth rate of 5.4 mg/hr/cm², or 0.43 mil/hr. The mirror-bright surface is manifested by the reflection of the graph paper from the surface. Figure 7(b) depicts a typical epitaxial layer grown on a [$\bar{1}\bar{1}\bar{1}$] GaAs substrate. The layer was grown at 920°C, at a growth rate of 47 mg/hr/cm², or 3.7 mils/hr.

In a transport reaction the amount of transporting agent incorporated into the grown layer is of interest. For this purpose, mass spectrographic studies were utilized. Table I shows that the source wafers were

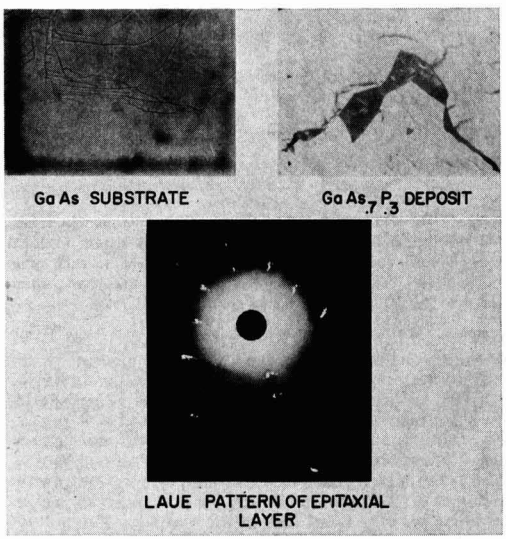

Fig. 6. Three areas on a GaAs substrate prior to growth, the resulting layers, and their Laue patterns are shown: (a) defective area.

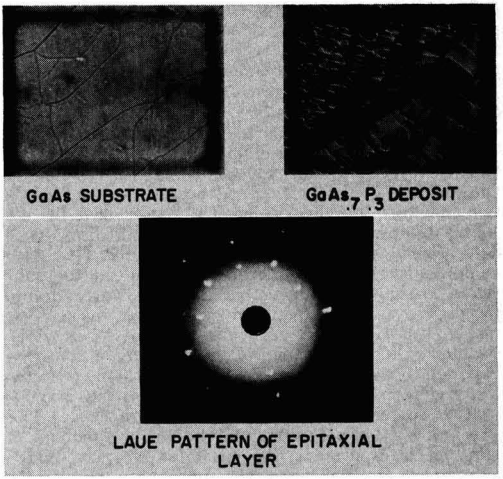

Fig. 6(b). Intermediate area.

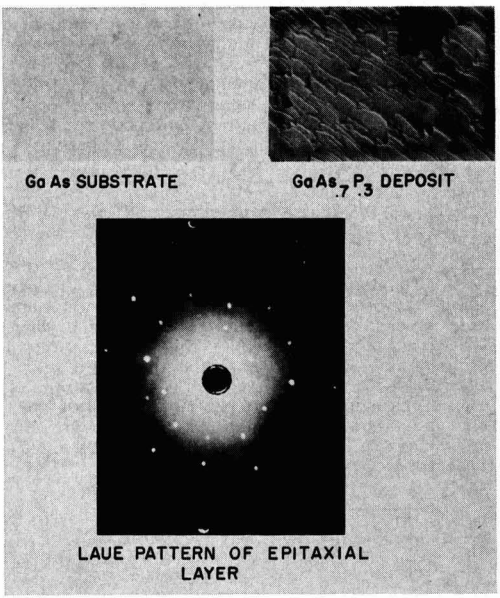

Fig. 6(c). Defect free area.

reasonably low in oxygen concentration. The oxygen content of the grown layers was found to be 100-1000 ppm, or 0.01-0.1 atomic per cent. This is the same range that previous workers (13, 14) found for the incorporation of halide transporting agents in halide vapor grown III-V compounds. A recent report (15) indicates that molybdenum is attacked by oxygen at 550°C; mass spectrographic analysis did not show the presence of any molybdenum in the epitaxial layers. This indicates that the reaction of water vapor with $GaAs_{1-x}P_x$ is favored over the molybdenum reaction.

Single-crystal, single-phase layers of $GaAs_{1-x}P_x$:Te were also grown using powdered sources. Both powdered $GaAs_{1-x}P_x$, and GaAs plus GaP were used. Preliminary investigations on the uniformity of these layers indicate that they are at least as homogenous as the layers grown from melt-grown source wafers.

Summary and Conclusions

It was found that $GaAs_{1-x}P_x$:Te can be homogenously transported in the close-spaced system. A con-

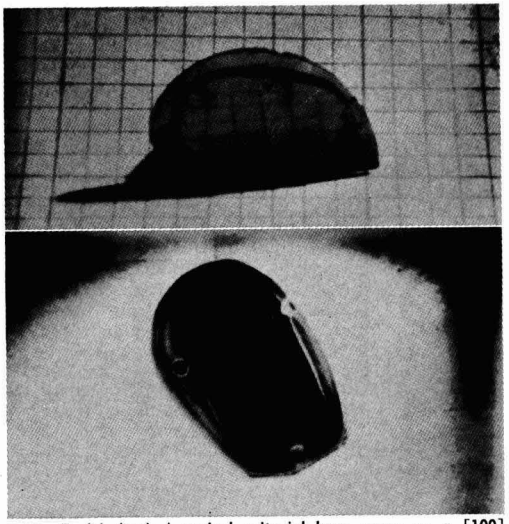

Fig. 7. (a) (top) A typical epitaxial layer grown on a [100] GaAs substrate is shown. (b) (bottom) Depicts a typical epitaxial layer grown on a [$\bar{1}\bar{1}\bar{1}$] GaAs substrate.

trolled amount of water vapor added to the hydrogen stream is the transporting agent. The rate of transport is dependent on $\sqrt{P_{H_2O}}$. In the range 2×10^{17} — $s \times 10^{18}$ Te/cc, the grown layer concentration corresponds to the source concentration in a 1:1 ratio. It was found that the amount of $GaAs_{1-x}P_x$ transported is dependent not only on the source temperature, but also on the temperature difference between source and substrate.

Acknowledgments

It is a pleasure to acknowledge the experimental acumen of J. F. Corboy, Jr. The author is indebted to P. G. Herkart for advice, encouragement, and useful discussions. Thanks are due to R. J. Paff for performing the lattice constant measurements, and to H. H. Whitaker for the mass spectrographic analysis. The author is indebted to P. Robinson for useful discussions and to D. Richman for a critical reading of the manuscript.

Manuscript received April 9, 1964; revised manuscript received Oct. 9, 1964.

Any discussion of this paper will appear in a Discussion Section to be published in the December 1965 JOURNAL.

REFERENCES

1. S. A. Ochs and J. I. Pankove, *Proc. IEEE.*, **52**, 713 (1964).
2. H. Schafer, H. Jacob, and K. Etzel, *Z. anorg. und allgem. Chem.*, **286**, 27 (1956); *ibid.*, **42**; H. Schäfer and B. Morcher, *ibid.*, **290**, 279 (1957).
3. G. R. Antell and D. Effer, *This Journal*, **106**, 509 (1959).
4. F. A. Pizzarello, *ibid.*, **109**, 226 (1962).
5. N. Holonyak, "Metallurgy of Semiconducting Materials," p. 49, Interscience Publishers, Inc., New York (1962).
6. M. Gershenzom and R. M. Mikulyak, *This Journal*, **108**, 548 (1961).
7. G. E. Gottlieb and J. F. Corboy, Jr., *RCA Review*, **24**, 585 (Dec. 1963).
8. C. J. Frosch, *This Journal*, **111**, 180 (1964).
9. F. H. Nicoll, *ibid.*, **110**, 1165 (1963).
10. S. Antkiv and V. H. Dibeler, *J. Chem. Phys.*, **31**, 1890 (1953).
11. C. J. Frosch and C. D. Thurmond, *J. Phys. Chem.*, **66**, 877 (1962).
12. C. J. Frosch and C. D. Thurmond, *This Journal*, **111**, 184 (1964).
13. R. Moest, *ibid.*, **109**, 1061 (1962).
14. W. J. McAleer, H. R. Barkemyer, and P. I. Pollak, *ibid.*, **108**, 168 (1961); G. R. Antell, *J. Appl. Phys.*, **31**, 1686 (1960).
15. E. A. Gulbransen, K. F. Andrew, and F. A. Brossart, *This Journal*, **110**, 952 (1963).

Measuring Mobility and Density of Charge Carriers Near a P-N Junction

D. Pomerantz

Laboratory for Physical Science, P. R. Mallory, Burlington, Massachusetts

ABSTRACT

Two types of probe measurement are described which allow the determination of the conductivity mobility and the density of majority carriers in the neighborhood of p-n junctions. The first of these measures the change in sheet conductivity of a layer as a function of the reverse bias applied to a junction bounding the layer. The second measures the capacitance of the junction *vs.* the reverse bias. The techniques are applied to silicon p-n junctions of both the epitaxial and diffused variety. A significant difference is observed in the mobility variation near these two types of junction.

As an aid in the analysis of junction semiconductor devices it is valuable to measure directly the physical properties of the semiconductor in the neighborhood of the junctions. The main properties of interest are the concentration, mobility, and lifetime of charge carriers. This work will describe a method of measuring the first two of these parameters and its application to two widely used silicon junction types; (i) junctions between a lightly doped epitaxial layer grown on a lightly doped substrate of opposite conductivity type and (ii) junctions produced by a heavily doped diffused layer in a lightly doped substrate of opposite conductivity type.

Experimental

Figure 1 illustrates a technique for measuring the differential sheet conductivity of a layer bounded by a junction. The experimental arrangement is similar to a conventional four point resistivity probe (1) except that two additional probes have been added, making contact with the substrate. The current probes, I_1 and I_2, supply a constant current, I, which flows in the n-layer of the sample illustrated, the junction acting as a barrier to current flow in the p-region. The voltage probes, V_1 and V_2, are connected to a high impedance voltmeter so that they do not draw any current and therefore measure the transverse potential drop in the

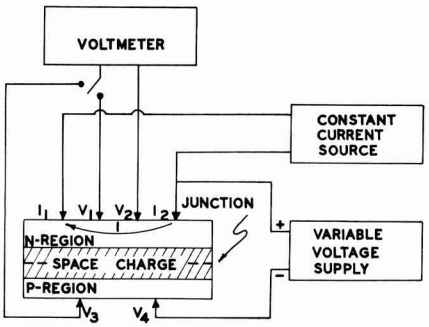

Fig. 1. Experimental arrangement for measurement of differential sheet conductance.

n-layer due to the current I. From this the sheet conductivity may be deduced. The voltage probe, V_4, applies a variable potential to the substrate with respect to the current probe I_2. The sign of this potential is such as to reverse bias the junction. Since the leakage current of the junction flows through probe V_4, it is not suitable for measuring the potential of the p-region. Another probe, V_3, is provided for this purpose which may be connected to the voltmeter through the switch. The voltage applied to the junction is then measured between probes V_2 and V_3. By increasing this applied reverse bias, the junction space charge region is caused to sweep mobile carriers out of the n-layer, decreasing its sheet conductivity. The measurement consists in determining the voltage difference between V_1 and V_2 as a function of the voltage applied to the junction, measured between V_2 and V_3.

The difference between two conductivity measurements at slightly different voltages is a measure of the conductivity of the particular lamina swept out by the space charge when the increment of voltage is applied. The principle of operation is similar to modulation of the channel resistance of a field effect transistor, except that care is taken to operate at sufficiently low currents so that the transverse voltage drop in the layer is small compared to the voltage applied to the junctions, *i.e.*, remote from pinchoff. The measurement may be made with either sign of current flow in the n-region, but more accurate results are obtained if the direction of the current I is such as to forward bias the point contact diode, I_2, through which voltage is applied to the n-layer. When this diode is reverse biased, variations in its reverse characteristic due to noise or surface effects produce variations in the potential of the n-layer. Excess junction leakage current flowing transversely in the n-region will produce an error in the voltage measured between V_1 and V_2. For the polarity of the current, I, shown in Fig. 1, this will increase the measured voltage. The amount of increase may be measured with the current source disconnected. This error voltage is then subtracted from the original reading to obtain the effect of the current I alone. The correction is unmeasurably small for junctions of good quality. The current I is adjusted to be sufficiently large to produce an accurately measurable voltage, but small enough so that injection of minority carriers into the base by the forward biased current probe is negligible. The latter effect is observable as a rapid increase in the current flowing in V_4, as I is increased. This is avoided as it signifies the presence of nonequilibrium carrier concentrations which produce modulation of the n-layer conductivity. Typical values of current lie between 0.2 and 0.5 ma. The measurement of differential sheet conductivity may be made on a whole slice if the junction is sufficiently free of defects. In this way different areas may be measured nondestructively. In practice this situation is rare, and it is convenient to etch onto the slice, through the junction, a pattern of rectangular mesas with dimensions of aproximately 1 by 4 probe spacings. For measuring the properties of both the n- and p-regions, rectangular dice of these dimensions are used.

In addition to the differential sheet conductivity, the carrier density as a function of position must be known in order to determine how the mobility varies in the n-layer. This is determined from capacitance *vs.* voltage measurements as shown in Fig. 2. Here a variable voltage is supplied to the two probes, C_1 and C_2, through a capacitance bridge. Two separate probes, V_2 and V_3, determine the voltage applied to the junction. To avoid errors due to the capacitance of the probes, C_1 and C_2, which are in series with the junction, two additional current supplies are used to forward bias these point contact diodes. The effect is to provide a low resistance in parallel with the capacitance of the contacts. Without this current flowing, the point contacts will be at almost zero bias and can easily have a capacitance which is comparable to the junction. This leads to an erroneously small result. The currents I_1 and I_2 are adjusted so that further increase produces no reduction in capacitance. In practice this leads to values of 20-50 μa.

Theory of Measurement

Figure 3 illustrates the distribution of space charge density near a reverse biased p-n junction. The dotted lines give the net amount of ionized fixed charge. To the right of the origin is plotted the charge density due to ionized donors net of ionized acceptors (N_d) as a function of distance into the n-region which has a thickness, t. To the left is plotted the charge density of ionized acceptors net of ionized donors (N_a) as a function of distance into the p-region.

The solid lines show the total space charge density, $\rho(v,x)$, which is produced when the fixed charge is stripped of its neutralizing mobile carriers by the built-in plus the applied voltage. For the purpose of calculating mobilities, it is not necessary to assume that the charge drops abruptly to zero at the edge of the space charge region. Figure 3 illustrates the more

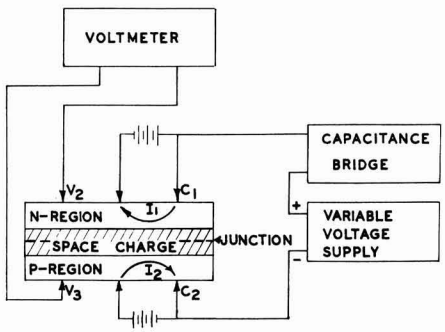

Fig. 2. Experimental arrangement for measurement of junction capacitance *vs.* applied voltage.

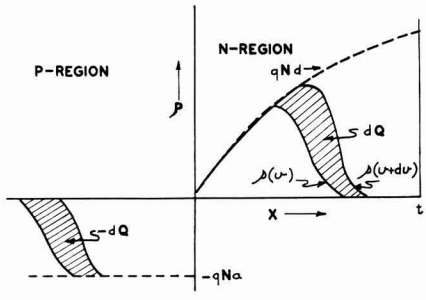

Fig. 3. The net fixed charge density (dashed) and the space charge density (solid) near a p-n junction.

gradual reduction characteristic of small applied voltages. An increase in applied voltage, dv, produces an increase, dQ, in the space charge on the n-side of the junction as shown in the figure. Over-all neutrality requires a space charge, $-dQ$, be produced on the p-side. The small signal capacitance per unit area at this particular voltage is just the ratio of the induced charge per unit area, dQ, to the inducing voltage, dv

$$c(v) = \frac{dQ}{dv} \quad [1]$$

where

$$Q(v) = \int_0^t \rho(v,x)\, dx \quad [2]$$

We now consider the change in sheet conductivity due to the same change, dv, in voltage. It will be seen that to a very good approximation this is attributable to the mobile charge of magnitude $-dQ$ which is removed from the fixed charge dQ in Eq. [1]. The total sheet conductivity of the n-layer is

$$\sigma_s = \int_0^t (nq\mu_n + pq\mu_p)\, dx \quad [3]$$

where n, p, μ_n, μ_p, the electron and hole concentrations and their mobilities are functions of x, the distance from the junction; and q is the electronic charge. The charge density is given by

$$\rho(x) = qp(x) - qn(x) + qN_d(x) \quad [4]$$

Substituting $n(x)$ from Eq. [4] into Eq. [3] gives

$$\sigma_s = -\int_0^t \rho(v,x)\mu_n\, dx + \int_0^t pq(\mu_p + \mu_n)\, dx + \int_0^t N_d(x)\, q\mu_n\, dx \quad [5]$$

In Eq. [5] the second integral is the contribution due to minority carriers plus an equal number of neutralizing majority carriers. This is entirely negligible except for near intrinsic silicon (*i.e.* > 1000 ohm-cm). Since the third integral is not a function of v we have

$$\frac{d\sigma_s}{dv} = -\mu_n \frac{dQ}{dv} \quad [6]$$

The quantity dQ, which is the differential of Eq. [2], is illustrated in Fig. 3. It is equal in magnitude (and opposite in sign) to the area density of mobile charge swept out of the region shown cross hatched in Fig. 3. The average mobility of these charge carriers is μ_n. The expression for the mobility is obtained by eliminating dQ/dv between Eq. [1] and Eq. [6]

$$\mu_n = -\frac{1}{c}\frac{d\sigma_s}{dv} \quad [7]$$

It is to be noted that μ_n is the true conductivity mobility for majority carriers, a quantity normally derived on theoretical considerations from the Hall or drift mobilities. Here it may be determined directly from measurable quantities. The mobility will normally be a function of the applied voltage v, reflecting the variation in crystal properties or impurity concentration at the edge of the space charge region. This voltage will in turn be related to distance from the junction through the capacitance measurement described below. In this way the edge of the space charge, probing into different laminae, determines the variation of mobility within the p- or n-region.

For an infinite sheet, thin compared to the probe spacing, the quantity σ_s in Eq. [7] is given by $\sigma_s = I(\ln 2)/\pi V$ (2) where V is the voltage measured between probes V_1 and V_2, Fig. 1. If the sample area is limited, other correction factors are required. These have been calculated by Smits (2). In the case of a rectangular sample comparable in width or narrower than the probe spacing, some precision is added to the mobility determination by the fact that the width of the sample drops out of Eq. [7]. In this case σ_s is given by (2).

$$\sigma_s = Is/VC'd \quad [8]$$

where s is the probe spacing, d the rectangle width, and C' a numerical factor tabulated in (2) and closely approximating unity for a narrow rectangle. This approximation corresponds to parallel current flow past the voltage probes. If the measurement is made at constant current, the following expression is obtained by differentiation of Eq. [8]

$$\frac{d\sigma_s}{dv} = -\frac{I}{V^2}\frac{dV}{dv}\frac{s}{C'd} \quad [9]$$

The capacitance per unit area c, is determined from the measured capacitance C, by $c = C/da$, where a is the rectangle length. Substituting this expression along with Eq. [9] in Eq. [7] gives

$$\mu_n = \frac{I}{V^2}\frac{dV}{dv}\frac{sa}{C'C} \quad [10]$$

from which d, the sample width, drops out. This expression has been used for obtaining the results described below. The accuracy of the determination is limited mainly by the measurement of the small voltage increment dV. In the measurements described below, dV is of the order of 10 mv and is determined to an accuracy of better than 1% using a precise high impedance differential voltmeter. Such accuracy is necessary to determine the relatively small variation of mobility with doping.

The equations for determining impurity concentration and distance from the junction from the measured values of $c(v)$ are

$$\frac{d}{dv}\left(\frac{1}{c^2}\right) = \frac{2}{qe}\left(\frac{1}{N_d} + \frac{1}{N_a}\right) \quad [11]$$

$$c = \frac{\epsilon}{s_a + s_d} \quad [12]$$

$$N_d\, ds_d = N_a\, ds_a \quad [13]$$

where ϵ is the dielectric constant and s_a, s_d, are the widths of the space charge layer in the p- and n-regions, respectively. Equations [11] and [12] are a generalization of those originally derived by Schottky (3) for the case where either N_d or N_a is large compared to the other. Equation [11] is proved by substituting Eq. [12] and then Eq. [13] into it, remembering that $qN_d\, ds_d = dQ = cdv$.[1] Equation [13] expresses the condition of over-all charge neutrality where ds_d and ds_a are the incremental increases in space charge penetration into n- and p-regions, respectively. In the derivation of these equations it is necessary to assume a sharp edged space charge region, a good assumption for applied voltages large compared to the built-in voltage. For small applied voltages the position coordinates s_a and s_d derived from the above relations must be considered to have an uncertainty of the order of the distance over which the space charge drops from qN_d or qN_a to zero. The mobility and impurity concentration which are determined as a function of s_a and s_d must therefore be considered as averages over this range.

In addition to Eq. [11]-[13] one other relationship is needed to determine the four quantities $N_a(s_a)$ and $N_d(s_d)$, when N_a and N_d are of comparable size. For the case of an epitaxial layer it is reasonable to assume a constant substrate doping, which is then measurable. As will be seen, this assumption may be verified from the results. For the case of a diffused junction there will be a narrow region on both sides of the junction which will be linearly graded, *i.e.*, $N_a = N_d$. As the space charge penetrates into the heavily diffused side of the junction this impurity concentration increases to a large value, eliminating its term from the right side of Eq. [11]. Using each of these assumptions in turn, N_d and N_a, determined from Eq. [11], are plotted as a function of $s_a + s_d$, the total space charge

[1] The author is indebted to E. Pittelli for this result.

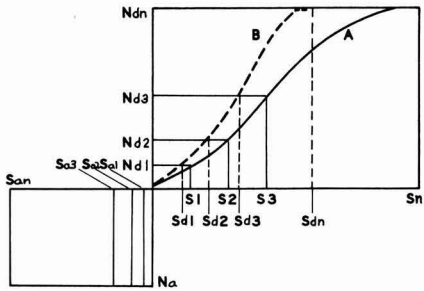

Fig. 4. Method of determining the relative penetration of space charge into the p and n-regions.

width, determined from Eq. [12]. The actual variation of $N_d(s_d)$ is then found by interpolating a curve which approaches the first situation asymptotically for a narrow space charge region and the second situation for a wide space charge region. While this process is not entirely free of ambiguity, a typical example, illustrated in Fig. 6, shows that the error incurred cannot be large.

It is now possible to relate the mobility directly to the net impurity concentration since both have been determined as a function of the total space charge width, $s_a + s_d$, through its dependence, Eq. [12], on the measured value of c. Examples of this result are illustrated by the curves of Fig. 5 and 6. If the differential sheet conductivity measurement is made on both sides of the junction, this relationship can be separately established in the p-and n-regions.

It only remains to separate the space charge into its two components, s_a and s_d. This is especially significant in epitaxial layers on lightly doped substrates since, in this case, a large part of the space charge region may penetrate into the substrate. If, as assumed previously, this region contains a uniform impurity concentration, N_a, the relative penetration of the space charge may be obtained by graphical integration of Eq. [13]. The process is illustrated in Fig. 4, where $s_1, s_2 \ldots s_n$, are successive values of space charge width, increasing incrementally; $N_{d1}, N_{d2}, \ldots N_{dn}$, are the corresponding values of net donor density on the n-edge of the space charge region; $s_{d1}, s_{d2}, \ldots s_{dn}$, are the corresponding penetrations of the space charge into the n-region and $s_{a1}, s_{a2}, \ldots s_n$, the penetrations of space charge into the p-region. The difference equations arising from Eq. [13] are

$$s_{d1} N_{d1} = 2 s_{a1} N_a, \; s_{d1} + s_{a1} = s_1 \qquad [14]$$

$$(s_{d2} - s_{d1})\ (N_{d2} + N_{d1}) = 2\,(s_{a2} - s_{a1}) N_a,$$

$$s_{d2} + s_{a2} = s_2 \qquad [15]$$

etc.

These equations are solved by choosing closely spaced values of s_1, etc., and determining the values of N_{d1}, etc., from the curve derived from Eq. [11], [12], *e.g.*, curve A of Fig. 4. The values of s_1 and N_{d1}, along with the measured N_a, are substituted into Eq. [14] which are solved for the two unknowns: s_{a1}, s_{d1}. These are substituted along with s_2 and N_{d2} into Eq. [15] which are then solved for s_{a2}, s_{d2}. The process continues as far as measurements have been made. The values of s_{d1}, etc., *vs.* N_{d1}, etc., give the actual variation of net donor concentration with distance from the junction, *e.g.*, curve B of Fig. 4. Using this result the position coordinates s_a, s_d, may now be related individually to C and hence to v since $C(v)$ is a measured function. In this way the mobility, previously determined as a function of N_d, is directly related to distance from the junction. For diffused junctions, such as Fig. 6, the penetration on the diffused side is normally quite small and may generally be neglected. When this is not the case it is again possible to use Eq. [13] and through a process of graphical integration determine the quantities s_a, s_d.

It is of interest to determine the range over which the above measurements may be carried out. To do this, we observe from Gauss' electrostatic theorem that the maximum field, which occurs at the junction, $E_{max} = Q/\epsilon \approx 300$ kv/cm. From this we obtain the maximum net area density of donors or acceptors which can be included in the space charge region before breakdown, *i.e.*, $Q/q \approx 3 \times 10^{12}/\text{cm}^2$. Thus, for example, impurities at an average density of $10^{15}/\text{cm}^3$ can be measured out to a distance of 30μ from the junction, a value which is not affected by the distribution of impurities on the other side of the junction. On the other hand, E_{max} may be calculated by integrating the charge due to the measured distribution of net donors or acceptors out to the point of breakdown. This technique is useful for detecting premature breakdown of junctions due to surface effects or field concentrators in the space charge region.

Results

The results of measurements of n-type epitaxial layers on p-substrates and n-type wafers with diffused p-type surface layers are shown in Fig. 5 and 6. For the epitaxial layer of Fig. 5, the solid lines give the net donor concentration, calculated from Eq. [11], and the mobility, calculated from Eq. [10], as a function of total space charge width, calculated from Eq. [12]. The value of N_a used in Eq. [11] was measured as $3.0 \times 10^{15}/\text{cm}^3$. The dashed curves are the result of the graphical integration of the solid curves using Eq.

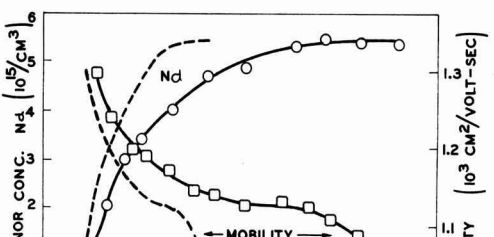

Fig. 5. Variation of mobility and impurity concentration in an n-type epitaxial layer on a p-type substrate. For the solid curves the abscissa is total space charge width. For the dotted curves abscissa is distance into the n-region measured from the junction.

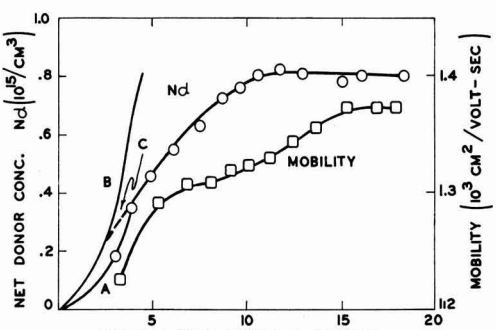

Fig. 6. Variation of mobility and impurity concentration in an n-type substrate with a p-type diffused layer. Curve A is for infinite impurity concentration on p-side of junction. Curve B is for a symmetrical junction. Curve C (dashed) is interpolated between A and B.

[13] as described above. In this case the abscissa is distance from the junction. In the net donor concentration we observe a slow increase in impurity concentration, approaching an asymptote about 3μ from the junction. This increase has been explained (4) as due to etch back of the relatively pure substrate material which dilutes the n-type impurity in the gas phase, so that the first deposited layer is less heavily doped. An alternative explanation is that during the initial growth stage the ratio of n-type impurity to Si deposited is lower than its ratio in the gas phase owing to selective decomposition of $SiCl_4$. This results in a boundary layer next to the growth interface which is enriched in impurities, the process continuing until a steady state is reached. In either case, a reduction in mobility is expected owing to the build-up of impurities in the layer as distance from the junction increases. This is observed as plotted in the two lower curves. The mobility appears to approach an asymptote at about the same position as the impurity concentration asymptote but then suffers another reduction as the surface of the layer is approached. The latter effect is not explained at the present time. As a simultaneous check on this determination of the impurity and mobility profiles it is observed that by integrating the product of these quantities and the electronic charge over the layer, the total sheet conductivity of the layer is obtained, a quantity which can be directly measured by the four probe technique. The limit of integration is determined by a bevel and stain measurement of the layer thickness. The result is expressed by

$$\sigma_s = \int_0^t q\mu_d(s_d)\, N_d(s_d)\, ds_d \qquad [16]$$

Since it is usually necessary to extrapolate μ_d and N_d some distance to the surface of the layer, Eq. [16] is only a rough check. For the specimen of Fig. 5 the difference between the calculated and measured values of σ_s is less than 5%.

In the case of the diffused junction, the mobility variation in the substrate as shown in Fig. 6 is opposite to its variation in the epitaxial layer. The sample is a deep (40μ) gallium diffused p-type region on a 5 ohm-cm n-type substrate. In this case the measured variation in μ_d is due to compensation of the substrate impurities by the tail of the gallium diffusion, so that the total impurity concentration increases as the junction is approached from the n-side, causing a reduction in mobility.

Summary

It has been shown that the conductivity mobility and carrier density may be directly measured in the vicinity of blocking junctions. The probe method of measurement does not require the application of permanent contacts and is therefore useful for characterization of materials to be fabricated into semiconductor devices. In epitaxial layers the mobility is found to increase as the junction is approached. In diffused junctions the mobility is found to decrease as the junction is approached from the substrate side. The difference is attributable to the fact that the diffused junction is produced by compensation, which results in a greater density of scattering centers at the junction than in the substrate, whereas the nature of epitaxial growth is such as to produce a smaller density of scattering centers at the junction than in the layer.

Manuscript received July 27, 1964.

Any discussion of this paper will appear in a Discussion Section to be published in the December 1965 JOURNAL.

SYMBOLS

I	total current in amperes flowing in probe I_1, Fig. 1.
N_a	atoms/cm^3 consisting of the excess of ionized acceptors over ionized donors.
N_d	atoms/cm^3 consisting of the excess of ionized donors over ionized acceptors.
t	thickness in cm of layer being measured.
ρ	space charge density in coulombs/cm^3.
v	voltage applied to junction, v.
x	distance in cm from junction.
Q	total space charge per unit area on the n-side of junction in coulombs/cm^2.
c	small signal capacitance per unit area of junction, farad/cm^2.
σ_s	sheet conductivity, mho/square.
n	number of mobile electrons per cm^3.
p	number of mobile holes per cm^3.
μ_n	conductivity mobility of electrons in cm^2/volt sec.
μ_p	conductivity mobility of holes in cm^2/volt sec.
q	electronic charge, 1.6×10^{-19} coulombs.
V	voltage measured between inner probes, V_1, V_2, Fig. 1.
s	probe spacing in cm.
d	width of sample or mesa in cm.
C'	dimensionless correction factor for sheet conductivity.
a	length of sample or mesa in cm.
C	capacitance of junction in farads.
ϵ	dielectric constant of semiconductor in farad/cm.
s_a	distance in cm between the junction and the edge of the space charge region in the p-region.
s_d	distance in cm between the junction and the edge of the space charge region in the n-region.
E_{max}	maximum value of electric field within the space charge, volts/cm.

REFERENCES

1. L. Valdes, *Proc. IRE*, **42**, 420 (1954).
2. F. M. Smits, *Bell Syst. Tech. J.*, **37**, 711 (1953).
3. W. Schottky, *Z. Physik*, **118**, 539 (1942).
4. D. Kahng, C. O. Thomas, and R. C. Manz, *This Journal*, **110**, 394 (1963).

Diffusion of Gold into Silicon Crystals

G. J. Sprokel and J. M. Fairfield

International Business Machines Corporation, Endicott and Poughkeepsie, New York, respectively

ABSTRACT

Profiles are obtained for gold diffusing into silicon wafers of finite thickness. The profiles do not obey Fick's law. The effects of shallow diffusions of phosphorous and boron on the gold concentration are described; gold concentration is higher in areas of high phosphorous concentration.

Gold is used quite extensively to control the charge storage time of high speed diodes and transistors. Therefore, the diffusion of gold into silicon wafers of finite thickness is important in the design and fabrication of these devices. The diffusion of gold into silicon has been discussed by Struthers (1), Boltaks (2), Dash (3), and more recently by Wilcox and LaChapelle (4). It has become apparent from these publications that gold diffuses quite fast (1, 2), probably occupying interstitial positions of the silicon lattice, and that at least part of these interstitial atoms may convert to substitutionals (3).

In the above diffusion studies experimental conditions were such that the diffusing gold never pene-

trated through the whole specimen. If, however, gold is allowed to reach the opposite surface, as it is in practical applications, unexpected effects are observed. The concentration near the opposite surface is higher than expected and is affected by the state of that surface. It is the purpose of this paper to discuss these effects in some detail.

Experimental Procedures

Briefly, the experimental procedure is as follows. Gold labeled with Au 199 is plated on and diffused into silicon wafers in an argon atmosphere. Thin slices are etched off sequentially, starting at the side opposite the plated surface. The amounts of gold and silicon in each etchant sample are determined, and concentration profiles are constructed from these data.

Wafers are cut from pulled silicon crystals, and the surfaces are lapped and etched. The concentration of electrically active impurities is about 10^{13} at./cm^3. The wafers are approximately 25 mil thick.

Some of these wafers were diffused with phosphorus or boron to study the effects of these diffusions on the gold concentration. Planar structures were used, having been prepared in the conventional way. Silicon oxide was grown thermally; windows were etched in using photolithography; phosphorus or boron was diffused in the window areas to a depth of approximately 1μ. Then gold was plated on the opposite side and diffused in.

Detail.—Carrier-free Au 199 obtained as gold chloride[1] is dissolved in HNO_3/HCl and freeze-dried. The residue is taken up in 1 ml of a plating bath containing $KAu(CN)_2$ 0.01*N*; KCN 0.2*N*; Na_2HPO_4 0.03*N* (5). Immediately before plating the surface is "roughed" using 600 grit SiC paper and cleaned ultrasonically. Adhering plates were obtained on all wafers. The plate contains 1.5 x 10^{18} at. of Au, sufficient for an average concentration of 4 x 10^{19} at./cm^3 in the wafer. The ratio of Au 199 to Au 197 is adjusted to about 10^{-4}, sufficient for a detection sensitivity of 5 x 10^9 at. Au/cpm.

The gold is diffused in an argon atmosphere to prevent oxidation of the wafer surface. The argon gas was monitored for Au 199. Evaporation of gold is negligible.

In preparation for the etching sequence, the wafer is cemented to a Teflon[2] rod with the plated side toward the Teflon. The rod is inserted into a polypropylene test tube, containing 5 ml etching solution cooled to about 0°C in melting ice, and rotated to provide gentle agitation. The etching solution used in most of this work is a mixture of 3 parts HNO_3 s.d. 1.4; 2 parts glacial acetic acid; and 1 part HF 48%. Etching times are adjusted to remove the amount desired, then the etching solution is replaced and the process repeated until the wafer is dissolved.

Immediately after etching all samples are assayed for gold by counting the Au 199 gamma peak at 0.158 Mev in a single channel gamma spectrometer. By comparing the count rates of the etchant samples with the count rate of known aliquots of the plating bath, the amount of gold in the etchant is calculated. The amount of silicon in the etchant is determined by neutron activation analysis. The etchant solution, transferred into a suitable polypropylene container, is irradiated with fast neutrons produced by the reaction T(d, n) He 4.[3] The assay of silicon is based on the reaction Si 28 (n, p) Al 28. The only interfering reaction is O 16 (n, p) N 16. Compton scattering from the O 16 gammas causes considerable background at the silicon peak. Therefore the etchant samples are cooled for 2.5 min before they are counted. The O 16 activity has now decayed to 10^{-6} of the original amount, while Al 28 activity has decreased only to 0.46. The neutron flux is not constant enough for quantitative work, therefore each etchant sample is irradiated together with a silicon standard. From this one can calculate the total flux for the particular irradiation period, but since the fast neutron flux is moderated by the etchant solution (essentially water) a correction is necessary. The correction can be obtained by irradiating a silicon standard together with a solution made by dissolving a known amount of silicon in etching solution. The sensitivity of the method for pure silicon, under the experimental conditions of this study, is about 5 μg/cpm at a background of about 4 cpm, and for the etchant solution about 10 μg/cpm at a background of about 10 cpm. This background depends on the chemicals used; in particular HNO_3 contains measurable amounts of silicon. The samples of etchant solution contain 5-20 mg of silicon. Therefore the sensitivity is quite adequate. Since chemical operations are not involved the method of assay is quite fast, about 10 min/sample.

The amount of silicon in the etchant solution determines the thickness of the slice removed from the wafer. The amount of gold in the etchant solution and the volume of the slice determine the local concentration of gold. The sum of the thickness of the slices should add up to the thickness of the wafer. The difference is usually less than 0.001 in., the average for all wafers checks within 0.0002 in. However, the standard deviation for one sample is about 25% of the average. Since this would cause a similar spread in the data for the gold concentration, determination of the actual amount removed greatly improves the accuracy of the data.

Results

Concentration profiles.—Figures 1 and 2 show concentration profiles after diffusion at 1000° and 1100°C, respectively. All profiles are characterized by a nearly horizontal central region. Near the gold side the concentration drops 2 or 3 orders of ten in a distance of 1 or 2 mils. Near the opposite side the concentration tends to increase. The concentration in the central

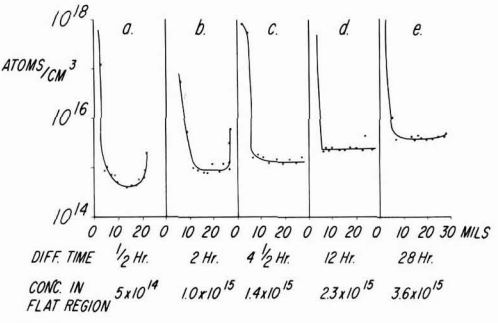

Fig. 1. Gold concentration profiles after diffusion at 1000°C

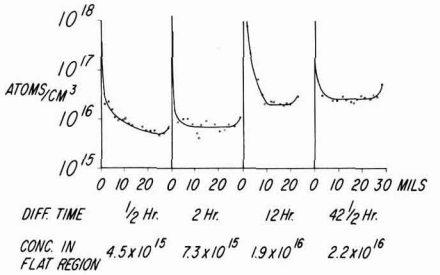

Fig. 2. Gold concentration profiles after diffusion at 1100°C

[1] Western New York Nuclear Research Center, Buffalo, New York.

[2] Registered Trade Mark, E. I. du Pont de Nemours Company, Wilmington, Delaware.

[3] The neutron generator is built by Texas Nuclear Corporation, Austin, Texas.

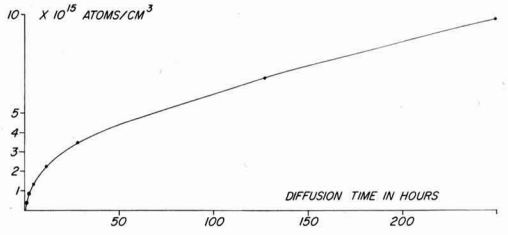

Fig. 3. Gold concentration in central region plotted vs. time, temperature 1000°C. Data are those given in Fig. 1 except the points at 128 and 256 hr. These were obtained by neutron activation analysis.

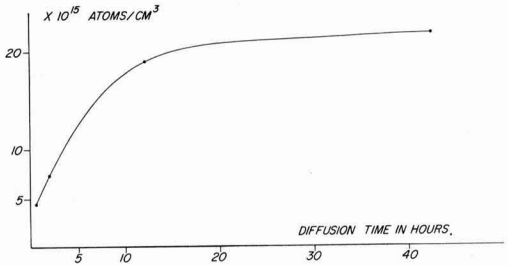

Fig. 4. Gold concentration in central region plotted vs. time, temperature 1100°C. Data from Fig. 2.

region increases with diffusion time as indicated in Fig. 3 and 4, but the location of the steep gradient near the gold side is independent of time. Therefore the steep gradient must be considered an artifact of the experiment. At the plated surface gold-silicon eutectic is formed. The eutectic melt does not wet the surface but may well extend, in localized spots, to a depth of a few milli-inches.

Radial homogeneity.—Data in the previous section refer to the average gold concentration in a slice. Autoradiograms of etched wafer surfaces indicate substantial homogeneity across the surface. However, nearly all autoradiograms made in the course of this study show spots of much higher gold concentration. The number of such spots is small except near the original wafer surface. Spots tend to conglomerate at the original surface, but a shallow etch removes most of this activity. The size of single spots on the film is of the order of 10μ. The activity in one spot cannot be measured directly from the optical density because the x-ray film is overexposed at that spot. To make an appreciable contribution to the total, the activity in one spot would have to be 10^6 times larger than the average, which is unreasonable. Therefore, wherever the number of spots is small, the contribution of this localized gold can be neglected.

Often the same configuration of spots appears in autoradiograms from several sequential etches. In such cases gold has clearly accumulated along lines extending into the crystal, probably dislocations. These lines may extend 5 mils or more. Since their number is small, typically less than 1/mm^2 they cannot contribute to a fast transfer of gold through the wafer.

If a wafer which has been shown to contain this type of gold accumulation is heated for a long time (20 hr or more), no appreciable change in the number of spots is found. Under these conditions there is no external supply of gold, and since the lattice is far from saturated one would expect the accumulations to disappear completely if they contributed to the transfer.

Surface effects.—The amount of gold collecting near a wafer surface depends on the surface preparation. It is smaller for etched surfaces than for etched and oxidized surfaces. If a gold diffused wafer is etched and heated again, gold collects near the surface mostly in localized spots which can be removed by a shallow etch in agreement with an earlier observation (7). The increase in the gold concentration under an oxide layer can be used to prepare autoradiograms of oxide-masked wafers. The window areas appear lighter.

Shallow phosphorous diffusions also affect the gold concentration. At high phosphorous concentrations (8 x 10^{20} at. P/cm^3 at the surface) the window areas are darker and have therefore collected more gold (Fig. 5a). However, at low concentrations (2 x 10^{20} at. P/cm^3 or less) the masked areas are darker. Therefore the mask dominates at low concentration (Fig. 5c).

The electrical junctions are about 1-2μ from the surface. If substantially more than this is etched-off, a pattern as in Fig. 5a reverses; the window areas are now lighter. A pattern as in Fig. 5c remains unchanged. Therefore, the effect of the masking still persists 10 or 20μ from the SiO_2/Si interface (Fig. 5b and 5d). The window areas in Fig. 5b and 5d are no longer sharply delineated but appear diffuse. Examining autoradiograms of gold in a phosphorous diffused area under a microscope shows that the gold is not uniformly distributed over the area but tends to build up near the edges (Fig. 6). Boron diffusion does not produce comparable effects but the highest concentration used was only 1 x 10^{20} at. B/cm^3.

Discussion

From Fig. 1-4 it is seen that the concentration of gold in bulk silicon, introduced from an infinitely large source at the surface, increases smoothly with time, rapidly for short diffusion times but only slowly for longer diffusion times. At 1100°C the gold concentration is 2.2 x 10^{16} at./cm^3 after 42 hr diffusion time. At 1000°C the concentration is 9.8 x 10^{15} at./cm^3 after 250 hr. Collins, Carlson, and Gallagher (7) have reported data on the solubility of gold in silicon. Details are not given, but by interpolating the graph in Fig. 1 of their paper, the solubility may be shown to be approximately 3 x 10^{16} at./cm^3 at 1100°C and 9 x 10^{15}

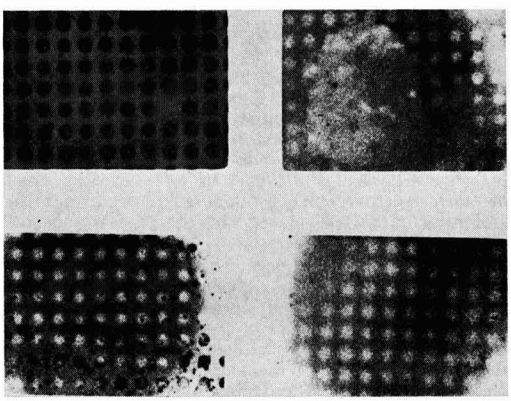

Fig. 5. Au 199 autoradiograms of P diffused wafers. Circular windows (diameter 400μ) etched in oxide mask. P diffused from PH_3. Junction depth 1-2μ. Au 199 diffused from a plate on the opposite surface. Excess removed prior to exposure. (a) (top left) 8 x 10^{20} P/cm^3. After Au diffusion oxide mask removed in HF. Window areas contain more gold than masked areas; (b) (top right) same as 5a but etched to a depth of 10μ. Window areas are now lighter. The area in the center indicates the spot where the oxide mask was removed prior to gold plating (to assure good contact); (c) (bottom left) 2 x 10^{20} P/cm^3. Window areas contain less gold than masked areas. Autoradiogram shows the original surface, before cleaning in HF. Notice spots of high Au concentration in 5c, absent in 5a; (d) (bottom right) Same as c but etched to a depth of 25μ. The pattern remains unchanged.

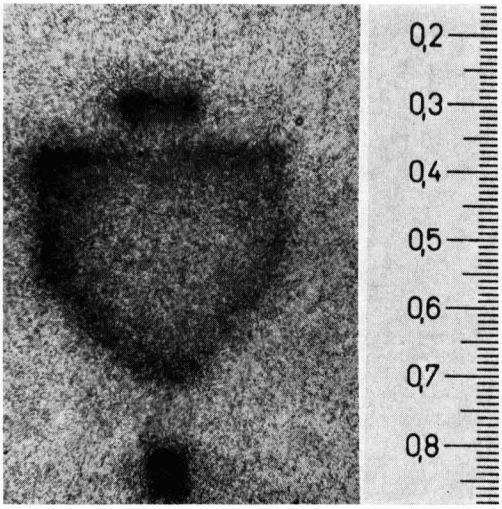

Fig. 6. Accumulation of gold in a phosphorous diffused area, starting at the circumference and proceeding inward. It appears that the intersection of mask and window has a larger effect on the gold concentration than the diffused phosphorous itself. (Scale 10μ/div.).

at./cm^3 at 1000°C. Numerically these data agree well; however from the slope of the curve in Fig. 3 it is doubtful whether solubility has been reached. The true solubility is probably slightly higher. The data in Fig. 3 and 4 will be used in a forthcoming paper (8).

The buildup of gold occurs much faster around areas of lattice imperfections or discontinuities (*e.g.*, surfaces, dislocations, phosphorous diffusion, etc.). This phenomenon can be explained by an interstitial-substitutional model, as discussed by Frank and Turnbull (9) for copper in germanium and used by LaChapelle and Wilcox (4). Gold diffuses rapidly as an interstitial but converts to a relatively immobile substitutional by combining with a lattice vacancy. This conversion occurs more rapidly near sources of vacancies.

Surfaces are sources of vacancies; thus the total concentration builds up near the surface as evidenced by the graphs in Fig. 1 and 2. Thermally oxidized surfaces can produce more vacancies than unoxidized surfaces. Mechanical damage of the surface can produce more vacancies still.

The observed accumulation of gold along lines extending into the crystal may well represent dislocations. A mechanism discussed by Dash (3) in which the collecting gold induces dislocations to climb could well be operative. The stability of these accumulations emphasizes the relative immobility of gold atoms in the substitutional state.

Finally, damage or dislocations from high surface concentrations of phosphorus act as sources of vacancies and thereby collect gold relatively rapidly. This fact is particularly important when high surface concentration phosphorous diffusions are used to make high speed diodes and transistors. In such devices, the amount of gold is intimately related to the charge storage times.

Conclusion

There is qualitative evidence for the interstitial-substitutional mechanism; a gold atom diffuses as an interstitial but is converted to a nearly immobile substitutional. The conversion occurs everywhere but is particularly prominent near sources of vacancies. Gold collects especially fast in areas prediffused with a large concentration of phosphorus.

Gold can be used to study damage done to a lattice by phosphorous diffusion or oxidation.

Manuscript received July 22, 1964; revised manuscript received Sept. 14, 1964. This paper was presented at the Toronto Meeting, May 3-7, 1964.

Any discussion of this paper will appear in a Discussion Section to be published in the December 1965 JOURNAL.

REFERENCES

1. J. D. Struthers, *J. Appl. Phys.*, **27**, 1560 (1956); **28**, 516 (1957).
2. B. I. Boltaks, G. S. Unlikov, and R. S. Malkovich, (English) *Sov. Phys. Solid State*, **2**, 2134 (1961). Also, B. I. Boltaks, "Diffusion in Semiconductors," Academic Press, New York (1963).
3. W. C. Dash, *J. Appl. Phys.*, **31**, 2275 (1960).
4. W. R. Wilcox and T. J. LaChapelle, *ibid.*, **35**, 240 (1964)
5. W. Blum and G. B. Hogaboom, "Principles of Electroplating," 3rd ed., McGraw-Hill Publishing Co., New York (1949).
6. G. Bemski and J. D. Struthers, *This Journal*, **105**, 588 (1958).
7. C. B. Collins, R. O. Carlson, and C. J. Gallagher, *Phys. Rev.*, **105**, 1168 (1957).
8. G. J. Sprokel, To be published.
9. F. C. Frank and D. Turnbull, *Phys. Rev.*, **104**, 617 (1956).

A Study of the Dissolution of Zinc in Buffered Acetic Acid Solutions

Robert S. Alwitt[1] and Robert S. Kapner

Department of Chemical Engineering, Rensselaer Polytechnic Institute, Troy, New York

ABSTRACT

The kinetics of zinc dissolution in buffered acetic acid solutions are described. The dissolution process occurred along the walls of zinc tubes with acid solutions passing through the tubes in laminar flow. Only a moderate degree of diffusional resistance in transporting reactants to the reaction surface was observed. The data indicate that molecular acetic acid as well as hydrogen ions participate in the cathodic reaction. Possible dissolution mechanisms are proposed based on simultaneous reactions involving hydrogen ion and molecular acid discharge at the metal surface. Only at high acid concentrations does the molecular acetic acid discharge reaction become important.

The purpose of this investigation was to obtain information on the kinetics of the dissolution of zinc by acetic acid. Using buffered acid solutions, in which the *p*H and molecular acid concentration could be varied independently, information was obtained on the role of the weak acid molecule in the dissolution process. There is little information in the literature on this point.

Kilpatrick and Rushton studied the dissolution of rotating zinc and magnesium cylinders in deaerated solutions of HCl, acetic acid (HAc), and other weak acids (1). They found the reaction rate to be dependent on rotational speed and viscosity, both indicative of a significant degree of diffusion control. However, for both HCl and HAc, the activation energy was about 10 kcal/mole, far greater than the 3-4 kcal/mole to be expected for a reaction under complete diffusion control. The reaction rate was first order with respect to total acid concentration, but not to the hydrogen ion concentration alone. They concluded that the surface reaction was due to both ionic and molecular acids, but the results were not clear-cut. Levich (2) reported a study of the dissolution of rotating magnesium disks in 0.1*N* HCl, 0.15*N* HAc, and 0.15*N* HCOOH. The data indicated that in all cases the reaction rate was determined by the diffusion of acid to the surface. Allbutt and Tolley (3) determined the dissolution rate of zinc in dioxan-water solutions of HCl. At sufficiently high dioxan concentrations an appreciable fraction of the HCl was present in molecular form. In these solutions the data indicated the possibility of direct reaction between zinc and covalent HCl.

The dissolution of a metal by an acid can be considered as consisting of simultaneous anodic and cathodic electrochemical processes. According to the Wagner-Traud theory of mixed potentials (4), which has been substantiated for simple systems, each process can be analyzed independently of the other. In this paper only the cathodic processes occurring on the zinc surface are discussed. In a strong acid, the usual cathodic reaction is reduction of hydrogen ions to atomic hydrogen and thence molecular hydrogen. With a weak acid, another possible cathodic reaction is reduction of the molecular acid species.

It was anticipated that dissolution would be under significant diffusion control, which would result in the reactant wall concentration being less than the bulk concentration. In such a situation it is imperative that the experimental reactor be of a design that will permit calculation of wall concentrations from experimentally measurable quantities. The two designs most frequently used for this purpose are the rotating disk and the tubular reactor. The latter was used in this study.

The "quasi-stationary" technique of Frank-Kamenetskii (5) was used to calculate wall concentrations. This method assumes that the conditions of diffusional transport can be considered independent of the course of the surface reaction. The fact that the diffusion and reaction processes are coupled by a surface boundary condition is neglected. This results in consideration only of transport in the direction normal to the surface, neglecting reactant that arrives due to longitudinal convective transport. Any error inherent in this method can be substantially reduced provided longitudinal concentration differences are kept very small. This can be easily accomplished in a differential reactor, one in which reactant conversion is minimized.

With these assumptions, the amount of reactant supplied at steady state to an element of reactor surface is

$$q = \beta (C - C_W) \qquad [1]$$

At steady state, q must equal the surface reaction rate. The definition of β, the diffusion velocity constant (or mass transfer coefficient) is $\beta = N_{Nu}D/d$. Since diffusion is considered to be independent of the surface reaction process, β can be determined from analogous heat transfer data or theory. With q and C determined experimentally it is a simple matter to calculate C_W.

Experimental

The dissolution of zinc by buffered and unbuffered solutions of acetic acid was studied in a tubular reactor. The ranges of the independent variables were: C_{HAc}, 10^{-3} to 10^{-2}M; *p*H, up to 6.0; N_{Re}, 50-1000. Sodium acetate was used as the buffering salt. Except for runs to determine the heat of activation, the temperature of the test section was maintained at 30° ± 1°C. Prepurified nitrogen was bubbled through the acid solution for 4 to 12 hr prior to the start of a run to remove dissolved oxygen. Reagent grade chemicals and distilled water were used throughout. The reactor section was made of 99.999% zinc. As-received zinc billets were pickled, recast in Pyrex tubes, machined to the dimensions of schedule 80 ¼ in. pipe, and chemically polished. These zinc tubes were annealed in an argon atmosphere for 24 hr at 350°C and then repolished. Metallographic examination at 400X showed no evidence of cold-work on the inner surface of a sample.

The test apparatus is pictured in Fig. 1. The test section consisted of three lengths of zinc tube connected by flange and O-ring assemblies to give a total length of 33.3 cm. The dissolution rate was low enough so that the inside diameter of the tubes did not change significantly during these runs. Entrance and exit

[1] Present address: Engineering Laboratories, Sprague Electric Company, North Adams, Massachusetts.

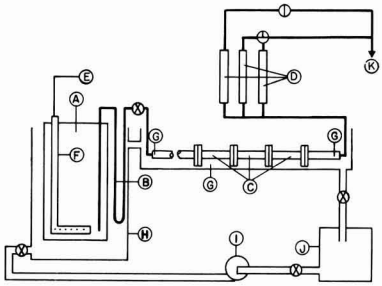

Fig. 1. Experimental apparatus: A, acid reservoir; B, glass heat exchanger; C, zinc tubes; D, Rotameters; E, N_2 supply; F, N_2 header; G, thermocouples; H, water drum; I, water pump; J, water surge tank; K, effluent.

sections were schedule 80 ¼ in. PVC pipe of sufficient length to insure well-developed laminar flow in the test section. Acid solution was fed through the reactor by maintaining a constant positive head at the outlet of the acid reservoir with a pressure-regulated source of nitrogen. Flow rate was regulated with the stopcocks after the rotameters. Reaction conditions were such that the hydrogen concentration never exceeded the solubility of hydrogen. The test section and polyethylene acid reservoir were held at constant temperature by a temperature controlled circulating water bath heated by immersion heaters not illustrated in Fig. 1.

Procedure.—When not in use, the test section was filled with distilled water. At the start of a run, 2 x $10^{-3}N$ HAc was run through for 40 min to remove any oxide build-up on the tube surface during storage in water. Acid made up to the desired composition in the reservoir was passed through the reactor at several flow rates. At the slowest flow rate it was found that after running for 20 min steady-state conditions were assured. At all flow rates, 20 min were allowed before collecting effluent samples. The concentration of zinc in the effluent was determined for each flow rate using a modification of the spectrophotometric method of Rush and Yoe (6, 7). At each acid composition 3-6 flow rates were run in random order. Corresponding to each effluent sample the potential of the zinc was determined with reference to a saturated calomel electrode (SCE) kept at 30°C in the same water bath. Potential readings were made with a Beckmann Model G pH meter. Further details of the experimental apparatus and procedure can be found elsewhere (8).

Results

From the data of replicate runs it was found that reaction rates were reproducible within ± 15.8% and corrosion potentials were reproducible within ± 6 mv, both at the 95% confidence level.

For each acid composition the least squares line for log C_{Zn} *vs.* log N_{Re} was determined. Some typical results are shown in Fig. 2. The average slope of all runs was —0.930 ± 10.3%. The slope was not a function of HAc concentration or pH. In the absence of diffusional effects the slope would be —1 and for complete diffusion control it would be —2/3. There is no theoretical reason for a linear relationship in the region of intermediate control. In the present case the justification is that the residual variance of the least squares lines was not significantly greater than the variance of replicate points.

Since there were some diffusional effects, the concentration of reactants at the wall were less than the bulk concentrations. The wall concentration of HAc was calculated using the approximate method of Frank-Kamenetskii (5) described above. For each acid composition the calculation was made at N_{Re} =

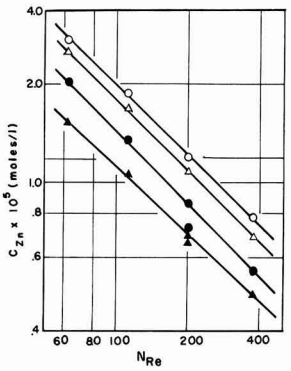

Fig. 2. Typical experimental results. ${}_BC_{HAc} \times 10^3$: ▲, 2.00; ●, 3.92; △, 7.76; ○, 10.04.

150, using the C_{Zn} from the least squares line to determine the average reaction rate over the reactor. The average Nusselt number for a tube of length L is $1.61(N_{Pe}d/L)^{1/3}$ (9). Over the range of bulk concentration used, the diffusivity of acetic acid varies less than 1% and was calculated to be 1.34 x 10^{-5} cm²/sec at 30°C (10). Using these values and the dimensions of the reactor, the value of β in Eq. [1] was 3.78 x 10^{-4} cm/sec. An experimental determination of β agreed within 5% with the calculated value. The fraction of acid reacted was always less than 3%, so the reactor was considered a differential reactor with bulk acid concentration equal to the inlet value.

The average value of the ratio ${}_WC_{HAc}/{}_BC_{HAc}$ calculated from Eq. [1] was 0.895. Ninety-five per cent of the values were greater than 0.75. Assuming no concentration gradient in acetate ion, the gradient in C_{H^+} was proportional to that in C_{HAc}. Figure 3 shows the relationship between C_{Zn} at N_{Re} = 150 (proportional to reaction rate) and wall concentration of HAc at various bulk pH values.

The electrode potential of the zinc was independent of flow rate. It was a function of acid concentration

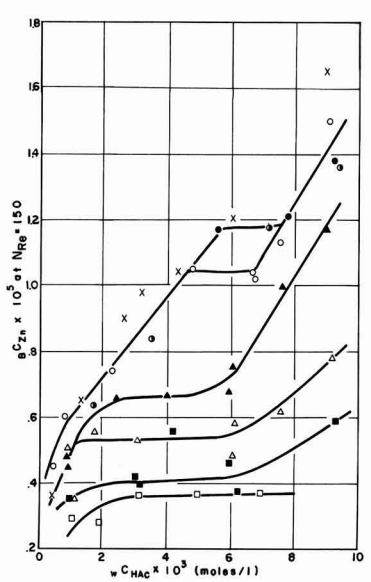

Fig. 3. Reaction rate *vs.* wall concentration of acetic acid. N_{Re} = 150; pH: X, no buffer; ●, 3.50; half dark circle, 3.80; ○, 4.10; ▲, 4.50; △, 5.00; ■, 5.50; □, 6.00.

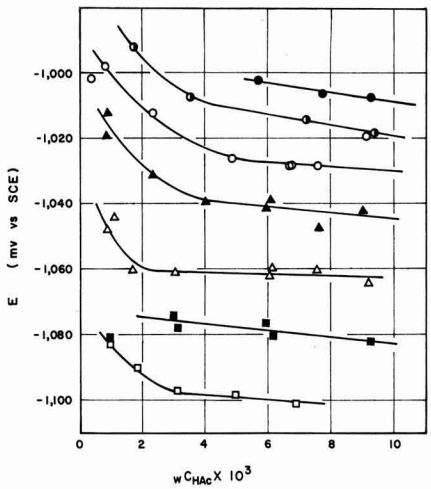

Fig. 4. Zinc potential *vs.* wall concentration of acetic acid. N_{Re} = 150; *p*H: ●, 3.50; half dark circle, 3.80; ○, 4.10; ▲, 4.50; △, 5.00; ■, 5.50; □, 6.00.

and *p*H, as shown in Fig. 4. Values of potential with unbuffered acid are not given since it was very difficult to obtain steady or reproducible results with these solutions. At a concentration of 5 x 10^{-3}M, acetic acid has a conductivity of only 100 μmhos. With this acid the impedance of the solution path between the zinc and the reference electrode was about one megohm. This is high enough to account for the observed erratic potential readings.

The change of reaction rate with temperature was determined for three solution compositions. The apparent energy of activation was determined from the slope of the log rate *vs.* $1/T$ plots shown in Fig. 5. The results were corrected for diffusional effects using a graphical relationship developed by Rosner (11). The results with each solution were as follows:

Solution		Activation energy (kcal/mole)	
C_{HAc} x 10^3	*p*H	Exptl.	Corr.
1.37	4.08	4.55	5.83
5.23	5.98	4.62	4.87
9.70	4.10	4.90	5.50

An average value of 5.4 kcal/mole would apparently be accurate within ± 10% over the range of experimental conditions.

Discussion

The transport of reactants to the zinc surface played a much smaller role in the over-all reaction rate than had been expected. The use of ultrahigh purity zinc (99.999%) and a reaction surface free of cold work apparently reduced the surface reaction rate sufficiently so that diffusion was not the predominant slow step.

The calculated wall concentrations are those that would exist at the zinc-solution interface in the absence of all other effects except convective forces and concentration gradients. However, at a metal-electrolyte interface there will exist an electric double layer (edl) with its associated electric field. The thickness of the edl varies, but is usually considerably less than 1000Å. Thus, within any reasonable experimental accuracy, the calculated wall concentration can be taken as that existing at the solution boundary of the edl. Uncharged species will be little affected by the edl, so the calculated wall concentration of HAc molecules are representative of the true interfacial concentration. However, ionic concentration in the edl is a function of potential and ionic strength as well as bulk

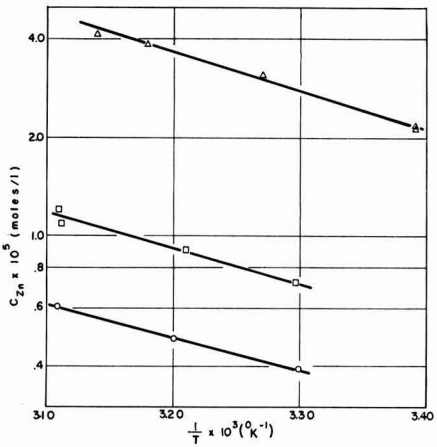

Fig. 5. Arrhenius plot for determination of over-all activation energy:

Symbol	$_BC_{HAc}$	*p*H	N_{Re}
□	1.37 x 10^{-3}	4.08	125
○	5.23 x 10^{-3}	5.98	200
△	9.70 x 10^{-3}	4.10	100

(wall) concentration.[2] At high ionic strength (> 1M), it can usually be assumed that ionic concentrations within the edl are the same as those outside the edl. In this study ionic strength was determined primarily by the sodium acetate added to adjust *p*H, and was always less than 1M. Thus, it was not possible to analyze the rate data quantitatively to evaluate possible reaction mechanisms without introducing several assumptions about the properties of the edl. However, qualitative analysis of the data yields some interesting information.

Examination of Fig. 3 shows that at each *p*H there is a range of C_{HAc} over which rate is independent of C_{HAc}. At lower and higher C_{HAc} the rate depends on C_{HAc}. In Fig. 4 it is seen that at each *p*H the electrode potential changes rapidly at low C_{HAc} and then changes little with further increase in C_{HAc}. The increasing reaction rate at low C_{HAc} and constant *p*H could be due to the changing potential rather than to a dependency on C_{HAc}. Since the potential is relatively stable at each *p*H at high C_{HAc}, the increase in reaction rate in this region appears to be a function of C_{HAc}. It is interesting that the data at high C_{HAc} can be extrapolated linearly to the origin with a slope dependent on *p*H and/or *E*. This is indicative of a reaction that is first order with respect to HAc.

The experimental data may be explained by a reaction scheme in which at low C_{HAc} the rate-controlling step of the cathodic reaction is a function of *p*H and *E*. At high C_{HAc} the rate-controlling step is a function of *p*H, *E*, and C_{HAc}. The simplest way for this to occur would be by means of parallel reaction paths, one path involving a proton and the other an HAc molecule. As the HAc concentration increased, the second reaction would be favored.

It is generally accepted that reduction of H^+ on a metal proceeds in the following sequence

$$H^+ + e \rightarrow H \qquad [2a]$$

followed by either

$$H + H \rightarrow H_2 \qquad [2b]$$

or

$$H + H^+ + e \rightarrow H_2 \qquad [2c]$$

[2] Breiter *et al.* (12) give a brief description of the effect of the edl on surface reactions. More detailed information is in chapters by Parsons and Frumkin in ref. (13).

It is possible that reactions analogous to [2a] and [2c] can occur involving HAc molecules, *e.g.*,

$$HAc + e \rightarrow H + Ac^- \qquad [3a]$$

$$H + HAc + e \rightarrow H_2 + Ac^- \qquad [3b]$$

At low C_{HAc} the rate-controlling step might be [2a], followed by [3a] at high C_{HAc}. Or, at low C_{HAc} the rate-controlling step might be [2b] or [2c] followed by [3b] at high C_{HAc}. The standard electrode potential is —0.280v for the reaction, $HAc + e = \frac{1}{2} H_2 + Ac^-$. When compared with the standard electrode potential of —0.763v for the reaction, $Zn = Zn^{+2} + 2e$, it is seen that the reduction of molecular acid is quite feasible in this system.

Other reactions first order with respect to C_{HAc} are also possible. For example, reduction to acetaldehyde

$$CH_3COOH + 2H^+ + 2e = CH_3CHO + H_2O \qquad E_o = -0.118v$$

Yakhontov (14) found small amounts of acetaldehyde present after reacting zinc with 40% and 60% acetic acid at 100°C. However, considering the conditions of the present experiment, it is doubtful that this reaction contributed significantly to the observed rate.

For a discharge reaction such as [2a] or [3a] the energy of activation is generally greater than 10 kcal/mole. The observed energy of activation was significantly less than this. If surface coverage with atomic hydrogen was high, a reaction between adsorbed H atoms or between adsorbed H atoms and a species in solution might proceed with a much lower activation energy. Among others, Bockris and Potter (15) reported a study that showed that on tungsten and nickel surfaces the heat of adsorption of H atoms falls considerably at coverages above about 70% until at about 90% coverage the heat of adsorption is about 5 kcal. Thus, the observed heats of activation may be indicative of significant surface coverage. Such coverage could explain the relative constancy of the heat of activation even when measured at conditions at which different reactions might be rate-controlling.

On this basis it does not seem likely that discharge of H^+ or HAc were rate-controlling steps. The data do not permit distinguishing whether reaction [2b] or reaction [2c] was rate-controlling at low C_{HAc}. Whichever one of these was controlling at low C_{HAc}, it appears that a reaction such as [3b] became dominant at high C_{HAc}.

Additional work to confirm these suggested reactions is in progress. Experimental studies are being made using sufficient supporting electrolyte which will permit estimates of wall concentrations of ionic species. With these data a quantitative treatment of the dissolution mechanism can be undertaken. The effect of soluble inhibitors on the kinetics of this dissolution process is also being studied.

Conclusions

1. The dissolution of zinc in acetic acid can proceed under only slight diffusion control.
2. Molecular acetic acid can take part in the cathodic reaction on zinc in acid solution.
3. The dissolution reaction appears to occur through parallel reaction paths, one path involving a proton and the other an HAc molecule. As the HAc concentration increases, the second reaction is favored.

Acknowledgment

The material presented here is part of a research program made possible by National Science Foundation grant G23484. One of the authors (RSA) was the recipient of a National Science Foundation Cooperative Fellowship during part of this program.

Manuscript received April 29, 1964; revised manuscript received Sept. 16, 1964.

Any discussion of this paper will appear in a Discussion Section to be published in the December 1965 JOURNAL.

REFERENCES

1. M. Kilpatrick and J. H. Rushton, *J. Phys. Chem.*, **34**, 2181 (1930); **38**, 269 (1934).
2. V. G. Levich, "Physicochemical Hydrodynamics," Prentice-Hall, Englewood Cliffs, N. J. (1962).
3. M. Allbutt and G. Tolley, *J. Appl. Chem.*, **11**, 52 (1961).
4. C. Wagner and W. Traud, Z. Elektrochem., **44**, 391 (1938).
5. D. A. Frank-Kamenetskii, "Diffusion & Heat Exchange in Chemical Kinetics," translated by N. Thon, Chapt. II, Princeton University Press, Princeton (1955).
6. J. T. McCall, G. K. Davis, and T. W. Stearns, *Anal. Chem.*, **30**, 1345 (1958).
7. R. M. Rush and J. H. Yoe, *ibid.*, **26**, 1345 (1954).
8. R. S. Alwitt, PhD thesis, Rensselaer Polytechnic Institute, Troy, New York (1963).
9. W. H. Linton and T. K. Sherwood, *Chem. Eng. Progr.*, **46**, 258 (1950).
10. V. Vitagliano and P. A. Lyons, *J. Am. Chem. Soc.*, **78**, 4538 (1956).
11. D. E. Rosner, AIChE Preprint No. 135, 54th Annual Meeting Dec. 1961.
12. M. Breiter, M. Kleinerman, and P. Delahay, *J. Am. Chem. Soc.*, **80**, 5111 (1958).
13. P. Delahay, Editor, "Advances in Electrochemistry & Electrochemical Engineering," Vol. 1, Interscience, New York (1961).
14. V. D. Yakhontov, *J. Gen. Chem. (USSR)*, **17**, 2054 (1947).
15. J. O'M. Bockris and E. C. Potter, *J. Chem. Phys.*, **20**, 614 (1952).

SYMBOLS

β	diffusion coefficient.
C	concentration, moles/liter.
D	diffusivity, cm^2/sec.
d	tube diameter.
E	electrode potential *vs.* reference electrode.
edl	electric double layer.
L	tube length.
mv	millivolts.
N_{Nu}	Nusselt number.
N_{Re}	Reynolds number.
q	flux.
SCE	saturated calomel electrode.
T	absolute temperature.

Subscripts: B, bulk solution; H^+, hydrogen ion; HAc, acetic acid; W, wall; Zn, Zinc ion.

Conductance of Glass Immersed in Molten Salts

Kurt H. Stern

National Bureau of Standards, Washington, D. C.

ABSTRACT

The electrical conductance of high SiO_2 glass was measured when immersed in a number of molten salts and salt mixtures between 800° and 900°C. Sodium and lithium ions diffuse into the glass, both from their own chlorides and from low concentrations in KCl. The glass comes to equilibrium with each melt composition, the time of equilibration depending on the particular ions in the melt. The activation energy of sodium and lithium ion conduction in glass is 75-84 kJ (18-20 kcal), with potassium it is variable between 105 kJ (25 kcal) and 167 kJ (40 kcal). The conductance method is not sufficiently precise to detect silver and cuprous ion diffusion into glass.

In spite of several studies of the behavior of glass in molten salt media the detailed processes involved in the interaction between various glasses and salts are not yet well understood. The present state of knowledge may be summarized as follows: (*A*) Electrical conduction in silica glasses is ionic (1, 2), the magnitude of the current depending on the kinds of ions, their concentration, and the temperature. (*B*) Silica glasses containing alkali metal oxides are cationic conductors, the oxide anions remaining fixed in the glass structure (2). (*C*) Activation energies for conduction are similar to those for diffusion, typically 84-168 kJ (20-40 kcal) (3). (*D*) When a glass initially containing ions is placed into a molten salt, ion exchange may take place, ions from the glass diffusing out and ions from the melt diffusing in (4, 5). Factors determining this exchange are not well known. (*E*) When a high-purity (low ion content) glass, such as fused silica, is placed in a molten salt, ions from the salt diffuse into the glass (7). There is some evidence that the smaller of two ions in a salt mixture will diffuse preferentially into the glass (7), but specific ion-glass interactions may also be significant (6). (*F*) The surface composition of an ion-containing glass may differ from that in the bulk, both in the presence and absence of salt. The equilibrium composition is that giving the minimum surface free energy (8). (*G*) Some glasses, *e.g.*, Vycor, contain bound water as OH groups in the silica structure. In a water vapor environment these OH groups move, leading to net diffusion of H_2O through the glass (9, 10). Nothing is known of the effect of this bound water on the transport of ions through the glass. (*H*) If a glass initially containing no ions, *e.g.*, pure silica, is exposed to a molten salt whose cations diffuse into the glass, electrical neutrality requires that an equivalent amount of anions migrate into the glass also. Information on this point is largely lacking, although there is some evidence that anions migrate through glass under an applied field (11).

The present paper reports a study of the electrical conductance of high-silica glass, mainly Vycor, immersed in various molten salts. Two effects were studied: (i) changes of conductance with time, caused by the immersion of the glass in a salt or salt mixture, (ii) changes of conductance caused by changes in the melt composition and temperature, which are independent of time.

Experimental

The conductance cells consisted of 13 mm O.D. Vycor glass U-tubes ~ 25 cm high, with a 1 mm thick glass partition in the center of each cell separating the legs. The bright platinum electrodes, 1 cm^2 in area, were suspended by sealed-on platinum wires from glass caps which fitted over the ends of the cell. Thus the electrodes could be removed easily for addition of salt to the cell and repositioned. Since the resistance of the salt had been found (in a similar tube without partition) to be negligible compared to that of the partition, the precise position of the electrodes did not affect the measurement.

In each measurement the salt composition in both compartments was the same. 15g of the salt or salt mixture under study was placed in the preheated cell, already positioned in the center of the furnace, melted, the electrodes were introduced, and measurements begun.

Using a Marshall control panel and packing the cell in vermiculite kept the temperature constant to within ± 1°. The temperature was measured by a chromel-alumel thermocouple whose hot junction was positioned just outside the center of the cell. Resistance was measured with a Jones and Josephs-type bridge with Wagner ground at 1 kc. Between 1 and 10 kc resistance was independent of frequency. High resistances were measured in parallel with a high-precision 10^4 ohm resistor. In a typical measurement the cell was filled with one salt and allowed to equilibrate; the resistance was measured as a function of temperature. The desired amount of a second salt was then added and the procedure repeated. Further additions were made until the cell was full. Each new experiment was started with a new cell. In some experiments the conductance was measured as a function of time until equilibrium was reached.

Since it proved impossible to reproduce precisely the cross section and thickness of the glass partitions in the various cells, the actual values of $1/R$ have little significance when comparing measurements made in different cells. Changes occurring with time and melt composition in the same cell and the temperature coefficient of conductance both in the same and different cells are significant, however.

Reagent grade NaCl, KCl, and KBr were dried under vacuum at 500°C; LiCl was vacuum dried above its melting point. Anhydrous CuCl was prepared by reduction of $CuCl_2$ by sulfurous acid (12). Reagent grade AgCl was used without further purification.

Results and Discussion

In many of the experiments the salt initially put in the cell was KCl because it was known that potassium ions diffuse into glass only to a slight extent (7). Thus the addition of a salt whose ions diffuse into glass to a greater extent can be detected by an increase in conductance. Since, in addition to diffusion of ions into the glass, ions may also diffuse out, only relatively large changes in conductance can be considered significant. Thus, although a noticeable change in conductance on addition of salt is evidence for some glass-salt interactions, the absence of such a change does not necessarily imply absence of interaction.

Since most experiments were carried out with Vycor the subsequent results refer to that glass unless otherwise indicated.

General observations.—In the initial experiments, carried out with KCl, the cell was heated to 800°C

and the salt added. Fluctuations in conductance occurred for several hours, both with Vycor and fused silica, the conductance decreasing during this period by as much as a factor of four. If the empty cell was kept at 800°C for several days before introducing the salt, fluctuations were much reduced. A slow decrease in conductance still occurred for several days subsequent to the addition of salt, probably because the diffusion of sodium ions out of the glass is the predominant effect. The removal of fluctuations on heating the empty cell suggests that structural changes or loss of bound water are taking place.

In all experiments the conductance eventually reached a steady value, although this usually required several days. After the first few hours, changes were quite slow. When a steady value had been reached the temperature dependence of the conductance was measured between 800° and 900°C. In virtually all cases the conductance ($1/R$) was a linear function of $1/T$ so that the activation energy (E_a) is independent of temperature in this range. The addition of a second salt to the KCl already in the cell may or may not produce a change in conductance. If the former, the process described above generally repeats, *i.e.*, the conductance changes again, in some cases over a period of several days until another equilibrium value is reached.

Experiments with specific systems are described below.

KCl-NaCl

The addition of either KCl or NaCl to a cell which has only been heated to bring it to the temperature of the experiment (800°-900°C) leads to a fairly rapid decrease of conductance for several hours. Since the effect occurs even with NaCl it cannot be attributed to the diffusion of Na^+ ions out of the glass, (as it can for KCl) but is probably due to structural rearrangements of the glass, *e.g.*, loss of bound water. It appears likely also that Na^+ ions do not diffuse immediately into such a glass.

If the glass has been heated for several days prior to salt addition only a slow decrease of $1/R$ takes place with KCl, as expected for the diffusion of Na^+ out of the glass.

To study the effect of NaCl addition on the equilibrium conductance value the empty cell was first heated at 650°C for three days. After KCl had been added, $1/R$ decreased slowly for three days at 830°C from 1.04×10^{-5} to 0.245×10^{-5} reciprocal ohms after which $1/R$ remained constant. The temperature was then varied randomly for several hours between 800° and 900°. All points fell on the same linear $1/R$ *vs.* $1/T$ plot. A weighed quantity of NaCl was then added. The conductance became steady in a few hours and the temperature coefficient was again determined. The procedure was repeated several times until the cell was full. Results are shown in Fig. 1. The mole fraction of NaCl (X_{NaCl}) is shown to the right of each curve. The conductance increases with increasing X_{NaCl} and the temperature coefficient decreases. Both effects are linear in X_{NaCl} as shown in Fig. 2, where the Arrhenius activation energy has been calculated from the conductances at 814° and 890°C.

If KCl is added to glass originally equilibrated with NaCl the effect is much smaller and in the opposite direction, *i.e.*, the conductance decreases slightly. For example, with NaCl alone $1/R = 10.1 \times 10^{-5}$ reciprocal ohms, with $X_{KCl} = 0.34$, $1/R = 6.4 \times 10^{-5}$ reciprocal ohms. The Arrhenius activation energy E_a remains virtually constant at 77.4 kJ (18.5 kcal). These results indicate that potassium ions replace sodium ions only slightly in the glass, but that because of their larger size they block some of the available conductance paths in the glass structure. The much higher activation energy observed for KCl alone and its decrease with added NaCl are consistent with this view and with recent observations of membrane potential measurements on this system (7).

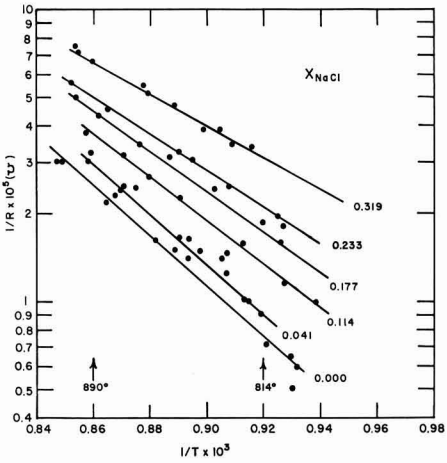

Fig. 1. Equilibrium conductance values of Vycor in various KCl-NaCl mixtures as a function of $1/T$.

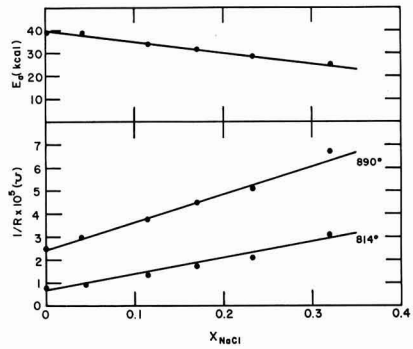

Fig. 2. Change in conductance and activation energy on the addition of NaCl to KCl, data of Fig. 1.

Similar, but less extensive, experiments were also carried out with fused silica (Vitreosil). The results were the same qualitatively, but much longer periods of time were required before constant conductance values were reached, possibly because this glass has less open pores than does Vycor.

KCl-LiCl

When LiCl is added to glass equilibrated with KCl, as described above, the conductance increases linearly with time, showing that lithium ions are diffusing into the glass. Figure 3 shows a typical plot for $X_{LiCl} = 0.055$. Even at this very low concentration lithium ions

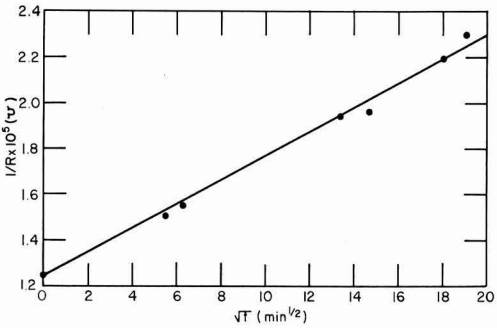

Fig. 3. Change in conductance of Vycor equilibrated with KCl on the addition of 5.5 mole % LiCl, 830°C.

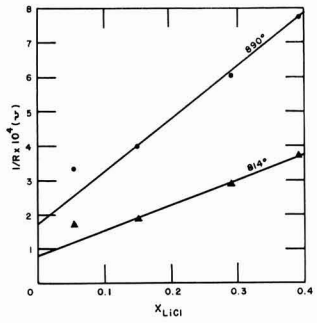

Fig. 4. Change in conductance of Vycor on the addition of LiCl to KCl.

are either displacing the slower potassium ions already in the glass or moving through unoccupied channels in the glass.

As with NaCl, new equilibrium conductance values are reached with successive additions of LiCl. Similarly, the conductance is linear in X_{LiCl} (Fig. 4). The activation energy remains constant as LiCl is added.

KCl-CuCl, KCl-AgCl

The addition of CuCl and AgCl to KCl produces no significant change in glass conductance up to 10 mole % added salt, the highest concentration used. This result does not imply that cuprous and silver ions do not diffuse into glass. That they in fact do so from their own pure molten salts is well known (6). However, when the glass has already been equilibrated with a salt whose ions penetrate the glass preferentially, diffusion of Cu^+ and Ag^+ is greatly reduced. For example, glass membrane potential experiments in the AgCl-NaCl (13) and CuCl-NaCl (14) systems indicate that nearly all of the cationic current is carried through the glass by sodium ions.

NaCl-LiCl

When the glass is initially equilibrated with NaCl instead of KCl the conductance is approximately ten times as great. This large increase indicates that both concentration and mobility of sodium ions in the glass are greater than those of potassium ions since the ionic mobilities probably do not differ by that much. The same conclusion was reached previously from experiments with NaCl additions to KCl.

When even small amounts of LiCl are added to NaCl the conductance rises still further. In contrast to the KCl-LiCl system, however, the increase in conductance occurs so rapidly, within a few minutes, that it cannot be followed accurately. A comparison of the two systems implies that the prior equilibration with NaCl has had a different effect on the glass structure than that with KCl (*cf.* Fig. 3), making it more permeable to Li^+ ions. Successive additions of LiCl cause corresponding increases in the conductance, the equilibrium values being linear functions of X_{LiCl}. Both this dependence and that on temperature are shown in Fig. 5 and 6. It thus appears that sodium ions do not occupy all of the possible conductance paths in the glass, possibly because some of them are too small for Na^+, although they can accommodate Li^+.

The effect of high NaCl concentration on glass can also be seen by comparing the increase in conductance produced by a given amount of salt. The addition of 10 mole % of NaCl and LiCl added to KCl increases the conductance by 8×10^{-7} and 12×10^{-7} reciprocal ohms, respectively; the addition of 10 mole % LiCl added to NaCl gives a change of 475×10^{-6}. This conductance increase is, however, almost entirely due to the very much larger initial conductance with NaCl as compared to KCl. Thus, the conductance increases by 22% when 10% LiCl is added to NaCl and by 15%

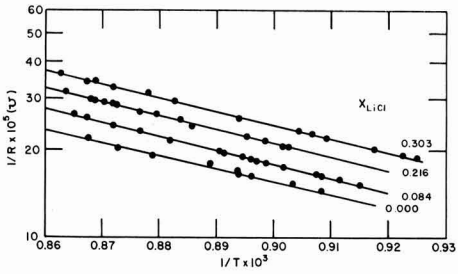

Fig. 5. Equilibrium conductance values of Vycor in various NaCl-LiCl mixtures as a function of $1/T$.

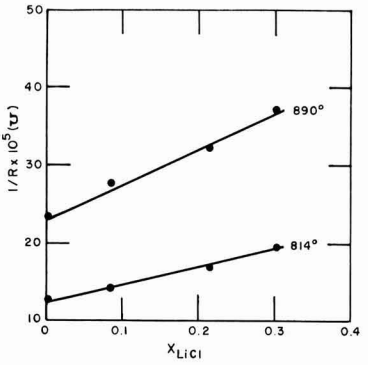

Fig. 6. Change in conductance of Vycor on addition of LiCl to NaCl

when it is added to KCl. These data suggest that the interaction of Na^+ ions with glass differs from that of the other alkali metal cations, but it is not known how.

The activation energy remains virtually constant at 75-84 kJ (18-20 kcal), as LiCl is added to NaCl, but this is not surprising since most of the current is still being carried by sodium.

KBr-KCl-NaBr

To see if a change in anion had any effect on the conductance a cell was initially filled with KBr. The conductance was low, as with KCl, and similarly decreased with time. Over a three-day period $1/R$ decreased from 4.9 to 3.1×10^{-6} reciprocal ohms while E_a increased from 26 to 29 kcal. The addition of KCl up to 20 mole % produced no significant change, the

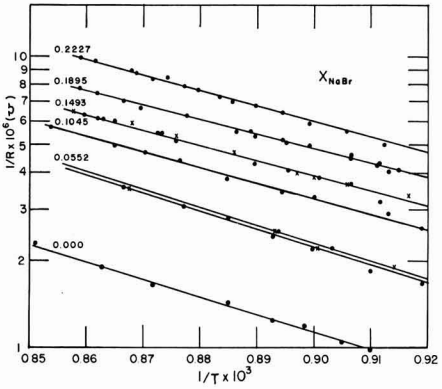

Fig. 7. Equilibrium conductance values of Vycor in NaBr-(76 mole % KBr-24 mole % KCl) as a function of $1/T$.

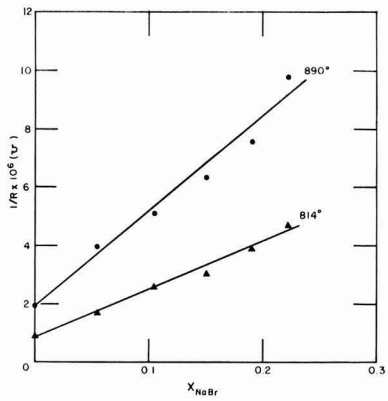

Fig. 8. Change of conductance of Vycor on addition of NaBr to a KBr-KCl melt, data of Fig. 7.

conductance decreasing slowly over a period of weeks. Evidently the effect of adding the smaller Cl^- ion is insignificant compared to the conductance decrease produced by Na^+ diffusion out of the glass.

After two weeks of equilibration with the above KBr-KCl mixture, 24 mole % KCl, NaBr was added. The conductance increased rapidly, the increase being linear in time, as expected. Subsequent additions of NaBr gave the data shown in Fig. 7. The two curves for $X_{NaBr} = 0.0552$ show the change in $1/R$ after one day, the increase with time being clearly much less than that due to a concentration change. As shown in Fig. 8 the increase in conductance is linear in X_{NaBr}, E_a decreasing from 11.2 to 96 kJ (27 to 23 kcal) over the concentration range shown.

Conclusions

The results of the present study are in general agreement with previous work bearing on the behavior of high-purity silica glass in molten salts.

1. The diffusion of potassium ion into glass is very small even when it is the only cation in the melt. In that case the predominant effect appears to be the diffusion of Na^+ out of the glass.

2. From KCl-NaCl and KCl-LiCl melts sodium and lithium ions, respectively diffuse into the glass. The glass comes to equilibrium with a given melt composition fairly rapidly, showing that a uniform ionic composition in the bulk of a $\sim$ 1 mm thick glass is established in a few hours.

3. When LiCl is added to NaCl in equilibrium with glass, Li^+ diffuses rapidly into the glass, showing that not all interstices are filled with Na^+, perhaps because some of them will only accommodate the smaller Li^+.

4. Although Cu^+ and Ag^+ are known to diffuse into glass from their own salts and probably also, although to a much lesser extent, from mixtures with alkali halides, the conductance method is not sufficiently sensitive to detect such diffusion.

5. The present work allows no definite conclusion to be drawn about anion diffusion into glass. Addition of Cl^- to Br^- produces no detectable change in conductivity. However, if the glass is to preserve its electrical neutrality as cations diffuse into it, anions must follow. It is conceivable, however, that partial charge separation in the glass occurs, with anions occupying only the surface layer (adsorption).

6. In general, the activation energy increases with decrease in permeability to a given ion, similar to the behavior with gases (15). The lowest values of E_a, 75 kJ (18 kcal), was observed for NaCl. With KCl E_a fluctuated considerably, probably depending on the residual sodium content of the glass. The highest value obtained was 163 kJ (39 kcal), but an occasional E_a as low as 105 kJ (25 kcal) was obtained with the salt. The addition of NaCl to KCl always lowered E_a.

Manuscript received Sept. 4, 1964. This paper was presented at the Toronto Meeting, May 3-7, 1964.

Any discussion of this paper will appear in a Discussion Section to be published in the December 1965 JOURNAL.

REFERENCES

1. G. W. Morey, "The Properties of Glass," Chap. XVII, Reinhold Publishing Co., New York (1938).
2. J. E. Stanworth, "Physical Properties of Glass," Chap. VI, Clarendon Press, Oxford (1950).
3. J. Halberstedt, *Z. anorg. u allgem. Chem.*, **211**, 185 (1933).
4. B. Lengyel, *Z. phys. Chem.*, **164**, 295 (1933).
5. B. Lengyel and A. Sammt, *ibid.*, **181**, 55 (1937).
6. J. A. Pask and C. W. Parmelee, *J. Am. Ceram. Soc.*, **26**, 265 (1943).
7. K. H. Stern and J. A. Stiff, *This Journal*, **111**, 893 (1964).
8. Ref. (2), Chap. VII.
9. A. J. Moulson and J. P. Roberts, *Trans. Faraday Soc.*, **57**, 1208 (1961).
10. T. Drury, G. J. Roberts, and J. P. Roberts, *Adv. Glass Techn.*, 249 (1962).
11. A. Berlin, Private communication.
12. "Inorganic Syntheses," Vol. II, p. 1, McGraw-Hill Book Co., New York (1946).
13. K. H. Stern, *J. Phys. Chem.*, **67**, 893 (1963).
14. K. H. Stern and S. E. Meador, To be published.
15. cf. Ref. (2), Chap. V.

June 1965 Discussion Section

A Discussion Section, covering papers published in the July-December 1964 JOURNALS, is scheduled for publication in the June 1965 issue. Any discussion which did not reach the Editor in time for the December 1964 Discussion Section will be included in the June 1965 issue.

Those who plan to contribute remarks for this Discussion Section should submit their comments or questions in triplicate to the Managing Editor of the JOURNAL, 30 East 42 St., New York, N. Y., 10017, *not later than March 1, 1965*. All discussion will be forwarded to the author(s) for reply before being printed in the JOURNAL.

Investigations of the Kinetics of Hydrogen and Oxygen Reactions on a Platinum Electrode in Acid Solution Using Pulse and Decay Techniques

Sigmund Schuldiner and Theodore B. Warner[1]

U. S. Naval Research Laboratory, Washington, D. C.

ABSTRACT

The influence of hydrogen partial pressure, current density, and temperature on the anodic oxidation of sorbed H and the anodic generation of sorbed O were determined. Electrode processes were evaluated and separated to give the following quantities: (*a*) the amount of H associated with a Pt surface and its immediate vicinity, (*b*) the extent of reaction of H atoms, absorbed in the metal interior, that migrate to the surface of the metal and are either ionized or react with O atoms, (*c*) the extent of reaction of H_2 from the solution phase, (*d*) the amount of O adsorbed on the Pt surface, and (*e*) the amount of O absorbed in the Pt surface layers (skin).

The kinetics of the open-circuit reaction of galvanostatically determined amounts of sorbed O with H_2 were determined. This investigation showed that absorbed O in Pt significantly affects coulometric measurements at pulse lengths longer than about 1000 μsec. The presence of absorbed O in the Pt can also materially affect the reaction rate of chemisorbed O with H_2. Under the experimental conditions, transport of reactants on the solution side was fast enough so that diffusion did not limit processes in either the H ionization or O sorption regions. The data indicated that migration of adsorbed species on the Pt surface to active sites was rate controlling in the O sorption region, except in the case of reaction of adsorbed O with H_2 when significant amounts of O were absorbed in the skin of the Pt. In this case the chemical reaction rate between adsorbed O and H_2 was retarded so that this chemical step appeared to be rate determining. Reaction rates of the adsorbed O and H_2 reaction under open-circuit conditions were determined at varying temperatures, adsorbed and absorbed O concentrations, and H_2 partial pressures.

This investigation was carried out to determine the influence of hydrogen partial pressure, current density, and temperature on (*a*) the anodic oxidation of adsorbed hydrogen

$$Pt-H \rightarrow H^+ + Pt + e^- \qquad [1]$$

where Pt— indicates a chemisorbed species, and (*b*) the anodic generation of atomic oxygen

$$H_2O + Pt \rightarrow Pt-O + 2H^+ + 2e^- \qquad [2]$$

on a platinum electrode. By use of relatively fast (*i.e.*, high current density) constant current anodic pulses, only that hydrogen already sorbed on the Pt electrode is ionized, and a given number of O atoms are generated and adsorbed on the electrode surface without a significant number of these O atoms absorbing into the outermost layers (skin) of Pt (1—3), or combining to O_2 and diffusing away into solution. By use of longer charging times (*i.e.*, low current densities), some H_2 in solution is ionized in addition to the originally sorbed hydrogen, and a large part of the deposited O atoms may be absorbed into the surface layers of Pt during the time of the applied pulse and more than a monolayer is deposited. Previous work at this Laboratory (1, 3), as well as the work of others, has indicated that O atoms formed during anodic polarization in the O sorption region primarily will either be chemisorbed on the Pt electrode surface or be absorbed in the surface layers of the Pt electrode. In addition, if H atoms are dissolved in the Pt bulk, they may migrate to the surface and either be ionized or react with O atoms.

It has been shown (1, 4) that the rate of reaction of molecular hydrogen in solution with chemisorbed O atoms at potentials above 0.9v (*vs.* NHE) is relatively slow, hence low-current-density-charging pulses were used to determine the combined amount of adsorbed and absorbed O and the reaction of adsorbed O with H_2. The amount of reaction involving H_2 can be determined by comparing such curves with charging curves obtained in hydrogen-free solution. The amount of H_i which migrates to the surface where it is oxidized can be determined in H_2-free solutions by subtracting the number of coulombs required to charge a Pt electrode, free of H_i, to the O_2 evolution potential from the number of coulombs required to charge the same Pt electrodes containing H_i over the same potential range. Thus, the amount of fast-reacting sorbed hydrogen, H_s, the additional hydrogen reacting from solution, H_2, and from the metal interior, H_i, the amount of O atoms adsorbed on the Pt surface, O_{ad}, the amount of O atoms absorbed into the skin of the Pt, O_{ab}, and the amount of reaction of H_2 with adsorbed O atoms can all be determined using the operational definitions of these quantities.

Experiments were conducted to determine the kinetics of the reaction of O_{ad} with H_2 under open-circuit conditions. Here the electrode was coulometrically charged (see Fig. 1b) with a known amount of O_{ad} or O_{ad} plus O_{ab} and the pulse terminated. The potential decay with time was then photographically recorded from an oscilloscope trace (see Fig. 1b) from which the time for reaction of O_{ad} with H_2 in solution plus H_i which migrates to the surface could be measured.

Breiter (5) also used a kinetic technique involving the reduction of chemisorbed oxygen with H_2. However, the method used in this paper varies in several important respects from that of Breiter. In our work we can distinguish between O chemisorbed on the electrode surface and that absorbed into the skin of the metal. Breiter's potentiostatic method (5) undoubtedly included both O_{ad} and O_{ab}. In this paper we shall show that the presence of O_{ab} can materially affect the rate of the reduction of O_{ad} with H_2. Breiter (5) determined the amount of sorbed O at a given anodic potential by using a cathodic sweep which did

[1] National Academy of Sciences Postdoctoral Resident Research Associate.

not clearly separate the oxygen region from the double layer region. In our work we form a given amount of O with an anodic charging pulse where we can separate the amount of O_{ad} present from the amount of O_{ab} dissolved in the Pt electrode. We can also correct for the double layer charge (1). The significance of Breiter's determination of reaction rates at given decay potentials is difficult to assess since his electrode probably contained both O_{ad} and O_{ab}. His reaction rates for different polarization potentials decreased with increased polarization potential, and since potentiostatic charging for 60 sec is adequate time for considerable absorption of O, his decrease in reaction rate can be explained by increased amounts of O_{ab} at higher polarizing potentials.

Our method does suffer in that it does not determine reaction rate as a function of decay potential, but yields the integrated reaction rate over the entire decay potential range. We can, however, limit the potential to which the electrode is anodically charged and thereby successively decrease the amount of O formed. This permits us to show the effects of reduced surface coverage of O on its reaction rate with H_2.

Experimental

The electrochemical system, gas purification trains, and general procedures have been described elsewhere (1-3). True areas (about 0.3 cm^2) of the working Pt bead electrode were defined using the method previously reported (1, 6), and cleanliness of the working electrode and solution was verified by the configuration of the anodic charging curve in the O sorption region (6). The electrolyte was 1M H_2SO_4 solution and was maintained at a constant temperature (±0.5°C) with a water bath. Water bubblers used to saturate the helium or hydrogen going into the cell were kept in the same constant temperature bath to maintain the same partial pressure of water vapor and thereby to keep the electrolyte concentration in the cell constant.

After pre-electrolysis of the solution, the temperature of the water bath was set at a given value and an appropriate mixture of hydrogen and helium (or one of these pure gases) was bubbled through the cell at given rates (0-1300 ml/min) as determined with one or two flowmeters. Zero stirring rate measurements were taken shortly after stopping the flow of a given gas or gas mixture into the cell. The electrometer, pulse generator, and oscilloscope used were the same as previously reported (3), as were the reference (Pt wire and miniature glass) and counter (Pd tube) electrodes. In order to polarize the Pt bead electrode up to the O_2 region with low current density pulses (< 5 ma/cm^2), long duration pulses (> 0.5 sec) were required. These pulses were generated with an Electronic Measurements Solid State (Model C612) Constant Current power supply, using a telegraph key to switch the current on and off. The resulting charging curves were photographed from the oscilloscope screen.

Single-shot, constant-current pulses were used to determine the anodic charging curves. After a current pulse, the electrode was permitted to recover to its normal open-circuit potential before the next pulse was applied. Pulse current densities, known to ±3%, were varied from 780 $\mu a/cm^2$ to about 3 amp/cm^2. The $\mu coul/cm^2$ of hydrogen ionized and oxygen formed were corrected for double layer charging by using a previously determined relationship between double layer capacitance and potential (1).

After anodic charging curves were taken under a variety of conditions, a series of photographs were made showing the polarization decay in H_2-saturated solution (varying H_2 partial pressures and temperatures) at the Pt bead electrode, which was previously charged with a known number of coulombs to a given potential in the O sorption region or somewhat beyond in the O_2 formation region. (Figure 1a delineates the various regions for the charging and decay traces.) In these experiments a charging pulse was set for a given duration and an oscillogram taken (see top charge curve in Fig. 1b). The oscilloscope sweep rate was then considerably slowed and the voltage amplification increased so that the pulse itself was largely off the screen and lasted only a very small fraction of the total time displayed. Then the decay curve (see decay curves in Fig. 1b) following pulse cut off ran for the length of the horizontal sweep until the potential and shape of the decay curve showed complete removal of sorbed oxygen. Thus, with this technique a known number of O atoms could be formed on the surface and the time required for their subsequent open-circuit reaction with molecular hydrogen in solution determined.

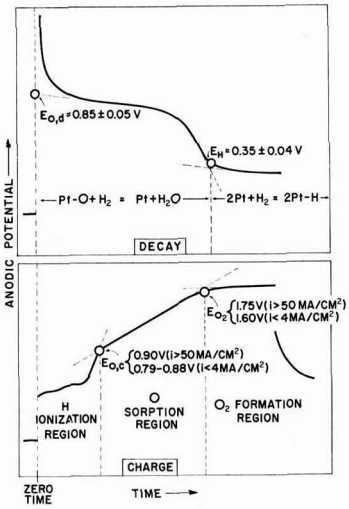

Fig. 1a. Oscilloscope traces: delineation and definition of the major reaction regions and potentials in charge and decay traces.

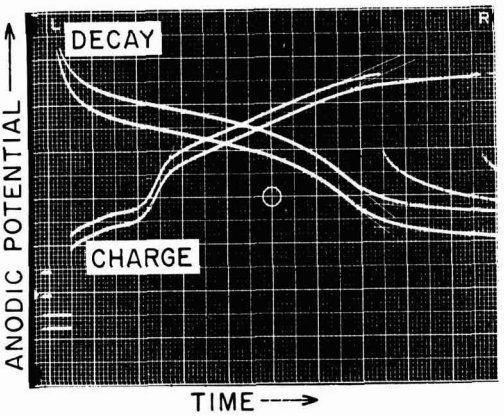

Fig. 1b. Typical anodic charging curves (50 μsec per horizontal division, 0.5v per vertical division, i = 2.61 A/cm^2) and decay curves (2000 μsec per horizontal division, 0.2v per vertical division) at 50°C and p_{H2} = 0.88 atm.

Anodic Charging Reactions

From the photographed anodic charging traces (Fig. 1b), the number of $\mu coul/cm^2$ of both ionized H and O formed on the Pt bead electrode was determined. These values were corrected for double layer charge. For high-current-density anodic pulses (1-3 amp/cm^2) only O_{ad} is formed and the number of coulombs

used to charge the O sorption region at room temperature was used to define the surface area (1) of the Pt bead. Under these conditions the O sorption region was assumed to require 420 μcoul/cm^2 to charge (equivalent to one monolayer, one-to-one correspondence with surface Pt atoms); the H ionization region was found to require 230 μcoul/cm^2 to charge. The 230 μcoul/cm^2 of H oxidized represents the amount of H (H_s) associated with the Pt surface under open-circuit conditions (p_{H_2} = 1 atm). Experimental evidence (1, 7) indicates that part of this hydrogen is chemisorbed on the Pt surface as atoms and part is absorbed primarily in the outermost layers of the Pt. The experimental data at 23°C showed that within experimental error, this quantity of H, for the higher current density pulses, was virtually independent of the hydrogen partial pressure in the cell (0.02 to 1 atm). This indicated that the amount of chemisorbed hydrogen in rapid equilibrium with H_2 gas above the solution is very small at room temperature and verified previous work from this Laboratory (1, 8).

At lower current densities the amounts of charge consumed in both the H and the O regions exceeded 230 and 420 μcoul/cm^2, respectively. These excesses of charge, q_{ex}, represented: (*a*) the amount of hydrogen in the H ionization region, $q_{H,ex}$, oxidized beyond the amount of hydrogen, H_s, originally associated with the surface before imposition of the anodic pulse, and (*b*) the excess charge in the O sorption region, $q_{O,ex}$, which was due primarily to the oxygen, O_{ab}, formed beyond that needed to form a single monolayer of O atoms, O_{ad}, plus any H_2 and H_i oxidized.

Figure 2 shows both the current density and the hydrogen partial pressure effects on $q_{H,ex}$ and $q_{O,ex}$. The $q_{H,ex}$ can come from two sources, the molecular hydrogen, H_2, bubbled into the cell and the hydrogen dissolved in the interior, H_i, of the Pt bead diffusing out to the surface. Estimations of the amount of H_i which diffused to the surface and then was oxidized were made in pure helium-saturated solutions (the electrode was first saturated with H_2, p_{H_2} = 1 atm, then the H_2 was replaced with He and charging curves were obtained). These experiments showed that with current density pulses of higher than 0.203 amp/cm^2, virtually no hydrogen diffused from the interior of the Pt bead to the surface during the charging pulse. At lower current densities, some hydrogen coming from this source was detected and the p_{H_2} = 0 points in Fig. 2a roughly indicate their values. Interestingly, the amount of H_i (about 300 μcoul/cm^2) diffusing to the surface at current densities of 3.53 ma/cm^2 and lower was essentially independent of current density.

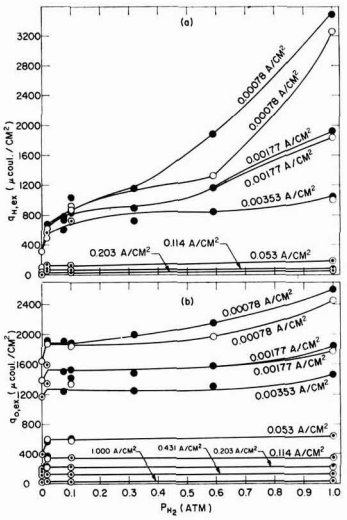

Fig. 2. Data from anodic charging curves at 23°C. Effects of current density, stirring, and hydrogen partial pressure on excess of charge in (a) the H ionization region, $q_{H,ex}$, and (b) the O sorption region, $q_{O,ex}$; ○, quiescent solution; ●, vigorously stirred solution.

The $q_{O,ex}$ appears to represent primarily the amount of O_{ab} in the skin of the Pt bead plus the possible reaction of H_2 and the H_i which diffused to the surface during anodic charging. Lack of stirring effects at current densities above 0.053 amp/cm^2 made it unlikely that a significant amount of oxygen was lost from the surface in the form of O_2 in the O sorption region. Reaction of O_{ad} with H_2 at potentials in the O sorption region has been shown to be slow (1, 4); however, the data in Fig. 2b show that at current densities of 3.5 ma/cm^2 and lower, a significant amount of reaction of O_{ad} with H_2 must occur. Here both stirring and increased hydrogen partial pressure cause an increase in the amount of charge consumed in the O sorption region. However, as the hydrogen partial pressure is decreased, eventually the number of coulombs of charge transferred does not vary even with stirring. But even at these low hydrogen partial pressures there evidently is some reaction of O_{ad} with H_2, because when the hydrogen partial pressure is reduced to zero, the amount of charge expended decreases. In fact, even at current densities as high as 0.203 amp/cm^2 there appears to be a significant amount of reaction of O with H_2. The fact that there are conditions under which hydrogen partial pressure and/or increased stirring does not affect the apparent amount of hydrogen reaction with O_{ad} means that under these conditions the transport of H_2 to the electrode surface by convection and diffusion is faster than the reaction of H_2 with O_{ad}.

At the lowest current density pulse applied (0.78 ma/cm^2), increased stirring rates above those used in the Fig. 2a data considerably lengthened the hydrogen ionization region on the oscilloscope trace. With a small decrease in current it was impossible to polarize the electrode beyond the hydrogen region. This showed that the exchange current density, i_o, for the hydrogen reaction is close to 0.78 ma/cm^2 and that extremely fast stirring is necessary to minimize diffusion polarization. This value checks previous steady-state measurements (9) from this Laboratory when the previous values are adjusted to correspond to the definition of true surface area used here. On the other hand, the length of the O_{ad} region was virtually independent of further increases in the hydrogen stirring rate, beyond the corresponding values shown in Fig. 2b, at 0.78 ma/cm^2. This demonstrated that i_o, for the reaction of H_2 with O_{ad}, is considerably less than 0.78 ma/cm^2, and it also follows that diffusion polarization of H_2 in the vigorously stirred solution was insignificant.

The data shown in Fig. 2b for the helium-stirred solution (p_{H_2} = 0, Pt electrode containing H_i) primarily gives the sum of H_i atoms which diffuse to the surface and are ionized and of O_{ab} generated during the anodic pulse. At the lowest current density this amounts to the equivalent of about four atomic layers of O.

Experiments conducted in helium-saturated solution in which H_i in the Pt bead was completely removed (potential *vs.* NHE was 0.47-0.59v) showed that the amount of O_{ab} in the skin of the metal was 910, 1020, and 1260 μcoul/cm^2 at current densities of 3.53, 1.77, and 0.78 ma/cm^2, respectively. The p_{H_2} = 0 values shown in Fig. 2b, for the same series of current densities, include oxidized H_i and O_{ab} and are 1170, 1400, and 1630 μcoul/cm^2, respectively. The amount of H_i which diffuses to the surface and is oxidized appears to level off at about 400 μcoul/cm^2 at the two lowest current densities, but at all these low current densities the H_i contribution is significant.

The $p_{H_2} = 0$ values shown in Fig. 2b therefore account for both oxidized H_i and O_{ab} and the difference between $q_{O,ex}$ values at $p_{H_2} > 0$ and $p_{H_2} = 0$ represents the amount of H_2 from solution which is ionized. The high $q_{O,ex}$ values for the low current density data indicate that the top layers of Pt atoms in the metal skin may be fairly well saturated with oxygen. As will be shown later this can have a marked effect on the catalytic behavior of Pt.

The data in Fig. 2 show large differences in $q_{H,ex}$ and $q_{O,ex}$ for given current density pulses. Using these curves the amount of H_2 ionized in the H ionization region and H_2 reacting in the O sorption region were separated from the total q_{ex} values and compared. This comparison showed that at current densities of 3.53 ma/cm^2 and lower, the number of equivalents of H_2 reacting in the O sorption region is considerably less than the number of equivalents of H_2 being ionized in the hydrogen region, even though the duration of the O sorption region is about twice as long. At current densities of 0.053 amp/cm^2 and higher the reverse occurs; here considerably more H_2 reacts per unit time in the O sorption region than in the H ionization region. These experimental facts show (*a*) that hydrogen diffusion cannot be rate controlling in both the H ionization and O sorption regions, otherwise the number of coulombs of H_2 per unit time reacting in both regions would be identical, (*b*) at low current densities, H_2 is ionized much faster in the H ionization region than H_2 reacts with O_{ad} in the O sorption region, therefore, H_2 diffusion cannot be rate controlling in the O sorption region, and (*c*) at the higher current densities, H_2 reacts with O_{ad} faster in the O sorption region than these molecules are ionized in the H ionization region; here one concludes that H_2 diffusion cannot be rate controlling in the H ionization region.

The exchange current densities of both the charge transfer and molecular dissociation steps of the hydrogen reaction have been shown (1, 8, 9) to be independent of the charging rate. Hence, the differences in the reaction rates of H_2 at the anodized Pt bead at low and high current densities must be in the O sorption region. We believe that the rate of reaction of H_2 with O_{ad} is faster with high current density pulses because less O is absorbed into the skin of the Pt under these conditions. The work which will be reported in the last section of this paper will further verify that the rate of the reaction between H_2 and O_{ad} is strongly dependent on the amount of O_{ab} in the skin of the Pt electrode.

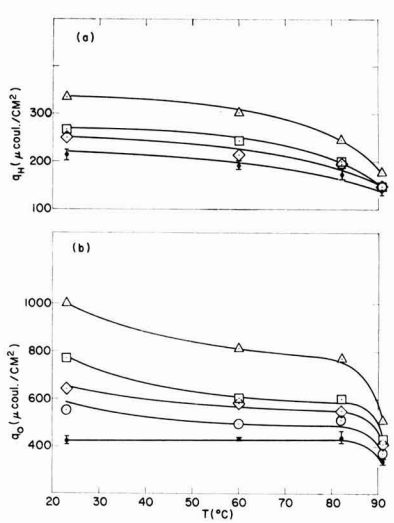

Fig. 3. Temperature effects on anodic charging curves: (a) q_H in hydrogen ionization region [Solid circle with I thru it, 0.43, 1.00, 1.69, 2.52 amp/cm^2; other symbols same as (b)]; (b) q_O in oxygen sorption region; △, 0.053 amp/cm^2; □, 0.114 amp/cm^2; ◇, 0.203 amp/cm^2; ○, 0.43 amp/cm^2; solid circle with I thru it, 1.00, 1.69, 2.52 amp/cm^2.

Temperature effects.—The effects of temperature on both the H ionization and O sorption regions are shown in Fig. 3. Data scatter is indicated for the high current pulses and was approximately the same for the other pulses. The curves in Fig. 3a for the H ionization region indicate that the effect of temperature is essentially the same for all current densities, the lower current density pulses showing additional discharge due to reaction of H_2 that comes from the solution. The fact that there is an inverse temperature effect seems to indicate that the lower H_2 partial pressure at higher temperatures would be an important factor. Nevertheless, the data in Fig. 2a clearly show that at the current densities involved the effect of H_2 partial pressure is essentially negligible at 23°C.

One important factor brought out by these curves (Fig. 3a) is that the amount of H_s decreases as the temperature increases. This can be seen especially for the high current density curve where the ionization of extra H_2 from solution would be unimportant. This decrease in the amount of H_s could be due essentially to the lower H_2 partial pressure at higher temperatures. Thus, even though the 23°C case apparently shows independence of the amount of H_s with p_{H_2}, this may be due to the fact that at this temperature the equilibrium between H_s and H_2 may take a relatively long time to be established. It could also well be that the loss of the bulk of the hydrogen from Pt is not through equilibration with H_2 dissolved in the solution, but is due to reaction with trace amounts of oxygen which leak into the system. Higher temperatures could both increase the amount of the oxygen leak and the rate of reaction of O_2 with H_s.

Because the curves in Fig. 3a are essentially parallel, the effect of temperature on $q_{H,ex}$ can be considered to be constant. Unfortunately, it is not possible with this data to separate H_2 partial pressure effects from temperature effects. Measurements were taken in both quiescent and stirred solution (zero and 1300 ml/min gas flow, respectively). Under both conditions, the numbers of coulombs measured for the data (except at the lowest current densities) shown in Fig. 2a were essentially the same. Where there is no stirring effect, we are led to believe that diffusion of H_2 from the solution was not the controlling factor. Hence, we conclude that the rate-controlling step for the ionization of the molecular hydrogen which comes from solution is the dissociation of H_2 to H.

Temperature effects (Fig. 3) in the O sorption region are quite different from those in the H ionization region. Figure 3b shows that at high current densities, where only surface adsorption of O occurs, q_O is independent of temperature with the exception of the 91°C value. The temperature invariance indicates that a transport or charge transfer step may be rate controlling. Here also diffusion in solution can be ruled out by the lack of stirring effects. The transport here would most likely involve either the migration of a water molecule to a site where it can be oxidized or the migration of an O atom to a suitable site on the electrode surface. The sudden drop in q_O at 91°C is difficult to explain. There are several possibilities: (*a*) the effects of electrode poisons would most likely increase at higher temperatures, and the reproducibility of the data being poorest at this temperature would tend to support this, and (*b*) the bonding of O_{ad} at 91°C may be such that a linear bond with surface Pt atoms no longer predominates and therefore full coverage would be less than 420 μcoul/cm^2. Our cleanliness tests at 91°C and after immediate lowering of temperature did not indicate impurity adsorption; however, we cannot be sure that some self-poisoning process did not occur at this temperature.

The lower current density (0.053-0.43 amp/cm²) data in Fig. 3b show a definite temperature effect of $q_{O,ex}$ throughout the entire temperature range. The curves are roughly parallel, and here again diffusion control in solution is unlikely due to the absence of stirring effects. The fact that there is an inverse temperature effect may be due to a decrease in the solubility of O in the metal skin as the temperature increases and thereby the rate of absorption which gives $q_{O,ex}$ decreases. Decreased hydrogen partial pressure is probably also a factor.

These temperature effects indicate that important changes are taking place, not only on the surface but in the surface layers of the Pt electrode. More work is contemplated on the absorption of O into the skin and the effects of these absorbed atoms on the surface reaction kinetics.

Chemical Reaction of Molecular Hydrogen with Chemisorbed Oxygen Atoms

The unique feature of the technique used to study the reaction of H_2 with O_{ad} is that electrochemical measurements were used not only to determine the kinetics of a chemical reaction occurring on a metal surface under open-circuit conditions, but the effects of the various sorbed species could be isolated. Accurate control of the amount of O_{ad} was possible by coulometric means. Also, the effects of O_{ab} on the rate of the surface reaction between O_{ad} and H_2 could be determined.

The data in Fig. 4 give the reaction rate

$$i_r = \frac{\text{number of } \mu\text{coul/cm}^2 \text{ of O generated during the anodic phase}}{\mu\text{sec required to reduce O with } H_2 \text{ which migrates to the surface}}$$

where i_r is expressed in amp/cm². The chemical reaction involved is

$$Pt - O + H_2 \rightarrow H_2O + Pt \qquad [4]$$

With the high current densities (1.66-3.36 amp/cm²) used to collect the data shown in Fig. 4, absorption of O during anodic charging was found to be negligible. The data for $q_O > 420$ μcoul/cm², $E_{O_2} \approx 1.8$v, also indicate that an excess of adsorbed O can be formed in the O_2 formation region. These excess O atoms are evidently not lost by diffusion into solution as O_2 in the fast pulse times used. This may indicate that initially at E_{O_2} at least as much as about another monolayer of O atoms can be held on the electrode surface. These extra O atoms may easily go into the interstitial holes in the Pt lattice (especially in the 110 plane). The potential may simply be a function of the coverage of surface atoms with O_{ad}. After these surface atoms are saturated, the holes in the lattice are filled without apparently affecting the potential and, as the data in Fig. 4 show, the reaction rate, i_r, of Eq. [4] is independent of the surface coverage from one monolayer up to about two monolayers. It is also possible that the extra oxygen is in the molecular form and is held in position firmly enough so that losses are negligible during both the formation of oxygen and reaction with H_2. A third possibility is that PtO_2 is formed at E_{O_2} before the generation of O_2. Molecular hydrogen then reacts with both PtO_2 and Pt-O at essentially the same rate.

Blank runs were made at 23°C to estimate the effects due to a terminating resistance used to maintain pulse shape. The electrode was first exposed to 1 atm H_2 saturated solution and then the H_2 was replaced with pure He. After sweeping out the solution with He for about 20 minutes, the potential became more anodic by about 60 mv. Decay traces in this solution (p_{H_2} calculated <0.01 atm) gave i_r values equal to a little over one-half of the i_r values found in the H_2 swept solutions. This means that i_r values shown in Figs. 4 and 5 should be reduced by about ½ to give true i_r values for the reaction of O_{ad} with H_2. Check runs were made also with the terminating resistance removed from the pulse output. These runs gave essentially a zero blank showing that the contribution of H_i to i_r was negligible, and the results checked those found using the terminating resistance corrected for its blank.

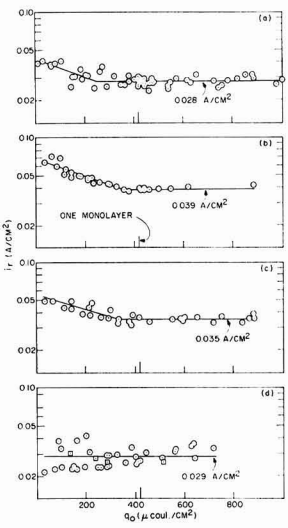

Fig. 4. Rates of reaction, i_r, of O_{ad} with H_2 obtained from decay curves following high current density anodic pulses terminated at various points in the O sorption or O_2 formation regions (no O_{ab} generated). (a) 23°C, 1.0-0.1 atm H_2; (b) 50°C, 0.88 atm H_2; (c) 70°C, 0.69 atm H_2; (d) 90°C, ⊙, 0.31 atm H_2; □, 0.09 atm H_2.

The values of i_r in the plateau regions of Fig. 4 can be considered to be essentially independent of both temperature and hydrogen partial pressure. (The data in Fig. 4a showed a random scatter of points at 0.1, 0.5, and 1 atm H_2 partial pressures.) The values shown in Fig. 4 were taken also at stirring rates beyond which i_r did not increase with increasing stirring. The lack of stirring rate and H_2 partial pressure effects eliminates the diffusion of H_2 from solution as the rate-controlling mechanism. The lack of H_2 partial pressure and temperature effects also eliminates the direct chemical reaction of H_2 with O_{ad} as a possible rate-determining step. A third possible controlling step is one which involves a dissociation of H_2 into atoms and its migration across the surface to active sites bearing O atoms where the reaction in Eq. [4] can occur. It is also possible that the rate-controlling step may be the migration of O_{ad} to the active sites where it can react with either atomic or molecular hydrogen.

The fact that i_r at $p_{H_2} = 1$ atm after subtracting the i_r at $p_{H_2} < 0.01$ atm gives values somewhat higher than 0.01 amp/cm², which is about one order of magnitude higher than i_o for the molecular hydrogen ionization reaction (0.00078 amp/cm² or 0.0015 amp/cm² on an apparent area basis), demonstrates that (*a*) diffusion of H_2 cannot be rate-controlling in the H ionization region because the reaction with H_2 shown in Eq. [4] occurs faster under equal stirring rates, and (*b*) that H_2 does not dissociate into atoms before reacting with O_{ad}, because here again the reaction of

O_{ad} with H_2 is faster than the ionization of H_2 which requires dissociation into atoms. Taking all of these facts into consideration, the most likely rate-controlling step for the reaction between H_2 and O_{ad} is the migration of O_{ad} atoms to active sites where they can directly react with H_2. Hence a reasonable rate-determining step can be postulated, even though the detailed reaction steps which comprise the over-all mechanism are not known.

At lower surface coverages, θ ($\theta < 1$), the data in Fig. 4 show that i_r increased as the surface coverage decreased. This suggested, since the most active sites would be covered with O_{ad} first, that the decrease in the number of inactive sites covered with O_{ad} reduced the amount of necessary migration to active sites and thereby i_r tended to increase. This argument also supports the O_{ad} migration step as the rate-controlling one.

When charging pulses from 0.053 to 1.0 amp/cm^2 were used to form the O sorption region, the rate of charging was slow enough so that some of the O atoms formed absorbed into the skin of the Pt bead and, possibly, some H_i atoms migrated to the surface (as shown in the previous section). Under these conditions, at the end of the charging pulse part of the O atoms formed were adsorbed on the Pt surface and part absorbed in the skin of the electrode. Loss due to reaction with H_i and with H_2 from solution during charging was significant mainly at current densities below 0.2 amp/cm^2, even at the lower current densities used only a fraction of the O_{ad} reacted with H_i or H_2 (see Fig. 2b).

The data in Fig. 5 were obtained with pulses which were terminated just at the end of the O sorption region (see, for instance, upper charge curve in Fig. 1b), but which were of such low current density that additional amounts of oxygen could dissolve in the Pt. This is in contrast to the data in Fig. 4, which were obtained with high current density pulses. Some of these latter pulses were long enough to charge well into the O_2 formation region, some were terminated just at the end of the O sorption region, and some were terminated at various points within the O sorption region.

Figure 5 shows that O_{ab} has a marked effect on i_r. The reaction current density, i_r, of Eq. [4] is sharply diminished as the amount of O_{ab} increases (correction of i_r for any reduction of O_{ad} due to migration of residual H_i to the surface during charging would tend to decrease i_r further). Figure 5a shows that i_r is a direct function of p_{H_2}. Figure 5b shows that although increased temperature tends to increase i_r (see i_r values in Fig. 5a at comparable partial pressures), the lowering of H_2 partial pressure with increasing temperature (owing to increased partial pressure of water vapor) exerts a stronger effect than temperature.

The data in Fig. 5 were also taken under vigorous stirring conditions where increased stirring rates did not change i_r; therefore diffusion control of H_2 was minimized. The results shown in Fig. 5 indicate that the reaction mechanism for Eq. [4] must be quite different than for the case where O_{ab} is insignificant. The dependence on H_2 partial pressure indicates that the reaction is controlled by the chemical reaction of H_2 with O_{ad}. The tendency of a positive temperature dependence also indicates such a reaction control. The increase in i_r as $q_{O,ex}$ decreases shows that the reaction rate increases as the amount of sorbed O decreases, and the change to the higher slope at low $q_{O,ex}$ values indicates that the reaction step is becoming so fast that the over-all rate i_r, approaches the comparable values shown in Fig. 4 where O_{ad} migration is the indicated rate-controlling step. Hence, in the region of the steeper slope (Fig. 5) there appears to be a mixed control of the reaction. This is also verified by the coming together of the curves in Fig. 5 at the lowest $q_{O,ex}$ values. This indicates that H_2 partial pressure and temperature effects become less important as in the data shown in Fig. 4.

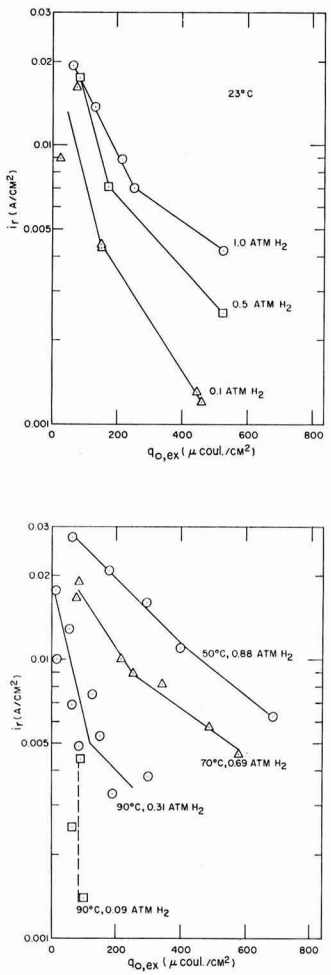

Fig. 5. Rates of reaction, i_r, of O_{ad} with H_2 obtained from decay curves following low current density anodic pulses terminated at end of O sorption region (O_{ab} present).

It is felt that the presence of O_{ab} in the Pt bead markedly lowers the heat of adsorption of O_{ad}. This in turn evidently slows the rate of the chemical combination of O_{ad} and H_2.

One of the most important results of this investigation is considered to be the application of the described technique for separating differently sorbed species associated with a surface and determining their effects on the rates of chemical reactions.

Conclusions

Use of the techniques described here has led us to conclude:

1. That platinum electrodes in sulfuric acid solution can absorb considerable quantities of oxygen and hydrogen in excess of the quantity present on the surface. In this work the oxygen was generated on the electrode surface electrolytically; the hydrogen was present in the solution.

2. That this absorption is fast. Measurable quantities of absorbed oxygen are found after anodic polarizations of 1000 μsec or longer.

3. That multiple monolayers can be absorbed if sufficient time of contact is allowed.

4. That desorption is slow. An effort is necessary to obtain an electrode free of these dissolved species. Coulometric studies involving oxidation or reduction of substances adsorbed on the surface of a platinum electrode can be seriously affected by the presence of these dissolved species as an unrecognized reactant (10).

5. That catalytic behavior of a platinum electrode is drastically affected by such absorbed species.

These conclusions, in turn, lead to the conclusion that the use of anodic pulses to clean an electrode prior to use may create more problems than it solves, and if used, extreme care must be taken to insure that the above processes do not influence the measurements.

Acknowledgments

The authors gratefully acknowledge the help of Professor P. H. Emmett of Johns Hopkins University, especially his suggestion that the surface migration of adsorbed species to active centers may be applicable for the reaction of O_{ad} with H_2.

Manuscript received June 8, 1964; revised manuscript received Sept. 23, 1964. This paper is to be presented at the San Francisco Meeting, May 9-13, 1965.

Any discussion of this paper will appear in a Discussion Section to be published in the December 1965 JOURNAL.

SYMBOLS

(Figure 1a delineates and defines the major reaction regions and potentials in the charge and decay traces. Wherever a quantity of material was determined coulometrically, double layer capacitance charging was corrected for.)

H_s hydrogen atoms associated with Pt atoms on the surface and immediately below the surface. Operationally, H_s is the time-independent amount of H atoms coulometrically measured with an anodic pulse that polarizes the electrode through the H ionization region in less than 1000 μsec. At a Pt electrode under 1 atm H_2 at 25°C, H_s = 230 μcoul/cm^2.

H_i hydrogen atoms located in the interior of a Pt electrode. Operationally, these H atoms do not migrate to the surface and react under the conditions referred to under H_s. H_i atoms only add to the measured number of coulombs at polarization times longer than 1000 μsec.

H_2 molecular hydrogen in the solution phase.

i_r number of μcoul/cm^2 of O generated during an anodic pulse divided by the time, in μsec, required to reduce this O with H_2 plus H_i which migrates to the surface.

O_{ad} oxygen atoms chemisorbed on the Pt electrode surface. By the definition of area used, these atoms are in a one-to-one correspondence with surface Pt atoms. Operationally, O_{ad} is the time-independent amount of O atoms coulometrically measured with an anodic pulse that polarizes the electrode through the O sorption region in less than 1000 μsec. At 25°C, O_{ad} = 420 μcoul/cm^2.

O_{ab} oxygen atoms absorbed in the skin of the Pt electrode. Operationally, these atoms only add to the measured number of coulombs at polarization times longer than 1000 μsec.

q_H the number of μcoul/cm^2 of reaction in the H ionization region.

q_O the number of μcoul/cm^2 of reaction in the O sorption region.

$q_{H,ex}$ the number of μcoul/cm^2 of hydrogen oxidized in the H ionization region in excess of the amount of hydrogen atoms (H_s) originally associated with the electrode surface before imposition of the anodic pulse. $q_{H,ex}$ is due to oxidation of H_i and H_2.

$q_{O,ex}$ the number of μcoul/cm^2 of charge expended in the O sorption region in excess of the amount required to generate the O atoms (O_{ad}) chemisorbed on the Pt surface. $q_{O,ex}$ is due to the formation of O_{ab} and of the oxidation of H_i and H_2.

θ fraction of available sites on the surface covered.

REFERENCES

1. S. Schuldiner and R. M. Roe, *This Journal*, **110**, 332 (1963).
2. S. Schuldiner and R. M. Roe, *ibid.*, **110**, 1142 (1963).
3. T. B. Warner and S. Schuldiner, *ibid.*, **111**, 992 (1964).
4. W. Nernst and E. Merriam, *Z. Phys. Chem.*, **53**, 235 (1905); O. Sackur, *ibid.*, **54**, 641 (1906); M. W. Breiter, *Electrochim. Acta*, **7**, 601 (1962).
5. M. W. Breiter, *This Journal*, **109**, 425 (1962).
6. S. Schuldiner and T. B. Warner, *J. Phys. Chem.*, **68**, 1223 (1964).
7. T. C. Franklin and S. L. Cooke, *This Journal*, **107**, 556 (1960).
8. C. H. Presbrey, Jr. and S. Schuldiner, *ibid.*, **108**, 985 (1961).
9. S. Schuldiner, *ibid.*, **106**, 891 (1959).
10. S. Schuldiner and T. B. Warner, *Anal. Chem.*, **36**, 2510 (1964).

Polarography of Lead Complexes in Glycolic Acid and Malonic Acid as Competing Chelating Agents

Tsai-Teh Lai and Ching-Chiang Hsieh

Department of Chemical Engineering, Cheng Kung University, Tainan, Taiwan, China

ABSTRACT

The polarography of lead complexes in glycolic acid, malonic acid, and in a mixture of glycolic acid and malonic acid has been studied in detail. With glycolic acid, $Pb(G)^+$ and $Pb(G)_2$ were identified. With malonic acid, evidence for the existence of $Pb(HA)^+$, $Pb(HA)_2$, and $Pb(A_2)^{-2}$ was obtained. In a mixture of glycolic acid and malonic acid as competing ligands to the lead ion, the complex species of $Pb(G)^+$, $Pb(G)(HA)$, and $[Pb(G)(A)]^-$ were formed. The electrode reactions and concentration dissociation constants of the complexes were given. The coordination ability between the lead ion with the following groups decreased in the order: $-COO^- > -OH > -COOH$.

The polarographic behavior of the complexes of uranium (VI) with glycolic (1) and malonic acid (2) has been investigated. The malonate complexes of iron (3) and chromium (III) (4) have been studied polarographically.

Although the polarography of lead complexes with tartaric acid has ben reported by Iwase (5), it was found that little has been done with other carboxylic or hydroxylic acids. In an attempt to determine what complexes of lead existed in the competing chelating

agents of glycolic acid and malonic acid, and to estimate their concentration dissociation constants, a detailed investigation by polarography was undertaken.

Experimental

Apparatus.—The apparatus and procedure used in this work were described previously (1).

The characteristics of the capillary were 1.10 $mg^{2/3}$ $t^{-1/2}$ at a mercury column height of 61 cm and an applied potential of —0.500v *vs.* SCE.

All polarographic solutions were allowed to stand at least 30 min before measurements were made to assure equilibrium. No maxima were encountered, and no suppressors were added to the solutions.

All experiments were carried out at 30° ± 0.1°C.

Chemicals.—The stock solution of 0.01M lead nitrate was standardized complexometrically with standard EDTA solution (6). A 2M stock solution of malonic acid and 1M stock solution of glycolic acid were prepared, and their exact concentrations were determined with carbonate-free sodium hydroxide solution which was standardized with potassium biphthalate of the National Bureau of Standards.

Results and Discussion

The half-wave potential for the lead complex PbA_x^{2-nx} at the dropping mercury electrode may be represented by

$$(E_{1/2})_c = (E_{1/2})_s + \frac{0.060}{2}\log K_c - \frac{0.060}{2}x \log [A^{-n}] \text{ (at 30°C)} \quad [1]$$

Here K_c is the concentration dissociation constant of the lead complex and $[A^{-n}]$ is the concentration of ligand.

If A^{-n} and B^{-m} represent chelating agents that compete for the electron pair donor groups to the lead ion, the half-wave potential of the resulting complex $PbA_xB_y^{(2-nx-my)}$ is expressible as

$$(E_{1/2})_c = (E_{1/2})_s + \frac{0.060}{2}\log K_c - \frac{0.060}{2}x \log [A^{-n}] - \frac{0.060}{2}y \log [B^{-m}] \quad [2]$$

When the ligand number x of A^{-n} is identical to the ligand number y of B^{-m}, Eq. [2] can be simplified to

$$(E_{1/2})_c = (E_{1/2})_s + \frac{0.060}{2}\log K_c - \frac{0.060}{2}x \log [A^{-n}][B^{-m}] \quad [3]$$

We then obtain

$$\frac{\Delta(E_{1/2})_c}{\Delta \log [A^{-n}][B^{-m}]} = -0.030\,x \quad [4]$$

This equation shows that if the value of the slope of $E_{1/2}$ *vs.* log $[A^{-n}][B^{-m}]$ is an integral multiple of 0.030, the ligand number of A^{-n} and B^{-m} are the same. That is, the ligand A^{-n} and B^{-m} will have identical coordination ability to the lead ion when the solution has the same concentration of A^{-n} and B^{-m}.

Reversible and diffusion controlled reduction.—Figure 1 shows the typical polarograms and the plots of log $i/(i_d - i)$ *vs.* $E_{d.e.}$ for lead ion solutions (curve I), containing glycolic acid (curve II), malonic acid (curve III), and glycolic acid and malonic acid (curve IV). It is obvious from Fig. 1 that the half-wave potential of simple lead ion in 0.1M KNO_3 solution at pH 3.50 is —0.397v *vs.* SCE and the half-wave potentials are all shifted to negative side by chelation with glycolic acid, malonic acid, and a mixture of glycolic acid and malonic acid.

The slopes of the conventional log plots for the polarograms of lead-glycolate, lead-malonate, and lead-glycolate-malonate system at various pH values were rounded up in Table I. The temperature coefficients of

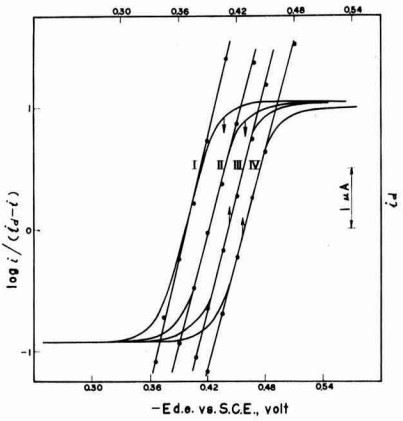

Fig. 1. Typical polarograms and log $i/(i_d-i)$ vs. $E_{d.e.}$ Polarograms of solutions containing 1.116 mM $Pb(NO_3)_2$, 0.1M KNO_3, at pH 3.50 with various chelating agents: (I) no chelating agent; (II) 0.1027M glycolic acid; (III) 0.0976M malonic acid; (IV) 0.1027M glycolic acid and 0.0976M malonic acid.

half-wave potential and diffusion current were also determined with the data listed in Table II. From Tables I and II, it is obvious that the three systems are all 2-electron reversible and diffusion-controlled reduction.

Lead-glycolic acid system.—Curve I in Fig. 2 represents the effect of pH on the half-wave potential of a lead-glycolic acid system. At pH < 2.35, the half-wave potentials are independent of pH and remain constant at $(E_{1/2})_s$ value, indicating that no chelation occurred. In the pH range 2.35-4.15, the slope of $E_{1/2}$ *vs.* pH is —0.028 showing that one hydrogen ion was required in releasing the coordinated glycolate anion from one mole of lead-glycolate complex to form glycolic acid. At pH > 4.15, the half-wave potentials became independent of pH value again, showing that no hydrogen ion was involved in the reduction of the complexes.

To determine the ligand number of the lead-glycolate complexes, the variation of half-wave potential with the concentration of glycolate ion was measured (Fig. 3). The concentration of glycolate anion was calculated from the nominal concentration of glycolic acid, the pH of the solution, and the pKa (3.82) (7), for glycolic acid.

In curve I of Fig. 3, the half-wave potentials are essentially independent of glycolic acid concentration

Table I. Slopes of $E_{d.e.}$ vs. log $i/(i_d-i)$

Systems	pH range	No. of polarograms	$E_{d.e.}$ *vs.* $-\log i/(i_d - i)$ low val.	high val.	avg.
Pb-Gly.	1.5-7.5	52	0.028	0.031	0.030
Pb-Mal.	1.5-7.5	54	0.028	0.032	0.030
Pb(Mal.)(Gly.)	1.5-7.5	65	0.028	0.031	0.030

Table II. Temperature coefficients of half-wave potential and diffusion current

Systems	pH	Temp range, °C	Temp coefficient of $E_{1/2}$ (mv/°C)	i_d (%/°C)
Pb-Gly.	5.3	13-25	−0.44	+1.7
		25-47	+0.27	
Pb-Mal.	5.3	13-47	−0.13	+1.4
Pb(Gly.)(Mal.)	5.3	13-47	−0.13	+1.6

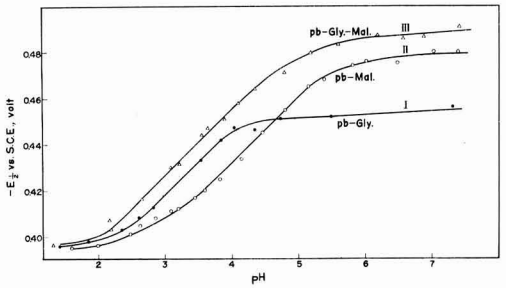

Fig. 2. Effect of pH on half-wave potential. Polarographic solutions containing 1.116 mM $Pb(NO_3)_2$, 0.1M KNO_3, and various chelating agents: (I) 0.205M glycolic acid; (II) 0.218M malonic acid; (III) 0.205M glycolic acid and 0.218M malonic acid.

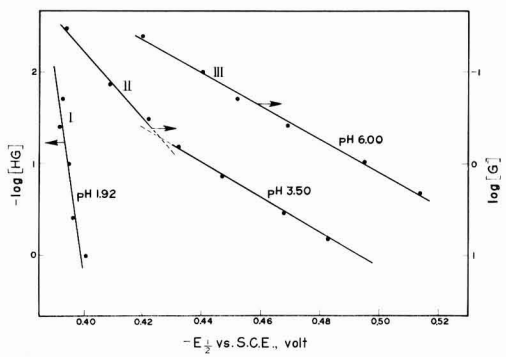

Fig. 3. Variation of half-wave potential of lead-glycolic acid system with ligand concentration: 1.116 mM $Pb(NO_3)_2$, 0.1M KNO_3.

at pH 1.92. This is in good agreement with the fact that no chelation occurred in the low pH region as mentioned above. Curve II in Fig. 3 consists of two straight lines which intersect at glycolate concentration 0.055M. The slopes of the lines are 0.028 and 0.055, corresponding to the ligand number of 0.92 and 1.83, respectively. Thus, the chelate species and electrode reactions in the pH range 2.35-4.15 can be written

$$[G^-] < 0.055M,$$
$$PbG^+ + H^+ + 2e + Hg = Pb(Hg) + HG \qquad (a)$$

$$[G^-] > 0.055M,$$
$$Pb(G)_2 + H^+ + 2e + Hg = Pb(Hg) + HG + G^- \qquad (b)$$

The slopes of curve III in Fig. 3 is 0.055, corresponding to the ligand number of 1.83. Thus, the chelate species and electrode reaction at pH > 4.15 may be expressed as

$$Pb(G)_2 + 2e + Hg = Pb(Hg) + 2G^-$$

Lead-malonic acid system.—It is obvious from curve II in Fig. 2, the half-wave potentials are independent of pH at pH < 2.25 and pH > 5.40. However, in the pH range 2.25-5.40, the half-wave potentials are dependent on pH, and the $\Delta E_{1/2}/\Delta pH$ is —0.028, indicating that one hydrogen ion was consumed in the electrode reduction.

As shown in Fig. 4, the diffusion current constants remain constant at 3.12 at pH lower than 5.25 and at 2.88 at pH greater than 5.25, revealing that two kinds of chelate species transform at pH 5.25. This result and the pK_2 value 5.36 (8) of malonic acid, evidenced that the ligand species is hydrogenmalonate ion at pH lower than 5.25, and is malonate ion at pH greater than 5.25.

The ligand number of the chelates were estimated from Fig. 5, in which the concentration of the hydrogenmalonate ion and malonate ion were calculated

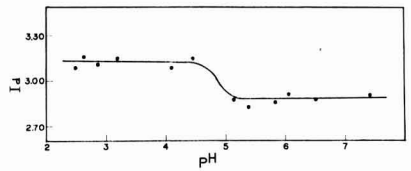

Fig. 4. Effect of pH on diffusion current constant of lead-malonate complexes.

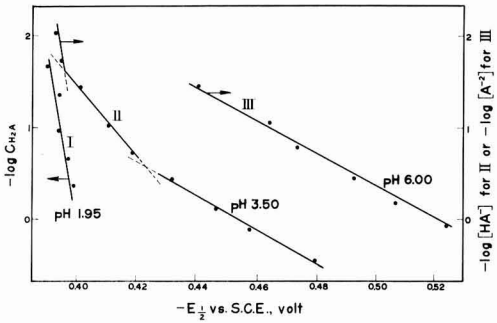

Fig. 5. Variation of half-wave potential of lead-malonic acid system with ligand concentration: 1.116 mM $Pb(NO_3)_2$, 0.1M KNO_3.

from the added concentration of malonic acid, the pH of the solution and using $pK_1 = 2.75$ and $pK_2 = 5.36$ (8).

Curve I in Fig. 5 shows that the ligand number is nearly equal to zero, *i.e.*, essentially no chelation occurred at pH lower than 2.25, which is in good agreement with the result of curve II in Fig. 2.

Curve II in Fig. 5 shows two breaking points at the hydrogenmalonate ion concentration of 0.025 and 0.27M. The first breaking point at 0.025M shows the starting point for chelation, namely, a concentration of hydrogenmalonate ion greater than 0.025M is required to assure the chelation with 1.116 mM lead ion. The ligand number of the lead-hydrogenmalonate chelates were found to be 0.87, and 1.80, as evidenced by the slopes of 0.026, and 0.055, respectively (curve II, Fig. 5).

Based on the forgoing discussion, the chelate species and electrode reactions in the pH range 2.25-5.25 can be expressed as

$$0.025M < [HA^-] < 0.27M,$$
$$Pb(HA)^+ + H^+ + 2e + Hg = Pb(Hg) + H_2A \qquad (a)$$

$$[HA^-] > 0.27M,$$
$$Pb(HA)_2 + H^+ + 2e + Hg = Pb(Hg) + HA^- + H_2A \qquad (b)$$

Above pH 5.40, the malonate ligand took the place of the hydrogenmalonate ligand, as predicted by the sudden drop of the diffusion current constant from 3.12 to 2.88 (Fig. 4). The slope of curve III in Fig. 5 is 0.057 from which the malonate ligand number is 1.90. Thus, above pH 5.40, the formula is $Pb(A)_2^{-2}$ and the electrode reaction will be

$$Pb(A)_2^{-2} + 2e + Hg = Pb(Hg) + 2A^{-2}$$

Lead-glycolic acid-malonic acid system.—Two kinds of chelating agents, glycolic acid and malonic acid, were used in competing for the electron pair donor groups to the lead ion, at the condition of nearly identical concentrations.

The $E_{1/2}$ *vs.* pH plot for this system appears as curve III of Fig. 2. The chelation starts at pH 2.1. The line obtained by varying the pH from 2.1 to 5.3 has a slope of —0.029, indicating that one hydrogen ion was involved in the reduction.

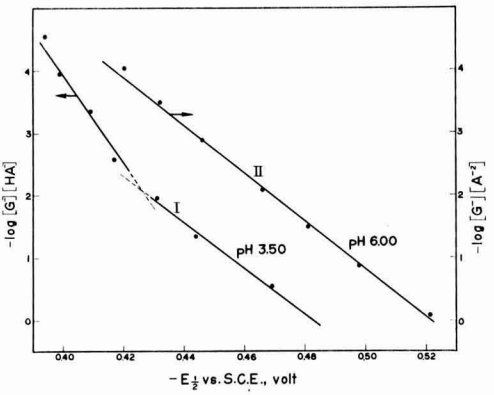

Fig. 6. Variation of half-wave potential of lead-glycolic acid-malonic acid system with ligand concentration: 1.116 mM $Pb(NO_3)_2$, 0.1M KNO_3.

In an attempt to apply Eq. [4], the plots of $E_{1/2}$ *vs.* log $[G^-]$ $[HA^-]$ for *p*H 3.50 and $E_{1/2}$ *vs.* log $[G^-]$ $[A^{-2}]$ for *p*H 6.00 are shown as curves I and II of Fig. 6, in which G^- and A^{-2} denote, respectively, glycolate ion and malonate ion.

In curve I of Fig. 6, the break occurs at $[G^-][HA^-] = 7.9 \times 10^{-3}$ M; the slope is 0.015 for the upper line and is 0.027 for the lower line. Let x and y be the ligand number of G^- and HA^- or A^{-2}. Applying the value of slope, 0.015, in Eq. [4], we get $x \neq y$ when $[G^-]$ $[HA^-] < 7.9 \times 10^{-3}$ M. It was already shown that the glycolate ion can complex with the lead ion only in a 1:1 ratio at lower ligand concentration. The same is true of the hydrogenmalonate ion. Hence $x = 1$ and $y = 0$ or $x = 0$ and $y = 1$ for the case $x \neq y$. This relation indicates that the chelate formed in the competing agents, may be either $Pb(G)^+$ or $Pb(HA)^+$ when $[G^-]$ $[HA^-] < 7.9 \times 10^{-3}$M. However, because of the greater stability of the $Pb(G)^+$ complex (as will be shown in the next section) the $Pb(G)^+$ rather than $Pb(HA)^+$ was considered as the most probable species. On the other hand the slope of the lower line, 0.027, is sufficiently close to 0.030, to yield a value of $x = y = 1$. This shows that the chelate species is Pb(G) (HA) when $[G^-]$ $[HA^-] > 7.9 \times 10^{-3}$M. Thus, the electrode reactions in the *p*H range 2.1-5.3 can be formulated as

$[G^-]$ $[HA^-] < 7.9 \times 10^{-3}$M,

$$Pb(G)^+ + H^+ + 2e + Hg = Pb(Hg) + HG \quad (a)$$

$[G^-]$ $[HA^-] > 7.9 \times 10^{-3}$M,

$$Pb(G)(HA) + H^+ + 2e + Hg = Pb(Hg) + HA^- + HG \quad (b)$$

Similarly, the slope of curve II in Fig. 6 at *p*H 6.0 is 1.026, giving $x \cong y$ and a chelate species of $[Pb(G)(A)]^-$. Thus, the electrode reaction at *p*H greater than 7.3 is

$$[Pb(G)(A)]^- + 2e + Hg = Pb(Hg) + G^- + A^{-2}$$

Concentration dissociation constants of chelates.—The over-all concentration dissociation constants of the chelates were determined by application of Eq. [1] and [2] in which $(E_{1/2})_s$ is —0.397v *vs.* SCE (curve I, Fig. 1). The *p*K values obtained for the chelates are summarized in Table III.

Table III. Concentration dissociation constants of lead complexes

Chelating agents	Ligand number	Chelate species	*p*K
Glycolic acid	0.92	$Pb(G)^+$	2.13 ± 0.03
	1.83	$Pb(G)_2$	3.24 ± 0.05
Malonic acid	0.87	$Pb(HA)^+$	1.37 ± 0.01
	1.80	$Ph(HA)_2$	1.88 ± 0.06
	1.90	$Pb(HA)_2^{-2}$	4.19 ± 0.07
Mix. of glycolic acid and malonic acid	0.90	Pb(G)(HA)	2.89 ± 0.07
	0.87	$[Pb(G)(A)]^-$	4.13 ± 0.06

The $Pb(G)^+$ chelate has the five-membered ring structure

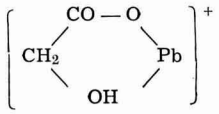

and the $Pb(HA)^+$ has the six-membered ring structure

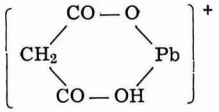

Pfeiffer (9) has shown that, in general, a five-membered ring is more stable than a six-membered ring when the ring is entirely saturated. This was proved by the *p*K values of 2.13 for $Pb(G)^+$ and 1.37 for $Pb(HA)^+$ as shown in Table III. These facts show that the coordination ability of the lead ion with —OH is stronger than that of the lead ion with —COOH.

As listed in Table III, the *p*K value of $Pb(A_2)^{-2}$ is 4.19 and that of $Pb(G)_2$ is 3.24, indicating that the coordination ability between the lead ion and $—COO^-$ is stronger than that between the lead ion and —OH. Thus, it was concluded that the coordination ability between the lead ion with the following groups decreases in the order $—COO^- > —OH > —COOH$. This order is in excellent agreement with the order of *p*K values (Table III): $Pb(A_2)^{-2}$ (4.19) > $[Pb(A)(G)]^-$ (4.13) > $Pb(G)_2$ (3.24) > Pb(G)(HA) (2.89) > $Pb(HA)_2$ (1.88)

Acknowledgment

The authors thank the National Council on Science Development, which supported the work described.

Manuscript received Aug. 27, 1964.

Any discussion of this paper will appear in a Discussion Section to be published in the December 1965 JOURNAL.

REFERENCES

1. T. T. Lai, S. N. Chen, B. C. Wang, and C. C. Hsieh, *Anal. Chem.*, **35**, 1531 (1963).
2. T. T. Lai and C. C. Hsieh, *J. Inorg. Nucl. Chem.*, **26**, 1215 (1964).
3. W. B. Schaap, H. A. Laitinen, and J. C. Bailar, Jr., *J. Am. Chem. Soc.*, **76**, 5868 (1954).
4. R. E. Hamm and R. H. Perkins, *ibid.*, **77**, 2083 (1955).
5. A. Iwase, *J. Chem. Soc. Japan*, **78**, 1411 (1957).
6. H. Flaschka and F. Huditz, *Z. Anal. Chem.*, **137**, 172 (1952).
7. R. T. Morrison and R. N. Boyd, "Organic Chemistry," p. 715, Allyn & Bacon, College Division, Rockleigh, N. J. (1959).
8. A. E. Matell and M. Calvin, "Chemistry of Metal Chelate Compounds," p. 514, Prentice-Hall Inc., Englewood Cliffs, N. J., (1956).
9. P. Pfeiffer, *Angew. Chem.*, **53**, 93 (1940).

Conductivity through Hydrogen Bonded Organic Compounds and Their Homogeneous Solutions

I. Conductivity of Aliphatic Alcohols and Their Benzene Homogeneous Solutions

M. F. Mayahi and A. E. Habboush

Department of Chemistry, College of Science, University of Baghdad, Iraq

ABSTRACT

The conductivity of methanol, ethanol, n-butanol, n-pentanol, and n-hexanol was measured at 30°C. The effect of an increase of one (—CH_2—) group in the carbon chain was determined by plotting molar conductivities *vs.* molar volumes (ml) of each pure alcohol; the slope of the straight line obtained was —55 units. The conductivity of these alcohols in benzene solution at 30°C was found to show a characteristic rise with concentration; the conductivity rises sharply at about 6M concentration of each alcohol. Such points are referred to as inflection points. The plot of molar conductivities of solutions *vs.* the volume of the solution containing one mole of each alcohol at the inflection point gives a straight line, the slope of which is —38 units.

The effect of the hydrogen bond on the conductivity of alcohols (1), solid organic (2) acids, and acidic solutions of water and alcohols (3) has been investigated previously. Mecke *et al.* (1) studied the conductivities of pure methanol, isopropanol, tertiary butyl alcohol, and benzyl alcohol, and the conductivities of their solutions in CCl_4, chlorobenzene and benzene. They found that conductivity decreased as branching in the carbon chain increases. Ubbelohde *et al.* (2) studied the conductivity of solid organic acids and found that the conductivity of the interhydrogen-bonded acids was a hundred times greater than those with intrahydrogen-bonded acids.

Conway *et al.* (3) worked on proton conductance in water and alcohols and observed the lower mobility of the proton as the alcohol hydrocarbon chain length increases. Our work is concerned with the conductivity of hydrogen-bonded compounds and in this paper we report the conductivities of pure methanol, ethanol, n-butanol, n-pentanol, n-hexanol, and also the conductivities of their solutions in benzene at 30°C.

Experimental

Materials.—Methyl alcohol was supplied by Fisher Scientific Company (certified reagent) containing 0.01 % water and was used without further treatment. Ethyl alcohol and benzene were of Analar grade of the British Drug Houses Company and used without further treatment. Butyl alcohol and hexanol were supplied by B.D.H. and were treated with $MgSO_4$ and distilled. Amyl alcohol was Analar grade of Merck & Company and was treated with $MgSO_4$ and distilled.

Apparatus.—A Wayne Kerr Universal bridge B221 was used with a special cell designed for low conductivity measurement, the distance between the platinized platinum electrodes being 0.35 cm.

Method.—Conductivity measurements were made at 30° ± 0.1°C. 5 ml of benzene or alcohol was transferred to the cell using syringe-type graduated 5-ml pipet. After reaching thermal equilibrium, the alcohol or benzene was added from an automatic 1-ml closed buret, graduated to 0.005 ml, to benzene. The cell was sealed immediately with strong adhesive tape to prevent further contact with air. The cell was stirred and readings were taken immediately until a constant value was obtained, experimentally found to be about 2 min. Separate experiments showed that the readings stay constant for 20 min except for solutions containing very high percentages of methyl or ethyl alcohols. For methanol and ethanol the value changed quickly with time, and the value after 2 min was taken. For further additions of alcohol or benzene the adhesive tape was removed from the buret inlet in the cover of the cell, and the buret tip was inserted in the inlet for quick delivery, and the cell was immediately resealed. Each titration curve was done completely in less than 2 hr.

The buret stopcock was treated with vacuum silicone grease which was soaked for two days in alcohol, boiled, the supernatant alcohol decanted, and the grease dried at 100°C before use.

Results and Discussion

The large increase in the initial values of pure methanol and ethanol are due to absorption of water from the air. The results show decrease in conductivity of the pure alcohols as shown in Fig. 1 and 2, as the carbon chain increases in line with observations made by Conway *et al.* (3) for proton mobility in alcohols. This decrease in conductivity is directly related to the per cent hydrogen bonding in these alcohols, such hydrogen bonding decrease with increasing carbon chain, as reflected from their boiling points, heat of vaporization, and thermal conductivities (4).

The effect of an increase of —CH_2— groups on conductivity can be estimated by plotting molar conduc-

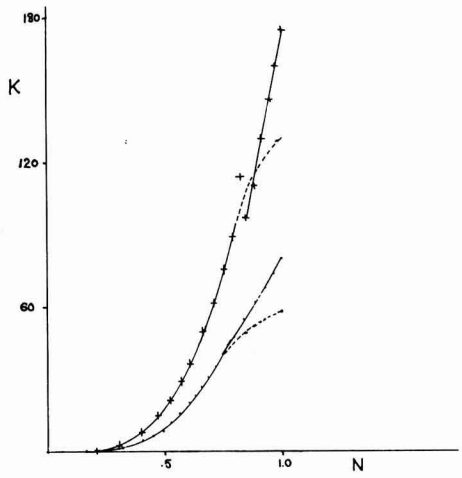

Fig. 1. Specific conductivity (*K*) x 10^8 ohm^{-1} cm^{1-} *vs.* mole fraction (*N*) for methyl alcohol (+) and ethyl alcohol (•) in benzene at 30°C. The straight line in each curve shows the effect of water in each system. The dotted parts are the extrapolation to the lowest reading of each alcohol.

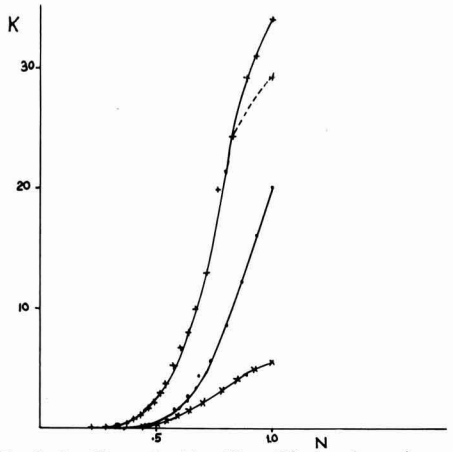

Fig. 2. Specific conductivity (K) x 10^8 ohm^{-1} cm^{-1} vs. mole fraction (N) for n-butyl alcohol (+), n-pentonol (•) and n-hexanol (X) in benzene. The dotted part is the extrapolation to the lowest reading for n-butanol at 30°C.

tivity *vs.* molar volume, Fig. 1. The slope of the straight line is —55 units.

The addition of an inert solvent to these alcohols should affect conductivities in the same manner as increasing the carbon chain in each alcohol. Such an effect is observed in the conductivities of alcohols when diluted with benzene. Plots of specific conductivity against mole fraction are shown in Fig. 1 and 2: for each alcohol there is a particular concentration at which the conductivity rises sharply with increasing concentration. These concentrations will be referred to as inflection points. This inflection indicates that the per cent hydrogen bonding of the alcohol has reached critical value, the meaning of which will be explained later. The inflection points were obtained from each curve by the usual method used to find end points in conductimetric titration; that is by drawing tangents to both ends of the curve, the point on the actual curve which corresponds to the intersection point of the tangents. The conductivity of the solution at that concentration corresponding to the inflection points was read directly from the curve. The inflection points are listed in Table I.

At the inflection points the hydrogen bond formation reaches a critical value, and the conductivity through such hydrogen-bonded chains rises sharply because the effective collisions between these chains is much greater than that between smaller chains present in solutions of lower concentrations. The increase in hydrogen bond formation when the concentration of alcohol is increased is amply verified in the literature by spectral work (4, 5). The inflection point of each alcohol occurs where the same number of moles of the different alcohols are present per unit of solution (*ca.* 6 moles/liter, Fig. 1 and 2, Table I). Table I shows that the conductivity of methanol at its inflection point is higher than that of hexanol at its inflection point, although there is the same number of

Table I. Inflection points taken from Figs. 1 and 2

Alcohol	Mole fraction of alcohol	Specific conductivity ohm^{-1} cm^{-1}, at inflection points	% v/v of alcohol	No. of moles/liter
Methanol	0.43	11.0 × 10^{-8}	26	6.35
Ethanol	0.50	8.0	36	6.18
Butanol	0.61	6.8	58	6.15
Pentanol	0.67	3.6	63	6.52
Hexanol	0.70	2.0	65	6.16

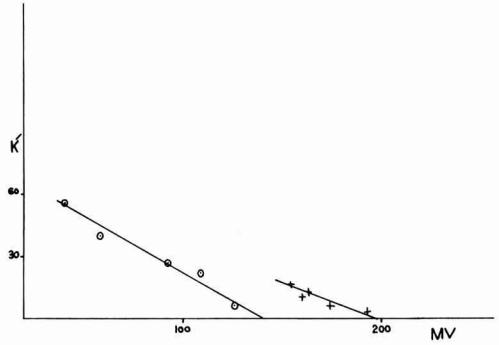

Fig. 3. Molar conductivity (K') x 10^6 ohm^{-1} cm^{-1} vs. molar volume (MV) for pure alcohols (⊙), and for alcohols in benzene at their inflection points (+) at 30°C.

moles/liter involved in each case. This is due to the fact that conductivity can proceed only through hydrogen bonds produced by effective collisions. The increased carbon chain length in the higher alcohols reduces these effective collisions by shielding the (OH) group in the alcohol molecule. This shielding is reduced to some extent in benzene solution but not entirely. The reduced shielding effect of the longer carbon chain is indicated by comparing the slopes obtained by plotting molar conductivities *vs.* molar volumes for the pure alcohols (—55 units) and for the solutions at the inflection points (—38 units) (Fig. 3).

The meaning of the slopes, as indicated earlier, is the decrease in molar conductivity brought about by an increase of one —CH_2— group in the carbon chain of the alcohol. The lower slope obtained for the inflection points in benzene solution indicates a reduction of the steric effect of the longer carbon chain and polymer chains also; the benzene straightens up these chains, thus reducing the shielding of the (OH) group and therefore increasing the effective collisions, which in turn causes the conductivity of the higher alcohols to increase relative to that of methanol. The large increase in conductivity caused by the small amount of absorbed water can be explained by the same reasoning: that is, the small water molecule, when hydrogen bonded between alcohol molecules, reduces the steric effect of the longer carbon chain, thus increasing the extent of hydrogen bonding in the whole system.

Our work, and that of Mecke (1), indicates the necessity of the hydrogen bonds for the conductivity of pure alcohols and their solutions. The solvents used in such systems were benzene, CCl_4, and chlorobenzene. The conductivity of these solvents, although small, is not negligible, especially at higher temperature (1).

It is difficult to explain the conductivity of such inert solvents as CCl_4 by the mechanism proposed by Mecke for the alcohol system, $HROH^+$----------O^-R $\rightleftarrows$HOR--------HOR. A different mechanism involving tunneling of electrons through solvent molecules might explain the conductivity of the inert solvents as that of CCl_4 (6, 7). This mechanism might also be involved in the conductivity of alcohols. The tunneling of electrons is easier through the hydrogen bonds (3) making the conductivity of alcohols higher than those of the inert solvents; accordingly the conductivity of alcohols should decrease with dilution.

Manuscript received Jan. 17, 1964; revised manuscript received July 14, 1964.

Any discussion of this paper will appear in a Discussion Section to be published in the December 1965 JOURNAL.

REFERENCES

1. R. Mecke and H. Zeininger, *Z. Elektrokem.*, **52**, 49 (1948); H. Zeininger and R. Mecke, *ibid.*, **54**, 174 (1950).
2. J. Mc. Pollock and A. R. Ubbelohde, *Trans. Faraday Soc.*, **52**, 1112 (1956).
3. B. E. Conway, J. O'M. Bockris, and H. Linton, *J. Chem. Phys.*, **24**, 834 (1956).
4. G. C. Pimentel and A. L. McClellan, "The Hydrogen Bond," Freeman (1960).
5. C. M. Huggin and G. C. Pimentel, *J. Phys. Chem.*, **60**, 1615 (1956).
6. D. D. Eley, *Research*, **12**, 293, (1959).
7. D. D. Eley and M. R. Willis, *J. Chem. Soc.*, **1963**, 1534.

Conductivity through Hydrogen Bonded Organic Compounds and Their Homogeneous Solutions

II. Conductivity of Phenol, o- and p-nitrophenol in Benzene and Ether

M. F. Mayahi and A. E. Habboush

College of Science, Baghdad University, Baghdad, Iraq

ABSTRACT

The conductivity of p-nitrophenol is more than that of o-nitrophenol in ether at 21°C. The solvent effect on conductivity is shown by measuring the conductivity of phenol in benzene and in ether at 21°C. The participation of the hydrogen-bonded complex C_6H_5OH-----$O(C_2H_5)_2$ in the conductivity of the system is postulated. Such complexing lowers the rate of increase in conductivity with concentration of phenol in ether compared to that in benzene.

The important influence of the hydrogen bond on conductivity was shown in Part I (1) for methanol, ethanol, butanol, n-pentanol, and n-hexanol. In this part we report the conductivities of phenol and benzoic acid in benzene and in ether, also o- and p-nitrophenol, and o- and p-nitrobenzoic acid in ether, all at 21°C.

Ubbelohde *et al.* (2) had shown that the conductivities of interhydrogen bonded solid organic acids are some hundred times greater than those of intrahydrogen bonded acids. Mecke *et al.* (3) studied the conductivities of o- and p-chlorophenol in CCl_4 at 20°C and found that the conductivities of the p-isomer is some hundred times greater than that of the o-isomer at 0.066 mole fraction.

Our work on the o- and p-nitrophenol and on o- and p-nitrobenzoic acid in ether shows differences similar to those reported by Ubbelhode (2) and Mecke (3).

Experimental

Materials.—o- and p-nitrophenol were commercial products and were twice recrystallized from alcohol before use. Benzoic acid and its o- and p-nitro compounds, phenol, benzene, and ether were of analytical grade and were used without further treatment

The method and apparatus for conductometric titrations were as described in Part I.

Results and Discussion

Figures 1 and 2 are plots of specific conductivity *vs.* molarity for phenol in benzene and in ether at 21°C. As in the case of alcohols (1) the conductivity is lowered as concentration is decreased. This decrease of conductivity is brought about by the decrease in per cent hydrogen bonding with dilution. Spectral evidence shows that phenol is interhydrogen bonded, and such bonds are broken on dilution with inert solvents (4). Thus interhydrogen bonding is important in the conductivity of phenol. Any other process which breaks the hydrogen bonding of phenol should bring about a decrease in conductivity. On this premise, the o-substituted phenol should have much lower conductivity than their p-isomer owing to the formation of the intrahydrogen bonding as indicated by spectral work (5). Such low conductivity was observed in our study of the conductivity of p- and o-nitrophenol in ether at 21°C. Figures 3 and 4 show the plot of specific conductivity *vs.* molarity for each isomer. The highest molarity used in each case was about the saturation point of each isomer. It is evident that the conductivity of p-nitrophenol is about six times more than that of o-nitrophenol in ether, even when the concentration of the latter compound is much higher. This ratio in conductivity would be still higher in noncomplexing solvents. This result is in good agreement with that found by Ubbelohde (2).

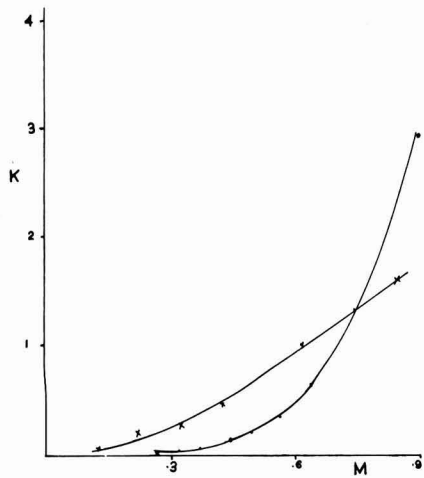

Fig. 1. Specific conductivity (K) x 10^{-8} ohm^{-1} cm^{-1} *vs.* molarity (M) for phenol in benzene (•) and in ether (X) at 21°C.

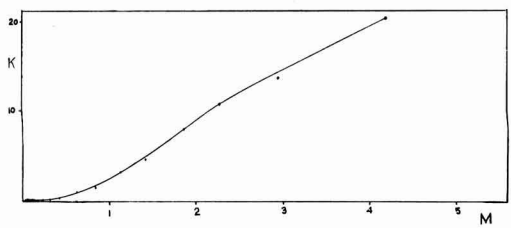

Fig. 2. Specific conductivity (K) x 10^{-8} ohm^{-1} cm^{-1} *vs.* molarity (M) for phenol in ether at 21°C.

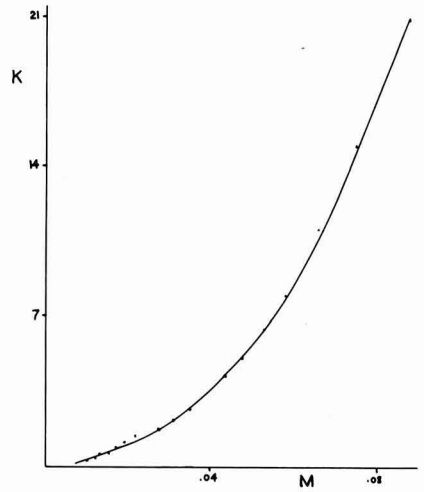

Fig. 3. Specific conductivity (K) x 10^{-8} ohm^{-1} cm^{-1} vs. molarity (M) for p-nitrophenol in ether at 21°C.

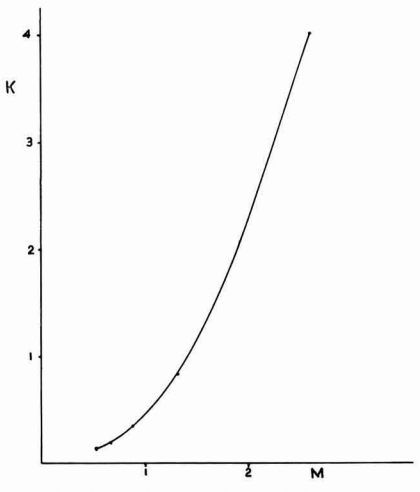

Fig. 4. Specific conductivity (K) x 10^{-8} ohm^{-1} cm^{-1} vs. molarity (M) for o-nitrophenol in ether at 21°C.

Inspection of Fig. 1, 2, and 4 shows that the conductivity of phenol is higher than those of o-nitrophenol in ether, indicating again the effect of intermolecular hydrogen bonding on conductivity. Also, the conductivities of benzoic acid which forms dimers and its o-NO_2 and p-NO_2 derivatives gave very small conductivities compared with that of phenol in ether (1.6M benzoic acid has a conductivity of 0.060 x 10^{-8} ohm^{-1} cm^{-1}).

The effect of solvent on conductivity is shown by comparing the conductivity of phenol in benzene and in ether (see Fig. 1 and 2). The rate of increase of conductivity of phenol is benzene is more than that of phenol in ether, as concentration is increased. This is due to the fact that the interhydrogen bonding of phenol is broken by the ether molecule, since the hydrogen bonding ether and phenol is stronger than between phenol molecules, as indicated by infrared study (6). However, Fig. 1 shows that the conductivity of phenol in ether is higher than that of phenol in benzene at the lower concentrations. Since the conductivity of an organic compound is increased when hydrogen bonding is involved, and (as indicated above) such hydrogen bonding is interrupted by ether molecules, then the higher conductivity of phenol in ether at the lower concentration must indicate that the hydrogen bonded complex between phenol and ether, *i.e.*, $C_6H_5OH\text{----}O(C_2H_5)_2$, is participating in the conductivity of the whole system. This involves an equilibrium between the phenol polymers and the indicated complex. After the intersection point of the two lines in Fig. 1 the conductivity of phenol in benzene is higher than that of phenol in ether, where the same concentrations are involved. This can be explained by assuming that there is greater increase in the formation of polymerized phenol in benzene than in ether.

A further example on the effect of solvent on conductivity is that of the difference in conductivity of benzoic acid in benzene (0.8M conductivity 0.0032 x 10^{-8} ohm^{-1} cm^{-1}) and in ether (0.8M conductivity 0.050 x 10^{-8} ohm^{-1} cm^{-1}). This difference is expected because benzoic acid is known to form closed dimers in benzene; these dimers are largely opened by the ether molecules (7).

Manuscript received Jan. 17, 1964; revised manuscript received July 14, 1964.

Any discussion of this paper will appear in a Discussion Section to be published in the December 1965 JOURNAL.

REFERENCES

1. M. F. Mayahi and A. E. Habboush, *This Journal*, **112**. 222 (1965).
2. J. M. Pollock and A. R. Ubbelohde, *Trans. Faraday Soc.*, **52**, 1112 (1956).
3. H. Zeininger and R. Mecke, *Z. Elektrochem.*, **54**, 174 (1950).
4. C. M. Huggin and G. C. Pemental, *J. Phys. Chem.*, **60**, 1615 (1956).
5. W. Luttke and R. Mecke, *Z. Phys. Chem.*, **196**, 56 (1950).
6. W. Luttke and R. Mecke, *Z. Electrochem.*, **53**, 241 (1949).
7 H. Hosoya, J. Tanaka, and S. Nagakura, *J. Molec. Spect.*, **8**, 257 (1962).

Hydrogen Evolution at a Solid Indium Electrode

James N. Butler and Manfred Dienst

Tyco Laboratories, Inc., Waltham, Massachusetts

ABSTRACT

Measurements of hydrogen overvoltage on solid indium electrodes were made in 0.1M $HClO_4$ at temperatures from 21° to 59.5°C. The slow step in the hydrogen evolution reaction is probably discharge of a hydrogen ion, as indicated by the exchange current (10^{-11} amp/cm²), transfer coefficient (0.5), effect of added iodide ion, and effect of acid concentration. The enthalpy of activation is 14.1 ± 0.5 kcal/mole at the reversible hydrogen potential and 10.0 ± 0.2 kcal/mole at the zero-charge point. From these values, an estimate of 50 ± 10 kcal/g atom is obtained for the heat of adsorption of hydrogen atoms on indium. The reaction is very sensitive to traces of oxygen, and the formation and removal of oxide films are discussed.

Indium offers an unusual opportunity for a detailed study of the hydrogen evolution reaction. In dilute acid, hydrogen evolution is the principal reaction over a potential range of more than 0.8v. The variation in reaction rate due to the influence of the double layer is greatest near the zero-charge point, which is known for indium and lies within the accessible range of hydrogen overpotential measurements. Thus indium is a good electrode on which to study how the hydrogen evolution reaction is influenced by the double layer. Indium also provides an interesting comparison with mercury, which has a similar hydrogen overpotential, but quite a different zero-charge point.

Although considerable work has been done on the dissolution of indium and indium amalgams and on the deposition of indium from solutions containing In^{+3} ions, no adequate measurements have been made of hydrogen overpotential on pure indium.

Bockris (1) made a brief survey of hydrogen overvoltage on eight metals in *1N* HCl in the current density range from 10^{-3} to 10^{-1} amp/cm², and among these was indium. The results of this study are included in Fig. 1. Because no attempt was made to exclude oxygen rigorously from the electrolyte or to remove all traces of superficial oxide films from the electrode, the results of this study must be regarded as preliminary.

Hydrogen evolution has been noted by several workers (2-4) when the rate of indium deposition in acid solution becomes limited by diffusion of In^{+3} to the electrode surface. Kangro and Weingärtner (2) made a study of the deposition of indium from acid solutions containing $In_2(SO_4)_3$ and H_2SO_4, on an indium-coated platinum electrode. They noted that at sufficiently high current densities hydrogen evolution, rather than indium deposition, was the primary process. Their current-potential curve obtained in a solution of pH = 0.86, containing 1% of $In_2(SO_4)_3$ is also shown in Fig. 1. Although the results agree roughly with those of Bockris, a large discrepancy exists in the slope of the Tafel line.

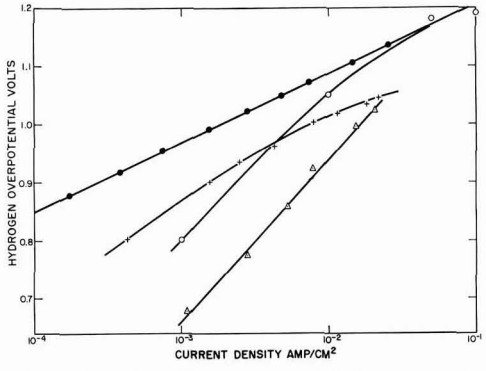

Fig. 1. Comparison of measurements of hydrogen overpotential by various workers: •, this work; ○, Bockris (1); +, Kangro and Weingärtner (2); △, Kochegarov *et al.* (3).

Kochegarov, Zaburdaeva, and Zyablova (3) performed a similar experiment, depositing indium from $In_2(SO_4)_3$-H_2SO_4 solutions onto a copper electrode. Their results, obtained at pH = 2.5 in a solution containing 0.1M $In_2(SO_4)_3$ (Fig. 1), agree with the results of Kangro and Weingärtner (2) at the highest current density, but the overvoltage values are generally much lower and the slope is closer to that of Bockris (1). In neither of these experiments was oxygen excluded from the solution, so that the current observed probably resulted not only from hydrogen evolution, but also from indium deposition and oxygen reduction. It is apparent from the above discussion that no systematic study has been made of In electrodes under conditions where hydrogen evolution is the only process taking place (34).

The necessity for rigorously removing oxygen from the solution when making measurements of hydrogen overvoltage has often been emphasized (5, 6), and the presence of differing amounts of oxygen in the electrolyte and on the electrode surface could account for the disagreement among the results of the three studies mentioned above. Furthermore, the slope of the Tafel lines in Fig. 1 varies between 120 and 280 mv. Although 120 mv is consistent with a slow-discharge mechanism for hydrogen evolution, a higher Tafel slope indicates that an additional process, such as indium deposition or oxygen reduction, is taking place (7, 8).

We have made accurate measurements of the hydrogen overpotential on indium in perchloric acid at several temperatures. These results are reported in this paper and discussed in terms of the transition state theory of reaction rates and the structure of the electrical double layer at the indium-electrolyte interface.

Experimental

A conventional three-compartment cell was used, with platinized platinum counter and reference electrodes. A Luggin capillary was positioned within 4 mm of the working electrode, and under the conditions of measurement, the resistance between the tip of the capillary and the electrode surface was 3-8 ohms. Measurements were made potentiostatically, using a Wenking electronic potentiostat (Brinkmann Instruments) together with a microammeter (Griebach, 0.5% accuracy).

The electrolyte was prepared from triple-distilled conductivity water and reagent grade perchloric acid (Baker). Except where noted, the concentration of perchloric acid was 0.100M. The solution was purified

by pre-electrolysis for 16 hr at a current of 10 ma, using a platinized platinum electrode as cathode. This cathode was removed from the solution before measurements were made. The solution was saturated with purified hydrogen throughout pre-electrolysis and all measurements. An oil-bath thermostat maintained the temperature constant within ±0.2°C from 20° to 60°C.

The cylindrical working electrode was made from 99.999% indium (American Smelting and Refining Company) and had a surface area of approximately 0.5 cm². It was electropolished in a 2:1 mixture of methanol and nitric acid, at an anodic current density of 0.3 amp/cm². After electropolishing, the electrode was thoroughly washed with conductivity water and introduced to the cell. The most reproducible measurements were obtained after the electrode had been polarized overnight in the cell at −1.0v. This effect was related to the removal of an oxide film and will be discussed in detail later.

The capacity of the electrode was measured by suddenly changing the current and observing on an oscilloscope the corresponding change in the potential of the electrode. For this measurement, the electrode was polarized galvanostatically.

From the initial linear increase of potential, the capacity was calculated using the relation

$$C = \Delta i(dt/dV)$$

where Δi is the current increment. If the current was increased by about 1 ma, the electrode potential increased linearly by about 4 mv in 16 μsec, corresponding to a capacity of about 4 μf (8 μf/cm²).

Results

In order to achieve reproducible values for the current-potential curve at low current-densities, it was necessary to prepolarize the indium electrode cathodically (usually at −1.0v with respect to a reversible hydrogen electrode) for an extensive period of time. Apparently the electropolished electrode was covered with a thin film of indium oxide, even though it appeared brightly metallic. At a temperature of 30°C, prepolarization for 16 hr at −1.0v was sufficient to remove the oxide film completely, as indicated by the fact that further prepolarization did not change the current-potential curve. During a typical prepolarization period, approximately 0.3-0.4 coul/cm² were passed in addition to the hydrogen evolution current observed on a clean electrode. If this were due entirely to removal of oxide film, the film on the electrode would have been approximately 0.1-0.2μ in thickness. Such a thick oxide film should have resulted in the appearance of interference colors, which were not observed. More likely, a large part of the additional current passed during prepolarization resulted from reduction of traces of dissolved oxygen in the electrolyte.

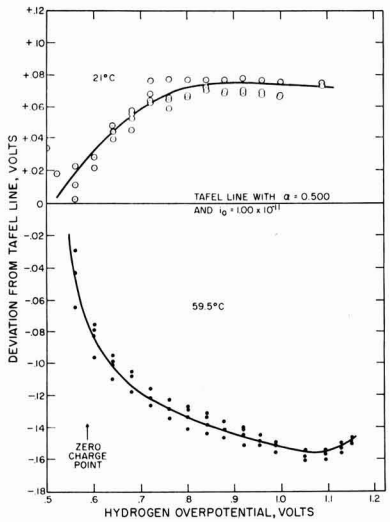

Fig. 2. Deviation of experimental current-potential curve from an arbitrary Tafel line with $\alpha = 0.500$ and $i_o = 1.00 \times 10^{-11}$.

The measured potential values were corrected for the iR drop to obtain overpotential values, which are listed in Table I. Each set of values is the average of two to four current-potential curves, taken with the potential increasing and with the potential decreasing.

In Fig. 2 are shown two sets of current-potential measurements at 21° and 59.5°C. To show the small differences between the measurements clearly, we have plotted the deviation of the experimental values from a Tafel line

$$\eta = \frac{RT}{\alpha \mathbf{F}} \ln(i/i_o) \qquad [1]$$

with arbitrarily chosen values of exchange current $i_o = 1.00 \times 10^{-11}$ amp/cm² and cathodic transfer coefficient $\alpha = 0.500$. Although there is a systematic deviation from the arbitrary Tafel line, the average difference between two points taken at a given potential at the same temperature is only about 4 mv. As can

Table I. Hydrogen overpotential on solid indium

Temperature dependence											
21.0°C		25.0°C		30.0°C		41.0°C		50.5°C		59.5°C	
η	i	η	i	η	i	η	i	η	i	η	i
η in volts, corrected for iR drop. i in μa/cm²											
0.500	0.10	0.480	0.078								
0.520	0.20	0.560	0.42	0.560	**0.54**						
0.560	0.52	0.600	0.78	0.600	1.24	0.600	0.80				
0.600	0.82	0.640	1.60	0.640	2.80	0.640	2.06	0.600	1.40		
0.640	1.30	0.680	3.55	0.680	6.39	0.680	5.25	0.640	3.45	0.600	2.20
0.720	4.05	0.720	7.85	0.720	14.5	0.720	12.5	0.680	8.95	0.640	5.03
0.760	9.15	0.760	17.1	0.760	31.9	0.760	29.3	0.720	21.9	0.680	11.6
0.800	18.9	0.800	37.8	0.800	74.3	0.800	64.5	0.760	50.3	0.720	28.3
0.840	39.3	0.839	82.0	0.839	167.	0.840	134.	0.800	110.	0.760	64.8
0.880	87.5	0.879	175.	0.878	377.	0.879	297.	0.839	231.	0.800	144.
0.920	191.	0.918	370.	0.917	833.	0.918	623.	0.879	490.	0.839	312.
0.959	427.	0.955	753.	0.953	1750.	0.955	1318.	0.917	1033.	0.878	665.
i in μa/cm²											
0.998	0.960	0.990	1.53	0.985	3.50	0.991	2.72	0.954	2.10	0.916	1.38
1.092	5.48	1.022	2.80	1.050	12.4	1.062	11.4	0.988	4.10	0.952	2.53
		1.071	7.10	1.093	26.4	1.111	27.0	1.055	15.1	0.985	5.26
		1.091	10.65	1.118	44.5	1.142	47.5	1.102	33.0	1.050	18.0
		1.107	14.35	1.141	63.5			1.135	55.8	1.093	38.0
		1.135	25.3	1.153	85.0					1.126	61.8
										1.150	88.8

be seen in Fig. 2, at 21°C, the deviations from the Tafel line became more positive at higher overpotentials, and at 59.5°C, the deviations became more negative at higher overpotentials. The data obtained at intermediate temperatures showed current-potential curves which were intermediate in shape bewteen the two extremes shown in Fig. 2.

As we shall explain in the discussion section, it seems likely that the slow step in the hydrogen evolution reaction on indium is the discharge of a hydrogen ion. For a reaction in which discharge of an ion is the rate-determining step, the measured overpotential includes not only the potential drop across the compact (Helmholtz) double layer, which drives the reaction, but also a potential drop across the diffuse (Gouy-Chapman) double layer, which does not influence the reaction rate (9-12). We have therefore used the relations derived by Frumkin (9, 13, 14) to obtain parameters which describe the experimental data. Unlike mercury, indium has a zero-charge point which falls at the lower end of the accessible range of overvoltage measurements: at —0.580v with respect to a reversible hydrogen electrode in 0.1M $HClO_4$ (15). This means that the contribution of the diffuse double layer to the total potential drop will vary appreciably over the range of potentials where we have measured the current-potential curves.

In order to apply Frumkin's equation to correct for the potential drop across the diffuse double layer, it is necessary to obtain ϕ_2, the potential of the outer Helmholtz plane, which is identified with the transition state for the hydrogen discharge reaction in the absence of specific adsorption. This potential is given by the equation (9, 16)

$$K\phi_0 = \left[\frac{2RT\,D\,D_0}{\pi}C_+\right]^{1/2}\sinh\left(\frac{\phi_2\mathbf{F}}{2RT}\right) \quad [2]$$

where R is the gas constant, T is the absolute temperature, D is the dielectric constant of water, $D_0 = 1.128 \times 10^{-12}$ coul volt^{-1} cm^{-1}, C_+ is the concentration of univalent electrolyte, $\mathbf{F}$ is the Faraday constant, K° is the integral capacity of the Helmholtz layer, and ϕ_0 is the rational potential of the electrode [potential with respect to the zero-charge point (16)].

The measured values of capacity are shown in Fig. 3, together with the interpolated curve which was used in the calculations, corresponding to the empirical equation

$$K = 8.9 + 2.75\ \phi_0 + 1.25\ \phi_0^2 \quad [3]$$

The measured capacity was somewhat lower than the 15 to 20 μf/cm^2 obtained with mercury (16), gallium (17), and lead (18), which may result from a thin residual oxide film.

For comparison, an alternative capacity function was obtained by extrapolating results obtained on a series of indium amalgams (19). This function presumably

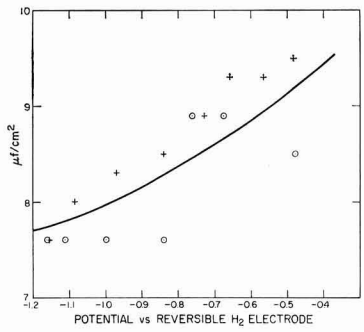

Fig. 3. Experimentally measured capacity and interpolated curve used for calculations (Eq. [3]). ○, Clean electrode; +, oxidized electrode; ——, interpolated curve Eq. [3].

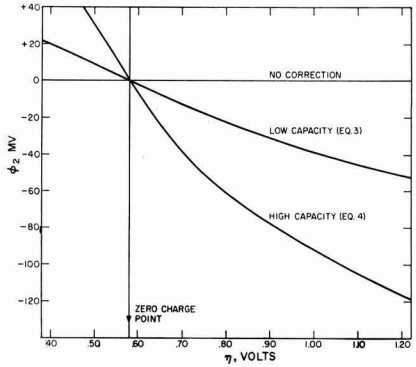

Fig. 4. Calculated values of the potential of the outer Helmholtz plane, ϕ_2, at 32°C.

is a good approximation to the capacity of pure supercooled liquid indium, and was

$$K = 42.0 + 46.6\ \phi_0 + 54.0\ \phi_0^2 \quad [4]$$

Equation [4] gave values in the range from 30 to 40 μf/cm^2.

In Fig. 4 are plotted two typical curves giving ϕ_2, the potential of the outer Helmholtz plane with respect to the bulk of the solution, as a function of the hydrogen overpotential. These were calculated using Eq. [3] and [4] to approximate K° in [2]. Note that when the high-capacity function given by Eq. [4] is used, the values of ϕ_2 obtained are nearly twice as large as when the low-capacity function given by Eq. [3] is used.

The overpotential for a reaction, where discharge of a hydrogen ion is the slow step, is given by the equation (9, 13, 14)

$$\eta = \frac{1-\alpha}{\alpha}\left(\phi_2 - \frac{RT}{\mathbf{F}}\ln[H^+]\right) + \frac{RT}{\alpha\mathbf{F}}\ln i - g_H + \text{const.} \quad [5]$$

where α is the cathodic transfer coefficient, i the current density, g_H the free energy of desorption of a hydrogen atom for the surface of the electrode, and $[H^+]$ the bulk concentration of hydrogen ions. Since we are holding the composition of the electrode and the concentration of hydrogen ion in the electrolyte constant, we can lump the constant terms into a corrected exchange current i_o'

$$\eta = \frac{1-\alpha}{\alpha}\phi_2 + \frac{RT}{\alpha\mathbf{F}}\ln(i/i_o') \quad [6]$$

where

$$\ln i_o' = (1-\alpha)\ln[H^+] + \frac{\alpha\mathbf{F}}{RT}g_H + \text{const.}$$

The corrected exchange current i_o' is different from the exchange current obtained from the simple Tafel Eq. [1] because of the term in ϕ_2, which corrects for the potential drop across the diffuse double layer. If $\phi_2 = 0$, Eq. [6] reduces to the simple Tafel equation.

Equation [5] can be cast into the form of a straight line

$$y = \alpha x + B \quad [7]$$

where

$$y = \frac{RT}{\mathbf{F}}\ln i + \phi_2$$

$$x = \eta + \phi_2 \quad [8]$$

The slope of this line is α and its intercept is

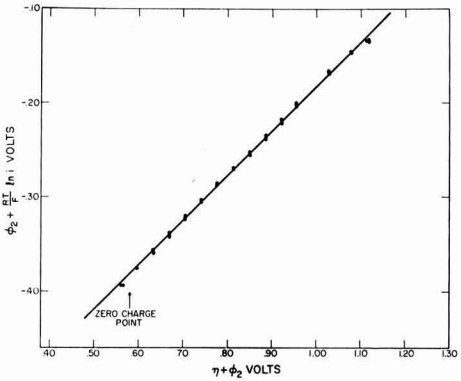

Fig. 5. Fit of experimental data to Eq. [5]. The temperature was 32°C, and the low-capacity function (Eq. [3]) was used to calculate ϕ_2. The correlation coefficient for the least-squares straight line is 0.9995. The best values for the parameters are $\alpha = 0.472 \pm 0.003$ and $-\log i_o' = 10.82 \pm 0.05$.

$$B = \frac{RT}{\mathbf{F}} \ln i_o' \qquad [9]$$

To obtain the parameters for each of the experiments conducted, ϕ_2 was calculated from Eq. [2] using the capacity function defined by either [3] or [4], and for each data point the quantities x and y, given by Eq. [8], were calculated. A least-squares straight line (Fig. 5) was fitted to the function $y(x)$, and from its slope and intercept were obtained the best values for α and $-\log i_o'$. The 95% confidence limits provide an estimate of the probable error in the measurements. These calculations were performed on an IBM 7094 computer.

The values so obtained are listed in Tables II and III, along with the values of α and $-\log i_o$ obtained when no correction is made for the potential drop across the diffuse double layer. From Table II, we can see that the larger the capacity, the smaller is α and the larger is i_o'.

Comparing the confidence limits on the parameters calculated with the high-capacity function, the low-capacity function, and with no correction, we can see that the best over-all fit is obtained with the low-capacity function. The high-capacity function gives a slightly better fit at the high temperatures, and no correction at all gives a slightly better fit at the low temperatures. The results obtained using the low-capacity function are probably the most realistic and will be used in the subsequent discussion.

Discussion

Mechanism.—In our calculations and in the following discussion of the results, we assume that discharge of a hydrogen ion is the rate-determining step in the hydrogen evolution reaction on solid indium. This mechanism is suggested by a number of observations, which we shall discuss here.

Table III. Effect of electrode preparation

Temperature 30°-32°C

History of electrode	Parameters of current-potential curve[a] α	$-\log i_o'$	No. points
1. Electropolished, reduced at −1.0v for 40 hr as 30°C	0.489 ± 0.004	10.83 ± 0.06	35
2. Electropolished, reduced at −1.0v for 16 hr at 25°C	0.472 ± 0.003	10.82 ± 0.04	59
3. Treatment 2, followed by redn. at −1.0v for 16 hr at 60°C	0.482 ± 0.002	10.80 ± 0.04	30
4. Clean electrode, oxidized for 5 min in air at 25°C (only points with $i > 10^{-4}$ amp/cm²)	0.459 ± 0.009	10.36 ± 0.14	16
5. Treatment 4, followed by redn. at −1.0v for 16 hr at 30°C	0.486 ± 0.004	10.84 ± 0.06	23
6. Clean electrode, left on open circuit (−0.4v) for 15 min	0.485 ± 0.006	10.84 ± 0.08	20

[a] Calculated using experimental capacity values given by Eq. [3].

The exchange current on indium is approximately 10^{-11} amp/cm² at 30°C, of the same order of magnitude as the exchange current on lead and mercury, metals for which considerable evidence indicates a slow discharge mechanism (8, 9, 20). As shown in Fig. 5, the data fit Eq. [5] over a wide range of potentials, including the zero-charge point of indium, where the largest deviation from Eq. [5] would be expected if discharge were not the slow step. The observed effect of the diffuse double layer is thus the same as is expected for a slow discharge mechanism. The observed transfer coefficient is very close to 0.50, indicating a symmetrical activation energy barrier. This also implies that discharge is the slow step (21).

One important effect of the slow-discharge mechanism is the extreme sensitivity of the hydrogen overvoltage to adsorbed species on the electrode (9, 20). A specifically adsorbed anionic species on the electrode lowers the overvoltage at small current densities. In a few experiments, we added potassium iodide to the electrolyte and observed that, at current densities below 10^{-4} amp/cm², the overvoltage was approximately 0.1v lower than in the absence of potassium iodide. This agrees qualitatively with the results observed on mercury, lead, and gallium (9, 17, 20). However, the effect observed could have been at least partially due to small amounts of oxygen or free iodine in the electrolyte, since the results were very irreproducible.

A further consequence of the slow-discharge mechanism is that the dependence of overvoltage on pH should be given by Eq. [5]. An experiment with 0.01M $HClO_4$ as electrolyte gave the results summarized in Table IV. According to Eq. [6], the quantity

$$-\log i_o' + (1-\alpha) \log [H^+]$$

should be independent of the electrolyte composition. In Table IV we see that it is the same within experimental error for both 0.1 and 0.01M $HClO_4$.

In view of the foregoing observations, it seems reasonable to assume that discharge of a hydrogen ion is the slow step of the hydrogen evolution reaction on indium.

Table II. Parameters of the current-potential curve

(errors are 95% confidence limits)

Temp, °C	Low-capacity[a] α	Low-capacity[a] $-\log i_o'$	High-capacity[b] α	High-capacity[b] $-\log i_o'$	Uncorrected[c] α	Uncorrected[c] $-\log i_o$	No. points
21.0	0.389 ± 0.011	10.19 ± 0.14	0.290 ± 0.020	9.27 ± 0.25	0.445 ± 0.009	10.74 ± 0.12	52
25.0	0.449 ± 0.003	10.86 ± 0.04	0.372 ± 0.011	9.98 ± 0.15	0.498 ± 0.002	11.15 ± 0.03	37
30.0	0.489 ± 0.004	10.83 ± 0.06	0.441 ± 0.004	10.55 ± 0.06	0.530 ± 0.004	11.19 ± 0.07	35
41.0	0.495 ± 0.005	10.77 ± 0.07	0.441 ± 0.005	10.41 ± 0.07	0.538 ± 0.005	11.14 ± 0.07	51
50.5	0.502 ± 0.006	10.44 ± 0.08	0.445 ± 0.005	10.05 ± 0.07	0.546 ± 0.006	10.81 ± 0.09	53
59.5	0.510 ± 0.006	10.22 ± 0.07	0.454 ± 0.004	9.87 ± 0.06	0.552 ± 0.006	10.57 ± 0.08	56

[a] Integral capacity obtained using Eq. [3].
[b] Integral capacity obtained using Eq. [4].
[c] No correction for potential drop across diffuse double layer.

Table IV. Effect of electrolyte concentration[a]

Conc. of $HClO_4$, moles/liter	0.100	0.010
Low-capacity[b]		
α	0.489 ± 0.004	0.40 ± 0.02
$-\log i_o' + (1 - \alpha) \log [H^+]$	10.83 ± 0.06	10.3 ± 0.3
$-\log i_o' + (1 - \alpha) \log [H^+]$	11.34 ± 0.06	11.5 ± 0.3
Uncorrected[c]		
α	0.530 ± 0.004	0.48 ± 0.02
$-\log i_o$	11.19 ± 0.07	10.8 ± 0.3

(a) Temperature 30°C.
(b) Integral capacity obtained using Eq. (3).
(c) No correction for diffuse double layer.

Enthalpy of activation.—According to the transition state theory (8, 21, 23), the enthalpy of activation for the discharge reaction is given by

$$\Delta H^{\ddagger} = RT^2 \left(\frac{\partial \ln i}{\partial T} \right)_{\eta} \qquad [10]$$

and depends on the potential at which the temperature coefficient is measured.

The temperature dependence of the corrected exchange current is shown in Fig. 6. These values were obtained using the capacity function given by Eq. [3]; however, the uncorrected values of exchange current, and the values obtained using the capacity function given by Eq. [4] differ only by an additive constant. The best straight line through the points obtained at the three highest temperatures gives $\Delta H^{\ddagger} = 14.1 \pm 0.5$ kcal/mole for the enthalpy of activation at the reversible hydrogen potential. The values obtained at the lower temperatures have been omitted because the effect of adsorbed oxygen or a thin oxide film makes Eq. [10] inapplicable.

Although it is conventional to calculate the enthalpy of activation at the reversible hydrogen potential, it is also significant to look at the enthalpy of activation at the zero charge point of the electrode. In Fig. 7 is plotted the current at the zero charge point [$\eta = 0.58$v (15)] as a function of the reciprocal temperature. The slope of the best line defined by the high temperature points is 10.0 ± 0.2 kcal/mole. In principle, the current at the zero charge point should be independent of the capacity function used to calculate the diffuse double layer correction. The effect of the capacity function on i_z, apparent in Fig. 7, reflects the effect of scatter in the current-potential values on the interpolation at the zero charge point.

In order to compare the enthalpy of activation for indium with that for mercury, it is desirable to refer

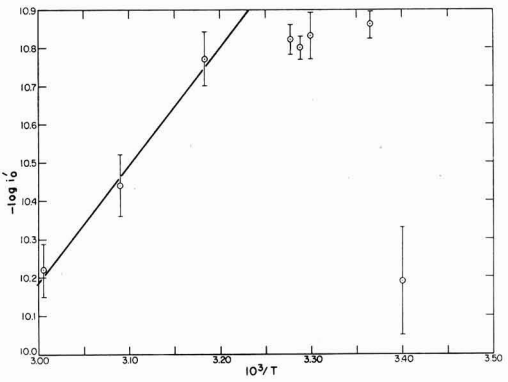

Fig. 6. Temperature dependence of the corrected exchange current. The straight line corresponds to an enthalpy of activation of 14.1 ± 0.5 kcal. The low-capacity function was used in calculating i_o'.

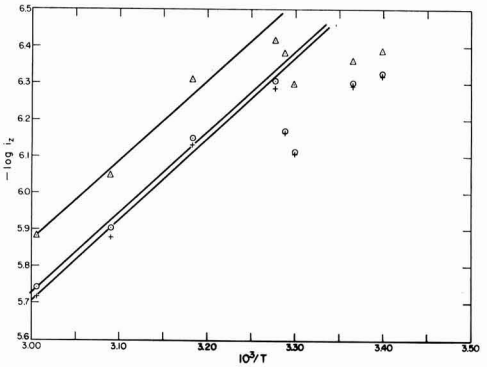

Fig. 7. Temperature dependence of the current at the zero charge point. All three straight lines have a slope corresponding to an enthalpy of activation of 10.0 ± 0.2 kcal. ○, Low capacity; △, high capacity; +, uncorrected.

both to the same potential relative to the zero-charge point. The reversible hydrogen potential in 0.1M $HClO_4$ is 0.165v positive with respect to the zero-charge point of mercury, but is 0.58v positive with respect to the zero-charge point of indium (15). Consequently, a comparison of $\Delta H^{\ddagger}$ at the reversible hydrogen potential will contain contributions from the temperature dependence of the double layer structure.

At the reversible hydrogen potential, $\Delta H^{\ddagger}$ for the hydrogen evolution reaction on mercury was determined by Post and Hiskey (23) to be 21.7 ± 0.2 kcal, and by Iofa and Mikulin (24) to be 21.1 ± 0.5 kcal. The potential dependence of the enthalpy of activation is given approximately by (23)

$$\Delta H^{\ddagger} = \Delta H^{\ddagger}_{rev} - \alpha \mathbf{F} \eta \qquad [11]$$

where $\Delta H^{\ddagger}_{rev}$ is the enthalpy of activation at the reversible hydrogen potential, and η, the cathodic overvoltage, is positive.

Equation [11] does not hold as well for indium as it does for mercury. This can be seen by calculating the difference in the enthalpy of activation on indium between the reversible hydrogen potential and the zero charge point. Using Eq. [11], this difference is calculated to be 6.7 kcal; the experimentally observed difference is only 4.1 kcal. For this reason, we feel it is more accurate to extrapolate the results for mercury than the results for indium.

Thus, at the zero charge point, $\Delta H^{\ddagger}$ for the hydrogen evolution reaction on mercury is 19.8 kcal, which may be compared with 10.0 kcal which we have observed for $\Delta H^{\ddagger}$ at the zero charge point on indium.

Similarly, but with less accuracy, we may compare the enthalpy of activation on mercury at the reversible hydrogen potential (+0.165v with respect to the zero-charge point) with that for indium at a potential of +0.165v with respect to the zero-charge point, an overpotential of 0.415v. For mercury, $\Delta H^{\ddagger}$ is 21.7 kcal; for indium, $\Delta H^{\ddagger}$ is 11.9 kcal.

Parsons and Bockris (22) have estimated, for mercury and nickel, the theoretical dependence of enthalpy of activation on the heat of adsorption of hydrogen atoms. Using a similar method, Rüetschi and Delahay (26) have calculated heats of adsorption for hydrogen atoms and correlated them with experimental values of overvoltage at constant current density.

Because of the similarity in hydrogen overvoltage between mercury and indium, it seems likely that the values of all parameters involved in the dependence of $\Delta H^{\ddagger}$ on heat of adsorption are approximately the same for mercury and indium (15). The curve of this dependence, calculated for mercury by Parsons and Bockris (22), is shown in Fig. 8. To show the uncertainty in such a calculation, two extreme estimates are

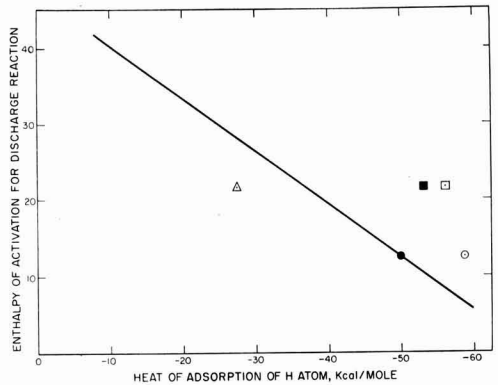

Fig. 8. Relation between enthalpy of activation and heat of adsorption of hydrogen atoms, with estimated values for mercury and indium. ——, Theoretical curve (22); ●, indium, this work; △, mercury (24, 25); □, mercury (27); ■, mercury (26); ○, indium (26).

shown for the heat of adsorption of hydrogen atoms on mercury: Frumkin, Iofa, and Bagozky (25) estimated this quantity to be approximately 28 kcal, whereas Conway and Bockris (27) estimated it to be approximately 57 kcal. The theoretical curve calculated by Parsons and Bockris (22) falls between these two extremes. Our value of 11.9 kcal for the enthalpy of activation for the hydrogen evolution reaction on indium (at a potential of +0.165v with respect to the zero-charge point) allows us to estimate that the heat of adsorption of hydrogen atoms on indium is 50 ± 10 kcal. This value is consistent with the value (56.6 kcal) estimated by Rüetschi and Delahay (26).

Effect of oxide film.—We have mentioned that, before reproducible measurements of overpotential could be obtained, it was necessary to remove the oxide film on the electrode by prolonged cathodic polarization. At temperatures below 30°C, this oxide film was not removed even after polarization for 16 hr at — 1.0v.

The oxide film we have observed is probably similar to the film formed on passivation of indium. Popova and Simonova (32) showed that anodic polarization of indium in both acid and alkaline solutions produce a passive oxide layer which corresponded approximately to a monolayer of oxygen. In 0.1M $HClO_4$, this passive oxide layer was apparently stable, even though In_2O_3 is thermodynamically unstable in acid solutions (33). A similar type of oxide film has been observed on solid gallium (18, 28). Indium antimonide is known to form a stable, coherent film of In_2O_3 both on thermal oxidation (29, 30) and on anodic oxidation (31). This film is difficult to reduce, even in acid solution (29).

Our observations on the oxide film formed on indium are in accord with these results. In our experiments, polarization of the indium electrode at — 0.6v for 16 hr failed to remove the oxide film; complete removal required an elevated temperature, as well as prolonged cathodic polarization at — 1.0v (See Table III).

The fact that indium forms such a stable oxide film causes a hysteresis effect in the current-potential curve when traces of oxygen are present. In Fig. 9, we see the current-potential curve observed when a freshly prepared electrode is introduced into the cell. As the cathodic overpotential is increased, the lower curve is obtained; the wave resulting from both the reduction of the oxide film and the diffusion-limited reduction of oxygen in the solution. If the electrode is held for several hours at 1.0v cathodic polarization, the current decreases. If the overpotential is then decreased, the upper curve is obtained. The wave for oxygen reduction is shifted to lower current densities, both because the concentration of oxygen in the solution is smaller and because part of the oxide film has been removed from the electrode.

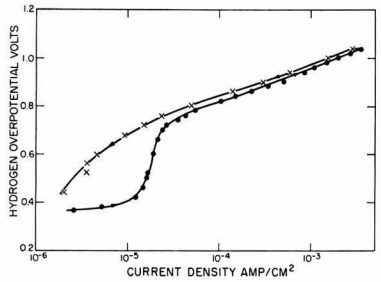

Fig. 9. Current-potential curve taken using a freshly prepared electrode. The lower curve was taken with overpotential increasing; the electrode was held at an overpotential of 1.04v for 2 hr and then the upper curve was taken, with overpotential decreasing.

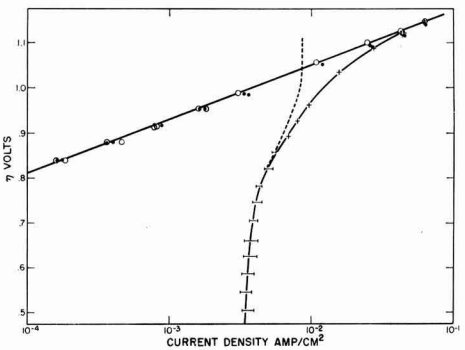

Fig. 10. Current-potential curve taken on a clean and oxidized electrode in the absence of oxygen and on an electrode in a solution saturated with oxygen. The oxygen reduction current was obtained by subtracting the current given by the upper curve from that given by the lower curve. Without oxygen: ●, clean; ○, oxidized. With oxygen: ———, total current; — — —, O_2 reduction current.

This wave definitely results from oxygen reduction, and not from In^{+3} reduction. If the electrode is prepolarized until the current-potential curve shows no hysteresis and obeys Eq. [5] over the accessible range of overpotentials, we may assume that the oxide film has been completely removed. If such an electrode is left on open circuit for 15 min, no effect is observed on the current-potential curve (Table III), indicating that no appreciable amount of In^{+3} exists in the solution due to chemical dissolution of the electrode. In contrast, if the electrode is removed from the cell and exposed to the air for only 1½ min, the subsequent polarization curve shows hysteresis and has the shape shown in Fig. 9. In order to restore the electrode to its former condition, it is necessary to polarize it cathodically for 16 hr. During this time, approximately 0.5 coulombs of charge pass through the cell in addition to that required to evolve hydrogen. This additional current is probably due both to reduction of oxide on the electrode and to the reduction of oxygen in the solution. These results are summarized in Table III.

The effect of bubbling oxygen over the electrode is shown in Fig. 10. The oxygen reduction current (dotted line) has been obtained by subtracting, from the total current, the current for hydrogen evolution at the same potential. Note that although the oxygen reduction current appears to be diffusion limited in the range of potentials shown, the limiting current in fact increases by about a factor of two at approximately

0.8v. This effect probably results from stirring by evolved hydrogen. At lower potentials, the limiting current for oxygen reduction is controlled by diffusion of oxygen through a boundary layer at the electrode surface. When the rate of hydrogen evolution becomes large enough, hydrogen bubble formation at the electrode surface disturbs this boundary layer and increases the maximum rate at which oxygen can diffuse to the electrode.

Another possible explanation of this phenomenon can be made in terms of the kinetics of reduction of the oxide film. If the rate of reduction of oxygen on the oxide film is slower than the rate of reduction of oxygen on a clean electrode, then, at potentials between 0.4 and 0.8v, a steady state is set up. The oxide film is reduced, but is regenerated by oxygen diffusing from the solution. However, at potentials above 0.8v, reduction of the oxide film itself is sufficiently fast that the electrode becomes free of oxide and oxygen reduction takes place directly on the surface of the metal. Because this reaction is faster, a higher limiting current controlled by diffusion of oxygen is reached.

An alternative kinetic explanation for the increase in oxygen reduction current at high potentials is that the oxide film catalyzes the hydrogen evolution reaction. This explanation is not correct. In Fig. 10 the data are given for an oxidized electrode and an oxide-free electrode under the same conditions. In the region covered by Fig. 10, the current-potential curves for hydrogen evolution, in the absence of oxygen, are identical on clean and oxidized electrodes. The oxide does not catalyze the hydrogen evolution reaction.

Acknowledgments

This work was supported by the Office of Naval Research, Materials Sciences Division, Contract No. NOnr-3765(00), ARPA Order No. 302-62. The authors thank Dr. A. C. Makrides for the penetrating criticism and helpful suggestions which he gave during the course of this work. Miss Evelyn Barron assisted with the calculations.

Manuscript received June 17, 1964; revised manuscript received Oct. 16, 1964. This paper was presented at the Washington Meeting, Oct. 11-15, 1964.

Any discussion of this paper will appear in a Discussion Section to be published in the December 1965 JOURNAL.

REFERENCES

1. J. O'M. Bockris, *Trans. Faraday Soc.*, **43**, 417 (1947).
2. W. Kangro and F. Weingärtner, *Z. Elektrochem.*, **58**, 505 (1954).
3. V. M. Kochegarov, F. I. Zaburdaeva, and E. A. Zyablova, *Zh. Priklad. Khim.*, **35**, 1376 (1962).
4. G. Serravalle and B. Mazza, *Electrochim. Acta*, **8**, 313 (1963). (Previous work by the Italian school is cited in this paper).
5. J. O'M. Bockris and R. Parsons, *Trans. Faraday Soc.*, **45**, 916 (1949).
6. A. Azzam, J. O'M. Bockris, B. E. Conway, and H. Rosenberg, *ibid.*, **46**, 918 (1950).
7. J. O'M. Bockris and E. C. Potter, *This Journal*, **99**, 169 (1952).
8. J. O'M. Bockris, "Modern Aspects of Electrochemistry," Vol. I, p. 209, Butterworths, London (1954).
9. A. N. Frumkin, "Hydrogen Overvoltage and Adsorption Phenomena. Part I. Mercury," in Vol. I. of "Advances in Electrochemistry and Electrochemical Engineering," p. 65, P. Delahay, Editor, Interscience, New York (1961).
10. R. Parsons, "Structure and Influence of the Double Layer," *ibid.*, p. 1.
11. M. Breiter, M. Kleinerman, and P. Delahay, *J. Am. Chem. Soc.*, **80**, 5111 (1958).
12. P. Delahay and M. Kleinerman, *ibid.*, **82**, 4509 (1960).
13. A. N. Frumkin, *Z. Physik. Chem.*, **A164**, 121 (1933).
14. A. N. Frumkin, *Discussions Faraday Soc.*, **1**, 57 (1947).
15. J. N. Butler and A. C. Makrides, *Trans. Faraday Soc.*, **60**, 1664 (1964).
16. D. C. Grahame, *Chem. Rev.*, **41**, 441 (1947).
17. K. Sabo and I. A. Bagotskaya, *Dokl. Akad. Nauk SSSR*, **149**, 139; **150**, 128 (1963).
18. U. V. Pal'm and V. E. Past, *ibid.*, **146**, 1374 (1962).
19. J. N. Butler, M. L. Meehan, and A. C. Makrides, *J. Electroanal. Chem.*, In Press (1965).
20. A. N. Frumkin, "Hydrogen Overvoltage and Adsorption Phenomena, Part II," in Vol. III of "Advances in Electrochemistry and Electrochemical Engineering," p. 287, P. Delahay, Editor, Interscience, New York (1963).
21. R. Parsons, *Trans. Faraday Soc.*, **47**, 1332 (1951).
22. R. Parsons and J. O'M. Bockris, *ibid.*, **47**, 914, (1951).
23. B. Post and C. F. Hiskey, *J. Am. Chem. Soc.*, **72**, 4203 (1950).
24. Z. A. Iofa and K. P. Mikulin, *Zhur. Fiz. Khim.*, **18**, 137 (1944).
25. A. Frumkin, Z. A. Iofa, and V. S. Bagozky, *ibid.*, **25**, 1117 (1951); **26**, 1854 (1952).
26. P. Rüetschi and P. Delahay, *J. Chem. Phys.*, **23**, 195 (1955).
27. B. E. Conway and J. O'M. Bockris, *J. Chem. Phys.*, **26**, 532 (1957).
28. G. Wolf, *Z. Physik. Chem. (Leipzig)*, **223**, 249 (1963).
29. A. J. Rosenberg and M. C. Lavine, *J. Phys. Chem.*, **64**, 1135 (1960).
30. A. J. Rosenberg, *ibid.*, **64**, 1143 (1960).
31. J. F. Dewald, *This Journal*, **104**, 244 (1957).
32. T. I. Popova and N. A. Simonova, *Isv. Akad. Nauk, SSSR, Ser. Khim.*, 1187 (1963).
33. M. Pourbaix, "Atlas d'Equilibres Electrochimiques," p. 439, Gauthier-Villars, Paris, 1963).
34. Note added in proof: Murtazaev and Nikol'skaya [*Dokl. Akad. Nauk Uz. SSR*, **21**, 31 (1964), *Chem. Abstr.*, **61**, 15661 (1964)] have studied hydrogen evolution on indium in KOH, HCl, and H_2SO_4. At 10^{-3} amp/cm^2 in acid, $\eta \cong 0.85$ volts compared to our value of 1.00 volts. This low overvoltage, together with the high Tafel slope (200-250 mv) indicates considerable oxygen in the electrolyte. Hence their current-potential curves do not correspond to hydrogen evolution alone.

Improved Porous Electrode for Studying Electrocatalytic Reactions of Gases and Vapors

G. Bianchi

Laboratory of Electrochemistry and Metallurgy, University of Milan, Milan, Italy

ABSTRACT

An improved porous electrode is described which is a convenient basis for a comparative study of electrocatalytic activity of noble metals and/or for investigations of electrocatalytic processes on gases. The suggested technique makes use of porous graphite disks having a part of their surface covered with a thin layer of catalyst kept in position by means of a thin network of sintered Teflon drops. Such an electrode is to be disposed horizontally with its upper catalyst side kept in the atmosphere of the concerned gas, the remaining part being immerged in the solution. Solution by capillarity moves upward to moisten catalyst. Teflon prevents solution from reaching a too high level which would submerge the catalyst. This way the triple contact electrode-solution-gas is complete and efficient, and both solution level and graphite porosity are not critical factors. Polarization curves and charge-discharge curves have been determined in order to evaluate performances of that porous electrode in various electrochemical systems and processes.

Investigation of electrochemical processes of gas sparingly soluble in aqueous solutions has its chief obstacle in the set up to be deviced to realize the contact electrode-solution-gas. Such a contact may be obtained by means of a porous electrode wet-proofed so that the contact between the gas and the solution is in the pores of the electrode itself. A similar artifice is applied in the fuel cells where porous electrodes with controlled porosity are used. However this method does not give satisfactory results when applied to draw polarization curves or charge-discharge curves or to make analogous determinations.

The structure of the electrode gives origin to concentration polarization in the gas phase and in the solution inside the pores of the electrode itself. Furthermore it is unavoidable to have incorrect determinations of polarization by ohmic losses taking place inside the porous electrode. On top of that must be put the hindrance offered to the construction of electrodes with reproducible properties, when electrodes activated in different ways are to be used, by the fact that the activation must be realized by deposition of the catalyst inside the pores of the electrode.

A different problem is the perfection of an experimental set up valid for studying and evaluating catalysts as Pt-Pd-Rh, etc., blacks involving electrochemical methods. This problem has been recently considered by Grubb and Michalske (1) who proposed a metal screen as a support for the pasted catalyst. The necessity for a method to evaluate the electrocatalytic activity of noble metals has been outlined recently in the case of ethylene anodic oxidation in acid solutions (2). Such a method can be perfected easily and rapidly as the evaluation of the catalysts may be done only by measuring the current at controlled potential for selected reactions of the electrode.

Suggested Technique

The newly suggested technique makes use of the properties of a porous graphite electrode suggested by Elmore and Tanner (3) having a part of its surface covered with a thin layer of an appropriate catalyst kept in position with Teflon. The electrode is disposed horizontally with the part covered with the catalyst kept in an atmosphere of gas and the remaining part immersed in the aqueous solution. The solution moves upward by capillarity through the pores of the electrode and moistens the catalyst layer. The Teflon wetproof layer also helps to prevent solution from reaching a too high level which would completely submerge the catalyst. On the other hand, this porous Teflon layer is very thin (about 0.2 mm) so that the concentration polarization on the gas side is negligible as long as very high current densities are not reached. This way the contact electrode-solution-gas is complete and satisfactory, and solution level is not a critical factor.

The detailed electrode previously described is shown in Fig. 1 together with the polarization cell used and the correct disposition of the Luggin-Haber's capillary to prevent ohmic losses in the polarization measurements (4).

The electrode is prepared in conformity with the following specifications: a disk of porous graphite 4 mm thick and 25 mm in diameter, pierced in the center to settle a Luggin-Haber's capillary, is covered over by a thick paste of the catalyst finely ground in distilled water, a slight depression being applied

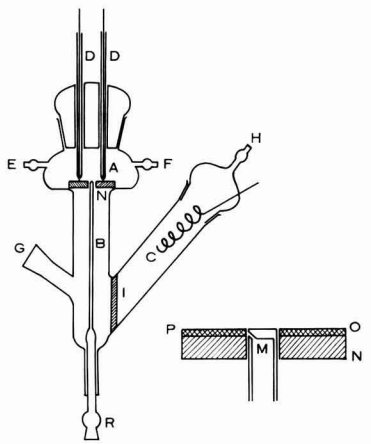

Fig. 1. Complete view of the cell using the porous electrode with capillary imbibition for measures of polarization with detail of the electrode and disposition of the Luggin-Haber's capillary: A, gas chamber; B, solution; C, counterelectrode; D, wires for connection with polarizing circuit and potentiometric circuit; E, inlet of the gas or vapor; F, outlet of the gas or vapor; G, connection with reservoir of solution; H, outlets of gas evolved at counterelectrode; I, sintered glass diaphragm; M, Luggin-Haber capillary with lateral opening positioned in the hole at the center of the electrode; N, porous graphite electrode; P, O, layer of catalyst; R, to reference electrode.

underneath the disk during the process. Both in the case of Pt black and of graphite powder activated with platinum the deposited catalyst amounts to about 5 mg/cm². The disk dried in a muffle furnace at 120°C is sprayed with an aqueous suspension of Teflon (du Pont 30) and afterwards heated *in vacuo* at 300°C for 3 hr to sinter the Teflon. The spraying of Teflon suspension should be done so that the Teflon cover results in a net involving 3 or 4 layers of drops, whose mean diameter is about 50μ. This can be achieved by spraying the Teflon, drying with hot air, spraying the Teflon again, drying, and so on. This wetproof Teflon cover protects the catalyst from mechanical damage and prevents the formation, during operation, of a veil of solution over the activated surface of the electrode without screening the catalyst itself.

If the studied catalyst can be damaged during the heating at 300°C necessary to sinter Teflon, the electrode could be used without the Teflon layer, too. In this case, however, the solution level is critical, and the current which the electrode can now supply is reduced to about 25%.

Such an electrode may be used as a research tool for studying electrochemical processes involving gases and vapors. In the latter case the vapors are flushed round the electrode by a stream of inert gas as disturbing phenomena of concentration polarization in the gas phase are unimportant as in the case of porous wet-proofed electrode.

Results

The performances obtained with this electrode are explained in some of the accompanying figures. Figure 2 shows potentiostatic curves of polarization related to the anodic ionization of hydrogen.

Curves A and B are obtained with two electrodes prepared by using graphite at different porosity but according to the same technique. The results are equivalent and prove that the properties of the porous graphite are not critical for the behavior of the electrode. Curves C and D are obtained with a catalyst different from that used for curves A and B and show the anodic ionization of pure hydrogen (curve C) or of a mixture 50% H_2 and 50% N_2 by volume.

The performance of the electrode does not vary with the time, even after several hours, and proves that the concentration polarization of the gas phase is so low that it cannot be appreciated.

The O_2 cathodic reduction on Pt black in 2.5M H_2SO_4 at 50°C is shown in Fig. 3. Polarization curve A is obtained with an electrode activated by cathodic polarization at + 200 mv (NHS); curve B with an electrode that worked for long time at + 700 mv. The variation of current is immediate when air is substituted for oxygen and *vice-versa* (Fig. 4). This fact, more than the ratio 5:1 between the current verified in the two cases, shows that the concentration polarization on the gas side is so low that no appreciable effect is produced.

Figure 5 illustrates the anodic oxidation of methanol in acid solution at 25°C. Methanol vapors are carried by a nitrogen stream.

Performances of various catalysts (platinum, iridium, rhodium, and ruthenium blacks) in the anodic

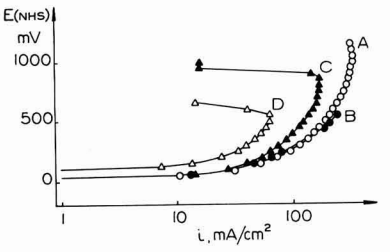

Fig. 2. Potentiostatic polarization curves for the hydrogen anodic ionization in acid solution 0.5M H_2SO_4 at 25°C. A, B, C, pure hydrogen; D, mixture of 50% H_2 and 50% N_2 by volume. For curves A and B the same catalyst is used but the supporting electrode is different: in one case (A) being graphite National S 2368, grade 45, porosity 48%; in the second one (B) being graphite Stackpole Carbon Co. PC 57 H, porosity 68%. For curves C and D the same electrode and the same catalyst is used. The catalyst is different from that used for curves A and B.

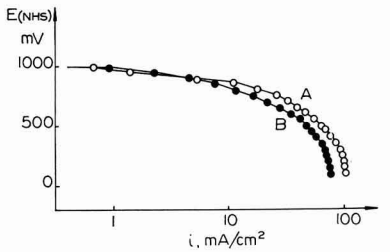

Fig. 3. Cathodic polarization curves for the reduction of O_2 in acid solutions at 50°C: A, electrode cathodically activated at + 200 mv, NHS; B, electrode after functioning for long time at + 700 mv, NHS.

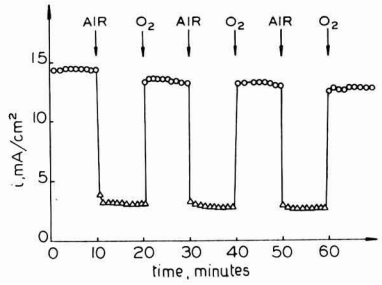

Fig. 4. Current response during cathodic reduction of oxygen at 700 mv, NHS, in acid solutions at 50°C, on alternated substitutions of oxygen for air and *vice versa*.

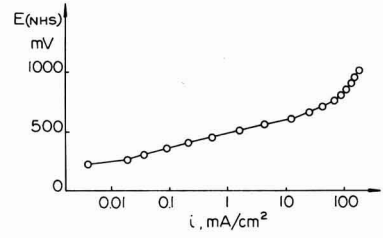

Fig. 5. Polarization curve for the anodic oxidation of methanol vapors carried by a stream of nitrogen in acid solution (0.5M H_2SO_4) at 25°C.

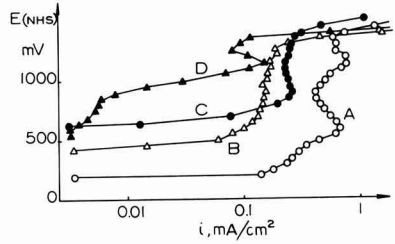

Fig. 6. Polarization curves for the anodic oxidation of propane in acid solution (0.5M H_2SO_4) in the presence of various catalysts at 25°C: A, platinum black (Engelhard); B, iridium black (Johnson and Matthey); C, rhodium black (Engelhard); D, rutenium black (Johnson and Matthey).

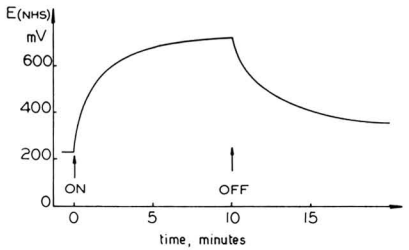

Fig. 7. Anodic charging curves at constant current (i = 0.5 ma/cm^2) and decay curve after anodic polarization for propylene in acid solution (0.5M H_2SO_4) at 25°C; platinum black as catalyst.

oxidation of propane in acid solution at 25°C are compared through the potentiostatic curves in Fig. 6, which confirm that platinum is the best catalyst for propane anodic oxidation (5).

The anodic charging curves related to propylene in acid solution in presence of platinum black are in Fig. 7. The electrodes were activated by anodic formation of platinum oxides followed by cathodic reduction at 200 mv (NHS). It is evident that during the anodic oxidation of propylene, the catalyst undergoes a process of slow poisoning.

Discussion

The results quoted in this paper put into evidence that the capillary imbibition porous electrode can be advantageously used as a research tool for studying the electrochemical processes of gases and vapors. It can furthermore be employed as a support for a hydrogen reference electrode, reliable and simple, with exchange currents as high as 10 ma/cm^2. It is also possible to foresee the utilization of such an electrode in fuel cells and industrial plants.

Acknowledgment

This research was sponsored by Consiglio Nazionale delle Ricerche, Roma.

Manuscript received Feb. 24, 1964.

Any discussion of this paper will appear in a Discussion Section to be published in the December 1965 JOURNAL.

REFERENCES

1. W. T. Grubb and C. J. Michalske, *This Journal*, **111**, 477 (1964).
2. H. Dahms and J. O'M. Bockris, *ibid.*, **111**, 728 (1964).
3. G. V. Elmore and H. A. Tanner, *ibid.*, **108**, 669 (1961).
4. R. Piontelli, G. Bianchi, *et al.*, *Z. Electrochem.*, **56**, 86 (1952); **58**, 54 (1954); **58**, 86 (1954).
5. W. T. Grubb, 16th Annual Power Sources Conf., p. 31 (1962).

Technical Notes

Oxidation by Transport through Blocking Pores

P. L. Harrison

Central Electricity Research Laboratories, Leatherhead, England

Under certain conditions the oxidation of mild steel in aqueous solutions in the temperature range 250°-400°C produces a double layer magnetite film, the inner layer of which is protective (1). In dilute alkaline solutions, the growth of this inner layer becomes extremely slow at a thickness of a few tens of microns, and there is some indication of a limiting thickness of about 50 μm. Under weakly acidic or strongly alkaline conditions (2, 3) the magnetite does not form as a protective layer and corrosion continues at a rapid rate. The mechanism of the corrosion process and the conditions leading to a nonprotective oxide have been the subject of many recent studies (4-6).

Some of this work (4, 5) has shown that the magnetite layer formed is porous. Measurements of the density of laboratory-grown magnetite (4) indicated a porosity of about 10% volume/volume, and electron microscopy of magnetite films 1000-2000Å thick (5) indicated that pores of 100-500Å are present between the particles of magnetite. Porosimetry studies (7) of an exceptionally thick magnetite deposit from part of a power-station boiler were in agreement with these measurements. Such porosity can be reconciled with a protective oxide layer by assuming that the pores gradually become blocked during the course of oxidation. It is known (1) that during oxidation metal ions pass out through the oxide as oxidant passes in. There is a possibility, therefore, of reaction taking place within the pores.

The growth of a porous oxide under conditions such that the pores become blocked during oxidation has been treated by Evans (8). He considers two cases. One case represents self-blocking in which the pores through which the reactants diffuse become blocked by the reaction taking place within them. If w represents the weight of metal oxidized and n represents the number of pores per unit area, then we have $\frac{dw}{dt} = k_1 n$ and $-dn = k_2 dw$ which give the asymptotic equation

$$w = \frac{n_o}{k_2}(1 - e^{-k_1 k_2 t}) \qquad [1]$$

where n_o is the value of n at $t = 0$.

The other case, termed mutual pore blocking by Evans, is one in which the oxide formed within a pore causes a compressive strain in the surrounding oxide, which closes up neighboring pores. The number of pores so blocked is proportional to the density of pores, so that the equations become

$$\frac{dw}{dt} = k_1 n \text{ and } -dn = k_3 n dw$$

These give the direct logarithmic equation

$$w = \frac{1}{k_3}\log_e (k_1 k_3 n_o t + 1) \qquad [2]$$

It is to be noted that, in the case of self-blocking, the weight of metal oxidized cannot exceed an amount represented by $w = n_o/k_2$. No such limit applies in the case of mutual blocking, so that at large values of t the extent and rate of oxidation is greater for the

mutual blocking case than for the self-blocking case. This arises because implicit in the equation $-dn = k_3\, ndw$ is the assumption that the pores responsible for causing blocking of neighboring pores do not themselves become blocked. Evans (9) suggests that the oxide growing within the pore becomes wedged across the pore in such a way that it fills part only of the cross section. As this oxide continues to grow, compressive strains are set up at the points of contact between it and the pore surface. The transmission of these strains through the bulk oxide causes neighboring pores to become blocked even though the intrapore oxide does not completely block the pore in which it is growing. Evans suggests that the effective resistance of this pore to the passage of reactants is unaltered, because, although the cross section is reduced at the site of the intrapore oxide, the strains this oxide imposes cause the cross section of neighboring lengths of the pore to be increased. He suggests that the two effects can be assumed to cancel each other out.

A further case of pore-blocking which is of interest is one in which the intrapore oxide responsible for the blocking of neighboring pores also causes blocking of the pore in which it is forming. This is a combination of the two cases considered by Evans. The relevant equations are

$$\frac{dw}{dt} = k_1 n \text{ and } -dn = k_2\, dw + k_3\, n\, d\, w$$

which give for the relation between extent of oxidation and time, the equation

$$w = \frac{1}{k_3} \log_e \left[1 + \frac{k_3 n_o}{k_2} (1 - e^{-k_1 k_2 t}) \right] \qquad [3]$$

The curves for this case and for the case of self-blocking pores only are given in Fig. 1. In order to aid comparison, the nondimensional quantities

$$W = \frac{wk_2}{n_o},\ T = k_1 k_2 t \text{ and } G = \frac{k_3 n_o}{k_2}$$

have been used.

Equations [1] and [3] then become

$$W = 1 - e^{-T} \qquad [4]$$

and

$$W = \frac{1}{G} \log_e [1 + G\,(1 - e^{-T})] \qquad [5]$$

respectively.

Curves for $G = 0.0$, 0.1, 1.0, and 10.0 are given in Fig. 1. Putting $G = 0$ reduces Eq. [5] to [4] the equation for self-blocking pores.

At small values of T Eq. [5] approximates

$$W = \frac{1}{G} \log_e (1 + G\,T) \qquad [6]$$

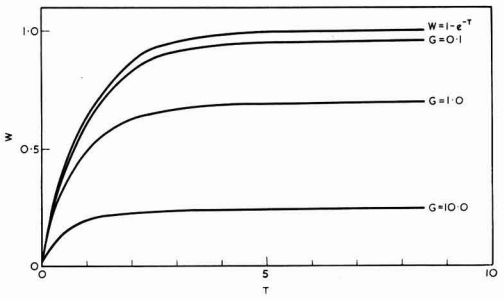

Fig. 1. Oxidation curves for pore blocking mechanism giving protective oxide: ord, W, dimensionless weight gain; abs, T, dimensionless time.

At large values of T, Eq. [5] approximates

$$W = \frac{1}{G} \log_e (1 + G) - \frac{1}{1 + G} e^{-T} \qquad [7]$$

From Eq. [6] and [7] it is seen that Eq. [5] represents a transition from a direct logarithmic growth law to an asymptotic growth law. In the early stages of oxidation when the pore density is relatively high, mutual blocking of pores will have the greatest influence on the growth law giving a direct logarithmic growth law. Measurements on the corrosion of mild steel to magnetite in alkaline solutions have suggested a logarithmic growth law at least in the early stages (4, 10). In the late stages of oxidation, when the pore density is relatively low, mutual blocking of pores will be relatively unimportant and self-blocking will have the greatest influence giving an asymptotic growth law. Such a transition would be consistent with the high degree of protection that magnetite formed during aqueous corrosion is capable of giving.

Under more strongly alkaline or weakly acidic conditions the magnetite formed does not afford protection, and a near linear oxidation rate is observed. There is no reason to assume that pore blocking does not occur under these conditions even though the oxide is nonprotective. However, with the rapid in-filling of pores that can be expected in the more corrosive conditions, the stresses built up within the oxide may become too large to be completely relieved by the blocking of neighboring pores. This excess stress could be relieved by shear strains which would create additional pores or cracks in the neighborhood of the blocked pore. Such a mechanism would introduce a term $-k_4\, dw$ into the expression for $-dn$ so that we have $-dn = (k_2 - k_4)\ dw + k_3 n\ d\ w$. The effect of the production of pores in this way is to reduce the importance of self-blocking of pores in the growth law, that is, to reduce the effective value of k_2. In the particular case of $k_4 = k_2$, the oxide grows wholly according to the direct logarithmic law. If $k_4 > k_2$, then effectively, $k_2 < 0$, and $-W$, $-G$ and $-T > 0$. Equation [5] then becomes

$$(-W) = \frac{1}{(-G)} \log_e [1 + (-G)\ (e^{(-T)} - 1)] \qquad [8]$$

For large $(-T)$ this approximates to the form

$$W = A + BT \qquad [9]$$

representing a linear growth law. This occurs at a time when the pore density approaches a value sufficient to give a balance between the rate of pore blocking and the rate of pore production. Curves of Eq.

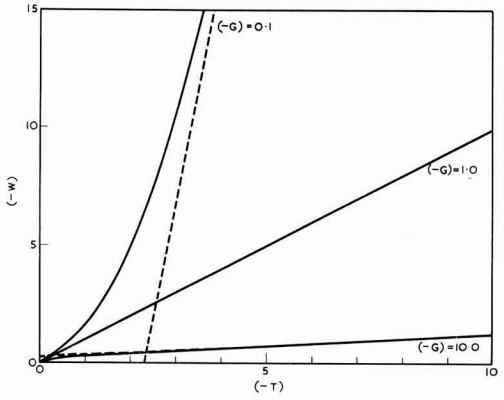

Fig. 2. Oxidation curves for pore blocking mechanism giving nonprotective oxide: ord, $(-W)$ dimensionless weight gain; abs, $(-T)$, dimensionless time.

[8] for values of $(-G)$ of 0.1, 1.0, and 10.0 are given in Fig. 2.

It is seen that a nonprotective oxide is not inconsistent with a pore blocking mechanism. The situation that is most likely to occur is that the stresses produced in the oxide do not become fully relieved in the early stages of oxidation, but slowly increase as the oxide thickens. This would have the effect of slowly increasing the value of k_4, perhaps to a limiting value, as the oxidation proceeded. If this limiting value of k_4 is greater than the value of k_2, the effective value of k_2, positive at the beginning of the oxidation, would eventually become negative. This would give the sequence, with increasing time of logarithmic, asymptotic, accelerating to linear for the oxide growth law, representing a transition from a protective to a nonprotective oxide layer.

Both protective and nonprotective magnetite layers have been produced on mild steel oxidized in aqueous solutions at high temperature. A simple extension of the theory of pore blocking by Evans can explain the appearance of these two oxide forms, and suggests that their appearance may depend on the same basic mechanism.

Acknowledgment

The work described in this note was carried out at the Central Electricity Research Laboratories, Leatherhead, and is published by permission of the Central Electricity Generating Board.

Manuscript received Oct. 2, 1964.

Any discussion of this paper will appear in a Discussion Section to be published in the December 1965 JOURNAL.

REFERENCES

1. E. C. Potter and G. W. W. Mann, "Proc. 1st Int. Congr. Metallic Corrosion," 49, Butterworths, London (1961).
2. E. C. Potter and G. W. W. Mann, *Chem. and Ind.*, 1768 (1963).
3. W. A. Fraser and M. C. Bloom, *Corrosion*, **18**, 163t (1962).
4. A. M. Adams, E. M. Field, D. R. Holmes, and R. C. Stanley, 2nd Int. Congr. Metallic Corrosion, New York, 1963.
5. E. M. Field, Corrosion Science Society Meeting, Cambridge, 1963.
6. M. C. Bloom, M. Krulfeld, and W. A. Fraser, *Corrosion*, **19**, 327t (1963).
7. British Coal Utilisation Research Association, Private communication.
8. U. R. Evans, "The Corrosion and Oxidation of Metals," Edward Arnold, London (1960).
9. U. R. Evans, Private communication.
10. A. J. Panson, Paper presented at the Houston Meeting of the Society, Oct. 9-13, 1960.

Synthesis of GaAs by Vapor Transport Reaction

H. R. Leonhardt

IBM Watson Research Center, Yorktown Heights, New York

Within the last few years vapor growth processes have become a common method to prepare single crystalline GaAs (1-6). In most cases the following reaction is used

$$3\,GaX + \frac{1}{2}\,As_4 \rightarrow 2\,GaAs + GaX_3 \qquad [1]$$

where X = Cl or I. The iodide disproportionation reaction is usually employed in closed tubes because iodine is a solid which makes the loading procedure of the ampoules fairly simple. For most purposes, however, flow systems are more attractive. Therefore, an iodide process suitable for such an open tube apparatus has been developed.

Elemental gallium and arsenic were used as the source materials, H_2-HI being the transporting agent. The hydrogen iodide was prepared *in situ* from hydrogen and iodine to insure sufficiently high purity of the carrier gas (7). There were mainly two reasons for combining synthesis and epitaxial growth of GaAs: (i) Since gallium and arsenic are available in high purity, one can expect that such a system has the potential to produce high-purity GaAs, especially since the low-temperature iodide process is utilized. (ii) Separate sources for the two components permit a wide variation in the composition of the reactive gas.

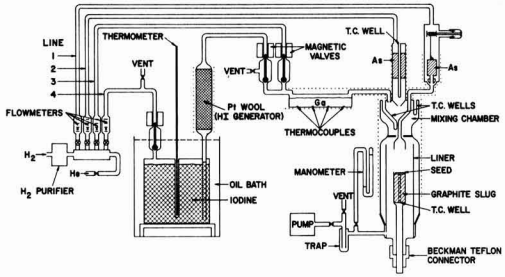

Fig. 1. Flow chart of GaAs vapor growth system

Figure 1 shows the basic features of the apparatus. Purified hydrogen can be fed into the system through four input lines. During the initial heat up period, the GaAs substrate is placed in a bell shaped shelter into which line 1 terminates, and hydrogen containing some arsenic is passed over it. The purpose of the arsenic is to prevent decomposition of the seed. Therefore, its pressure which is controlled by the temperature of the arsenic source in line 1 has to be kept above the dissociation pressure of the seed crystal. Assuming solid-vapor equilibrium for the arsenic, thermodynamic calculations show that the arsenic temperature has to be $\geq$ 190°C for a substrate preheating temperature of 750°C which was generally used. Data for the calculations were taken from the literature (8-10). For the actual decomposition process, lines No. 2 and 4 are used. The arsenic in line 2 is transported in elemental form. In 4, iodine is evaporated and converted to hydrogen iodide which reacts subsequently with gallium to form gallium iodides. The arsenic and gallium source are heated by multizone furnaces which provide a constant temperature over the entire length of the two zones. The gas streams from lines 2 and 4 are mixed in a chamber which is kept sufficiently hot so that no GaAs can form in it, the appropriate temperature being determined by calculations which will be described in the next section. In the deposition chamber the gases are cooled down so that GaAs precipitates.

Such a two-line system brings some complications with it since the conditions in the different zones have to be adjusted to each other. The best theoretical approach to this problem possible at the present time is a thermodynamic analysis which has been made with the following assumptions: (A) Thermodynamic

equilibrium is achieved in each part of the system. (B) All important vapor phase species are known. (C) The partial pressures of the various species follow the ideal gas law. (D) The total pressure p_t equals 1 atm throughout the entire system. (E) All solids and liquids are pure phases. (F) The conditions are chosen so that the gas streams from line 2 and 4 in Fig. 1 yield a mixture in the mixing chamber which is in equilibrium with solid GaAs.

The first assumption has been checked for the three most critical zones: the iodine, the gallium, and the arsenic source. Studies on the evaporation rate of iodine by Reisman, Berkenblit, and Alyanakyan (11), and on the rate for the Hi-Ga reaction by Silvestri (12) have been used to demonstrate the validity of the assumption for the iodine and the gallium source. For the arsenic source kinetic calculations were made based on data given by Brewer and Kane (13). Under all conditions the relaxation time of the solid-vapor equilibrium for the arsenic was found to be orders of magnitude shorter than the residence time of the transporting hydrogen gas in the source chamber, which means that also at the arsenic source equilibrium obtained. In order to check the assumption on the total pressure, p_t has been measured at the input side of the system. It was found to be only a few Torr above atmospheric pressure, *i.e.*, $p_t = 1$ atm is a good approximation.

Table I. Vapor phase species in the system

Abbreviations: A, arsenic source; G, gallium source; D, deposition chamber; M, mixing chamber; I, iodine source; p_t, total pressure; f_n, flow rate in line n, c, $\left(\frac{\text{gallium content}}{\text{arsenic content}}\right)_M$

Zone	Vapor phase species
A	As_2, As_4, H_2
I	I_2, H_2
G	GaI, GaI_3, HI, I_2, I, H_2
M, D	GaI, GaI_3, HI, I_2, I, H_2, As_2, As_4

It can be readily demonstrated that the system is defined thermodynamically by specifying the following experimental parameters: 1, the ratio of the flow rates; 2, the temperature T_A of the arsenic source; 3, the temperature T_M and the ratio c between the gallium and arsenic content of the vapor phase of the mixing chamber; and 4, the temperature T_D in the deposition chamber. These specifications and a series of independent equilibria provide a sufficient number of equations, shown in Table II, to calculate the partial pressures of the various vapor phase species (Table I) and the appropriate temperatures at the iodine and the gallium source.

From the partial pressures in the mixing and deposition chamber one can determine the gallium to

Table II.

Zone	Equation or equilibrium[a, b]		Reference
A	$4As(s) \rightleftarrows As_4$	$\log K_1 = -\frac{6{,}777}{T} + 7.678$	(9)
A, M, D	$As_4 \rightleftarrows 2As_2$	$\log K_2 = -\frac{13{,}029}{T} + 7.981$	(10)
M, D, G	$GaI_3 \rightleftarrows GaI + I_2$	$\log K_3 = -\frac{10{,}250}{T} + 6.71 \log T - 14.2$	(8, 14, 15)
M, D	$GaI_3 + 2GaAs(s) \rightleftarrows 3GaI + \frac{1}{2}As_4$	$\log K_4 = -\frac{23{,}650}{T} + 19.4$	(8)
M, D, G	$2HI \rightleftarrows H_2 + I_2$	$\log K_5 = -\frac{622.4}{T} - 0.834$	(16)
M, D, G	$I_2 \rightleftarrows 2I$	$\log K_6 = -\frac{7{,}991}{T} + 5.481$	(17)
I	$I_2(s) \rightleftarrows I_2$	$\log K_7 = -\frac{3{,}513}{T} - 2.013 \log T + 13.374$	(18)
G	$2Ga(l) + GaI_3 \rightleftarrows 3GaI$	$\log K_8 = -\frac{11{,}000}{T} + 12.4$	(8)
A, M, D, G, I	Total pressure condition: $\Sigma p_i = p_t = 1$ atm **all species**	(p_i = partial pressure of species i)	
M	Conservation of arsenic and hydrogen:	$\left(\frac{4p_{As_4} + 2p_{As_2}}{2p_{H_2}}\right)_A = \left(\frac{4p_{As_4} + 2p_{As_2}}{2p_{H_2} + p_{HI}}\right)_M \frac{f_2 + f_4}{f_2}$	
M	Specification of gallium to arsenic ratio in M:	$c = \frac{p_{GaI} + p_{GaI_3}}{4p_{As_4} + p_{As_2}}$	
I	Conservation of hydrogen and iodine:	$\left(\frac{p_{GaI} + 3p_{GaI_3} + 2p_{I_2} + p_I + p_{HI}}{2p_{H_2} + p_{HI}}\right)_M = \left(\frac{p_{I_2}}{p_{H_2}}\right)_I \frac{f_4}{f_2 + f_4}$	
G		$= \left(\frac{p_{GaI} + 3p_{GaI_3} + 2p_{I_2} + p_I + p_{HI}}{2p_{H_2} + p_{HI}}\right)_G \frac{f_4}{f_2 + f_4}$	
D		$= \left(\frac{p_{GaI} + 3p_{GaI_3} + 2p_{I_2} + p_I + p_{HI}}{2p_{H_2} + p_{HI}}\right)_D \frac{f_1 + f_2 + f_4}{f_2 + f_4}$	
G	Conservation of gallium and iodine:	$\left(\frac{p_{GaI} + p_{GaI_3}}{p_{GaI} + 3p_{GaI_3} + 2p_{I_2} + p_I + p_{HI}}\right)_M = \left(\frac{p_{GaI} + p_{GaI_3}}{p_{GaI} + 3p_{GaI_3} + 2p_{I_2} + p_I + p_{HI}}\right)_G$	
D	Stoichiometry of gallium arsenide:	$\left(\frac{(p_{GaI} + p_{GaI_3}) - (4p_{As_4} + 2p_{As_2})}{2p_{H_2} + p_{HI}}\right)_M = \left(\frac{(p_{GaI} + p_{GaI_3}) - (4p_{As_4} + 2p_{As_2})}{2p_{H_2} + p_{HI}}\right)_D$	

[a] Pressure unit: 1 atm
[b] (s) = solid
(l) = liquid
unindicated = vapor species

iodine ratio y_M and y_D in the two zones. The difference Δy between these quantities is the amount of gallium which should precipitate as GaAs according to thermodynamics in the deposition chamber per equivalent of iodine:

$$\Delta y = y_M - y_D$$

$$= \left(\frac{p_{GaI} + p_{GaI3}}{p_{GaI} + 3p_{GaI3} + 2p_{I2} + p_I + p_{HI}} \right)_M - \left(\frac{p_{GaI} + p_{GaI3}}{p_{GaI} + 3p_{GaI3} + 2p_{I2} + p_I + p_{HI}} \right)_D$$

Δy represents the maximum value for the experimental growth rate which one can expect in the system for a given set of conditions.

A large number of cases with different values for the parameters was calculated on an IBM 7090 computer. For practical use, a few were selected on the basis of high Δy values and reasonable temperatures for the gallium and iodine source.

Epitaxial GaAs has been grown successfully in this open tube iodide system using gallium[1] of 99.9999% and arsenic[2] of 99.999% purity. The substrate surfaces were prepared by means of a chemical polishing technique which has been developed recently by Reisman *et al.* (19).

Some of the results are shown in Table III and Fig. 2. Under the conditions indicated in Table III the effective deposition rates (*i.e.*, only the growth on the seed crystal is taken into account) were appreciably smaller than the calculated values. This is at least partly due to the fact that GaAs precipitated not only on the substrate but also on the walls of the reaction tube and on the seed holder.

Figure 2 shows the effect of deposition temperature on the surface perfection. Deposits grown at 620°C on substrates oriented in the <111> A direction (which is the gallium terminated side) developed many pyramids within a short time (Fig. 2a), and as the growth continued a few big pyramids took over (Fig. 2b). Better results in terms of surface smoothness were obtained at higher deposition temperatures (Fig. 2c). Above 650°C, however, the deposition rate started to decrease appreciably. The rates between 620° and 650°C were in the order of 20 μ/hr. Runs were also made with substrates oriented in the <111> B and the <100> direction. In agreement with results reported for the closed tube iodine process (1) only polycrystalline growth could be obtained on <111> B substrates. Deposits grown in the <100> direction were epitaxial, but the surfaces showed a very dense pattern of pyramids.

The electrical properties of the vapor grown material summarized in Table III were determined from

[1] Alcoa Chemicals.

[2] Cominco Products, Inc.

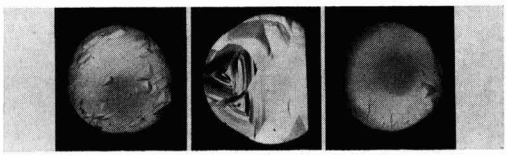

Fig. 2. Deposits grown for different lengths of time t and at different deposition temperatures T: (left) t_a = 45 min, T_a = 620°C; (center) t_b = 4 hr 30 min, T_b = 620°C; (right) t_c = 45 min, T_c = 650°C.

Hall and resistivity measurements. All deposits were n-type. The results were obtained from samples which had been grown thick enough so that the original substrate could be removed. Two series of experiments were made under different conditions. Between the first and the second one the arsenic source had to be replenished. Aside from that the various source materials were not changed between runs. In Table III the runs are listed in chronological order. The increase in mobility and the decrease of the carrier concentration in the course of the first series shows that the system became cleaner from run to run. The abrupt deterioration of the vapor grown material after the arsenic source had been reloaded indicates that a substantial fraction of the impurities came either from the arsenic or was introduced during the loading procedure (*e.g.*, the system might have become contaminated with silicon when the arsenic container was sealed).

In the two series of runs the deposits were grown under different arsenic pressures. Theoretically one would expect that with increasing arsenic pressure the concentration of free electrons in the grown GaAs would decrease and the hole concentration increase due to a decrease in arsenic and an increase in gallium vacancies.[3] However, this effect was apparently much smaller than the effect of contaminants on the electrical properties so that it could not be observed.

In Table III the best values for the mobilities are appreciably higher than what has been found normally in vapor grown GaAs (22). Together with their strong temperature dependence this might be an indication that the material was not severely compensated.

Acknowledgments

The author would like to thank Mr. J. V. Lyons for participating in the initial part of this work, Dr. A. Reisman for helpful discussions, and Mr. E. Baran for his assistance in the experimental work. He also wants to acknowledge the support which he received from Miss A. Kuhlke and Dr. R. Kelisky by making the computer calculations, from Dr. S. E. Blum by supplying the GaAs substrates, and from Dr. J. F. Woods and Mr. S. Baliozian by making the electrical measurements.

[3] This has been observed in a number of II-VI compounds (20, 21).

Table III. Deposition rates and electrical properties of vapor grown GaAs

Growth conditions	Calculated growth rate, mg/hr	Experimental growth rate, mg/hr	Exp. growth rate / Calc. growth rate, %	Carrier conc. [10^{16} cm^{-3}] Room temp.	Carrier conc. [10^{16} cm^{-3}] 77°K	Mobility [cm^2/v sec] Room temp.	Mobility [cm^2/v sec] 77°K
T_{As} = 407°C T_I = 76°C T_{Ga} = 434°C T_{mix} = 800°C T_{dep} = 620°C $f_{As} = f_{Ga}$ = 50 cm^3/min Substrate orientation: <111>A Growth time: 11 hr	232 232 232 232 232	10 15.7 13.8 13.1 14.0	4.3 6.8 6.0 5.6 6.0	2.6 2.9 2.3 1.5 1.4	1.9 1.6 1.6 1.1 1.0	5,370 5,680 5,800 6,150 6,530	9,680 12,670 11,870 14,600 16,170
T_{As} = 487°C T_I = 82°C T_{Ga} = 410°C T_{mix} = 800°C T_{dep} = 620°C $f_{As} = f_{Ga}$ = 50 cm^3/min Substrate orientation: <111>A Growth time: 10 hr	276 276	17.3 18.0	6.3 6.5	2.1 0.7	1.5 0.5	5,710 5,850	8,050 9,870

Manuscript received Aug. 18, 1964. This paper was presented at the Toronto Meeting, May 3-7, 1964.

Any discussion of this paper will appear in a Discussion Section to be published in the December 1965 JOURNAL.

REFERENCES

1. V. J. Lyons and V. J. Silvestri, *This Journal*, **108**, 177C (1961).
2. A. Hagenlocher, *ibid.*, **108**, 213C (1961).
3. R. L. Newman and N. Goldsmith, *ibid.*, **108**, 213C (1961).
4. F. V. Williams and R. A. Ruehrwein, *ibid.*, **108**, 177C (1961).
5. R. R. Moest and B. R. Shupp, *ibid.*, **109**, 1061 (1962).
6. C. J. Frosch and C. D. Thurmond, *ibid.*, **109**, 301C (1962).
7. A. Reisman and M. Berkenblit, *ibid.*, **111**, 60C (1964).
8. V. J. Silvestri and V. J. Lyons, *ibid.*, **109**, 963 (1962).
9. Landolt-Börnstein, "Zahlenwerte und Funktionen," Vol. II, 2a, Springer Verlag, Berlin (1960).
10. D. R. Stull and G. C. Sinke, "Thermodynamic Properties of the Elements," Advances in Chemistry Series, No. 8 (1956).
11. A. Reisman, M. Berkenblit, and A. Alyanakyan, *This Journal*, **110**, 186C (1963).
12. V. Silvestri, Paper presented at the Washington Meeting of the Society, Oct. 11-15, 1964.
13. L. Brewer and J. S. Kane, *J. Phys. Chem.*, **59**, 105 (1955).
14. L. L. Quill, "The Chemistry and Metallurgy of Miscellaneous Materials, Thermodynamics," University Microfilms Inc., Ann Arbor, Mich.
15. W. Fischer and O. Jubermann, *Z. anorg. u Allgem. Chem.*, **227**, 227 (1936).
16. G. M. Murphy, *J. Chem. Phys.*, **4**, 344 (1936).
17. "Selected Values of Chem. Thermodyn. Prop.," Circ 500 Ser. III, Nat. Bureau of Standards (1961).
18. L. J. Gillespie and L. H. D. Fraser, *J. Am. Chem. Soc.*, **58**, 2260 (1963).
19. A. Reisman and R. L. Rohr, *This Journal*, **111**, 1425 (1964).
20. R. F. Brebrick, *J. Phys. Chem. Solids*, **24**, 27 (1963).
21. J. Bloem, *Philips Research Repts.*, **11**, 273 (1956).
22. F. V. Williams, *This Journal*, **111**, 886 (1964).

A Chemical Polish for Lead Telluride

M. R. Lorenz

IBM Watson Research Center, Yorktown Heights, New York

The preparation of PbTe surfaces free of damage has been investigated by several workers using various techniques. The results of these studies have recently been tested and summarized (1). Briefly there exists a satisfactory electrochemical polish (2). A chemical polish (3) which can produce film (1) and damage free flat surfaces (3) is also known. Although the reported chemical polish may be ideal for flat surface preparation, it has the disadvantage of requiring a mounted sample. The purpose of this communication is to describe a new and simple chemical polish for PbTe which does not have any limitation with regard to geometry. The polished surfaces are indistinguishable from those obtained by use of the electrochemical polish (2).

Test samples consisted of both single and polycrystalline wafers as well as irregular shaped PbTe crystals. The polishing solution was composed of saturated aqueous $K_2Cr_2O_7$ and concentrated nitric acid. The volume ratio of the two components is fairly limited and is between 4.2 and 5.0 with the optimum at about 4.5. A typical polishing solution would consist of 40 cc saturated $K_2Cr_2O_7$ solution and 9 cc concentrated HNO_3. For large crystal charges or dissolution of thick layers the solution volume would of course require a corresponding increase to avoid rapid dilution of the polish strength. The PbTe samples were placed in a Pyrex basket which was fused to a Pyrex rod. By rotating the basket while suspending it in the solution, at room temperature, the test samples were subjected to a good polishing action. Similarly good action was achieved by placing samples directly into a solution beaker and stirring the solution vigorously with a magnetic stirrer. When surfaces appeared satisfactory the samples were well rinsed in H_2O and dried. The rate of material removed for the above conditions was measured on a number of samples for various periods of time. The results show a dissolution rate which varied between 20 and 40 μ/min. Temperature control during polishing appears not extremely critical. However, tests at 45°C indicate a dissolution rate nearly double that at 25°C without any appreciable change in the surface finish.

Sometimes a smooth polished crystal may have a barely perceptible golden colored film on the surface. The occasional appearance of the film is not understood but is no cause for concern since it can be readily removed. Film covered samples were placed in 50% NaOH solution. The solution was heated to 100°-120°C and then left to cool back to room temperature. The samples were rinsed in dilute HCl solution and then thoroughly rinsed in distilled water and dried. The above treatment removed any visible surface film but does not lead to cracking of samples due to thermal shock as had been noted earlier (3, 1).

The procedure described here is simple and quick. It suffers no restriction with regard to geometry. However, as any chemical polish it requires slight variations on the part of the experimentalist to achieve the desired results.

The application of the PbTe polishing solution to GeTe, SnTe, and SnSe was attempted with little success. Variations of the $K_2Cr_2O_7$ to HNO_3 ratio did not lead to any improvement. A mixture of 20 parts of saturated $K_2Cr_2O_7$, 11 parts of HCl, and 1 part of HNO_3 gave visibly smooth shiny surfaces on SnTe. After a few minutes, the shiny surfaces showed slight discoloration which was easily removable by dipping into 20% NaOH solution. Microscopic investigation, however, indicated that the SnTe surfaces were in general ripply and pitted. Similar surfaces could be obtained on GeTe when a mixture of 20 parts of saturated $K_2Cr_2O_7$ and 1 part of HNO_3 was used.

Acknowledgment

The author wishes to thank Mr. L. Buszko for his diligent assistance in this work.

Manuscript received Sept. 3, 1964.

Any discussion of this paper will appear in a Discussion Section to be published in the December 1965 JOURNAL.

REFERENCES

1. M. K. Norr, "Polishes and Etches for Tin Telluride, Lead Sulfide, Lead Selenide and Lead Telluride," NOLTR 63-156, U.S. Naval Ordnance Laboratory, White Oak, Maryland (1963).
2. M. K. Norr, *This Journal*, **109**, 433 (1962).
3. P. H. Schmidt, *ibid.*, **109**, 879 (1962).

Transpiration Studies of the Ge-I_2-Inert Gas System

A. Reisman, M. Berkenblit, and S. A. Alyanakyan

IBM Watson Research Center, Yorktown Heights, New York

Recently, the results of thermodynamic analyses of the Ge-I_2 solid-vapor system in the presence of inert and/or reactive gases at constant total pressure were presented (1, 2). The data derived from these analyses were intended as guides in designing and operating an open tube disproportionation system for growing Ge single crystals epitaxially via reaction [1]

$$GeI_4 + Ge \rightleftarrows 2GeI_2 \qquad [1]$$

Use of the data in an experimental system, however, depends on the degree of equilibrium that is achieved in equilibrating a carrier gas with solid phases at certain critical points in the open tube flow train. In the Ge-He-I_2 system these points are; the halogen source, the germanium source, and the deposition region.

The present report describes studies of transpiration phenomena in the above system. In essence these studies involved determining the flow conditions at different temperatures which were necessary for a He stream to equilibrate physically with an iodine source, and for an I_2-He mixture to equilibrate chemically and physically with a Ge bed. Because of the results obtained, it will be seen that there are interesting aspects in the flow rate ranges in which the I_2-He gas is not in equilibrium with the Ge. Studies of the deposition region have not been conducted pending the construction of a complete vapor transport train.

Experimental Procedure

Figure 1 is a schematic representation of the iodine bed employed. The design of this bed enables passing of the incoming gas stream through either the iodine source or a bypass. Both the source and bypass chambers contain glass beads to increase the heat capacity of the bed to offset cooling effects due to gas flow and evaporation. Figure 2 is a schematic representation of the train used in the experimental evaluation of the iodine bed efficiency. The He carrier gas was purified in a John Mickel Associates purifier, which in turn is followed by a flow meter, the iodine source, thiosulfate absorption traps, and a wet test meter. Without prepurification of the carrier gas, the thiosulfate solutions, maintained at a starting *p*H of 7, invariably decomposed with the liberation of sulfur due to the presence of CO_2 as an impurity in the He.

All experiments were conducted on as-received semiconductor grade iodine. Before using this material, the packed bed was flushed for several hours with the carrier gas.

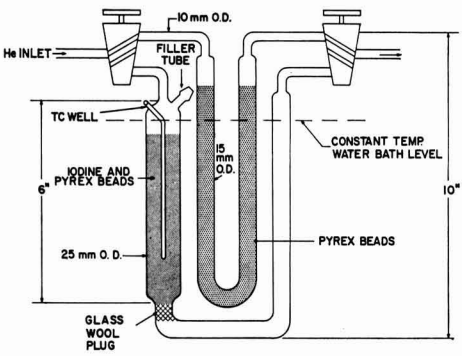

Fig. 1. Iodine source bed design

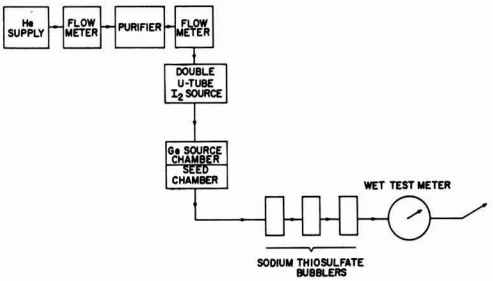

Fig. 2. Schematic representation of I_2 transpiration train

Since no convenient method analogous to that employed for the iodine analysis suggested itself for the Ge system, it was decided to determine the Ge quantity removed from the source bed by a weight loss method. Figure 3 shows the experimental arrangement used to obtain data at 400°, 450°, and 620°C. The design employed facilitates disassembly of the reaction train to enable weighing the Ge bed.

Results and Discussion

Iodine transpiration studies.—Although the equilibrium flow rate range can be evaluated by plotting iodine gas phase concentration *vs.* flow rate for each of the iodine source temperatures investigated, values of the halogen source vapor pressure were also computed. Comparison of these values with those in the literature insure against the possibility of a systematic error in our method of evaluating iodine gas phase concentration leading to incorrect absolute values. These values are important in comparing the Ge-I_2 reaction data with the thermodynamic results mentioned previously. Two series of transpiration experiments were conducted, one with an iodine source at 50.5°C, the other with the iodine source at 61.8°C. At all flow rates up to approximately 0.9 l/min, the systems appeared to be in equilibrium.[1] The calculated vapor pressures for the two temperatures were 2.14 ± 0.06 mm and 4.79 ± 0.07 mm, respectively. Comparison of these approximate values with those of Baxter and Grosse (3) who used a more sophisticated transpiration technique indicates that no major systematic errors

[1] Vapor pressures were calculated with the aid of the equation below. Assuming ideal gas behavior and a constant value of atmospheric pressure (1 atm), the partial pressure of iodine in atm is given by

$$p_{I_2} = n_{I_2}/[n_{I_2} + \frac{V}{RT_M}(1 - p_{H_2O})]$$

where n_{I_2} is the number of moles of iodine, determined by titration of the thiosulfate solutions, that are carried in the volume V measured at a wet test meter whose temperature is T_M and where p_{H_2O} is the vapor pressure of water at T_M.

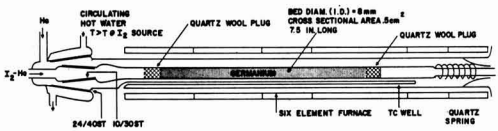

Fig. 3. Germanium source bed design used to study I_2-Ge-He system.

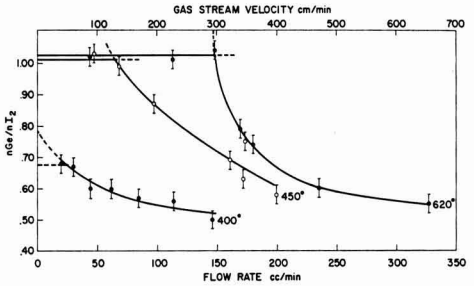

Fig. 4. Transpiration data for the Ge-I_2-He system

were involved in the iodine analysis. The values obtained by them were 2.24 and 4.83 mm, respectively.

Ge-I_2 *transpiration studies.*—On the basis of the thermodynamic analyses (1, 2) in the temperature interval 350°-650°C, the value of the vapor phase component mole ratio Ge/I_2 as a function of temperature is limited at the lower temperature by a value of 0.5 coinciding with the semiconductor-halogen species stoichiometry GeI_4. At the higher temperature, the limiting value of this ratio is 1.0 coinciding with the semiconductor-halogen species stoichiometry GeI_2. Consequently, it was expected that for the three temperatures studied, 400°, 450°, and 620°C, the flow rates at which solid-gas phase equilibrium are attained would lead to values of the Ge/I_2 ratio within the limits defined by the thermodynamic analyses. Again, as with the studies involving iodine equilibrium, the equilibrium flow rate region for Ge can be evaluated by plotting Ge vapor phase concentration *vs.* flow rate. As a check to insure against some systematic error leading to incorrect absolute Ge transport values, the I_2 and Ge transpiration data were used to calculate Ge/I_2 component mole ratios in both the equilibrium and nonequilibrium flow rate regions.

In measurements of the type under consideration linear gas stream velocities are more significant than gas flow rates since the latter are independent of equipment geometry. As no simple means of establishing the linear gas stream velocities in the packed Ge bed could be evolved, a reference velocity scale based on the hypothetical velocities that would have obtained in an unpacked bed of the dimensions shown in Fig. 3 was calculated for the flow rates employed. This velocity scale is meant only to provide some feeling for the gas residency time in the Ge bed. The arbitrary Ge particle size distribution used in this investigation was 52.2% retained on No. 8 U.S. Standard Sieve Series, 18.2% retained on No. 12, 16.3% retained on No. 20, 8.6% retained on No. 40, 2.7% retained on No. 60, and 2.0% passing hrough No. 60. Repeated bed packing of newly crushed, sieved, and "white etched" Ge provided reasonably reproducible data. It is to be noted that the use of any other arbitrary particle size distribution would merely have shifted the flow rate at which the gas effluent from the Ge bed became saturated, but would not have altered the equilibrium Ge/I_2 ratio obtained at a given temperature.

Figure 4 presents the Ge/I_2 mole ratios derived from both the iodine and Ge measurements as a function of flow rate (also in terms of the hypothetical linear gas stream velocity mentioned above).

The significant features of this figure may be summarized as follows:

1. At 400°C, it could not be established whether equilibrium was achieved at the lowest measurable flow rate. The smooth curve can be extrapolated to zero flow in two ways, one assuming that equilibrium has been achieved at finite flows, the other assuming equilibrium is achieved only at zero flow. In the latter instance, the zero flow intersection provides an equilibrium Ge/I_2 ratio in reasonable agreement with that predicted thermodynamically, *i.e.,* 0.78 and 0.83, respectively.

2. At higher temperatures, equilibrium appears to have been achieved within the limits of experimental uncertainty, the equilibrium flow rate range increasing with increasing temperature. Thus at 450°C, a theoretical value of 0.95 is predicted and 1.01 ± 0.04 is obtained experimentally. At 620°C, a theoretical value of 0.99 is predicted and 1.03 ± 0.03 is obtained experimentally.

3. Most significant, however, are the implications concerning the reaction mechanism between Ge and I_2 that may be drawn from the data in the nonequilibrium regions of the three curves. In each instance it is observed that with increasing flow rate the curves tend toward a limiting value of 0.5. This implies that the reaction of Ge with iodine proceeds via the two step mechanism

$$Ge_{(s)} + 2I_{2(v)} \rightleftarrows GeI_{4(v)} \qquad [2]$$

$$GeI_{4(v)} + Ge_{(s)} \rightleftarrows 2GeI_{2(v)} \qquad [3]$$

The first of these reactions appears to be rapid since even at the fast flow rates we have never observed free iodine passing through the Ge source bed (the asymptotic approach of the curves to a value of 0.5 supports this visual observation). The second reaction is markedly slower than the first. As the latter is the desired one in this vapor transport reaction, it represents a serious experimental limitation in the design of an efficient, reproducible germanium-iodine disproportionation open tube scheme. Thus, if one operates within the nonequilibrium linear gas stream velocity range, the tendency to form GeI_4 increases with increasing flow rate, resulting ultimately in a readily achievable worst case of zero transport efficiency (4).

Manuscript received April 9, 1964; revised manuscript received Nov. 2, 1964. This work was supported in part by AFCRL Contract No. AF 19(628)-2648. The paper was presented in part at the New York Meeting of the Society, Sept. 29-Oct. 3, 1963.

Any discussion of this paper will appear in a Discussion Section to be published in the December 1965 JOURNAL.

REFERENCES

1. A. Reisman and S. A. Alyanakyan, Paper presented at the New York Meeting of the Society, Sept. 29-Oct. 3, 1963.
2. A. Reisman and S. A. Alyanakyan, *This Journal,* **111**, 1154 (1964).
3. G. P. Baxter and M. R. Grosse, *J. Am. Chem. Soc.,* **37**, 1061 (1915).
4. Recently, P. Balk of this laboratory in studies of the Ge-Cl_2, Ge-I_2, and Ge-Br_2 interactions by other techniques has concluded that a two-step mechanism is involved in the Ge-Br_2 case and very probably also involved in the other two systems. See Proc. of the Int. Conf. of the Phys. and Chem. of Solid Surfaces, June 21-26, 1964, Brown University.

Brief Communications

An A-C Conductive Adhesive for Testing Electroluminescent Devices

Alexander Baczewski

General Telephone & Electronics Laboratories, Inc., Bayside, New York

This communication deals with the compounding of an inexpensive material which allows temporary adhesion of the conductor to an electroluminescent device.

Many electroluminescent devices consist of a conductive transparent material, an electroluminescent layer and an aluminum back electrode prepared by high-vacuum evaporation. It is very difficult to repair pinholes and small blemishes in the electroluminescent layer once the aluminum back electrode has been applied. A temporary electrode that would make it possible to find such defects before the aluminizing step would allow the preparation of defect-free devices. Such an electrode must provide good electrical contact to the sometimes very rough electroluminescent layer, and it should be easy to apply and remove. Although water dispersions of graphite can be used for this purpose, the water is deleterious for most devices and may magnify or even cause defects. In addition, the black color of the conductor will detract from the brightness of a device. Alloys of mercury, indium, and thallium can be used for this purpose since they have very low melting points and wet almost any surface; these alloys, however, are extremely toxic and quite expensive (1).

It is well known that the reaction products of boric acid and aliphatic polyhydroxy compounds and their ammonium salts are good conductors of electricity (2). Some of these compounds dissolve in ethylene glycol; such solutions are also good conductors and are colorless, water-free liquids. They have been used formerly in the manufacture of capacitors (3). A solid polyhydric alcohol increases the viscosity without decreasing the conductivity; hence, it is possible to mix ethylene glycol, mannitol, boric acid, and ammonia in such a way that a very viscous, clear mass results which may be used as an adhesive; the amounts are not critical. Table I gives a few examples.

Table I. Polyol-ammonia-boric acid combinations

Constituent	% by weight			
Ethylene glycol	44	44	44	23
Mannitol	7	7	28	28
Boric acid	35	28	21	42
Ammonia	14	21	7	7

The solutions were prepared in the following manner. Various amounts of ethylene glycol, mannitol, and boric acid were mixed and aqueous ammonia was added while the temperature was slowly raised to 125°C with vigorous stirring. The temperature was maintained at 125°C for 5 min and then at 100°C for 2 hr without stirring. The resulting adhesive was kept in a desiccator.

One of these compounds was spread on paperbacked aluminum foil and the coated foil pressed onto a non-aluminized electroluminescent lamp. When the lamp voltage was increased slowly, thin spots lit up, and pinholes could be found before shorting occurred. The foil was removed and the adhesive was washed off with methanol. After elimination of the defects, and subsequent application of the evaporated electrode, the lamp brightness was equivalent to that of defect-free lamps that had not undergone this treatment.

Acknowledgment

Most of the experimental work was performed by V. Quistorff.

REFERENCES

1. V. J. King, *Rev. Sci. Instr.*, **32**, 1407 (1961).
2. T. Moeller, "Inorganic Chemistry," p. 763, John Wiley & Sons, New York (1957).
3. Standard Handbook for Electrical Engineers, p. 5-27, McGraw Hill Book Co., Inc., New York (1949).

The Formation of $FeSn_2$ during the Electrodeposition of Tin on Iron

W. Roger Buck, III, and Henry Leidheiser, Jr.

Virginia Institute for Scientific Research, Richmond, Virginia

The resistance to corrosion of commercial tinplate in some environments appears to be related to the characteristics of the iron-tin alloy $FeSn_2$ which is formed at the interface between the two metals during heat-treatment following the electrodeposition step (1). The purpose of this communication is to point out that fine-grained $FeSn_2$ is formed during electrolysis of iron in an alkaline bath but is not formed during electrolysis in an acid bath. This experimental result may have important consequences in focusing attention on a variable which appears to be subject to control.

Tin was electroplated on ⅜ in. iron cylinders (both Ferrovac-E and type-L steel) with a hemispherical end from the following two baths: acid bath: $SnSO_4$ 100 g/l, H_2SO_4 30 g/l, tartaric acid 30 g/l; alkaline bath: $Na_2SnO_3 \cdot 3H_2O$ 90 g/l, NaOH 7.5 g/l, NaOAc 15 g/l, 30% H_2O_2 0.5 ml/l. Both baths were operated

at 70°. The majority of the experiments were carried out at a current density of 3 amp/dm^2 and a plating time of 30 sec. These conditions are equivalent to an average deposit thickness of approximately 6000Å in the acid bath assuming 100% current efficiency, and to an average deposit thickness of approximately 2300Å in the alkaline bath assuming deposition from the Sn(IV) state and a current efficiency of 75%. The iron samples were polished in a commercial chemical polishing reagent, MirroFe, and were abraded with levigated alumina immediately before plating. The grain size of the deposit from the acid bath was of the order of 10^{-2} mm in diameter and of the order of 10^{-4} mm in diameter in the alkaline bath as indicated by x-ray diffraction analysis. Grain-size modifiers were not added to the acid bath as is the commercial practice.

The deposits were examined by x-ray diffraction using unfiltered iron radiation and grazing incidence on the hemispherical surface. This technique is remarkably sensitive to small amounts of crystalline material when the strong diffraction line occurs at planar spacings above 2.5Å. The diffraction line of iron at 2.03Å and the diffraction lines of tin at 2.92 and 2.79Å were clearly visible in all experiments. The strongest diffraction line of $FeSn_2$ at 2.56Å was used to determine its presence.

A faint line due to $FeSn_2$ was occasionally visible when the sample was x-rayed immediately after deposition of tin from the alkaline bath: it was always visible when the sample was annealed at 100° in boiling water for 10 min or more after deposition. $FeSn_2$ was not detected when deposition was carried out from the acid bath. Annealing the sample for as long as 60 hr at 100° in boiling water did not result in the formation of $FeSn_2$ identifiable by x-ray diffraction techniques.

The alkaline bath differs from the acid bath in many respects but particularly in the fact that hydrogen is codeposited with tin in the alkaline bath. The importance of hydrogen was examined by several methods: (*A*) the sample was electrolytically precharged with hydrogen immediately before electrodeposition of tin from the acid bath; (*B*) the tin concentration in the acid bath was lowered to 0.001 of its ordinary value (0.1 g/l $SnSO_4$) and deposition was carried out at 8 amp/dm^2 and low current efficiency; (*C*) tin was electrodeposited from solutions containing 0.002-0.010 g/l of dissolved tin at 100°. $FeSn_2$ was occasionally detected in (*A*), it was detected in (*B*) after annealing at 100° for 10 hr, and it was always detected in (*C*). These experiments suggest that the codeposition of hydrogen favors the formation of $FeSn_2$.

The $FeSn_2$ diffraction line was very clear on samples in which iron was subjected to electrolysis at 1 amp/dm^2 for 6 hr in boiling 0.1M Na_2CO_3 solutions containing 0.002 g/l dissolved tin. Based on prior studies with radioactive tin (2) the rate constant for the pickup of tin by metallographically polished iron at 100° is 2×10^{-8} g/cm^2-sec$^{1/2}$. If the tin forms $FeSn_2$ as a continuous film, this rate constant indicates that a film 30Å thick should be formed in 6 hr. The clear diffraction line suggests that appreciably more $FeSn_2$ is present at the interface than is expected on the basis of thermal diffusion only. These experiments agree with experiments in the indium-antimony system (3) in which it was found that electrolysis increased the rate of formation of InSb.

Manuscript received Sept. 22, 1964.

Any discussion of this paper will appear in a Discussion Section to be published in the December 1965 JOURNAL.

REFERENCES

1. G. G. Kamm and A. R. Willey, "1st Int. Congress on Metallic Corrosion," p. 495, Butterworth's Press, London (1961).
2. W. Roger Buck, III, A. N. J. Heyn, and Henry Leidheiser, Jr., *This Journal*, **111**, 386 (1964).
3. Melvin C. Hobson and Henry Leidheiser, Jr., To be published.

Cryoscopic Studies of the Melting Point of Silver in High Pressure Oxygen

J. K. Johnstone[1]

Institute for Atomic Research and Department of Ceramic Engineering, Iowa State University, Ames, Iowa

The behavior of gases in metals is becoming increasingly important. Although this subject has received extensive attention for solid metals at pressures up to 1 atm, less emphasis has been placed on liquid metals at pressures above 1 atm.

The purpose of this work is to obtain data on the dissolution and behavior of oxygen in liquid silver at higher pressures. The system was chosen owing to the high solubility of oxygen in the liquid metal. Observations were made on the depression of the freezing point of silver as the oxygen pressure over the silver was increased.

Sieverts and Hagenacker (1) used the silver-oxygen system to show that the solubility of a diatomic gas in a liquid metal is proportional to the square root of the gas pressure, thereby proving that the gas dissolves as atoms rather than molecules (Sieverts' law for dilute solutions). This work was later confirmed by Stacie and Johnson (2) with respect to the solubility of oxygen in solid silver.

The only investigator who has studied the oxygen solubility in liquid silver at pressures substantially greater than 1 atm is Allen (3). The maximum pressure reported by Allen is 13.9 atm. The work also confirmed approximately Sieverts' law up to this pressure. The work reported here extends the pressure range to slightly more than 147 atm.

Since only the freezing point depression was measured, the discussion that follows will be based on the solubility data reviewed in Lumsden (4).

Experimental

The apparatus consisted of a resistance furnace mounted concentrically in a cylindrical, water-cooled pressure-vessel. The apparatus was essentially the same as that used by Baker (5) in a study of calcium carbonate where it is described in detail.

The furnace incorporated a porcelain tube with an inside diameter of 12 mm and a wall thickness of 2 mm. The tube was wound to a length of 9½ in. with 20 gauge 9:1 platinum-rhodium wire.

The pressure-vessel, which has been described previously, was constructed from a section of auto-frettaged gun-barrel with an inside diameter of 5.5 cm and a wall thickness of 2.75 cm. The space between the furnace and the vessel wall was packed with alumina powder.

The pressure and heating (cooling) rate were controlled manually. By this method, the pressures were accurate to ±0.5% and the freezing point temperatures were accurate to ±1°. Three Bourdon test gauges of 10 in. diameter were required to cover the pressure range of 1-147 atm.

Granular silver (— 20 mesh) of 99.9% purity and silver foil 0.004 in. thick and better than 99.9% purity were used for samples. Oxygen gas of 99.5% purity was used. The remaining 0.5% was argon. The available oxygen pressure was the limiting factor in this series of experiments. The oxygen was supplied from standard 2000 psi bottles from which 147 atm was the maximum attainable pressure. All thermocouples were made of Pt-Pt 13% Rh wire.

[1] Mr. Johnstone is the second recipient of the F. M. Becket Memorial Award of the Electrothermics and Metallurgy Division of the Society. See p. 120C of the May 1964 JOURNAL. The research was conducted under the supervision of Dr. E. H. Baker, Nuffield Research Group, Imperial College of Science and Technology.

The general procedure involved placing the sample in a crucible which was then placed in the furnace. The pressure-vessel was sealed in a nearly horizontal position to help eliminate convection currents caused by high-density gases at elevated temperatures and the furnace was heated at a rapid rate—15° to 20°/min —to 600°. At this temperature, the vessel was pressurized to the desired value after several flushings with oxygen at 20 atm pressure. From this point, the procedure was varied according to one of three methods used for the actual freezing point determination.

The first method employed was that of noting the thermal arrest in the cooling curve at the freezing point of the silver. The sample consisted of slightly more than 7g of granular silver placed in a silica crucible. A thermocouple encased in a silica tube was centered in the mass of silver. The sample was raised to a temperature approximately 30° above the expected freezing point of the silver and maintained at this temperature for 40 min. It was then cooled at a rate of 1°/min and the arrest temperature determined.

The method produced satisfactory results up to a pressure of 10 atm. At this pressure, the heat losses, owing to the high gas density, were of such magnitude that the arrest was very indistinct.

The second method involved the use of a D. T. A. technique. A strip of silver foil, 1 mm wide and 5-8 mm long was substituted for the junction of a thermocouple. (The best results were obtained when each end of the silver strip was welded to one of the thermocouple leads.) A standard thermocouple sealed in an alumina sheath was fixed next to the sample to insure an accurate measure of the temperature of the silver strip. The two thermocouples were then placed in a silica crucible and packed with — 10 mesh alumina granules. The alumina particles insured that the silver strip did not come into contact with the crucible as well as helping to eliminate further any convection currents in the gas.

The sample was heated to within 20° of the expected melting point where the heating rate was reduced to approximately 1.5°/min. At the melting point of the silver, the strip broke thus destroying the differential trace; this provided a well defined melting point.

This method provided accurate and consistent results up to a pressure of 50 atm. At this pressure the welds of the differential thermocouple leads to the silver strip oxidized causing an erratic emf.

The third and most reliable method involved the use of an independent electric circuit. The arrangement of the sample and the temperature thermocouple was identical to the D. T. A. method. However, rather than welding the sample to thermocouple leads, it was welded to two pure gold wire leads. The gold leads completed an electric circuit which consisted of a 1.5v dry cell battery, a 5000 ohm series resistance and a milliammeter, thereby providing an independent circuit.

The procedure for heating the sample was described in the previous method. When the silver strip melted, the electric circuit was broken as indicated by the milliammeter.

This method provided an extremely sharp and well defined melting point. Furthermore, at oxygen pressures up to 147 atm, there was no evidence of any oxidation of the welds between the silver strip and

gold wire or of the gold itself. This method was used to check several lower pressure results obtained by the previously described methods and good agreement was found.

At the conclusion of the test series, the thermocouples were checked to see if the surface oxidation of the thermocouple wire reported previously affected the emf which would result in faulty temperature measurement. The thermocouples were tested by determination of the melting point of potassium chloride in an oxygen pressure of 90 atm. Comparison of the observed and known melting point indicated that the thermocouple junctions were not measurably affected by the oxygen gas.

Results and Discussion

The experimental results are presented graphically in Fig. 1, where P is the oxygen pressure and T is absolute temperature. Due to the extremely small solubility of oxygen in solid silver (2), the curve can be regarded as representing the freezing point depression of pure silver.

The inset in Fig. 1 shows the relationship between the freezing point depression (curve A) and the silver oxide dissociation equilibrium (curve B). The equilibrium dissociation pressure of silver oxide was derived experimentally by Lewis (6) and confirmed by Keyes and Hara (7). The curve is defined by the equation

$$\log P = -\frac{2859}{T} + 6.2853$$

and covers a pressure range of from 20.5 atm to 388.3. atm. Brewer (8) has expressed doubt as to the reliability of the work done by Lewis (6) and Keyes and Hara (7) but offers no argument to support his position.

Allen extrapolated his work to intersect the silver oxide dissociation curve to determine a possible eutectic point for the Ag-Ag_2O system. This extrapolation (as well as a summary of past work involving the Ag-O_2-Ag_2O system) has been presented graphically by Vacher (9) and yields a eutectic with a temperature of 507°C and an oxygen pressure of 414 atm (point a, Fig. 1-inset). At the present, this work neither confirms nor disproves the values obtained by Allen. However, the freezing point depression data is tending toward the point suggested.

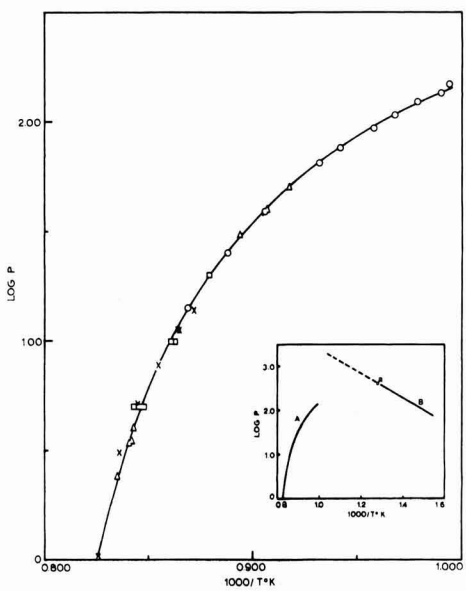

Fig. 1. Pressure-temperature diagram of freezing point depression: □, thermal arrest method; △, D. T. A. method; ○, independent electric circuit method; X, results obtained by Allen (3). Inset: Pressure-temperature diagram of freezing point depression (curve A) in relation to dissociation of Ag_2O (Curve B).

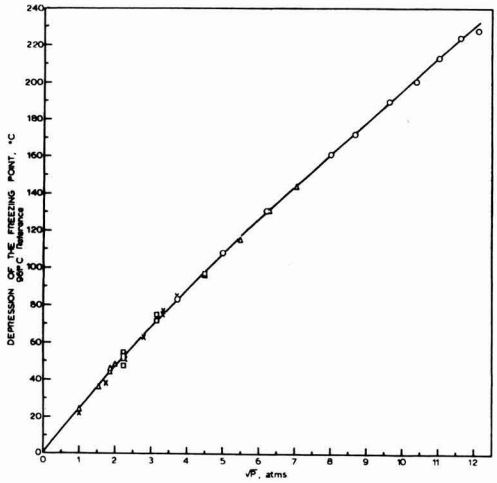

Fig. 2. Freezing point depression — $\sqrt{P}$ diagram

Allen showed for his range of pressures and temperatures (*i.e.*, to 13.9 atm and 876°C) that the depression of the freezing point was proportional to the $\sqrt{P}$. It is of interest to plot $\sqrt{P}$ against the freezing point depression for the results from the present work (Fig. 2). For pressures up to 4 atm a fair linearity is observed. At higher pressures and correspondingly higher concentrations of oxygen, deviation from the initial slope is apparent. This is to be expected at high concentrations and temperature changes.

The activity of the silver on the freezing point curve can be calculated by the van't Hoff equation in the form of

$$\ln a_{Ag} = \frac{\Delta H_{fus}}{R}\left[\frac{1}{T} - \frac{1}{T_{M.P.}}\right]$$

where $\Delta H_{fus} = 2855$ cal/mole (9) and $T_{M.P.} = 1234$°K. (By application of the Clausius-Clapeyron equation at the maximum pressure observed, it was calculated-assuming that the volume for liquid silver containing dissolved oxygen is not greatly different from the volume of pure liquid silver—that the lowering of the freezing point due to the pressure alone was less than 2°. Therefore, it is valid to consider the lowering of the freezing point of silver to be due solely to the solution of oxygen in the melt.) Using the eutectic temperature given by Allen, the activity of silver is calculated to be 0.508.

If the solution were roughly an ideal solution of oxygen atoms $N_o \cong 0.492$, where N_o is the atom fraction of oxygen in solution. This is greater than the oxygen content of pure liquid Ag_2O ($N_o = 0.333$). It is apparent that the oxygen at higher concentrations is present in some form other than oxygen atoms so that a greater depressive effect could be obtained for a given amount of dissolved oxygen. The possibility of the oxygen combining with silver to form Ag_2O is worth consideration. Such compound formation would certainly explain the observed temperature depression but, unfortunately, said formation can not be confirmed by the present work.

If the oxygen were present solely as oxygen atoms, the eutectic temperature would need to be higher than 642° (obtained through application of the van't Hoff equation for $N_o = 0.333$). It is difficult, however, to assign a reasonable equilibrium pressure at such a eutectic point limit which would fall on the silver-silver oxide line. Consequently, since the true state of

the dissolved oxygen at high concentrations is not known, it is preferable at this stage to regard the system as one involving Ag_2O.

From the above, it can be seen that it is essential to determine the compositions of the melts along the freezing point depression curve and to evaluate the pressure-temperature relation at the true eutectic point. Apparatus is being constructed for the last studies which will be made by Dr. E. H. Baker.

Acknowledgments

The author wishes to thank The Electrochemical Society for the F. M. Beckett award which made his participation in this work possible. Appreciation is also due Dr. E. H. Baker for his patient and invaluable guidance and Professor F. D. Richardson for his cooperation.

References

1. A. Sieverts and J. Hagenacker, *Z. physikal Chem.*, **68**, 115 (1909).
2. E. W. R. Stacie and F. M. G. Johnson, *Proc. Roy. Soc.*, **112A**, 542 (1926).
3. N. P. Allen, *J. Inst. Metals*, **49**, 317 (1932).
4. J. Lumsden, "Thermodynamics of Alloys," pp. 250-253, The Institute of Metals, London (1952).
5. E. H. Baker, *J. Chem. Soc.*, **87**, 464 (1962).
6. G. N. Lewis, *J. Am. Chem. Soc.*, **28**, 139 (1906).
7. F. G. Keyes and H. Hara, *ibid.*, **44**, 479 (1922).
8. L. Brewer, *Chem. Rev.*, **52**, 1 (1952).
9. K. K. Kelley, *U.S. Bur. of Mines Bull.*, No. **584**, 163 (1960).

Manuscripts and Abstracts for Fall 1965 Meeting

Papers are being solocited for the Fall Meeting of the Society, to be held at the Statler-Hilton Hotel in Buffalo, N. Y., October 10, 11, 12, 13, and 14, 1965. Technical sessions probably will be scheduled on: Batteries (including Symposia on Charging Characteristics of Batteries and Characteristics of Electrodes during Charging), Corrosion, Electrodeposition (including Symposium on Thin Film Technology), Electronics-Semiconductors, Electrothermics and Metallurgy (including a Symposium on Zirconium and Its Alloys).

To be considered for this meeting, **triplicate copies of the usual 75-word abstract, as well as of an extended abstract of 500-1000 words** (see notice on page 29C of this issue), must be received at The Electrochemical Society, 30 East 42 St., New York, N. Y., 10017, *not later than May 17, 1965.* (Papers solely sponsored by the Corrosion Division **do not** require an extended abstract.) *Please indicate on 75-word abstract for which Division's symposium the paper is to be scheduled, and underline the name of the author who will present the paper.* No paper will be placed on the program unless one of the authors, or a qualified person designated by the authors, has agreed to present it in person. Clearance for presentation of a paper at the meeting should be obtained before the abstract is submitted. An author who wishes his paper considered for publication in the JOURNAL or ELECTROCHEMICAL TECHNOLOGY should send triplicate copies of the manuscript to the Managing Editor of the appropriate publication 30 East 42 St., New York, N. Y., 10017. Concerning papers to be published in the JOURNAL, see notice on per page charge on page 32C of this issue.

Presentation of a paper at a technical meeting of the Society does not guarantee publication in the JOURNAL or ELECTROCHEMICAL TECHNOLOGY. However, all papers so presented become the property of The Electrochemical Society, and may not be published elsewhere, either in whole or in part, unless permission for release is requested of and granted by the Editor. Papers already published elsewhere, or submitted for publication elsewhere, are not acceptable for oral presentation except on invitation by a Divisional program Chairman.

FUTURE MEETINGS OF
The Electrochemical Society

★ ★ ★

San Francisco, Calif., May 9, 10, 11, 12, and 13, 1965

Headquarters at the Sheraton Palace

Sessions will be scheduled on Electric Insulation, Electronics (including Luminescence and Semiconductors and a Symposium on Optical Masers), Electro-Organic (including a Symposium on Industrial Organic Chemistry and a Symposium on Elucidation of Electro-Organic Electrode Processes jointly with the Theoretical Electrochemistry Division), Electrothermics and Metallurgy (including joint Symposium on Molten Salts jointly with the Theoretical Electrochemistry Division and, also, a Symposium on Strengthening Mechanisms in Nonmetallics), Industrial Electrolytic (including a Symposium on Electrolytic Diaphragms and Battery Separators jointly with the Battery Division and, also, a Symposium on the Production of Chlorine without Caustics)

★ ★ ★

Buffalo, N. Y., October 10, 11, 12, 13, and 14, 1965

Headquarters at the Statler-Hilton Hotel

Sessions probably will be scheduled on Batteries (including symposia on Charging Characteristics of Batteries and Characteristics of Electrodes during Charging), Corrosion, Electrodeposition (including Symposium on Thin Film Technology), Electronics—Semiconductors, Electrothermics & Metallurgy (including a Symposium on Zirconium and its Alloys)

★ ★ ★

Cleveland, Ohio, May 1, 2, 3, 4, and 5, 1966

Headquarters at the Sheraton-Cleveland Hotel

★ ★ ★

Philadelphia, Pa., October 9, 10, 11, 12, and 13, 1966

Headquarters at the Sheraton Hotel

★ ★ ★

Dallas, Texas, May 7, 8, 9, 10, and 11, 1967

Headquarters at the Hilton Hotel

★ ★ ★

Papers are now being solicited for the meeting to be held in Buffalo, N. Y., October 10, 11, 12, 13, and 14, 1965. **Triplicate copies of the usual 75-word abstract, as well as of an extended abstract of 500-1000 words** (see notice on the following page), are due at The Electrochemical Society, 30 East 42 St., New York, N. Y. 10017, *not later than May 17, 1965 in order to be included in the program.* (Papers sponsored solely by the Corrosion Division **do not** require an extended abstract.) *Please indicate on 75-word abstract for which Division's symposium the paper is to be scheduled, and underline the name of the author who will present the paper.* No paper will be placed on the program unless one of the authors, or a qualified person designated by the authors, has agreed to present it in person. Clearance for presentation of a paper at the meeting should be obtained before the abstract is submitted. An author who wishes his paper considered for publication in the JOURNAL or ELECTROCHEMICAL TECHNOLOGY should send triplicate copies of the manuscript to the Managing Editor of the appropriate publication, 30 East 42 St., New York, N. Y., 10017. Concerning papers to be published in the JOURNAL, see notice on per page charge on page 32C of the issue.

Presentation of a paper at a technical meeting of the Society does not guarantee publication in the JOURNAL or in ELECTROCHEMICAL TECHNOLOGY. However, all papers so presented become the property of The Electrochemical Society, and may not be published elsewhere, either in whole or in part, unless permission for release is requested of and granted by the Editor. Papers already published elsewhere, or submitted for publication elsewhere, are not acceptable for oral presentation except on invitation by a Divisional program Chairman.

Extended Abstract Book Publication Program for the Society's 1965 Fall Meeting in Buffalo, N. Y.

The Board of Directors has provided that the National Office shall assist Divisions with the mechanics of publishing Extended Abstracts for sessions involving 15 or more papers at our National Meetings.

The Divisions will handle the technical editing of the abstracts following which the Society Office will arrange for the printing and distribution of the books, thus relieving Division representatives of this responsibility. Each Division program will be the subject of a separate Extended Abstract Book. Papers sponsored solely by the Corrosion Division **do not** require an extended abstract.

This means that each author who submits a paper for presentation at our meeting should do three things:

1—Submit *three* **copies of the usual 75-word abstract of the paper for publication in the printed program of the meeting;**

2—Simultaneously submit *three* **copies of an extended abstract of the paper of 500-1000 words; and**

3—Send the 75-word abstract and the 500-1000-word extended abstract to Society Headquarters, 30 East 42 St., New York, N. Y., 10017, *not later than May 17, 1965.*

The Extended Abstract Books will be published by photo-offset reproduction *from typewritten copy submitted by the author.* Special care should therefore be given to the following typing instructions so as to establish uniformity in printing:

1—Abstracts are to be 500-1000 words in length.

2—Use white bond paper, size 8½ x 11 inches.

3—Abstracts should be typed SINGLE space.

4—Use 1¼ inch margins at the top and bottom and at the sides of each page.

5—All copy, including figures, symbols, and corrections, should be in black ink.

6—Figures should be pasted in within the typing dimensions indicated. Captions should be typed not wider than figure dimensions and pasted in proper place in the abstract. Figure captions should appear at bottom of figure. Table titles should appear at top of tables.

7—Wherever possible, avoid use of halftones.

8—Title of paper should be in capital letters. Author(s) name and affiliation should be typed immediately below. It is not necessary in the heading or body to designate paper as "Extended Abstract," or quote the Divisional Symposium involved.

9—Mail to Society Headquarters *unfolded.*

Members and JOURNAL subscribers will receive notice of Extended Abstracts Books to be scheduled for publication. The notices will be accompanied by order blanks for the copies desired. Orders should be submitted with remittance. The advance orders will be necessary for estimating numbers of books to be printed and will be mailed to purchasers prior to the Buffalo meeting. Some extra copies will be available at the meeting but the advance-paid order is the only way to be assured of getting copies.

Current Affairs

Yeager, Campbell, and Bechtold to Take Office in San Francisco

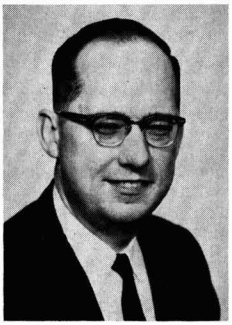

Ernest B. Yeager

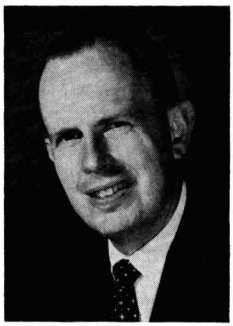

Ivor E. Campbell

Richard F. Bechtold

As a result of the recent annual election, in which the voting is by mail ballot, Ernest B. Yeager has been elected the new President (1965-1966) of The Electrochemical Society, Ivor E. Campbell has been elected Vice-President (1965-1968), and Richard F. Bechtold has been elected Secretary (1965-1968). They will take office at 8:00 A.M. Thursday, May 13, 1965, in San Francisco, Calif., during the Annual Spring Meeting of the Society.

Dr. Yeager, Professor of Chemistry, Western Reserve University, Cleveland, Ohio, replaces Dr. Lyle I. Gilbertson, who will continue as a member of the Board of Directors.

Dr. Ivor E. Campbell will complete in May, his second three-year term as Secretary of the Society.

Mr. Richard F. Bechtold, manager, Inorganic Chemical Products, Chemicals Department, The Dow Chemical Co., Midland, Mich., begins his first year of his three-year term as Secretary.

Dr. Ralph A. Schaefer, The Electric Storage Battery Co., Yardley, Pa., will start his second year as Treasurer.

Book Reviews

"Thermodynamics of Irreversible Processes," by P. Van Rysselberghe. Published by Blaisdell Publishing Co., New York, 1964. 152 pages; $7.50.

The monograph reviewed here is designed to introduce the intermediate student as rapidly as possible to irreversible thermodynamics, but avoiding, in the words of the introduction, "any discussion of fundamentals which would duplicate what is available in current textbooks." Since excellent textbooks do exist in this field which quite properly concern themselves with an exposition of fundamental principles, this monograph becomes a collection of calculations, unilluminated by the spirit of intellectual adventure.

The material covered is the standard one, treated more thoroughly and understandably by de Groot or Prigogine. Since principles are avoided, the discussion seems to lack coherence. At no point is the conceptual leap from "thermostatics" to the thermodynamics of irreversible processes mentioned. The Onsager relations are not justified. This reviewer objects to an original feature of this monograph: entropy, defined as a state function, is introduced in the chapter headed "First Law of Thermodynamics." The second law is not mentioned until two chapters hence and then is given no explicit justification. As a matter of fact, it is not clear what the second law really says. Furthermore, the concepts "reversible" and "irreversible" are used greatly in Chapter Two; they are not defined till Chapter Three.

Since the mathematical level of this book is the same as de Groot's, for example, it is not clear what purpose has been served by publishing what are admittedly informal lecture notes. I would strongly discourage any novice in the field from learning it here.

A. Biermann
City College of New York

"Comprehensive Analytical Chemistry, Vol. IIA, Electrical Methods," Edited by C. L. Wilson and D. W. Wilson. Published by Elsevier Publishing Co., Amsterdam, 1963. 268 pages; $11.00.

The stated aim of "Comprehensive Analytical Chemistry" is "to provide a work which, in many instances, should be a self-sufficient reference work; but where this is not possible, it should at least be a starting point for any analytical investigation." It is intended "to be utilized directly, not only by professional analytical chemists, but also by those workers whose use of analytical methods is incidental to their other work rather than continual."

Vol. IIA "begins the presentation of the various instrumental and physical methods that have been developed, largely in recent years, to supplement the classical processes described in Vol. I." It consists of an introduction and chapter on Electrodeposition by A. J. Lindsey, followed by chapters on Potentiometric Titrations and Conductometric Titrations by D. G. Davis, and High Frequency Conductometric

(Impedimetric) Titrations by T. S. Burkhalter.

In keeping with these stated objectives, the most useful features of this book are the descriptions of practical procedures for quantitative electrodeposition in Chapter II, and the tables of titrants and titration conditions for various reactions in Chapters III, IV, and V. As a convenient reference volume for information of this type, this book can be recommended.

Unfortunately, it shows signs of failings common to many multiauthored works. Judging from the lack of recent references (only three references more recent than 1959 were noted) the writing must have been completed several years ago. The approach is quite conventional, often to a distressing degree. In Chapter II, only reversible electrode reactions are considered, and archaic terms such as "minimum hydrogen overvoltages" are used. The brief section on diffusion in electrodeposition is confusing and downright misleading. In Chapter III, the Nernst equation is applied to irreversible electrode systems such as the permanganate-manganous ion couple and applied to calculations of the equivalence-point potentials of ferrous iron or vanadyl ion titrations with permanganate. The treatment of potentiometric acid-base titrations in nonaqueous solvents, of metal-ion indicating glass electrodes, and of the precision null-point potentiometric" method of Malmstadt are examples of subjects treated inadequately or omitted altogether. In Chapter V, no reference later than 1957 appears. Recent applications of high frequency titrations, such as Lewis acid base reactions, are therefore not included.

Altogether, this book cannot be recommended as a reliable source of fundamental background theory in electroanalytical chemistry, but it can serve the practicing chemist as a source of procedures and references for many practical applications.

H. A. Laitinen
University of Illinois

"Chemical Equilibria and Reaction Rates at High Pressure," by M. G. Gonikberg. Translated from the Russian. Published by The Israel Program for Scientific Translations, Israel, 1964. 212 pages; $8.00.

This is the only book dealing with high-pressure known to me, which is devoted entirely to purely chemical effects. Techniques of high-pressure research and physical changes induced by high-pressure are not discussed. In spite of this limitation the treatment is rather uneven and clearly reflects the interests of the authors and his colleagues at the N. D. Zelinsky Institute for Organic Chemistry of the Academy of Science of the U.S.S.R. in the fields in which they have made their own attempts at interpreting and generalizing experimental results, while in other areas the text is little more than an enumeration of references and their contents. The latter is in itself of interest since the coverage of the large volume of Russian work is more thorough than would perhaps be found in an English review, and since it includes much work done at a few hundred atmospheres which is often arbitrarily excluded from reviews of "high-pressure" research. Unfortunately the book is out of date as a review. The latest Russian reference is 1960 and the most recent other reference is 1959. In fact at least two review articles of the chemical aspects of high-pressure research have appeared in English since the book was written.

In Part I there is, under the heading "Mixtures of Real Gases," a discussion of some empirical equations of state followed by the discussion of a few industrially important equilibria. (Ammonia synthesis, methanol synthesis, hydration of ethylene, alkylation of hydrocarbons.) The next chapter deals with liquid and solid phase systems and mentions some decomposition, isomerization, and ionic dissociation equilibria. The discussion of gas-liquid and gas-solid solubility relations which follows is based mainly on Hildebrand's work. The final chapter of Part I gives a thermodynamic treatment of the effect of pressure on adsorption and then discusses the partial molar volume of electrolytes.

Part II deals with reaction rates and is again subdivided into chapters dealing with gaseous reactions, heterogeneous gaseous reactions, liquid phase reactions, and a short section on solid phase reactions. Some important contributions from the author's laboratory fall under these headings and are dealt with very thoroughly, particularly where the results, or their interpretation, are found to contradict other work. The

Battery Symposia Plans for 1965 Fall Meeting in Buffalo, N. Y., October 10-14, 1965

The Battery Division of the Society is planning symposia on "Charging Characteristics of Batteries" and on "Characteristics of Electrodes During Charging" for the 1965 Fall Meeting in Buffalo, N. Y., October 10-14, 1965. General sessions are also planned.

Triplicate copies of the usual 75-word abstract, as well as of an extended abstract of 500-1000 words (see notice p. 29C of this issue) should be sent to The Electrochemical Society, 30 East 42 St., New York, N. Y., 10017, or to Mr. T. J. Hennigan, Goddard Space Flight Center, Code 636-2, Greenbelt, Md., 20771, *not later than May 17, 1965.*

Symposium on Thin Film Technology Planned for 1965 Fall Meeting in Buffalo, N. Y., October 10-14, 1965

The Electrodeposition Division of the Society is planning a symposium on "Thin Film Technology" for the 1965 Fall Meeting to be held in Buffalo, N. Y., October 10-14, 1965. Papers are solicited in both basic and applied areas. Communications and inquiries should be addressed to Dr. I. W. Wolf, Ampex Corp., 401 Broadway-Ms 3-21, Redwood City, Calif.

Triplicate copies of the usual 75-word abstract as well as of an extended abstract of 500-1000 words (see notice p. 29C of this issue) should be sent to The Electrochemical Society, 30 East 42 St., New York, N. Y., 10017, *not later than May 17, 1965.*

Papers Solicited for Symposium on Zirconium and its Alloys for Fall 1965 Meeting in Buffalo, N. Y., Oct. 10-14, 1965

A Symposium on Zirconium and Its Alloys is being organized by the Electrothermics and Metallurgy Division as part of the 1965 Fall Meeting of The Electrochemical Society to be held in Buffalo, N. Y., October 10-14, 1965.

Sessions will be held on: Mechanisms of Corrosion and Oxidation Processes; Mechanisms of Hydrogen Pickup; Deformation and Fracture; Transformation and Diffusion; and Irradiation Effects.

Papers should consider the fundamental nature of the processes involved.

Symposium Co-Chairmen are: E. C. W. Perryman, Chemistry and Metallurgy Div., Atomic Energy of Canada Ltd., Chalk River, Ont., Canada and J. P. Pemsler, Ledgemont Lab., Kennecott Copper Corp., 128 Spring St., Lexington, Mass., 02173.

Triplicate copies of the usual 75-word abstract, as well as an extended abstract of 500-1000 words must be received at Society Headquarters, 30 East 42 St., New York, N. Y., 10017, *not later than May 17, 1965.*

Publication of papers from this Symposium is planned.

Authors are therefore requested to submit three copies of each manuscript to Dr. W. W. Smeltzer, Dept. of Metallurgical Engineering, McMaster University, Hamilton, Ont., Canada, as soon as is possible, prior to presentation of the paper at the National Meeting of the Society.

Frederick W. Fink Named Recipient of Frank Newman Speller Award

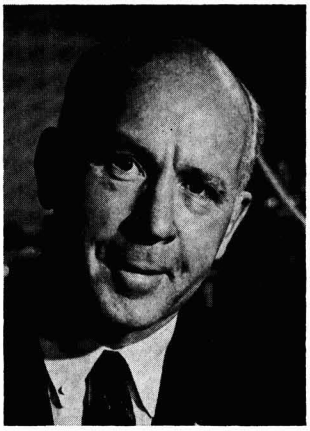

Frederick W. Fink, Battelle Memorial Institute, Columbus, Ohio, internationally recognized authority on the corrosion of materials, has been named to receive the Frank Newman Speller Award—one of the highest honors the National Association of Corrosion Engineers can bestow.

Formal presentation of the award, given in recognition of his contributions to corrosion engineering, will take place at the Association's annual conference in March in St. Louis, Mo.

A member of the staff of Battelle's Columbus Laboratories since 1938, Mr. Fink has had a key role in much of the Institute's corrosion research, particularly studies related to nonferrous metals and stainless steels. Currently he guides much of the Institute's expanding marine corrosion research activity. During the first half of this year he was on leave, serving as visiting professor of corrosion at the technical University of Denmark.

His studies have resulted in 47 technical papers and publications covering such diverse topics as the attack of magnesium by marine environments, metallic corrosion caused by flue-gas condensates, and corrosion in oil well equipment. Other subjects covered include corrosion problems involving such unusual metals as titanium, zirconium, beryllium, niobium, thorium, and uranium.

After receiving his electrical engineering degree from Cornell University in 1935, Mr. Fink studied and conducted corrosion research for two years at the University of Cambridge in England, where he received his master's degree.

Mr. Fink has been active in Society affairs, particularly in the Corrosion Division, following in the footsteps of his father, Colin Garfield Fink.

---

chapter on heterogeneous gas reactions discusses some industrially interesting reactions and ends with a section on the effect of compacting pressure on the activity and capacity of various catalysts. The longest discussion in this part of the book deals with liquid phase reactions and a rather controversial model for the transition state of SN_2 type reactions. This represents one of the major interests of the author and a good review of the, mostly quite old, material is given.

Part III starts with a rather superficial discussion of the effect of pressure on competing and on successive reactions, but then goes on to discuss some interesting polymerization reactions, and there is some attempt at generalizing the results of many different investigations. This is followed by a description of the author's own work on destructive hydrogenation which, like polymerization, proceeds by a free radical chain mechanism. Finally some work on the alkylation of hydrocarbons and the synthesis of hydrocarbons from carbon monoxide is described.

In conclusion I should say that the book is of interest to one who is concerned with the industrial possibilities of high-pressure reactions, but that there are more recent (and more expensive) books available which cover the field on a more academic level.

A. H. Ewald
University of Sidney

Division News

Electrodeposition Division

The annual meeting of the Electrodeposition Division was held in Washington, D. C., on October 14, 1964. It was presided over by the Chairman, Dr. Dennis R. Turner. The minutes of the last meeting were read and a financial report was presented by the Secretary-Treasurer, Mr. E. J. Smith.

A report on the Thin Film Technology Symposium to be presented at the Buffalo meeting in 1965 was given by Dr. Irving W. Wolf. Papers are being invited. The Electronics and Electrothermics and Metallurgy Divisions have expressed an interest in jointly sponsoring this symposium. Details are being worked out.

Future symposia were discussed and several suggestions will be investigated.

A report on "Modern Electroplating," Second Edition, was presented by Dr. F. A. Lowenheim who related that the book is selling very well.

Dr. H. J. Read reported on The Pennsylvania State conference on Electrodeposition. It was confirmed that the conference will be held at Penn State during the week of August 8, 1965. Dr. Read will contact people who may be interested in attending this symposium shortly after January 1, 1965.

The regular election of the Division was held. The slate of nominees was presented by Dr. D. Gardner Foulke, Chairman, Nominating Committee. There being no additions, the slate, as presented, was

Page Charge Adopted for the JOURNAL

Increased costs of publication have made it necessary for The Electrochemical Society to institute a per page charge for publication in the JOURNAL.

At the Meeting of the Board of Directors held in New York on September 29, 1963 a charge of $35.00 per printed page was established by the Board of Directors, on recommendation of the Publication and Finance Committees, for papers published in the JOURNAL. This action becomes effective for papers received after February 1, 1964.

A 10% reduction in the page charge will apply to papers authored by one or more members of The Electrochemical Society and/or by one or more employees of Patron or Sustaining Members of the Society.

Papers are accepted for publication on the basis of merit by established practices of review. Acceptance of future papers for publication will not be dependent on payment of this invoice. Where funds are not available for payment of this charge it will be waived by The Electrochemical Society.

unanimously elected. The new officers are as follows:

Chairman—Dan Trivich, 16204 Northlawn, Detroit 21, Mich.

Vice-Chairman—E. J. Smith, Coated Products, National Steel Corp., Weirton, W. Va.

Secretary-Treasurer—J. Petrocelli, Engineering Dept., Ford Motor Co., Detroit, Mich.

Members at Large—Fielding Ogburn, National Bureau of Standards, Connecticut and Van Ness, Washington, D. C., and I. W. Wolf, Ampex Corp., 401 Broadway, Redwood City, Calif.

The outgoing Chairman, Dr. Dennis R. Turner, received a note of thanks from those present at the conclusion of the meeting.

E. J. Smith,
Vice-Chairman

Personals

Edmund C. Potter, formerly scientific adviser at the Central Electricity Research Laboratories, Leatherhead, Surrey, England, has been appointed deputy director at the Water Research Association, Ferry Lane, Medmenham, Marlow, Buckinghamshire, England.

William H. Redanz has been named product manager for electrical products in the marketing organization of the Carbon Products Division of Union Carbide Corp. In his new position, Mr. Redanz will have product responsibility for boron nitride, spectroscopic products, and various electronic applications of carbon and graphite.

Gordon K. Teal has been appointed director of the Institute for Materials Research, National Bureau of Standards. Dr. Teal at present is assistant vice-president-international technical director for Texas Instruments Inc. and, early in January 1965, will accept the government responsibility for a period of approximately two years.

New Books

"Simultaneous Rapid Combustion, Microchemical Research Papers, of Mirra Osipovna Korshun, Vol. I," Edited by J. A. Kuck. Translated from the Russian. Published by Gordon and Breach Science Publishers, New York, 1964. 560 pages; $27.50.

There are 56 papers on quantitative organic microanalysis, mostly by Miss Korshun, who died in 1958. The latest paper cited dates from 1960.

"Concise Dictionary of Atomics," by A. Del Vecchio. Published by Philosophical Library, New York, 1964. 262 pages; $6.00.

A glossary of terms, with brief biographies of some scientists who have made contributions in the field.

"Electrical Conductance, Density, and Viscosity," by G. J. Janz, A. T. Ward, and R. D. Reeves. Published by Technical Bulletin Series, Rensselaer Polytechnic Institute, Troy, N. Y., 1964. 180 pages; $2.50.

Conductance, density, and viscosity data at round temperature values for 126 inorganic compounds as single-salt-melts. Based on an assessment of the original data (1830-1964), recalculated, graded, and weighed by computor.

News Items

1964 Annual Index for the Journal

The Annual Index for Volume 111 (1964) appears in this issue of the JOURNAL. There are two parts: Part I, the February JOURNAL; Part II, the Index for Volume 111 (1964). Part II is inserted in front of cover three of the JOURNAL.

Reprints of the Index can be obtained about March 15, 1965 by writing to The Electrochemical Society, Inc., 30 East 42 St., New York, N. Y., 10017.

Extended Abstract Books Available

The Electrochemical Society has entered into an agreement with Walter J. Johnson, Inc. to handle back issues of Extended Abstract Books from our twice yearly National Meetings, starting with the year 1963.

Although there are several titles which have sold out, many are available through the Johnson organization.

For orders and full particulars, please contact: Walter J. Johnson, Inc., 111 Fifth Avenue, New York 3, N. Y.

Obituary

Mrs. Lee O. Case

It is with deep regret that the Society announces the passing of Mrs. Lee O. Case (Ava to many of her friends). Mrs. Case died unexpectedly on December 15. Memorial Musical Services were held at the new School of Music Building, at the University of Michigan, on December 18 at 3:00 P.M.

Section News

(Left to right) Jerome Kuderna, Ralph J. Hovey, E. L. Koehler, Clifford A. Hampel, Raymond G. Chelton, Simon P. Gray, Jr., and Richard Scott Modjeska.

Chicago Section

On Thursday, December 10, 1964, the Chicago Section held a Past Chairmen's Award Meeting at the Chicago Engineers Club, in Chicago.

Awards were presented to Past Chairmen of the Chicago Section, shown in the above photograph, in recognition of services rendered to the Society.

Guest speaker for the technical portion of the meeting was Dr. David Levinson, Professor of Metallurgy, University of Illinois. His topic was "Principles and Applications of the Electron Microprobe."

James H. Lloyd,
Secretary

Cleveland Section

The Cleveland Section of the Society held a joint meeting with the Chemical Professions of Cleveland which took place on November 10, 1964 at the Cleveland Engineering and Scientific Center in Cleveland.

The following are the chairmen from six societies who took part in the joint meeting: Mr. A. Arters, American Chemical Society, Mr. John O'Hay, American Institute of Chemists; Mr. L. V. McCarty, The Electrochemical Society; Dr. L. L. Winters, Alpha Chi Sigma; Mr. Ralph Wolfe, Jr., Chemical Sales Club; and Dr. Emerson Lynn, Jr., American Institute of Chemical Engineers.

Guest speakers of the evening were Dr. J. S. Millis, Western Reserve University, whose topic was "The Changing Scene in the Education of Scientists," and Dr. Louis Gordon, Case Institute of Technology, who spoke on "Education of the Chemist, Today and Tomorrow."

L. F. Urry,
Program Chairman

Detroit Section

The 1964-1965 season of the Detroit Section of the Society is now well under way, the following two very rewarding talks have been delivered to date.

On October 1, 1964 Professor Thedford P. Dirkse, chairman of the Department of Chemistry, Calvin College, Grand Rapids, Mich., gave a talk entitled "The Silver Oxide Electrode." The various oxides and oxidation states of silver in strongly alkaline solutions were discussed. Special emphasis was placed on those aspects of these oxides which are significant in the operation of silver alkaline batteries. In addition, the current situation regarding the structure of AgO was discussed.

On November 19, 1964 Mr. James E. Stephenson, representative of the Michigan Patent Law Association, spoke on "Basic Patent Law and Its Future." This talk gave a general outline of the present status of Patent Law with some predictions of future developments. The patent law situation in various foreign countries was also covered.

The discussion session after each talk was quite lively and indicated that the topics covered were of great interest to the members of the Section.

George C. Allen,
Vice-Chairman

Indianapolis Section

The Indianapolis Section held its first fall, 1964 meeting on December 1, 1964 at Butler University. About forty attendees heard Dr. Robert B. Watson from the Army Research Office give an interesting and informative presentation of "Lasers and Their Applications."

Dr. Watson demonstrated a gas laser and Dr. Milton Stern from the Linde Speedway Laboratory provided a display of ruby and other crystals.

Lowell F. Howard,
Secretary-Treasurer

New York Metropolitan Section

At the Board Meeting preceding the last meeting of the New York Metropolitan Section of the Society, the problems of encouraging student participation in the activities of the Society were discussed. As a result of this discussion, a motion was passed providing funds for this program.

Under this plan, professors interested in electrochemistry at local schools will be encouraged to bring interested graduate students to attend the dinner meetings as guests of the Section. This problem was initiated with the January 13th meeting. Current plans call for approximately 3 graduate students to be invited to each of the meetings of the season.

Jerome Goodkin,
Assistant Secretary

Pittsburgh Section

The Pittsburgh Section of the Society held a symposium on "Intermetallic Compounds" on October 30, 1964 at the Jones and Laughlin Graham Research Lab. in Pittsburgh. The meeting was most interesting and was well attended. The following papers were presented:

W. G. Fricke—"Interface Reactions in Soldering, Welding, and Brazing of Aluminum."

D. Feucht—"Semiconductor Heterojunction Interfaces."

W. T. Reynolds—"A Review of Superconducting Intermetallic Compounds."

G. G. Kamm—"The Role of the Tin-Iron Alloy in Tinplate Corrosion."

Discussion by M. G. Vucich and W. Batz.

H. E. Biber—"A Further Study of the Kinetics of Formation of Iron-Tin Alloy Layers."

J. R. Conner,
Secretary-Treasurer

Positions Wanted

R&D with small-medium size company in the capacitor field. Have European degree and several years U.S. experience. *Reply to Box A 303, c/o The Electrochemical Society, Inc., 30 East 42 St., New York, N. Y. 10017.*

Ph.D. equivalent, 30, single, U.S. citizen, 6 years industrial R & D in deposition (electroless, electrolytic, vacuum) of metals (from electroforms to thin films) for industrial finishes and electronic devices. Thorough physical, structural, electrical and magnetic investigation, and mechanisms of electrodeposition. East or Midwest preferred. *Reply to: Box A 305, c/o The Electrochemical Society, Inc., 30 East 42 St., New York, N. Y., 10017.*

Position Available

Chemical or Electrical Engineer experienced in storage battery manufacturing Southwest U.S. area. Mail details of education, experience, and personal background to *Box A 304,* c/o The Electrochemical Society, Inc., 30 East 42 St., New York, N. Y., 10017.

The Electrochemical Society

INSTRUCTIONS TO AUTHORS OF PAPERS

(Revised as of 4/1/64)

Address all correspondence to the Editor, JOURNAL OF THE ELECTROCHEMICAL SOCIETY, 30 East 42 St., New York, N. Y., 10017

GENERAL

Manuscripts must be submitted in triplicate to expedite review. They should be typewritten, double-spaced, with 2½-4 cm margins.

Title should be brief, followed by the author's name and professional connection. Authors should be as brief as is consistent with clarity and should omit introductory or explanatory material which may be regarded as familiar to specialists in the particular field. Proprietary and trade names should be avoided if possible; if used, they should be capitalized to protect the owners' rights.

Authors may suggest qualified reviewers for their papers, but the JOURNAL reserves the right of final choice.

TYPES OF ARTICLES

Technical Articles must describe original research of basic nature and must have adequate scientific depth. Articles of wide diversity of interest are appropriate, but subjects primarily covered in other specialized journals (*e.g.*, analytical or nuclear chemistry) are not considered appropriate. An ***Abstract*** of about 100 words should state the scope of the paper and summarize its results. Suitable headings and subheadings should be included, but sections should not be numbered. Articles in recent issues of the JOURNAL should be consulted for current style.

Technical Notes are used for reporting briefer research, developmental work, process technology; new or improved devices, materials, techniques, or processes which do not involve more extensive basic scientific study. No abstract is required.

Brief Communications are used only to report new information of scientific or technological importance which warrants rapid dissemination.

ILLUSTRATIONS

Drawings and ***Graphs*** ordinarily will be reduced to column width, 8.3 cm, and after such reduction should have lettering no less than 0.15 cm high. Lettering must be of letter-guide quality. India ink on tracing cloth or paper is preferred, but India ink on coordinate paper with blue ruling is acceptable. The sample graph shown on the reverse page conforms to suggestions of the American Standards Association (ASA Report Y15.1-1959).

Photographs should be used sparingly, must be glossy prints, and should be mailed with protection against folding. ***Micrographs*** should have a labeled length unit drawn or pasted on the picture.

Captions for figures (including photographs) must be included on a separate sheet. Captions and figure numbers must *not* appear in the body of the figure; they will be removed if they do.

Numerical Data should not be duplicated in tables and figures.

EQUATIONS

Mathematical Equations should be written on a single line if possible, and parentheses, brackets, the solidus (/), negative exponents, etc., may be used freely for this purpose. Authors are urged to consult Chapter VI of the "Style Manual" of the American Institute of Physics (available for $1.00 at American Institute of Physics, 57 East 55 St., New York, N. Y., 10022) and to follow the patterns described there.

SYMBOLS

If more than a few ***Symbols*** are used, they should be defined in a list at the end of the paper, with units given. For example:

$a, b \ldots =$ empirical constants of Brown equation

$f_i^\circ =$ fugacity of pure ith component, atm

$D_v =$ volume diffusion coefficient, cm^2/sec

ABBREVIATIONS UNITS

The AIP "Style Manual" referred to here gives a suitable list of common ***Abbreviations.*** Units usually will be abbreviated without periods throughout the text, as sec, min, hr, cm, mm, etc. **Metric Units** should be used throughout, unless English units are clearly more appropriate in the area of discussion.

POTENTIAL SIGNS

Electrode Potentials: Authors are urged to state and make use of the polarity of test electrodes with respect to the reference electrode used, *i.e.,* Zn is normally negative, Cu normally positive with respect to the standard hydrogen electrode. The sign for the emf of a cell should conform to the free energy change of the chemical reaction as written or implied, in accordance with the definition $\Delta G = -nFE$. These suggestions agree with the IUPAC conventions adopted in 1953. If any other convention is used, it should be stated clearly and used consistently throughout the manuscript.

REFERENCES

Literature References should be listed on a separate sheet at the end of the paper in the order in which they are cited in the text. Authors' initials must be given, and the style and abbreviations adopted by *Chemical Abstracts* should be used. Any recent issue of the JOURNAL may be consulted.

PUBLICATION CHARGE

A charge of $35 per printed page is made for publication of technical material in THIS JOURNAL. A 10% reduction is allowed if at least one author of an article is an ECS member or an employee of a Patron or Sustaining Member firm. However, acceptance of a manuscript is in no way dependent on such payment, and the charge may be waived in individual cases.

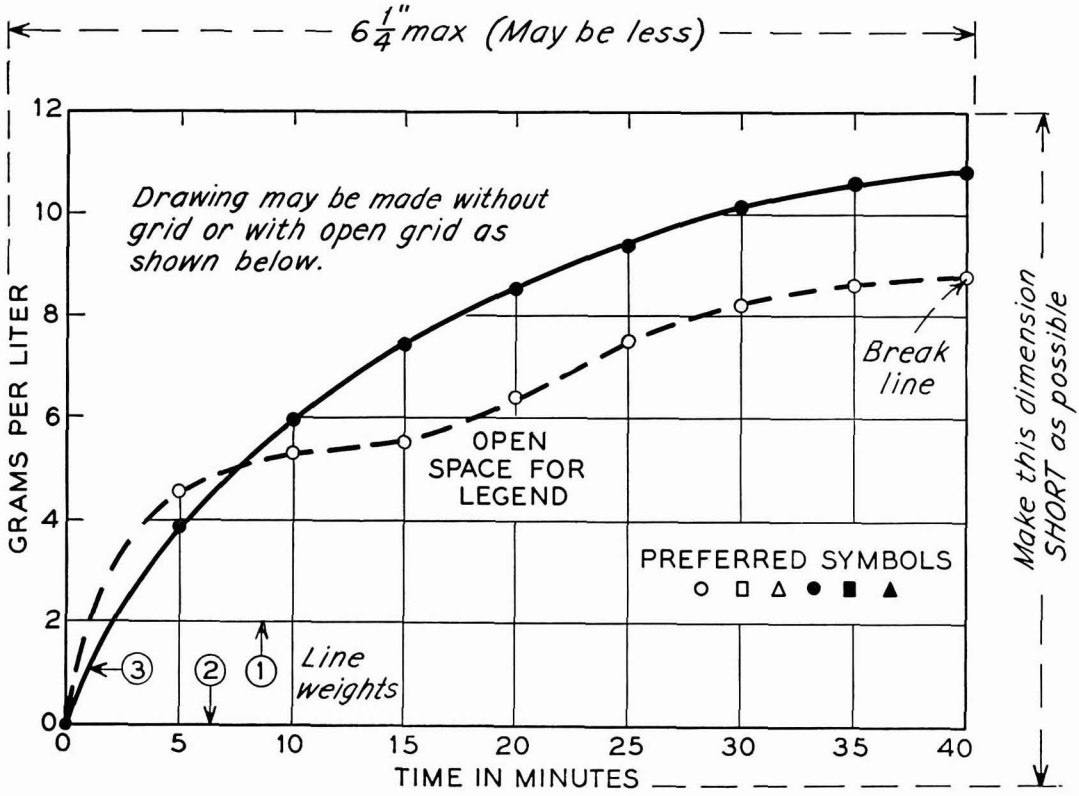

Remarks: Line weight 2 is used for borders and zero lines. When several curves are shown, each may be numbered and described in the caption. Lettering shown is approximately ⅛ in. In plotting current or potential as ordinate, increasing negative values should go down.

SAMPLE CURVE DRAWING FOR REDUCTION TO $\frac{1}{2}$ SIZE

The Electrochemical Society

Patron Members

Aluminum Co. of Canada, Ltd.,
Montreal, Que., Canada
The Dow Chemical Co.,
Chemical Dept., Midland, Mich.
Metals Dept., Midland, Mich.
International Nickel Co., Inc.,
New York, N. Y.
General Electric Co.
Capacitor Dept., Hudson Falls, N. Y.
Chemical Laboratory, Knolls Atomic Power Laboratory, Schenectady, N. Y.
Chemical and Materials Engineering Laboratory, Advanced Technology Laboratories, Schenectady, N. Y.
Chemistry Research Dept., Schenectady, N. Y.
Direct Energy Conversion Operation, West Lynn, Mass.
Lamp Division, Cleveland, Ohio
Materials & Processes Laboratory, Large Steam Turbine-Generator Dept., Schenectady, N. Y.
Metallurgy and Ceramics Research Dept., Schenectady, N. Y.
Olin Mathieson Chemical Corp.,
Chemicals Div., Research Dept., New Haven, Conn.
Union Carbide Corp.
Divisions:
Carbon Products Div., New York, N. Y.
Consumer Products Div., New York, N. Y.
Westinghouse Electric Corp., Pittsburgh, Pa.

Sustaining Members

Air Reduction Co., Inc., New York, N. Y.
Allen-Bradley Co., Milwaukee, Wis.
Allied Chemical Corp.
General Chemicals Div., Morristown, N. J.
Alloy Steel Products Co., Inc., Linden, N. J.
Aluminum Co. of America,
New Kensington, Pa.
American Metal Climax, Inc.,
New York, N. Y.
American Potash & Chemical Corp.,
Los Angeles, Calif.
American Smelting and Refining Co.,
South Plainfield, N. J.
American Zinc Co. of Illinois,
East St. Louis, Ill.
American Zinc, Lead & Smelting Co.,
St. Louis, Mo.
M. Ames Chemical Works, Inc.,
Glen Falls, N. Y.
Ampex Corp., Redwood City, Calif.
Armco Steel Corp., Middletown, Ohio
Basic Inc., Bettsville, Ohio
Bell Telephone Laboratories, Inc.,
New York, N. Y. (2 memberships)
Bethlehem Steel Co., Bethlehem, Pa.
(2 memberships)
Boeing Co., Seattle, Wash.
Burgess Battery Co., Freeport, Ill.
(2 memberships)
Burndy Corp., Norwalk, Conn.
Canadian Industries Ltd., Montreal,
Que., Canada
Carborundum Co., Niagara Falls, N. Y.
Chrysler Corp., Detroit, Mich.
Consolidated Mining & Smelting Co. of Canada, Ltd., Trail, B. C., Canada
(2 memberships)
Continental Can Co., Inc., Chicago, Ill.
Corning Glass Works, Corning, N. Y.
Diamond Alkali Co., Painesville, Ohio
Wilbur B. Driver Co., Newark, N. J.
(2 memberships)
E. I. du Pont de Nemours & Co., Inc.,
Wilmington, Del.
Eagle-Pitcher Co., Chemical and Metals Div.,
Joplin, Mo.
Eastman Kodak Co., Rochester, N. Y.
Eltra Corp.,
Prestolite Div., Toledo, Ohio
C&D Batteries, Conshohocken, Pa.
Electric Storage Battery Co.,
Philadelphia, Pa. (2 memberships)
Engelhard Industries, Inc., Newark, N. J.
(2 memberships)
The Eppley Laboratory, Inc., Newport, R. I.
Exmet Corp., Bridgeport, Conn.
Fairchild Semiconductor Corp., Palo Alto,
Calif.
FMC Corp.
Inorganic Chemical Div., Buffalo, N. Y.
Chlor-Alkali Div., South Charleston, W. Va.
Foote Mineral Co., Exton, Pa.
Ford Motor Co., Dearborn, Mich.
General Motors Corp.
Allison Div., Indianapolis, Ind.
Delco-Remy Div., Anderson, Ind.
Research Laboratories Div., Warren, Mich.
General Telephone & Electronics
Laboratories Inc., Bayside, N. Y.
(2 memberships)
Globe-Union, Inc., Milwaukee, Wis.
B. F. Goodrich Chemical Co.,
Cleveland, Ohio
Gould-National Batteries, Inc.,
Minneapolis, Minn.
Great Lakes Carbon Corp., New York, N. Y.
Hanson-Van Winkle-Munning Co.
Matawan, N. J. (2 memberships)

(Sustaining Members con'd)

Harshaw Chemical Co., Cleveland, Ohio (2 memberships)
Hercules Powder Co., Wilmington, Del.
Hill Cross Co., Inc., West New York, N. J.
Hoffman Electronics Corp., Semiconductor Div., El Monte, Calif.
Honeywell Inc., Minneapolis, Minn.
Hooker Chemical Corp., Niagara Falls, N. Y. (3 memberships)
HP Associates, Palo Alto, Calif.
Hughes Research Laboratories, Div. of Hughes Aircraft Co., Malibu, Calif.
International Business Machines Corp., New York, N. Y.
International Minerals & Chemical Corp., Skokie, Ill.
International Resistance Co., Philadelphia, Pa.
ITT Federal Laboratories, Div. of International Telephone & Telegraph Corp., Nutley, N. J.
Jones & Laughlin Steel Corp., Pittsburgh, Pa.
K. W. Battery Co., Skokie, Ill.
Kaiser Aluminum & Chemical Corp.
Div. of Chemical Research, Permanente, Calif.
Div. of Metallurgical Research, Spokane, Wash.
Kawecki Chemical Co., Boyertown, Pa.
Kennecott Copper Corp., New York, N. Y.
Leesona Moos Laboratories, Div. of Leesona Corp., Jamaica, N. Y.
Arthur D. Little, Inc., Cambridge, Mass.
Lockheed Aircraft Corp., Missiles & Space Div., Sunnyvale, Calif.
Mallinckrodt Chemical Works, St. Louis, Mo.
P. R. Mallory & Co., Indianapolis, Ind.
Melpar, Inc., Falls Church, Va.
Metal Pumping Services Cleveland, Ohio
Miles Chemical Co., Div. of Miles Laboratories, Inc., Elkhart, Ind.
Monsanto Chemical Co., St. Louis, Mo.
M&T Chemicals Inc., Detroit, Mich.
National Cash Register Co., Dayton, Ohio
National Lead Co., New York, N. Y.
National Research Corp., Cambridge, Mass.
National Steel Corp., Weirton, W. Va.
North American Aviation, Inc., El Segundo, Calif.
Northern Electric Co., Montreal, Que., Canada
Norton Co., Worcester, Mass.
Owens-Illinois Glass Co., Toledo, Ohio
Pennsalt Chemicals Corp., Philadelphia, Pa.
Phelps Dodge Refining Corp., Maspeth, N. Y.
Philco Corp., Research Div., Blue Bell, Pa.
Philips Laboratories, Inc., Briarcliff Manor, N. Y.
Pittsburgh Plate Glass Co., Chemical Div., Pittsburgh, Pa.
Potash Co. of America, Carlsbad, N. Mex.
Radio Corp. of America
Electronic Components and Devices, Lancaster, Pa.
Tube Div., Harrison, N. J.
RCA Victor Record Div., Indianapolis, Ind.
Raytheon Co., Waltham, Mass.
Reynolds Metals Co., Richmond, Va.
Shawinigan Chemicals Ltd., Montreal, Que., Canada
Socony Mobil Oil Co., Inc., Dallas, Texas
Speer Carbon Co.
International Graphite & Electrode Div., St. Marys, Pa.
Sprague Electric Co., North Adams, Mass.
Stackpole Carbon Co., St. Marys, Pa.
Stauffer Chemical Co., New York, N. Y.
Texas Instruments, Inc., Dallas, Texas
Metals and Controls Corp., Attleboro, Mass.
3M Company, St. Paul, Minn.
Titanium Metals Corp. of America, Henderson, Nev.
Tyco Laboratories, Inc., Waltham, Mass.
Udylite Corp., Detroit, Mich. (4 memberships)
United States Borax & Chemical Corp., Los Angeles, Calif.
United States Steel Corp., Pittsburgh, Pa.
Univac, Div. of Sperry Rand Corp., New York, N. Y.
Universal-Cyclops Steel Corp., Bridgeville, Pa.
Upjohn Co., Kalamazoo, Mich.
Western Electric Co., Inc., Chicago, Ill.
Wyandotte Chemicals Corp., Wyandotte, Mich.
Yardney Electric Corp., New York, N. Y.